Searching for Solar Axions in the eV-Mass Region with the CCD Detector at CAST

Julia Katharina Vogel

FAKULTÄT FÜR MATHEMATIK UND PHYSIK
ALBERT-LUDWIGS-UNIVERSITÄT FREIBURG

Searching for Solar Axions in the eV-Mass Region with the CCD Detector at CAST

Dissertation
zur
Erlangung des Doktorgrades
der
Fakultät für Mathematik und Physik
der
Albert-Ludwigs-Universität
Freiburg im Breisgau

vorgelegt von
Julia Katharina Vogel
aus Memmingen

April 2009

Dekan:	**Prof. Dr. Kay Königsmann**
Leiter der Arbeit:	**Prof. Dr. Kay Königsmann**
Referent:	**Prof. Dr. Kay Königsmann**
Korreferent:	**Prof. Dr. Markus Schumacher**
Tag der Verkündigung des Prüfungsergebnisses:	**20. Mai 2009**

Contents

Chapter 1

Introduction

> The most exciting phrase to hear in science, the one that heralds the most discoveries, is not “Eureka!” (I found it!) but “That’s funny...”.
>
> **Isaac Asimov**, Scientist and Author

Surprises have always played an important role in scientific research because an indication of where to look for new physics is generally originating from those parts of a theory which fail to describe reality. The Standard Model (SM) of particle physics has been quite successful in providing explanations to numerous problems. Nevertheless it is unlikely to be the final theory, since it falls short of answering many important questions. The SM includes, for instance, only three of the four fundamental forces, since it does not account for gravity. Furthermore there are at least 19 arbitrary parameters required to fit the available data. Another of the puzzling questions the SM is unable to answer is the so-called strong CP-problem in Quantum Chromodynamics (QCD), the theory of strong interactions. This problem is the baffeling question why the strong force in nature does not appear to break the combination of charge conjugation and parity transformation as expected from theory.
A possible solution to the strong CP-problem was formulated by Roberto Peccei and Helen Quinn in 1977. Unlike other attempted answers to this open question, they managed to explain the apparent conservation of CP in strong interactions by introducing just one additional symmetry, which is now referred to as the Peccei-Quinn-symmetry (PQ-symmetry). When this new symmetry is spontaneously broken at a yet unknown breaking scale f_a, it gives rise to a Goldstone boson as Steven Weinberg and Frank Wilczek pointed out independently in 1978. This new neutral and light pseudo-scalar particle is the axion. Since these hypothetical particles tidy up a problem of physics, Wilczek named them with a whimsical smile after a washing detergent.

Axions, if they exist, could play an important role in the history of the universe. They may have been produced shortly after the Big Bang and could still be created today in the core of stars as for example our Sun. Relic axions produced in the early universe could contribute significantly to the cold dark matter component of the cosmos. Dark matter is expected to account for about 20% of the density of the universe.

The original axion theory as suggested by Peccei and Quinn, which assumes the spontaneous breaking of the PQ-symmetry around the electroweak scale, could be ruled out rather quickly. The search for so-called *invisible* axions, however, still continues. These axions of masses below 1 eV would couple only very feably to fundamental particles and thus be extremely challenging to detect. In order to constrain the parameter space possible for axions, various bounds have been derived from astrophysics and cosmology. Thus the remaining window in which axions can still exist reaches from masses of μeV to about 1 eV. Various experiments have been searching for the elusive particle in and close to this mass region. Different methods have been applied in the attempt to detect the hypothetical particle, with most experiments employing the so-called Primakoff effect. It allows for conversion of axions into photons and vice versa in the presence of strong electromagnetic fields.

The Sun as the closest available celestial source of axions is especially attractive for studies. Experiments attempting to observe Primakoff-produced solar axions are generally referred to as helioscopes. The most sensitive existing helioscope is the CERN Axion Solar Telescope (CAST), which utilizes a prototype of a superconducting LHC dipole magnet providing a magnetic field of up to 9 T. CAST is able to follow the Sun twice a day during sunset and sunrise for a total of about 3 h. At both ends of the 10 m long magnet X-ray detectors have been mounted to search for photons from Primakoff conversion. Installed on one end of the magnet, a conventional Time Projection Chamber (TPC) searches for the signature of axions during sunset. On the other side of the solenoid two further detectors are mounted waiting for an axion signal during sunrise. One of the ports of the dipole is covered by a novel MICROMEsh GAseous Structure (MICROMEGAS, MM) detector, while the other is occupied by an X-Ray telescope consisting of X-ray mirror optics with a Charge Coupled Device (CCD) as a focal plane detector. For the latest runs of CAST the TPC covering both magnet bores was replaced by two additional MICROMEGAS detectors to further improve the sensitivity of the experiment.
In order to investigate different axion mass ranges, the CAST experiment consists of two phases. In its first stage with an evacuated magnetic field region, masses up to 0.02 eV were investigated with very high sensitivity. To extend this range towards higher masses, helium has been filled inside the cold bore, restoring the coherence for axions-to-photon conversion. Since the magnet is operated at 1.8 K, ^{4}He gas can only be used up to a pressure of 16.4 mbar, for which it liquefies, and it has to be substituted by ^{3}He to continue the search.

The most sensitive detector system used at CAST is the X-ray telescope. Its two constituents, i.e. the X-ray mirror optics and the CCD detector, were originally built for satellite space missions. Their combined use provides the X-ray telescope with the highest axion discovery potential of all CAST detectors during both, Phase I and II, along with an excellent imaging capability. The implementation of the X-ray mirror optics suppresses background by a factor of 155, since the photons are focused from the magnet aperture area of 14.5 cm^2 to a spot of roughly 9.3 mm^2 on the CCD chip. Consequently the sensitivity of the CAST experiment profits significantly from the use of the X-ray telescope.

The first phase of CAST succeeded in 2004 with two years of data yielding an upper limit on the axion-to-photon coupling of $g_{a\gamma} < 8.8\times10^{-11}$ GeV^{-1} (95% C.L.) for axion masses $m_a \lesssim 0.02$ eV.

During the first part of Phase II in 2005 and 2006 the magnet was filled with ^{4}He gas. CAST measured a total of 162 different pressure settings, 149 of them were covered by the CCD detector. The measured ^{4}He pressures reached from 0.08 mbar to 13.43 mbar in steps of 0.08-0.09 mbar. Thus axion masses up to 0.4 eV were covered with high sensitivity extending the axion search far into formerly unexplored regions preferred by theoretical models. Since 2007, CAST has been aquiring data with ^{3}He covering more than 250 pressure settings up to date. In this way the limits will be pushed further into the model regions.

This thesis is devoted to the analysis of the ^{4}He data acquired with the CCD detector at the CAST experiment. As result of this analysis, an upper limit on the axion-to-photon coupling constant $g_{a\gamma}$ will be determined, since no significant signal above background was observed.
A general introduction to Quantum Chromodynamics and the origins of the strong CP-problem, which led to the postulation of the axion as a possible solution, will be given in Chapter 2. Following this an overview of general axion physics can be found in Chapter 3, which includes a discussion of axion properties and the different axion models that have been suggested. Furthermore constraints on the axion mass and its coupling to fundamental particles obtained from astrophysics, cosmology and past or present axion experiments will be discussed. In Chapter 4, the focus is then put on axions originating from the core of the Sun, which helioscopes are attempting to detect. Here especially the expected solar axion flux and the probability of conversion for axions into photons in the presence of a strong magnetic field will be of interest. CAST as such a helioscope experiment will be presented in Chapter 5 including an introduction to the experimental setup, the movement system and its surveillance as well as the vacuum and gas systems of the experiment. The CAST detectors utilized for the ^{4}He phase will be briefly described. Following this a more detailed look at the X-ray telescope detector system will be taken in Chapter 6. The basis of the analysis presented in this thesis is the data acquired during CAST's Phase II with ^{4}He gas in the cold bore and therefore in Chapter 7 an overview on these data will be given. Following this, the analysis will be presented in Chapter 8 and it will result in the most stringent experimental upper limit on $g_{a\gamma}$ in a wide axion mass range. Chapter 9 will conclude this work summarizing the results. The axion parameter space CAST explores in its Phase II is especially interesting, since it is favored by theoretical axion models and no other experiment so far has been able to investigate this promising mass range with a sensitivity comparable to the one of CAST.

Chapter 2

The Strong CP-Problem in Quantum Chromodynamics

In order to provide an introduction to axion physics, this chapter will give a brief overview of the standard model (SM) of particle physics. Secondly its most important symmetries, namely parity transformation (P), charge conjugation (C) and time reversal (T) will be covered. Following this, it will be shown how a violation of the combination of the former two symmetries (CP) is naturally embedded in the electro-weak interactions in the SM. Then the situation for the strong interactions will be introduced which will lead to the theoretical problems referred to as $\mathrm{U(1)_A}$-problem and strong CP-problem. They can be solved by the introduction of a new symmetry which will result in a new (yet hypothetical) particle, the axion.

2.1 The Standard Model of Particle Physics, Symmetries and Gauge Theories

The standard model of particle physics provides a description of the elementary particles and three of the four known interactions between them. It is a realtivistic quantum field theory and includes the electroweak theory as well as quantum chromodynamics (QCD) in the frame of the structure $\mathrm{SU(3)_C}\times\ \mathrm{SU(2)_L}\times\ \mathrm{U(1)_Y}$. Here the gauge group $\mathrm{SU(3)_C}$ forces the existence of the gluon fields which enable the strong interactions between quarks. The corresponding charge in this case is color. The other two symmetry groups, $\mathrm{SU(2)_L}$ and $\mathrm{U(1)_Y}$, represent the electroweak interaction theory with the corresponding weak charge isospin L and (weak) hypercharge Y, respectively. The elementary particles of the SM are fermions, i.e. quarks and leptons, and vector bosons which are mediating the fundamental forces: photons for the electromagnetic interactions, W and Z bosons for the weak interactions and the gluons for the strong interactions. The Higgs boson as the remainder of the Higgs field after electroweak symmetry breaking has not (yet) been observed but will be looked for eagerly at the Large Hadron Collider (LHC) at CERN[1] in the near future. The major drawback of the SM is that it does not include the fourth interaction (gravity) and that its 19

[1] Conseil Européen pour la Recherche Nulcléaire

free parameters[2] have to be determined experimentally since they cannot be derived directly from the theory.
As already indicated above, symmetries play an important role in Physics. They are connected with conservation laws via Noether's theorem which states that there is a correspondance of a conservation law (i.e. a conserved current and charge) with the invariance of the Lagranian under a continous symmetry [1]. Instead of deducing conservation laws from symmetries of the Lagrangian, one can also approach the situation from the opposite direction, i.e. obtain the necessary symmetries of the Lagrangian using observed conservation laws.
Symmetries can be classified in two major groups, namely local and global symmetries. If a symmetry holds at all points in space-time, then it is referred to as global, while it is local if it is valid for a certain subset of space-time. The latter symmetries are especially interesting in physics, since they provide the basis for gauge theories. In general, transformations can be either continuous or discrete giving rise to continuous and discrete symmetries, respectively. In order to describe continuous symmetries, Lie groups are applied, while for discrete ones finite groups fulfill the requirements. Examples for continuous symmetries are translations in time and space as well as rotations in space. Invariance under translations in time leads to energy conservation, translations in space yield linear momentum conservation and rotations in space conserve the angular momentum if the theory is invariant under this symmetry. These groups are the Lorentz and more generally Poincaré groups. The symmetries describing non-continuous changes in a system, i.e. discrete symmetries, can be found in the SM in the form of symmetries of charge conjugation (C-symmetry), parity transformation (P-symmetry) and time inversion (T-symmetry). Under charge transformations, particles and antiparticles are exchanged, while parity transformations reverse the space coordinates. Time reversal simply means that the direction of time is inverted. These symmetries will be described in more details in Section 2.2.
Coming back to local symmetries, which are often referred to as gauge symmetries and which form the basis of the SM, let us consider internal symmetries, i.e. symmetries which do not depend on the space-time coordinates. Such symmetries are for example U(1), SU(2) and SU(3). It should be noted here that invariance under the U(1) gauge transformation leads to conservation of electric charge, lepton number and hypercharge, SU(2) to conservation of isospin and SU(3) invariance conserves baryon number and quark color. Quark flavor conservation is only an approximate SU(3) invariance.

2.2 CPT Symmetry and CP-Violation

Partity Transformation: P-Symmetry

The first important example of a discrete symmetry transformation is parity. This transformation refers to the inversion of all spatial coordinates, $(x, y, z) \rightarrow (x', y', z')$, and the corresponding operator of this transformation is parity P. Thus for a scalar wave function Ψ the parity transformation is defined by

$$P\Psi(\vec{r}, t) = \pi\Psi(-\vec{r}, t). \tag{2.1}$$

[2]The 19 free paramters are nine fermion masses, three coupling constants, four CKM quark-mixing angles, the Higgs doublet and the θ-parameter.

The possible eigenvalues of P are either $\pi = +1$ (even parity) or $\pi = -1$ (odd parity), since applying P twice yields the original system ($P^2 = 1$). Scalars have a parity of 1, pseudoscalars of -1, while vectors (i.e. polar vectors) have $P = -1$ and pseudovectors (i.e. axial vectors) show $P = 1$. If one considers the effect of spatial transformations on the electric and magnetic field E and B one finds that E is odd under P while B is even.
In the SM, P-symmetry is conserved in electromagnetic and strong interactions provided that one can assign an intrinsic parity to the particles. The value of the intrinsic parity is opposite for particles and their antiparticles. In weak interactions, parity is not conserved but even maximally violated for charged current weak interactions. This violation can be seen in the so-called τ-θ-puzzle, where two decays for charged strange mesons were found, namely

$$\theta^+ \rightarrow \pi^+ + \pi^0, \tag{2.2}$$

$$\tau^+ \rightarrow \pi^+ + \pi^+ + \pi^-, \tag{2.3}$$

which have different parity in the final state and were expected to have also different parity in the initial state, i.e. being two different particles. However it turned out that τ and θ are the same particle, now known to be the positive kaon K^+, and the explanation for the observation was that in weak interaction parity is not conserved. Another way to see maximal parity violation is that only left-handed neutrinos, i.e. spin aligned opposite to the direction of flight, and right-handed antineutrinos, i.e. spin along the direction of flight, exist [2].

Charge Conjugation: C-Symmetry

Under the charge conjugation operation the sign of the inner quantum numbers of a particle is changed. Thus this discrete symmetry is a transformation which turns particles into their antiparticles and the other way round but leaves all other coordinates unchanged. Both, strong and electromagnetic forces conserve this C-Symmetry, while in weak interactions, invariance under C is not given. This is due to the fact that C-transformations do not change the chirality and thus a left-handed neutrino would be transformed into a left-handed antineutrino, which are not included in the SM. Thus in weak interactions C-symmetry is maximally violated.

Time Reversal: T-Symmetry

The operation of time reversal, T, is the replacement of t by $-t$ which causes the direction of the momenta and spins to be reversed. The influence of T on all complex numbers is that they are replaced by their complex conjugates under this operation. In electromagnetic and strong interactions T-symmetry is conserved.

CPT-Theorem

A combined operation of C, P and T in any order plays a special role in Physics. As the Pauli-Lüders theorem [3] states, any quantum field theory which is constructed from fields of spin 0, 1/2 and 1 by local interactions which are invariant under the proper Lorentz group is invariant under CPT transformations. The SM is one example of such a theory. Given T invariance, CP invariance follows directly from the CPT theorem.

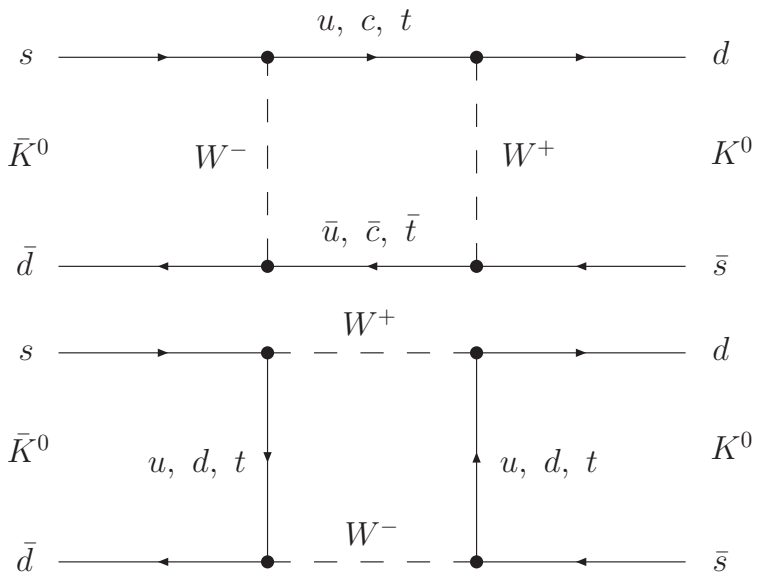

Figure 2.1: Box diagram for neutral kaon oscillations.

CP-Symmetry and the Neutral Kaon System

The combination of charge conjugation and parity transformation (CP-symmetry) implies basically that a process in which all particles are exchanged with their antiparticles is equivalent to the mirror image of the original process. It seems to be conserved in strong and electromagnetic interactions. Also for weak interactions it appeared at first sight that even though neither C- nor P-symmetry are conserved seperately, the theory was invariant under the combination of both. However, CP-violation was first observed experimentally in the decay of neutral Kaons. As a matter of fact, there are two different types of violation of this symmetry: indirect and direct violation. The former indicates that the violation occurs due to the mixing of the neutral kaon K^0 with its antiparticle $\bar{K}^0$ ($\Delta S = 2$, see Fig. 2.1) while the latter occurs in the actual decay process ($\Delta S = 1$).
The neutral Kaon K^0 and its antiparticle $\bar{K}^0$ are produced as two clearly distinguishable states in strong interaction processes, e.g. $\pi^- + p \rightarrow K^0 + \Lambda$ and $\pi^- + p \rightarrow \bar{K}^0 + \bar{\Lambda} + 2n$. They are thus

$$|K^0\rangle = |d\bar{s}\rangle \text{ with strangeness } S = +1, \tag{2.4}$$

$$|\bar{K}^0\rangle = |\bar{d}s\rangle \text{ with strangeness } S = -1. \tag{2.5}$$

The K^0 cannot be its own antiparticle due to the fact that kaons carry strangeness, which is conserved in strong interactions. Thus two different neutral kaons must exist. While they decay via weak interactions into two or three pions ($\Delta S = 1$), K^0 and $\bar{K}^0$ simultaneously can mix via the interaction with W-bosons ($\Delta S = 2$). If one assumes that CP-symmetry is conserved in weak interactions, then the physically observable states should be given by the CP-eigenstates. Being particle and antiparticle K^0 and $\bar{K}^0$, i.e the strong eigenstates, cannot be the CP-eigenstates in

question. A linear combination of the neutral kaons however provides what is needed

$$K_1 = \left(K^0 - \bar{K}^0\right)/\sqrt{2},\ CP = +1, \tag{2.6}$$

$$K_2 = \left(K^0 + \bar{K}^0\right)/\sqrt{2},\ CP = -1. \tag{2.7}$$

Since CP invariance is assumed these states can only decay in a CP-conserving way which yields two different decay modes. K_1 can only decay into a two-pion final state which has $CP = 1$, while K_2 must decay into three pions ($CP = -1$). The mass of K_2 is just a little larger than the mass of the three pions, hence this decay process is expected to be very slow compared to the K_1 decay (factor of about 600) [4]. Experimentally one was able to confirm the existence of two neutral Kaon versions with very different lifetimes, namely K_S and K_L[3]. An implication of CP-symmetry is that one should be able to identify $K_S = K_1$ and $K_L = K_2$. In this case, K_L should decay exclusively into three pions and thus at a certain distance away from the source, one should not be able to observe any 2-π decays.
In 1964, Cronin and Fitch [5] found that a small part of a K_L beam decays into two pions. This implies that the observed K_L and K_S are not identical with the pure CP-eigenstates but contain a small fraction ϵ of the respective other eigenstate

$$K_S = \frac{(K_1 - \epsilon K_2)}{\sqrt{1 + |\epsilon|^2}}, \tag{2.8}$$

$$K_L = \frac{(K_2 + \epsilon K_1)}{\sqrt{1 + |\epsilon|^2}}. \tag{2.9}$$

The value of ϵ here has been determined to be $|\epsilon| = (2.229 \pm 0.010) \times 10^{-3}$ [5,6]. This phenomenom is called indirect CP-violation, because it occurs in the mixing but is observed only in the decay process.
Direct CP-violation, i.e violation directly in the decay, has also been observed, but is smaller by about a factor of 1000 than the indirect effect. Both are present since mixing and decay arise from the same interaction with the W boson. The Cabibbo-Kobayashi-Maskawa-Matrix (CKM-Matrix) actually allows for CP-violation as will be shown in the following section. Another sector in which CP-violation is observable is in the decay of B-mesons in experiments such as BaBar at SLAC [7] or Belle at KeK [8].

CP-Violation in the Standard Model

In order to understand CP-violation in general, it is necessary to take a closer look at its origin in the SM.
While in strong and electromagnetic interactions a change in quark flavor is not allowed, in weak interactions the family symmetry is broken and mixing of quarks becomes possible. CP-violation is included in the SM by a complex phase in the CKM matrix. It is in principle a direct consequence of the fact that there are three quark families (or more) with different masses for each of the up-type quarks and each of the down-type quarks. The different families of particles would not mix and no

[3] S stands for short-lived while L for long-lived.

CP-violation would occur if quarks were massless. In the SM, the mechanism to break the family symmetry and obtain mass is supposed to be the Higgs mechanism. This generates a violation of CP-symmetry via charged current interactions as will be shown in the following [9].
For the strong interactions the quark fields are represented as $U = (u, c, t)$ and $D = (d, s, b)$. They form a basis and are mass eigenstates. If one wants to refer to the mass of a quark, it is one of these states, which are unique. For the weak interactions there is no unique set of weak eigenstates (up-type and down-type). The basis can here be written as $U' = (U_1, U_2, U_3)$ and $D' = (D_1, D_2, D_3)$. Here each of the quark fields is a linear combination of the mass eigenstates constructed such that U_i is the partner of D_i with i=1,2,3. In the Standard Model the electroweak Lagrangian consists of terms accounting for the kinetic energies of both the fermion and the gauge boson fields as well as their interactions with themselves and with each other. It shows an invariance under the local symmetry group SU(2)×U(1). Charged-current (CC) interactions are interactions between the left-handed quarks and the charged weak vector boson $W^{\pm}$. The Lagrangian is given by [9]

$$L_{CC} \propto \bar{U}'_L \gamma^\mu W^{\pm}_\mu D'_L + H.C., \tag{2.10}$$

where H.C. refers to the hermitian conjugate of the preceding term and the subscripts L refers to the left-handed components of the quark field. Through the coupling of the quarks to the scalar[4] Higgs field, they acquire mass. The mass matrices $M_U(i, j)$ and $M_D(i, j)$ correspond to nine coupling constants each, which appear due to the Higgs exchange between any pair of up-type states and any pair of down-type quarks, respectively. These mass matrices are symmetric but may have off-diagonal terms yielding the following mass term in the Lagrangian

$$L_m = \bar{U}'_R M_U U'_L + \bar{D}'_R M_D D'_L + H.C. \tag{2.11}$$

Diagonalization of the mass matrices can be done by applying unitary transformations[5] for left-handed fields (L_U, L_D) and right-handed fields (R_U, R_D) such that

$$\begin{aligned} U'_L &= L_U U_L, \\ U'_R &= R_U U_R, \\ D'_L &= L_D D_L, \\ D'_R &= R_D D_R, \end{aligned} \tag{2.12}$$

and thus the mass matrix can be written as

$$\Lambda_U = R_U^\dagger M_U L_U = L_U^\dagger M_U^\dagger R_U = \begin{pmatrix} m_u & 0 & 0 \\ 0 & m_c & 0 \\ 0 & 0 & m_t \end{pmatrix}, \tag{2.13}$$

where it can be seen that the eigenvalues of the mass matrix M_U are m_u, m_c, and m_t. They are the real quark masses. In the same way one can obtain m_d, m_s, and m_b for M_D. Thus, the mass term in the Lagrangian can be expressed by the quark fields as

$$L_m = m_u \bar{u}u + m_c \bar{c}c + m_t \bar{t}t + m_d \bar{d}d + m_s \bar{s}s + m_b \bar{b}b. \tag{2.14}$$

[4] Since the Higgs field is a scalar it couples quarks of left-handed and right-handed helicity.
[5] This is possible since the matrices are symmetric.

Applying now Eq. (2.12) to rewrite Eq. (2.10), one obtains

$$L_{CC} \propto \bar{U}_L L_U^\dagger \gamma^\mu W_\mu^\pm L_D D_L + H.C., \tag{2.15}$$

which becomes using the definition $V = L_U^\dagger L_D$

$$L_{CC} \propto \bar{U}_L \gamma^\mu W_\mu^\pm V D_L + H.C. \tag{2.16}$$

This unitary hermitian matrix V is physically observable and generally referred to as the quark-mixing matrix or Cabibbo-Kobayashi-Maskawa-Matrix (CKM-Matrix) [10]. Now it can be seen how CP-violation occurs. Writting Eq. (2.16) as

$$L_{CC} \propto V \bar{U}_L \gamma^\mu W_\mu^+ D_L + V^* \bar{D}_L \gamma^\mu W_\mu^- U_L, \tag{2.17}$$

and transforming it with the CP operation one obtains

$$CP(L_{CC}) \propto V \bar{D}_L \gamma^\mu W_\mu^- U_L + V^* \bar{U}_L \gamma^\mu W_\mu^+ D_L. \tag{2.18}$$

So in principle the two terms are just exchanged under CP transformation except for the fact that the CKM-Matrix is replaced by its complex conjugate. Thus if V is real, no CP-Violation occurs, while if it is complex this will give rise to non-invariance under CP.
In general, a complex $n \times n$ matrix has n^2 entries and thus $2n^2$ real parameters. If the matrix is unitary this reduces the number by n^2. By redefining the relative quark phases one can further decrease the number of parameters by $(2n-1)$. Thus there are $(n-1)^2$ independent parameters left, of which $n(n-1)/2$ are rotation angles and $(n-1)(n-2)/2$ are phases (see Ref. [9] and references therein). If we had two families of quarks ($n = 2$) then this yields one rotation angle only (Cabibbo angle θ) while in the case of three families one phase and three rotation angles are left as independent parameters. Given the fact that the masses of both up-type and down-type quarks are neither zero nor equal, the phase may be non-zero and thus the matrix is complex causing CP-violation. Its values represent the effective coupling between up-type and down-type quarks for the weak interactions and one generally writes

$$\begin{pmatrix} d' \\ s' \\ b' \end{pmatrix} = \begin{pmatrix} V_{ud} & V_{us} & V_{ub} \\ V_{cd} & V_{cs} & V_{cb} \\ V_{td} & V_{ts} & V_{tb} \end{pmatrix} \begin{pmatrix} d \\ s \\ b \end{pmatrix}. \tag{2.19}$$

The CKM matrix can be parametrized following Wolfenstein [6] with four parameters (λ, A, ρ and η)

$$V = \begin{pmatrix} 1-\lambda^2/2 & \lambda & A\lambda^3(\rho - i\eta) \\ -\lambda & 1-\lambda^2/2 & A\lambda^2 \\ A\lambda^3(1-\rho-i\eta) & -A\lambda^2 & 1 \end{pmatrix} + \mathcal{O}\left(\lambda^4\right), \tag{2.20}$$

and it was determined to be [6]

$$V = \begin{pmatrix} 0.97383^{+0.00024}_{-0.00023} & 0.2272^{+0.0010}_{-0.0010} & 0.00396^{+0.00009}_{-0.00009} \\ 0.2271^{+0.0010}_{-0.0010} & 0.97296^{+0.00024}_{-0.00024} & 0.04221^{+0.00010}_{-0.00080} \\ 0.00814^{+0.00032}_{-0.00064} & 0.04161^{+0.00012}_{-0.00078} & 0.999100^{+0.000034}_{-0.000004} \end{pmatrix}. \tag{2.21}$$

As shown above, CP-violation in the Standard Modell arises from quark-to-Higgs coupling and (at least) three families are needed. Then the CKM-Matrix is complex and with the fact that no pair of quarks with the same charge is degenerate in mass, CP-symmetry is violated.
Thus, CP-violation in the electroweak sector of the SM is a natural consequence. In the following the case of the strong interactions will be studied and it will be shown that the perturbative approach to this sector conserves CP, but does not describe the strong interactions appropriately. This so-called $\mathrm{U(1)_A}$-problem will be solved by introducing an additional term in the Lagrangian at the price of losing CP-invariance, which is known as the Strong CP-problem and can be solved in different ways.

2.3 From QED to QCD: The Lagrangian

Quantum Chromodynamics (QCD) is the theory of strong interactions. In contrast to Quantum Electrodynamics (QED), QCD is a non-Abelian[6] field theory. This is due to the fact that the gauge bosons of QCD, the gluons, carry color charge themselves and can thus interact with each other in contrast to photons, the gauge bosons of QED. Thus the gauge group shows a more complicated structure for QCD, i.e. SU(3), as in the case of QED, for which the gauge group is U(1).
The Lagrangian density in QED is given by

$$\mathcal{L}_{\mathrm{QED}} = \bar{\psi}(\gamma^\mu i D_\mu - m)\psi - \frac{1}{4}F_{\mu\nu}F^{\mu\nu}, \tag{2.22}$$

with the field ψ representing electrically charged particles, $\bar{\psi}$ being its Dirac ajoint, γ^μ representing the dirac matrices, $D_\mu = \partial_\mu - ieA_\mu$ the gauge covariant derivative and $F_{\mu\nu}$ being the electromagnetic field strength tensor. The coupling constant e is the electron charge and A_μ the covariant four-potential of the electromagnetic field. The field tensor can be written as

$$F_{\mu\nu} = \partial_\mu A_\nu - \partial_\nu A_\mu. \tag{2.23}$$

In QCD the perturbative Lagrangian can be derived in the same way as

$$\mathcal{L}_{\mathrm{pert}} = \sum_n \bar{\psi_n}(\gamma^\mu i D_\mu - m_n)\psi_n - \frac{1}{4}G^a_{\mu\nu}G^{\mu\nu}_a, \tag{2.24}$$

where now ψ_n denotes the quark fields with n being the quark flavor. Furthermore the covariant derivative is defined here as $D_\mu = \partial_\mu - igA_\mu$ with coupling g. Also the potential is now different: $A_\mu = T^a A^a_\mu$ with the matrices T^a being the generators of SU(3) and an additional field or potential A^a_μ known as Feynman's *universal influence* [11]. The index a is the gluon color index running from 1 to 8 (thus eight generators, the Gell-Mann matrices). Instead of $F_{\mu\nu}$ we find here the gluon field tensor $G_{\mu\nu}$ as

$$G_{\mu\nu} = \partial_\mu A_\nu - \partial_\nu A_\mu + g[A_\mu, A_\nu]. \tag{2.25}$$

The last term vanishes in QED since it is an Abelian gauge theory and thus the commutator equals zero. In QCD this term accounts for the self-coupling of the gluons.

[6] Non-Abelian means that the underlying group it is non-commutative.

2.4 The U(1)$_{\mathrm{A}}$-Problem and its Solution

2.4.1 The U(1)$_{\mathrm{A}}$-Problem

Perturbative calculations in QCD, i.e. by expanding the fields around the ground state (vacuum), as done in Eq. (2.24) provide only an approximate description of the theory. The reason for this is that in the chiral limit ($m_n \to 0$), $\mathcal{L}_{\mathrm{pert}}$ is invariant under global axial and vector transformations U(1)$_{\mathrm{A}}$ and U(1)$_{\mathrm{V}}$, respectively. While vector transformations treat left-handed and right-handed particles in the same way, i.e.

$$\psi_L \to \mathrm{e}^{i\theta}\psi_L, \psi_R \to \mathrm{e}^{i\theta}\psi_R, \tag{2.26}$$

axial transformations act differently on left and right-handed parts

$$\psi_L \to \mathrm{e}^{i\theta}\psi_L, \psi_R \to \mathrm{e}^{-i\theta}\psi_R. \tag{2.27}$$

An invariance under both symmetries implies both vector and axial currents to be conserved. The non-violation of U(1)$_{\mathrm{V}}$ leads to baryon number conservation, which is an exact symmetry, while an invariance under U(1)$_{\mathrm{A}}$ should be observable in the hadron spectrum (parity degeneracy). However this has not been observed experimentally. Considering the less extreme limit of u, d and s quark masses being small compared to the scale of QCD, chiral symmetry can be considered as a reasonable approximation. The expected spontaneous symmetry breaking (SSB) would result in eight massless (for $m_u = m_d = m_s = 0$) Goldstone-Bosons. In case of small masses for the quarks, the particles forming this pseudoscalar octet are only approximately massless and the corresponding particles have been observed, namely π, K and η. If, in addition, a U(1)$_{\mathrm{A}}$-Symmetry is present in the theory, a pseudoscalar flavor singlet is expected corresponding to a ninth conserved axial current. A candidate for this ninth particle η_1 has to match the quantum numbers ($J^P = 0^-$) and should be a light partner to the pion. Its mass is expected to be [12, 13]

$$m(\eta_1) \leq m(\pi)\sqrt{3}. \tag{2.28}$$

The only candidate[7] available is the η' which has the right quantum numbers but is too heavy with a mass[8] of 957.78 MeV as compared to the pion mass which is around 135 MeV [6]. This discrepancy is known as the η-mass problem or the U(1)$_{\mathrm{A}}$-Problem. A detailed description of the U(1)$_{\mathrm{A}}$-Problem can be found in [13].

2.4.2 The θ-Vacuum and the Solution to the U(1)$_{\mathrm{A}}$-Problem

A solution to the U(1)$_{\mathrm{A}}$-Problem has been presented by t'Hooft [15]. He introduces an anomalous symmetry breaking known as axial or Adler-Bell-Jackiw (ABJ) anomaly[9], which means that the

[7] The light partner needed for the pion has to be a flavor singlet. Since the η-meson corresponds approximately to the flavor octet η_8 the only candidate is the η' since $|\eta'\rangle \approx |\eta_1\rangle = \frac{1}{\sqrt{3}}\left(|u^\uparrow \bar{u}^\downarrow\rangle + |d^\uparrow \bar{d}^\downarrow\rangle + |s^\uparrow \bar{s}^\downarrow\rangle\right)$ [12, 14].

[8] Note that in the present thesis in general natural units, i.e. $\hbar = c = 1$, have been used.

[9] As Weinberg pointed out before already in [13], the U(1)$_{\mathrm{A}}$ problem could be solved using the ABJ anomaly or it could be avoided by the introduction of elementary spin-zero fields which are strongly interacting. This latter approach would however spoil the advantages of models with quarks and gluons only.

symmetry is broken in the quantum theory but not classically. In the case at hand, this results in an additional term $\mathcal{L}_\theta$ to the Lagrangian

$$\mathcal{L}_\theta = \theta \frac{g^2}{32\pi^2} G^a_{\mu\nu} \tilde{G}^{\mu\nu}_a, \tag{2.29}$$

where g is the coupling constant and $G^a_{\mu\nu}$ the gluon field strength tensor as given in Eq. (2.25). Its dual $\tilde{G}^{\mu\nu}_a$ is given by

$$\tilde{G}^{\mu\nu}_a = \frac{1}{2} \epsilon^{\mu\nu\rho\sigma} G_{\rho\sigma}. \tag{2.30}$$

In order to understand the origin of this term, one should first take a look at the QCD vacuum also referred to as θ-vacuum. Since QCD is a non-Abelian field theory, the vacuum reveals a complicated structure. More precisely, this means that the ground state is a superposition of an infinit number of degenerate vacua characterized by a topological winding number n. These vacua $|n\rangle$ are not invariant under all possible gauge transformations and thus they are not the proper vacuum. The ground state, often referred to as θ-vacuum, can be obtained as a superposition of the degenerate vacua and is gauge-invariant. It can be expressed as

$$|\theta\rangle = \sum_{n=-\infty}^{\infty} \mathrm{e}^{-\mathrm{in}\theta} |\mathrm{n}\rangle, \tag{2.31}$$

with $0 \leq \theta \leq 2\pi$ [16–18]. By calculating the transition amplitude

$$\langle \theta' | \mathrm{e}^{-Ht} | \theta \rangle = \sum_{n'} \sum_{n} \mathrm{e}^{\mathrm{i}(\mathrm{n}'\theta' - \mathrm{n}\theta)} \langle \mathrm{n}' | \mathrm{e}^{-\mathrm{Ht}} | \mathrm{n} \rangle, \tag{2.32}$$

between θ-vacua with according winding numbers n and n', one obtains an additional expression to the Lagrangian $\mathcal{L}_\theta$ (in Minkowski space) as

$$\mathcal{L}_\theta = \theta q, \tag{2.33}$$

where q is the so-called Pontryagin index and is defined as the difference between the chosen sets of winding numbers

$$q = n - n' = \frac{g^2}{32\pi^2} G^a_{\mu\nu} \tilde{G}^{\mu\nu}_a. \tag{2.34}$$

The parameter θ is introduced to consider all classical solutions with $-\infty < q < +\infty$. For a more detailed discussion the reader is referred to [17].
Taking into account electroweak interactions, one has to substitute θ in Eq. (2.29) by $\bar{\theta}$ with

$$\bar{\theta} = \theta + \theta_{\mathrm{weak}} = \theta + \arg(\det \mathrm{M}), \tag{2.35}$$

where M denotes the quark mass matrix and thus the additional term in the Lagrangian becomes

$$\mathcal{L}_{\bar{\theta}} = \bar{\theta} \frac{g^2}{32\pi^2} G^a_{\mu\nu} \tilde{G}^{\mu\nu}_a, \tag{2.36}$$

and the QCD Lagrangian can thus be written as

$$\mathcal{L}_{\mathrm{QCD}} = \mathcal{L}_{\mathrm{pert}} + \mathcal{L}_{\bar{\theta}}. \tag{2.37}$$

The additional term is renormalizable and gauge-invariant. It solves the $\mathrm{U(1)_A}$-Problem but at the same time it creates a new challenge since the introduced term is not invariant under CP, which leads to the strong CP-Problem.

2.5 The Strong CP-Problem

In order to see why this new term in the QCD Lagrangian violates CP, it is best to consider a corresponding term in QED containing the electromagnetic field strength tensor $F_{\mu\nu}$, given by [12]

$$F_{\mu\nu}\tilde{F}^{\mu\nu} = 4\vec{E}\cdot\vec{B}. \tag{2.38}$$

Under P transformation one obtains

$$P(\vec{E}) = -\vec{E}, \tag{2.39}$$
$$P(\vec{B}) = +\vec{B}, \tag{2.40}$$

and application of the C-operator yields

$$C(\vec{E}) = -\vec{E}, \tag{2.41}$$
$$C(\vec{B}) = -\vec{B}. \tag{2.42}$$

Thus CP-symmetry is violated, since C is conserved while P is violated. In contrast, a term of the form $F_{\mu\nu}F^{\mu\nu}$ as in Eq. (2.22) or Eq. (2.24) will only yield a term proportional to $(B^2 - E^2)$, which is CP conserving.
The CP-violating effects expected from the term in Eq. (2.36) could be large, unless $\bar{\theta}$ is very small. From first principles, there is no obvious reason why the two terms forming $\bar{\theta}$ in Eq. (2.35) should both be very small or of opposite sign, such that they cancel.
The $\bar{\theta}$-dependence[10] of the electric dipole moment of the neutron d_n (NEDM) is predicted in the MIT[11] bag model [20] to be

$$d_n = 32.7 \times 10^{-3} e \frac{3 m_u m_d m_s}{m_u m_d + m_u m_s + m_d m_s} R^2 \bar{\theta}. \tag{2.43}$$

Using a bag radius of $R \approx (140\ \text{MeV})^{-1}$ as well as $m_d/m_u = 1.8$, $m_s/m_d = 20$ and $m_s \approx 300$ MeV one obtains

$$d_n = 8.2 \times 10^{-16}\ \bar{\theta}\ \text{e cm}. \tag{2.44}$$

Other authors [21] propose

$$d_n = 2.7 - 5.2 \times 10^{-16}\ \bar{\theta}\ \text{e cm}, \tag{2.45}$$

while the latest experimental limit on the EDM of the neutron is [6, 22]

$$|d_n| < 2.9 - 6.3 \times 10^{-26}\ \text{e cm}\ (90\ \%\ C.\ L.). \tag{2.46}$$

Comparing Eq. (2.45) and (2.46) results in the conclusion that $\bar{\theta} \leq 10^{-10}$. Such a small $\bar{\theta}$ is perfectly allowed but it needs an explanation, since this would imply fine-tuning of the two addends contributing to $\bar{\theta}$.
The strong CP-Problem, i.e. why there is no CP-violation in strong interactions, can be formulated in a different way, namely as the question why $\bar{\theta}$ is such a small quantity. Following t'Hofft, this is also referred to in the literature as the *naturalness problem*[12].

[10] A more detailed description of how the $\bar{\theta}$-dependence of d_n is obtained, can be found in Ref. [19].

[11] Massachusetts Institute of Technology

[12] According to t'Hofft's definition [23], naturalness of a theory with a parameter α means that with $\alpha \to 0$ the symmetry of the theory increases.

2.6 Solution(s) to the Strong CP-Problem

To solve the CP-Problem, mainly three types of solutions have been suggested in the literature[13]: the least likely solution involves zero quark masses, a second approach is referred to as soft-CP solution and sets $\theta = 0$, while the third and most elegant way of solving the problem is known as the axion-solution. In the following, the first two approaches will be briefly described and then the axion solution as suggested by Peccei and Quinn [24] will be presented, since it is the relevant solution for this thesis and forms the basis for the following chapters.

2.6.1 Zero Mass Quark

Assuming that the mass of one quark[14] is zero, the θ parameter can be eliminated from the Lagrangian. In this case, the freedom to apply $\mathrm{U(1)_A}$ rotations is regained and through the ABJ anomaly the CP violating term could be absorbed. Calculations of the quark mass ratio m_u/m_d in Lattice-QCD strongly disfavor the massless up-quark idea [25]. Furthermore, the problem would just be transfered from inside the SM to beyond the SM: instead of finding an explanation for the smallness of θ, one would have to provide an answer to why the quark mass is zero. Although it was thought that in some extentions of the SM, a zero mass up-quark comes naturally into existence as discussed in detail in Ref. [26], it was eventually possible to rule out the massless up-quark possibility [27].

2.6.2 Soft Weak CP-Violation

A second possibility to address the strong CP-Problem is to set $\theta = 0$ in Eq. (2.35) and thus impose CP-symmetry on the QCD Lagrangian. The observed CP-violation in weak interactions must then be the result of spontaneous symmetry breaking, so-called soft-CP [28]. In general this creates a non-vanishing $\bar{\theta}$ due to the fact that $\theta_{\mathrm{weak}} \neq 0$. The violation of weak CP by a spontaneous mechanism must be checked using various weak phenomena. At present, weak CP violation data fit the CP-violation according to Kobayashi and Maskawa, while it will be difficult to fit these data with the spontaneous weak CP-violation since the differences are drastic [6]. So far there still exist some beyond-the-SM-scenarios which solve the strong CP-Problem using soft-CP, which have not yet been ruled out, but the proposed models will face extreme difficulties satisfying the upper bounds on $\bar{\theta}$ obtained from the electric dipole moment of the neutron.
A more detailed overview can be found for example in Ref. [29].

2.6.3 The Peccei-Quinn Solution

The most popular and also most promising solution to explain why $\bar{\theta}$ is so small has been suggested by Peccei and Quinn in 1977 [24]. It is especially attractive in view of the fact that the possibility of the massless-quark explanation is ruled out and for the soft CP solution one-loop suppression is needed to achieve compatibility with experimental limits. The fundamental concept of this approach is to make $\bar{\theta}$ a dynamical variable, i.e a phase, with a minimum value at zero instead

[13] A more detailed description of these types of solution can be found in Ref. [17].
[14] An obvious choice would be the up-quark.

of having it as a parameter (or coupling constant) of the theory. In case of $\bar{\theta}$ as a parameter, different $\bar{\theta}$'s imply different theories, while in the case of a dynamical variable different $\bar{\theta}$'s will just distinguish different vacuum states in one given theory. It then has to be shown that $\bar{\theta} = 0$ is the true vacuum.
In order to obtain $\bar{\theta} = 0$, Peccei and Quinn introduced a new global, chiral symmetry $\mathrm{U(1)_{PQ}}$, which is known as the Peccei-Quinn-Symmetry (PQ-Symmetry). $\mathrm{U(1)_{PQ}}$ is spontaneously broken at the energy scale of the symmetry, f_a[15], yielding a Goldstone boson which is massless at the classical level but acquires a small mass through the axial anomaly and instanton interactions. This pseudo-Goldstone boson is the axion [30, 31].
The new field yields an additional term $\mathcal{L}_{\mathrm{Axion}}$ to the QCD Lagrangian $\mathcal{L}_{\mathrm{QCD}}$ such that

$$\mathcal{L}_{\mathrm{QCD}} = \mathcal{L}_{\mathrm{pert}} + \mathcal{L}_{\bar{\theta}} + \mathcal{L}_{\mathrm{Axion}} \tag{2.47}$$

$$= \mathcal{L}_{\mathrm{pert}} + \bar{\theta}\frac{g^2}{32\pi^2} G^a_{\mu\nu}\tilde{G}^{\mu\nu}_a + \mathcal{L}_{\mathrm{Axion}}, \tag{2.48}$$

where the new term is given by

$$\mathcal{L}_{\mathrm{Axion}} = \mathcal{L}_{\mathrm{kin}} + \mathcal{L}_{\mathrm{int}} - V_{\mathrm{eff}}. \tag{2.49}$$

The first term represents the kinetic energy given by $\mathcal{L}_{\mathrm{kin}} = -\frac{1}{2}(\partial_\mu a)(\partial^\mu a)$. The second term takes into account further interactions of the axions. The third term can be written as

$$V_{\mathrm{eff}}(a) = -C_a \frac{a}{f_a}\frac{g^2}{32\pi^2} G^a_{\mu\nu}\tilde{G}^{\mu\nu}_a, \tag{2.50}$$

with C_a being a parameter depending on the model. The axion field is represented by a, g is the strong coupling constant and f_a is the scale of the spontaneous symmetry breaking (SSB) of the PQ-Symmetry. $V_{\mathrm{eff}}(a)$ takes into account interactions of axions with gluons and is very similar in structure to the CP violating term $\mathcal{L}_{\bar{\theta}}$ in Eq. (2.36). The vacuum expectation value of the axion field $\langle a \rangle$ can be obtained by calculating the extrema of the potential, i.e. here

$$\left\langle \frac{\partial V_{\mathrm{eff}}(a)}{\partial a} \right\rangle = -C_a \frac{g^2}{32\pi^2 f_a}\langle G^a_{\mu\nu}\tilde{G}^{\mu\nu}_a \rangle \stackrel{!}{=} 0. \tag{2.51}$$

Thus the vacuum expectation value of the axion field $\langle a \rangle$ is

$$\langle a \rangle = -\frac{f_a}{C_a}\bar{\theta}, \tag{2.52}$$

and the CP-violating $\bar{\theta}$-term in QCD is compensated for. The true vacuum is at $\bar{\theta} = 0$ and it can be shown [17] that the minimum of the effective potential is at $a = 0$. Further minima can be found due to the periodicity of $\bar{\theta}$ for $\langle a \rangle = 2n\pi f_a/C_a$, where n is an integer.
So in order to explain, why no CP violation is observable in strong interactions, although initially expected, there is basically just one thing left to be proven: the existence of the (so far still hypothetical) axion.

[15] Sometimes f_a is also referred to as f_{PQ}.

Chapter 3

The Axion

After having arrived at the conclusion that the existence of an axion would solve the strong CP-problem via the Peccei-Quinn mechanism, this chapter will give an overview on general axion physics. Firstly, the properties of the axion and its couplings to fundamental bosons and fermions will be presented without distinguishing different axion models. Then the original axion, also referred to as *visible* or Peccei-Quinn-Weinberg-Wilczek (PQWW) axion, will be discussed. After this heavy axion has been ruled out experimentally, different *invisible axion models*, which assume a light axion, were introduced and will be presented here. The section following considers the axion as a dark matter candidate. After this, astrophysical bounds on the axion and cosmological limits will be discussed and the chapter will conclude with possibilities to detect *invisible axions* by reviewing the past and present axion searches as well as providing a brief outlook on future axion experiments.

3.1 Properties and Coupling of Axions

The most important parameter which determines the properties of the axion and its coupling to fundamental particles is the symmetry breaking scale of the newly introduced PQ-Symmetry $\mathrm{U}(1)_{\mathrm{PQ}}$, denoted by f_{PQ} or f_a[1]. A priori, the breaking scale is arbitrary, since it just represents the curvature of the axion potential, which has its minimum for $\bar{\theta} = 0$, and thus initially all values are allowed for the breaking scale. The same is valid for the axion mass and the coupling constants for axions to various particles, since both are inversely proportional to f_a

$$g_{ai} \propto \frac{1}{f_a}, \tag{3.1}$$

$$m_a \propto \frac{1}{f_a}. \tag{3.2}$$

Here the index i represents the particle the axion couples to. In order to look for and discover the axion, it is essential to know about its coupling to ordinary matter. The coupling constant

[1] In the literature, f_a is sometimes defined as f_{PQ}/N or f_a/N with N being the color anomaly. For a generic discussion of the axion properties the model-dependent integer N is not needed and can be absorbed in the definition of f_a as it will be done here [32, 33].

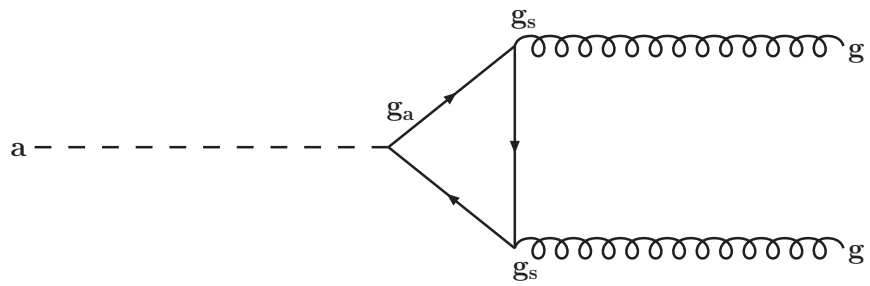

Figure 3.1: Triangle loop diagram for the axion-to-gluon coupling. Here g_s is the strong coupling constant, while g_a is the axion-fermion Yukawa coupling.

is sometimes also denoted as g_{aii} (instead of g_{ai} as above) in order to describe the coupling more accurately. As will be shown, different axion models can be distinguished by the existence (or non-existence) of couplings with certain particles. However, generic to all models is the axion-gluon coupling as well as the coupling to photons, which is a consequence of the former.

3.1.1 Couplings of the Axion to Fundamental Particles

Axions can couple to fundamental bosons and fermions. The interactions of axions with photons and fermions contribute to the interaction term $\mathcal{L}_{\text{int}}$ in the additional term $\mathcal{L}_{\text{Axion}}$ to the QCD-Lagrangian introduced due to the PQ-solution (see Eq. (2.49)). More explicitly, the interaction part can be written as

$$\mathcal{L}_{\text{int}} = \mathcal{L}_{a\gamma} + \mathcal{L}_{af}, \tag{3.3}$$

where $\mathcal{L}_{a\gamma}$ describes the interaction of axions with photons and $\mathcal{L}_{af}$ the interaction with fermions. These two summands can be written as[2] [34]

$$\mathcal{L}_{a\gamma} = g_{a\gamma} a \, \vec{E} \cdot \vec{B}, \tag{3.4}$$

$$\mathcal{L}_{af} = i\frac{g_{aN}}{2m_N}\partial_\mu a \left(\bar{\psi}_N \gamma^\mu \gamma_5 \psi_N\right) + i\frac{g_{ae}}{2m_e}\partial_\mu a \left(\bar{\psi}_e \gamma^\mu \gamma_5 \psi_e\right), \tag{3.5}$$

where the indices N and e represent nucleon and electron, respectively. In the following, the different couplings will be studied in more detail.

Interactions with Bosons

Coupling to Gluons Axions couple to gluons as shown in Fig. 3.1 via a triangle loop due to the chiral anomaly. This yields a contribution

$$\mathcal{L}_{aG} = \frac{\alpha_s}{8\pi f_a} a G_a^{\mu\nu} \tilde{G}^a_{\mu\nu}, \tag{3.6}$$

with the strong fine-structure constant α_s. Due to this interaction of axions with gluons, they

[2] In the case of only one Goldstone boson present in the considered Feynman diagram, it is possible to substitute the pseudo-vector coupling $i(g_{ak}/2m_k)\partial_\mu a \left(\bar{\psi}_k \gamma^\mu \gamma_5 \psi_k\right)$ by a pseudo-scalar coupling $i g_{ak} a \left(\bar{\psi}_k \gamma_5 \psi_k\right)$ with $k = N, e$ for nucleon or electron.

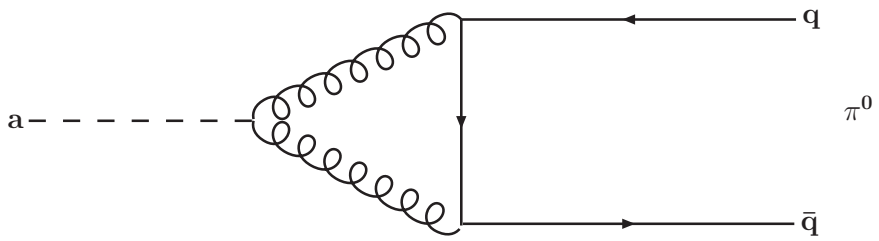

Figure 3.2: Axion mixing with $q\bar{q}$ states and thus with π^0 through coupling to gluons. In this way, axions can acquire a small mass.

can also mix with pions (see Fig. 3.2) and the initially masslessly contructed axion acquires a mass [32, 35]

$$m_a = \frac{m_{\pi^0} f_\pi}{f_a} \left(\frac{z}{(1+z+w)(1+z)} \right)^{1/2} \simeq 0.60 \text{ eV} \frac{10^7 \text{ GeV}}{f_a}, \tag{3.7}$$

where the pion mass $m_{\pi^0} = 135$ MeV and its decay constant $f_\pi = 93$ MeV have been used along with the quark mass ratios z and w [36]

$$z \equiv \frac{m_u}{m_d} = 0.553 \pm 0.043, \tag{3.8}$$

$$w \equiv \frac{m_u}{m_s} = 0.029 \pm 0.004. \tag{3.9}$$

There is still some variation in the values of z. Recent results for z vary from $0.350 - 0.600$ [6]. The coupling of gluons to axions is present in all axion models. And as a direct consequence from this interaction, also the coupling of axions to photons is generic in all axion models.

Coupling to Photons Through the mixing of pions with axions, axions also couple to photons as is shown in the upper part of Fig. 3.3. The contribution of the axion-photon interaction to the Lagrangian can be formulated as

$$\mathcal{L}_{a\gamma} = -\frac{1}{4} g_{a\gamma} F_{\mu\nu} \tilde{F}^{\mu\nu} a = g_{a\gamma} \vec{E} \cdot \vec{B} a, \tag{3.10}$$

where $g_{a\gamma}$ represents the coupling constant for coupling of axions to photons and the axion field is denoted by a. Furthermore $\vec{E}$ and $\vec{B}$ represent the electric and magnetic field, respectively.
A further contribution to the coupling between the two particles can appear in models in which standard fermions carry PQ-charges in addition to the electric charges. Then, the interaction can also take place via a fermionic triangle loop (see lower part of Fig. 3.3) analog to the case of the axion-gluon coupling (see Fig. 3.1, where g_s has to be replaced by the electric charge of the lepton). The axion-photon coupling constant is then given by [32]

$$g_{a\gamma} = \frac{\alpha}{2\pi f_a} \left(\frac{E}{N} - \frac{2\,(4+z+w)}{3\,(1+z+w)} \right), \tag{3.11}$$

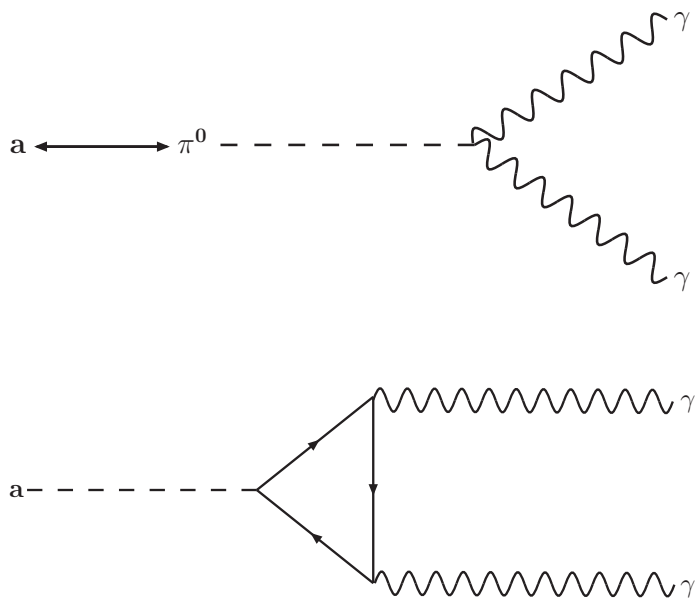

Figure 3.3: Axion-photon coupling. Top: Axion-Photon coupling via mixing of axions with pions. Bottom: Additional contribution to the coupling of axions to photons via a triangle loop through fermions carrying both PQ and electric charges.

where α is the fine-structure constant ($e^2/4\pi \approx 1/137$) and E/N a model dependent term which will be discussed in the following. Furthermore, z and w are the same quark mass ratios as given in Eq. (3.8) and in Eq. (3.9). Thus the coupling constant can be obtained as

$$g_{a\gamma} = \frac{\alpha}{2\pi f_a}\left(\frac{E}{N} - 1.92 \pm 0.08\right) = \frac{\alpha}{2\pi f_a} C_\gamma. \tag{3.12}$$

The ratio E/N is the quotient of electromagnetic anomaly E and color anomaly N [33, 37]. They can be described by

$$E \equiv 2\sum_f X_f Q_f^2 D_f, \tag{3.13}$$

$$N \equiv \sum_f X_f, \tag{3.14}$$

where X_f represents the PQ-charge of the fermion f, while Q_f stands for its electric charge in units e. Furthermore, $D_f = 1$ for color singlets (charged leptons) and $D_f = 3$ for color triplets (quarks). The color anomaly N is an integer and equals the number of degenerate ground states of the effective potential for the axion field. In Section 3.3 it will be discussed, which values the E/N can acquire in different axion models. Consequently, the axion-photon coupling can be either enhanced for large E/N or suppressed if E/N is small.

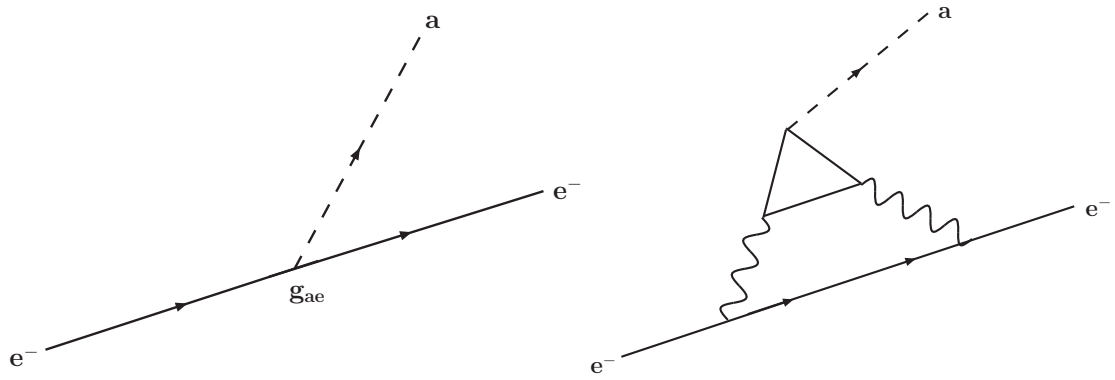

Figure 3.4: Axion-electron coupling. Left: Contributing Feynman diagram for direct axion-electron coupling which is possible only in models in which fermions carry PQ-charge (see DFSZ model). Right: Radiatively induced coupling of axions to electrons at a one-loop level. This coupling is present even in models in which fermions do not carry PQ-charge (see KSVZ model).

Interactions with Fermions

Axions do not only interact with bosons but also with fermions. From this interaction one obtains the following contribution to the Lagrangian

$$\mathcal{L}_{af} = \frac{g_{af}}{2m_f} \left(\bar{\psi}_f \gamma^\mu \gamma_5 \psi_f\right) \partial_\mu a, \tag{3.15}$$

with f representing the fermion, m_f being the fermion mass and g_{af} the coupling constant of the axion-fermion interaction, which can be explicitly written as

$$g_{af} = \frac{C_f \, m_f}{f_a}, \tag{3.16}$$

and plays the role of a Yukawa coupling with an effective PQ-charge[3] C_f. Via $\alpha_{af} = g_{af}^2/4\pi$ an *axionic fine-structure constant* can be defined [32]. In the following, the coupling to electrons and the effective coupling to nucleons will be considered. The reason for the latter one being that there are no free quarks below the QCD scale $\Lambda_{\mathrm{QCD}} \approx 200$ MeV and thus only the effective coupling to nucleons can be observed. The effective coupling to nucleons arises from direct axion coupling with quarks and results in roughly equal parts from mixing with π^0 and η.

Coupling to Electrons There are two possible important couplings of axions to electrons, which are shown in Fig. 3.4. On tree level (see left part of Fig. 3.4), a direct coupling of axions to electrons is only possible, if electrons carry PQ-charge and thus $C_e \neq 0$. This is the case for some axion

[3]The effective PQ-charge is defined in order to absorb the color anomaly N by setting it as $C_f = X_f/N$. The equivalent has also been done with f_a. It is actually given by $f_a = f_{\mathrm{PQ}}/N$. If one wants to be more precise X_f has to be replaced by X_f', which is the PQ-charge X_f shifted by a certain value, such that the axion does not mix with the Z^0 [32].

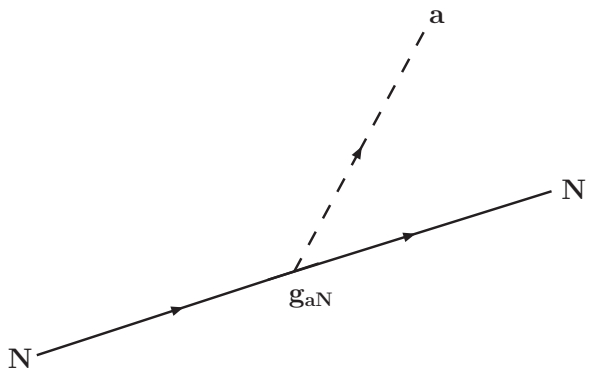

Figure 3.5: Feynman diagram of direct axion-to-nucleon coupling. Even axions which do not couple to light quarks at tree-level still have a coupling to nucleons since the axion nucleon coupling partly results from axion-pion mixing and partly from the shown direct coupling of axions to nucleons.

models (DFSZ[4], see Section 3.3), while in others this coupling is absent. The latter models such as the KSVZ[5] model (see as well Section 3.3), are for this reason also referred to as *hadronic* axion models.
If present, the coupling yields a contribution to the Lagranian as given in Eq. (3.15) with a coupling constant [32]

$$g_{ae}^{\mathrm{tree}} = \frac{C_e m_e}{f_a} = 0.85 \times 10^{-10} m_a C_e \ \mathrm{eV}^{-1}, \tag{3.17}$$

where the effective PQ-charge $C_e = X'_f/N$ depends on the axion model as mentioned above.
Even if C_e is zero and thus this direct coupling does not appear (*hadronic* models), there is still a higher order coupling from the Feynman diagram in the right part of Fig. 3.4. This so-called radiatively induced coupling of axions to electrons at the one loop level arises from the anomalous two-photon coupling of the axion (see lower part of Fig. 3.3) and yields a coupling g_{ae}^{rad} which is smaller than g_{ae}^{tree} [37].

Coupling to Nucleons The coupling of axions to nucleons consists of two different but approximately equal contributions: the coupling of axions to light quarks at tree-level and the mixing of axions with pions. In this way, even so-called *hadronic* axions (KSVZ axions), which do not couple to light quarks at tree-level, but only to a heavy exotic quark species, still show a coupling to nucleons comparable to the one in non-hadronic models [34]. This is important in view of deriving bounds on the axion mass from the supernova SN 1987A (see Section 3.5.4), in which mainly the coupling of axions to nucleons is involved. Here, the derived bounds are essentially the same for different axion models. In Fig. 3.5, the Feynman diagram of the contribution from direct coupling is shown. The coupling constant is given by [32]

$$g_{aN} = \frac{C_N m_N}{f_a} = 1.56 \times 10^{-7} m_a C_N \ \mathrm{eV}^{-1}. \tag{3.18}$$

[4]This axion model has been named after its initiators Dine, Fischler, Srednicki and Zhitnitskiĭ [38, 39].
[5]This axion model has been introduced before the DFSZ model by Kim, Shifman, Vainshtein, and Zakharov [40, 41].

The effective PQ-charges differ for protons and neutrons and are given by [33, 37, 42]

$$C_p = (C_u - \eta)\,\Delta u + (C_d - \eta z)\,\Delta d + (C_s - \eta w)\,\Delta s, \tag{3.19}$$

and

$$C_n = (C_u - \eta)\,\Delta d + (C_d - \eta z)\,\Delta u + (C_s - \eta w)\,\Delta s, \tag{3.20}$$

with $\eta \equiv (1 + z + w)^{-1}$ and the quark mass ratios z and w as given in Eq. (3.8) and in Eq. (3.9). The effective PQ-charges of the quarks are represented by C_u, C_d and C_s. Δq is the contribution to the nucleon spin as carried by the quark q with $q = u, d, s$. Δq has been determined in Ref [43] and recently been updated [44]

$$\Delta u \approx +0.84, \quad \Delta d \approx -0.43, \quad \Delta s \approx -0.09, \tag{3.21}$$

with a rough uncertainty of ± 0.02 each.

Further Processes

There are some further processes involving axions, which are important in the frame of the astrophysical considerations discussed in Section 3.5.
For axion models with tree-level coupling to electrons, the dominating axion emission processes in main sequence stars, white dwarfs and red giants are bremsstrahlung and Compton-like processes as shown in Fig. 3.6.
In the same objects, the dominant emission process for hadronic axions is the Primakoff effect (see Fig. 3.7), since here the coupling to electrons is strongly suppressed. In the electric field of charged particles, e.g. in a plasma, a photon can be converted into an axion via this Primakoff effect [45]. This process and its inverse turn out to be very important in the search for the axion, since it can be used to reconvert axions into photons by providing a strong magnetic field.
Finally, in neutron stars both models show the same dominant emission process, namely nucleon-axion bremsstrahlung according to the Feynman diagram in Fig. 3.8.
These processes will be revisited in Section 3.5 after the summary of different axion models (Section 3.3).

3.1.2 Lifetime of Axions

A general observation as stated in Eq. (3.1) is that all couplings are inversely proportional to the PQ-symmetry breaking scale f_a. Also the axion mass m_a is $\propto 1/f_a$ and this implies that the larger f_a is the smaller the axion mass m_a and the weaker the coupling of the axion to ordinary matter becomes. As discussed, the coupling of axions to two photons arises due to the electromagnetic anomaly of the PQ-symmetry. Axions can decay into two photons and the lifetime of the axion is given by [46]

$$\tau_{a\to\gamma\gamma} = 6.8 \times 10^{24} \frac{(m_a/\mathrm{eV})^{-5}}{\left[(E/N - 1.92)/0.72\right]^2}\ \mathrm{s}, \tag{3.22}$$

or, following [29], it can be expressed in terms of the axion-to-photon coupling constant as

$$\tau_{a\to\gamma\gamma} = \frac{2.24 \times 10^{14}}{g_{a\gamma}^2} \left(\frac{m_a}{\mathrm{eV}}\right)^{-3} \mathrm{s} = \frac{0.5 \times 10^{-3} t_U}{g_{a\gamma}^2} \left(\frac{m_a}{\mathrm{eV}}\right)^{-3}, \tag{3.23}$$

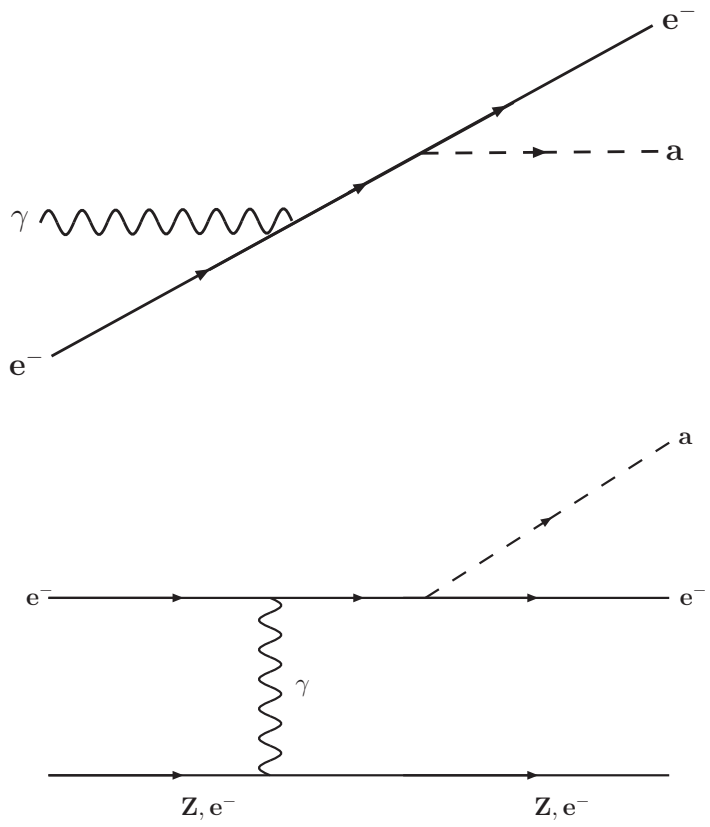

Figure 3.6: Upper image: Compton-like process for axion models with axion-electron coupling at tree-level. Together with the bremsstrahlungs process shown in the lower part of this figure, Compton scattering is the main axion emission process in main sequence stars, white dwarfs and red giants. Lower image: Electron-bremsstrahlung process for axion models with axion-electron coupling at tree-level.

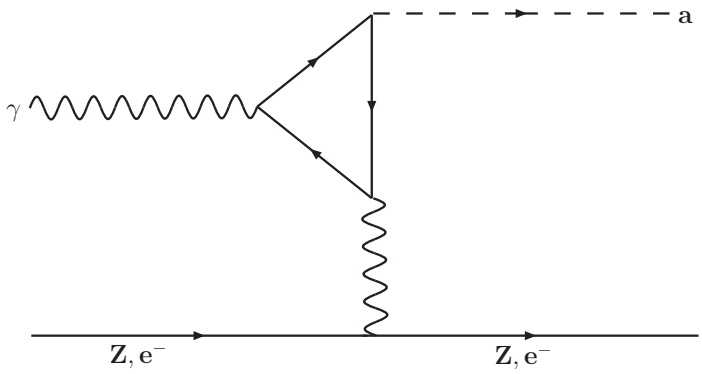

Figure 3.7: The Primakoff effect is the dominant axion emission process in hadronic models for main sequence stars, horizontal branch stars, red giants and white dwarfs.

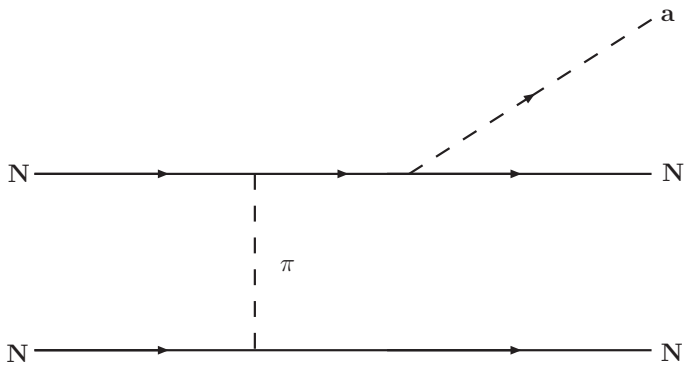

Figure 3.8: Axion-nucleon bremsstrahlung is the most important axion emission process in neutron stars.

where the age of the universe $t_U \approx 4.35 \times 10^{17}$ s and thus for a coupling of order unity an axion of mass 0.08 eV has roughly the lifetime t_U. Light axions are thus very stable, while very heavy axions (which have been ruled out as will be shown in Section 3.2) have a rather short lifetime.

3.2 The Peccei-Quinn-Weinberg-Wilczek-Axion

The original axion from the proposed additional symmetry of Peccei and Quinn [24, 30, 31] was based on the assumption that the symmetry breaking scale of the PQ-symmetry was of the order of the electroweak scale $f_{\text{weak}} \approx 250$ GeV. This would imply an axion mass of larger than 150 keV, but this kind of axion was ruled out quickly. It is often referred to as PQWW-axion named after its initiators Peccei, Quinn, Weinberg and Wilczek. The other commonly used name for this "heavy" axion is *visible axion* in opposition to the later defined *invisible* or very light axions, which physicists started to look for, after the PQWW-axion was ruled out.

3.2.1 Mass of the Visible Axion

Peccei and Quinn adopted a weak interaction model which was rich enough to include weak CP-violation [24, 47] and in which the coupling of axions to leptons and quarks could be calculated straightforward. The interaction strength of axions with fermions could be obtained using current algebra methods. Two Higgs-doublets had to be introduced in order to obtain the necessary overall chiral U(1)-Symmetry of the Lagrangian. The Higgs doublets are assumed to have non-vanishing vacuum expectation values (VEV) λ_1 and λ_2. Their ratio is denoted by x and chosen positive with $x > 1$. The symmetry breaking scale is then obtained as

$$f_a = \sqrt{\lambda_1^2 + \lambda_2^2} = \left(\sqrt{2} G_F\right)^{-1/2} \equiv f_{\text{weak}} \approx 250 \text{ GeV}, \tag{3.24}$$

where G_F denotes the Fermi coupling constant. Bardeen and Tye calculated the axion mass [35] using standard current algebra methods to be

$$m_a = N\left(x + \frac{1}{x}\right)\frac{\sqrt{z}}{1+z}\frac{f_\pi m_\pi}{f_a}. \tag{3.25}$$

Here N denotes the number of quark generations, z is given in Eq. (3.8), the pion mass is $m_\pi = 135$ MeV and the corresponding decay constant $f_\pi = 93$ MeV. This formula corresponds in principle to Eq. (3.7) with $w \ll z$. Thus the axion mass can be calculated to be

$$m_a = 25N\left(x + \frac{1}{x}\right)\ \text{keV}. \tag{3.26}$$

Since $N \leq 3$ and $f_a \approx 250$ GeV, one obtains $m_a \gtrsim 150$ keV, due to the fact that $(x + 1/x) \geq 2$ for $x \geq 1$.

3.2.2 Lifetime of the Visible Axion

Bardeen and Tye [35] also provided calculations for the lifetime of the visible axion based on its decay into two photons assuming $E/N = 8/3$ in Eq. (3.22) as

$$\tau_{a\to\gamma\gamma} \approx \frac{\tau_{\pi^0}}{z}\left(\frac{m_{\pi^0}}{m_a}\right)^5 \approx 0.7\times 10^{-5}\left(\frac{1\ \text{MeV}}{m_a}\right)^5\ \text{s}, \tag{3.27}$$

with z being the quark mass ratio given in Eq. (3.8). Thus for an axion of 150 keV one expects a lifetime of about 0.1 s. Furthermore, for an axion heavier than 1 MeV, the lifetime can be much shorter, since the decay of axions into an electron-positron pair will be allowed [47]. This yields a lifetime of

$$\tau_{a\to e^+e^-} = \frac{8\pi f_a^2 x^2}{m_a^2\sqrt{m_a^2 - 4m_e^2}}, \tag{3.28}$$

with the electron mass m_e. For $x \approx 1$ and an axion mass of a few MeV's, the lifetime gets considerably smaller, namely 10^{-8}-10^{-9} s.

3.2.3 The Last Curtain for the Visible Axion

The PQWW-axion had been quickly ruled out by a combination of astrophysical arguments and direct experimental searches. The main astrophysical limit to eliminate the original axion follows from axion emission and its effect on stellar evolution of red giants. The most sensitive laboratory experiments looked for rare decays of Kaons and quarkonia, such as

$$K^+ \ \to a + \pi^+, \tag{3.29}$$

and

$$J/\psi \ \to a + \gamma, \tag{3.30}$$

$$\Upsilon \ \to a + \gamma. \tag{3.31}$$

Since no such decays could be observed, it was possible to conclude that the visible axion does not exist.

One of these experiments, as a representative example, was the Crystal Ball experiment[6], which

[6]For a description of the Crystal Ball detector see for example Ref. [48].

was looking for the direct coupling of axions to heavy quarks [31, 49]. This was accomplished by determining the branching ratios for J/ψ and Υ decays as given in Eq. (3.30) and Eq. (3.31). While the branching ratio for J/ψ decaying to $\gamma + a$ is given as

$$B\left(J/\psi \to \gamma a\right) = B\left(J/\psi \to \mu^+\mu^-\right) \frac{G_F m_c^2 x^2}{\sqrt{2}\pi\alpha} \propto x^2, \tag{3.32}$$

the decay rate for the corresponding Υ decay is

$$B\left(\Upsilon \to \gamma a\right) = B\left(\Upsilon \to \mu^+\mu^-\right) \frac{G_F m_b^2}{\sqrt{2}\pi\alpha x^2} \propto \frac{1}{x^2}. \tag{3.33}$$

Here, x is once more the ratio of the vacuum expectation values of the two Higgs doublets, G_F the Fermi constant and α the fine structure constant. The mass of the quark q is represented by m_q, i.e. $m_c = 1.4$ GeV and $m_b = 4.9$ GeV. In contrast to other experiments, which are limited in sensitivity to a certain range in x, this ratio can be elimintated by the Crystal Ball experiment due to the different x-dependence in the coupling of axions to quarks of charge $+2/3$ and $-1/3$ by combining the two branching ratios from Eq. (3.32) and Eq. (3.33) to obtain a parameter-free prediction [49]

$$\begin{aligned} B\left(J/\psi \to \gamma a\right) \cdot B\left(\Upsilon \to \gamma a\right) &= \frac{1}{2} B\left(J/\psi \to \mu^+\mu^-\right) \cdot B\left(\Upsilon \to \mu^+\mu^-\right) \left(\frac{G_F m_c m_b}{\pi\alpha}\right)^2 \\ &= (1.4 \pm 0.3) \times 10^{-8}. \end{aligned} \tag{3.34}$$

In this formula, the error results from experimental uncertainties in the $\mu^+\mu^-$ branching ratios. Further uncertainties arise from the quark masses, which could result in an additional factor of 2. The upper limit derived by the Crystal Ball experiment is together with measurements from the LENA experiment at DORIS and the CUSB collaboration at CESR [48] given by

$$B\left(J/\psi \to \gamma a\right) \cdot B\left(\Upsilon \to \gamma a\right) < 5.6 \times 10^{-10}, \tag{3.35}$$

and with this one can roughly obtain that

$$f_a \gtrsim 10^3 \text{ GeV or } m_a \lesssim 6 \text{ keV}. \tag{3.36}$$

Thus, the standard axion had been ruled out.

3.3 The Invisible Axion

Since the original PQWW-axion had not been observed in experiments, a different kind of axion, the invisible axion [50], was introduced. Due to the fact that the breaking scale f_a is in principal arbitrary, it could be chosen much larger than the electroweak symmetry breaking scale. This leads to a much weaker coupling and a smaller mass than initially expected for the PQWW-axion. For this reason, a more appropriate name for these axions would be *very light axions*, since there exist experimental possibilities to detect them, such that they are not invisible after all.
The simplest case of such an axion model is the so-called Kim-Shifman-Vainshtein-Zakharov

(KSVZ) model. Here, an exotic heavy quark Q carrying PQ-charge is introduced, since it is assumed that the ordinary quarks, leptons and Higgs fields do not carry PQ-charge. In a second model, the Dine-Fischler-Srednicki-Zhitnitskiĭ (DFSZ) model, introduced shortly afterwards, no additional heavy quark is needed. Instead, supplementary Higgs doublets are introduced, such that both Higgs doublets and light quarks carry non-zero PQ-charges.
Several variations of both scenarios, which will be described in the following, exist.

3.3.1 The KSVZ-Model

The first of the invisible axion models was suggested by Kim [40], Shifman, Vainshtein, and Zakharov [41]. This model is simple in the sense that the mechanism suggested by Peccei and Quinn decouples completely from ordinary particles, meaning that, at low energies, interactions between axions and matter or radiation only occur via the axion-gluon coupling generic to the PQ-scheme via an exotic heavy quark carrying PQ-charge. Ordinary fermions do not carry PQ-charge in the KSVZ model, that is $C_e = C_u = C_d = C_s = 0$. For this reason the KSVZ axions are also referred to as hadronic axions, since they do not couple to electrons at tree-level as described in Section 3.1.1. The weaker higher order coupling discussed in the same section exists, however.
The only particle which carries PQ-charge in the KSVZ model is the new heavy quark Q, which has to be introduced. The exotic Q couples to a complex scalar field σ, which does not participate in weak interactions, i.e. an SU(2) $\times$ U(1) singlet. This field has a large expectation value, which is proportional to the breaking scale f_a. The mass of Q is of the order hf_a, where h is the Yukawa coupling. Although the axion would couple mostly to the new heavy quark, it would still mix with the light quarks due to the color anomaly [51].
Hadronic axions couple to nucleons as decribed by Eq. (3.18) and the effective PQ-charges can be obtained by evaluation of Eq. (3.19) and Eq. (3.20) as

$$C_p = -0.39, \tag{3.37}$$
$$C_n = -0.04, \tag{3.38}$$

and the coupling for both nucleons is then

$$g_{ap}^{\mathrm{KSVZ}} = \frac{C_p m_p}{f_a} = -6.01 \times 10^{-8} m_a \,\mathrm{eV}^{-1}, \tag{3.39}$$
$$g_{an}^{\mathrm{KSVZ}} = \frac{C_n m_n}{f_a} = -0.69 \times 10^{-8} m_a \,\mathrm{eV}^{-1}. \tag{3.40}$$

The coupling of axions to photons is described by Eq. (3.12). The parameter E/N varies for different KSVZ models, thus suppressing ($E/N = 2$) [33] or enhancing ($E/N = 6$) [52] the axion to photon coupling. The case of $E/N = 0$ is often referred to as the standard KSVZ model. In general, for KSVZ axions E/N can be calculated as

$$\frac{E}{N} = 6Q_{\mathrm{heavy}}^2, \tag{3.41}$$

where Q_{heavy} is the electric charge of the heavy quark Q which can take values of $Q_{\mathrm{heavy}} = 2/3, -1/3, 1, 0$ [52] and thus the ratio of the anomalies can be between 0 and 6. Other authors

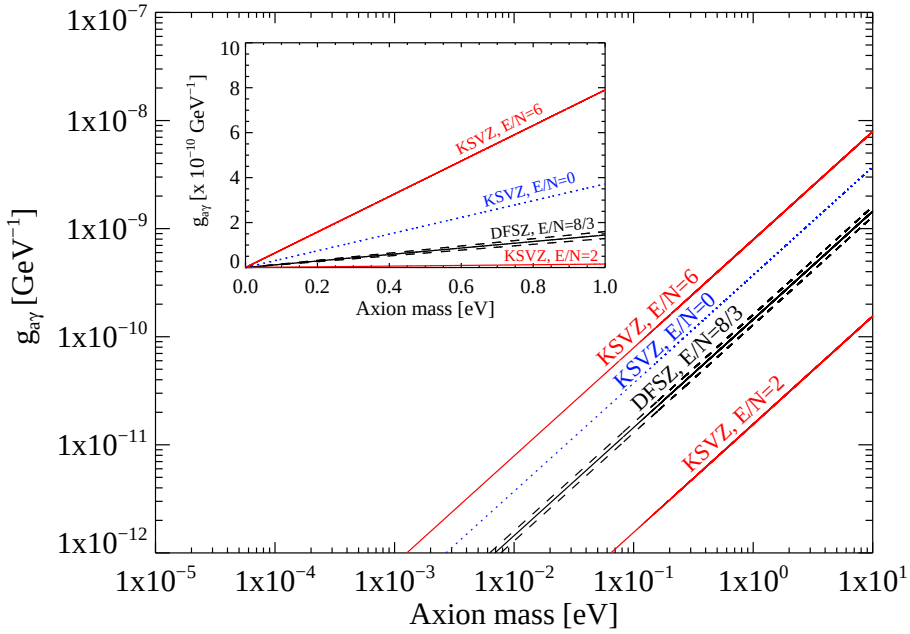

Figure 3.9: The two most common invisible axion models KSVZ and DFSZ are plotted in the region normally displayed in experimental exclusion plots on the axion-to-photon coupling depending on the axion mass. For KSVZ axions $E/N = 2$ and $E/N = 6$ are shown (red), while for the DFSZ model $E/N = 8/3$ is used (black solid line). Additionally, the error band is added here in form of dashed black lines. The inserted plot shows the same models but in linear scale to emphasize the effect of suppression in case of $E/N = 2$.

quote slightly higher values [53]. In Fig. 3.9, the most commonly used range of ratios ($E/N = 2$ and 6) and the standard KSVZ model ($E/N = 0$) are shown.
A possible disadvantage of this model might be that there is no clear physical motivation for the introduction of a heavy quark. Furthermore, it seems astonishing that the light quarks seem to be insensitive to the PQ-symmetry, although the $\bar{\theta}$-parameter, which is removed by the introduction of the PQ-symmetry, has its origin in the low energy theory. Moreover, the KSVZ axion might be very feably interacting, if the coupling to photons is strongly suppressed and thus it might be extremely difficult to detect.

3.3.2 The DFSZ-Model

The DFSZ model has been suggested shortly after the KSVZ model by Dine, Fischler, Srednicki [39] and Zhitnitskiĭ [38].While the KSVZ model decreased the axion mass by decreasing its coupling to ordinary matter and therefore needed to introduce both additional scalars and a supplementary quark, which are all neutral with respect to interactions in the electroweak sector, the DFSZ model follows a different philosophy. Again the axion is invisible, since it is connected to a SU(2) $\times$ U(1) singlet field σ with a large expectation value. The PQ-symmetry can be seen as a

chiral rotation, which acts on right-handed quarks and lepton fields [51]

$$u_R \rightarrow e^{-i\alpha X_1} u_R, \tag{3.42}$$
$$d_R \rightarrow e^{-i\alpha X_2} d_R, \tag{3.43}$$
$$e_R \rightarrow e^{-i\alpha X_2} e_R, \tag{3.44}$$

where $X_1 \neq -X_2$ has to be assumed to assure a chiral transformation for the quarks. This symmetry can be incorporated in the standard model by the introduction of (at least) two Higgs doublets Φ_1 and Φ_2: one couples only to right-handed quarks of charge $2/3$, while the other interacts only with right-handed quarks of charge $-1/3$ and right-handed charged leptons. Some fine-tuning is necessary in order to obtain a breaking scale much bigger than the electroweak scale, which could be seen as a disadvantage of this model. However, no new exotic heavy quarks have to be introduced as in the KSVZ model, since the known fermions are assumed to carry PQ-charge. A further advantage is that the DFSZ model can be easily incorporated in Grand Unified Theories (GUTs). In supersymmetric extensions of the standard model, two Higgs doublets rather than one are generally required. Ergo both, supersymmetry and PQ-symmetry, demand Higgs fields of identical SU(2) $\times$ U(1) properties, although the physics in the Higgs sector might differ [51].
In the DFSZ model, axions can couple to electrons at tree level, since electrons carry the effective PQ-charge

$$C_e = \frac{\cos^2\beta}{N_f}, \tag{3.45}$$

where N_f is the number of families and $\cos^2\beta = x^2/(x^2+1)$ is a parametrization of $x = \lambda_1/\lambda_2$, which is the ratio of the vacuum expectation values (VEVs) of the Higgs doublets[7]. The coupling constant can thus be obtained from Eq. (3.17)

$$g_{ae}^{\mathrm{DFSZ}} = 0.85 \times 10^{-10} m_a \frac{\cos^2\beta}{N_f}\ \mathrm{eV}^{-1} = 0.28 \times 10^{-10} m_a \cos^2\beta\ \mathrm{eV}^{-1}, \tag{3.46}$$

where $N_f = 3$ has been used.
For the coupling of DFSZ axions to nucleons the following equations apply

$$C_d = C_s = C_e = \frac{\cos^2\beta}{N_f}, \tag{3.47}$$
$$C_u = \frac{\sin^2\beta}{N_f}. \tag{3.48}$$

Using Eq. (3.19) and Eq. (3.20) along with $N_f = 3$, one obtains for the effective PQ-charge of proton and neutron:

$$C_p = -0.10 - 0.45\ \cos^2\beta, \tag{3.49}$$
$$C_n = -0.18 + 0.39\ \cos^2\beta. \tag{3.50}$$

The effective PQ-charges of the fundamental fermions for both KSVZ and DFSZ models are shown in Fig. 3.10. Quite a variety of DFSZ models exists differing mainly in the choice of the PQ-

[7] See Ref. [32] for a more extended explanation.

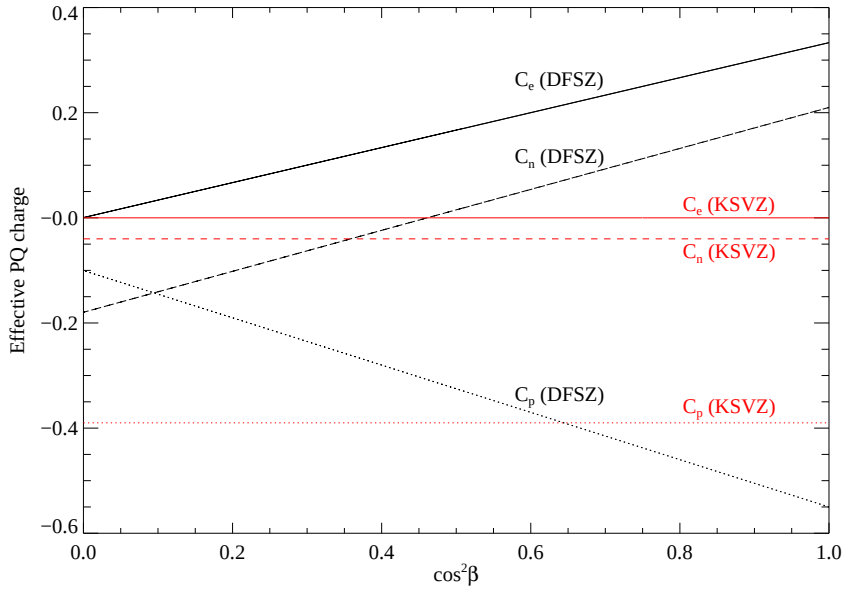

Figure 3.10: The model-dependent effective Peccei-Quinn charges are shown depending on the parametrization $\cos^2\beta$ of the ratio $x = \lambda_1/\lambda_2$ with the VEV λ_i $(i = 1, 2)$. While for the KSVZ model the effective charges of electron (C_e), proton (C_p) and neutron (C_n) are constant, they vary in the DFSZ scenario depending on $\cos^2\beta$.

charges [52].
For the coupling of axions to photons, E/N in the minimal DFSZ model is given by $8/3$ for any GUT since

$$\frac{E}{N} = \frac{2}{3}\frac{4X_u + X_d + 3X_e}{X_u + X_d}, \tag{3.51}$$

and $X_e = X_d$. Thus the coupling is, following Eq. (3.12),

$$g_{a\gamma}^{\mathrm{DFSZ}} \approx -0.74\,\frac{\alpha}{2\pi f_a}. \tag{3.52}$$

In Fig. 3.9, the minimal DFSZ model is illustrated along with the KSVZ model.

3.3.3 Other Models

It might be interesting to know that especially recently new models involving (still) hypothetical pseudoscalar particles have been proposed and studied with extended interest. Axion-like particles (ALPs) are new light spin-zero neutral particles which couple to two photons in the same way the axion does [54]. Further searches for exotic particles within the ALP community include quests for mini-charged particles from hidden sector physics involving paraphotons [55]. Sometimes the invisible axions are also referred to as WISPs (Weakly Interacting Sub-eV Particles [56]).

3.4 Axions as Dark Matter Candidate and the Origin of Axions

Several observations such as rotation curves of spiral galaxies, gravitational lensing and fluctuations in the cosmic microwave background (CMB) imply the existence of a new kind of matter which is not interacting electromagnetically. Therefore it is called dark matter (DM). Using precision cosmology the geometry of the universe has been constrained to be flat. Furthermore, it has been calculated that it consists of about 73% of dark energy[8] and roughly 23% of non-baryonic dark matter, while only about 4% are provided by ordinary baryonic matter. Dark matter could be composed of elementary particles which have mass, but do not carry electric charge. The interaction of such particles with ordinary matter is expected to be extremly feable, which makes it difficult, yet not impossible, to detect them.
Neutrinos are the only standard model particles which could account for the DM. But since they would contribute to the so-called hot dark matter (HDM), they cannot be the only DM component because this would contradict the observed structure of the universe. So far, it is not clear, what DM is made of, but the two most promising candidates are WIMPs[9] and axions.
A famous example of a WIMP is the lightest supersymmetric particle (LSP), such as a neutralino, which is part of the minimal supersymmetric extention of the SM. What makes WIMPs so attractive is that they are thermal relics, i.e. they have once been in thermal equilibrium with baryons and radiation. Thus, their cosmological history is relatively simple in the sense that their abundance only depends on their interaction rate [57]. Possible WIMP masses range from a few GeV up to the TeV scale.
For axions, it is more complicated to calculate the relic density, since this quantity depends on the production mechanism which is not necessarily thermal. This will be shown in the following section as well as in Section 3.6, where the cosmological history of axions will be described in more detail.

3.4.1 Axions as Dark Matter Candidates

Different sources and production mechanisms for axions in the early universe and nowadays exist. In the early universe, three distinct processes are believed to be responsible for the production of so-called relic axions [34]: thermal production [58], coherent production by the misalignment effect in the early universe [59] and the decay of axion strings, which are primordial topological defects [60]. Which of these processes dominates is still under discussion, since this depends not only on the axion mass but also on whether or not inflation took place.
Thermally produced axions, which have a mass in the eV range, would form a hot dark matter (HDM) component. Thermal relics were once in equilibrium with baryons and radiation. These relics survived to present days. Their number density can thus be predicted without strong model dependence.
The misalignment effect or the decay of axion strings on the other hand would provide very low-mass axions, which would contribute to the cold dark matter (CDM). These non-thermal relic axions would have been produced as Bose condensate during the QCD transition phase. Due

[8] The theoretical concept of dark energy is connected with Einstein's cosmological constant, which is still widely discussed. Given percentages might vary depending on the applied models.

[9] Weakly Interacting Massive Particles

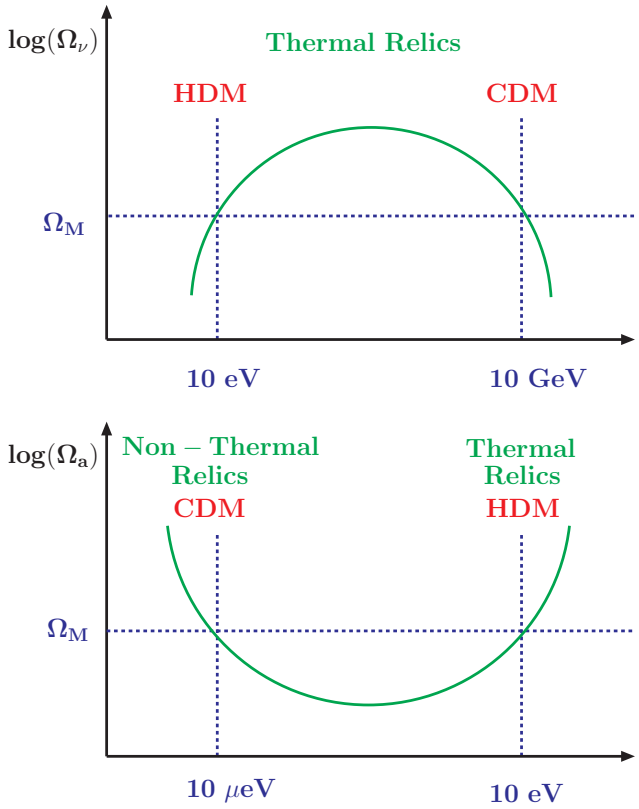

Figure 3.11: Top: Schematic Lee-Weinberg curve for neutrinos. Since neutrinos are thermal relics, they are HDM if they are light and CDM if they have larger masses. These heavy neutrinos have been ruled out by experiments. Bottom: Schematic Lee-Weinberg curve for axions. For small masses, axions are non-thermal relics and could provide part or all of the CDM. Heavier axions could also function as HDM if they were produced thermally [62].

to their low mass, their interaction strength would be so feable that they were never in thermal equilibrium.

The change-over between thermal and non-thermal production is likely to be around a PQ-scale of 10^8 GeV. In Fig. 3.11, the schematic Lee-Weinberg curves [61] for neutrinos (top) and axions (bottom) are shown. Here, matter density of neutrinos Ω_ν and axions Ω_a is provided as a function of the particle's mass. The total matter density, i.e. taking into account baryonic and non-baryonic components, is indicated by Ω_M.

Generally, the classification in HDM and CDM depends on whether the dark matter particle was relativistic or not at the time when the horizon of the universe enclosed sufficient matter for a galaxy to be formed. Thus the determining parameter for particles to be in thermal equilibrium with baryons and radiation is the mass of the particle. Since neutrinos are thermal relics, light neutrinos would contribute to the HDM component while heavier neutrinos would be cold. In principle the same reasoning is true for WIMPs.

For axions, this distinction is more complicated and depends mainly on the initial conditions which

are assumed. The result is that for low masses, axions are non-thermal relics and qualify as CDM, while heavier axions as thermal relics could provide part of the HDM of the universe.
It is worth mentioning, that beside these relic particles, axions could also be produced nowadays. Primakoff conversion of blackbody photons in strong electromagnetic fields produces axions or axion-like particles in the core of stars, such as for example our Sun. In this way it provides an additional energy loss channel for stars. A detailed description of solar axions will follow in Chapter 4.
One more way to produce axions today is to create them in a laboratory by sending a strong laser beam through a transverse magnetic field[10].Here the Primakoff effect is used as well. More details will be given in Section 3.7.

3.5 Astrophysical Axion Bounds

Since the strong CP-Problem is solved for any value of the PQ breaking scale f_a, the axion mass m_a is initially arbitrary. Astrophysical observations along with arguments based on cosmology are able to preclude certain mass ranges, in which axions are not viable. This proves helpful for experiments, which can then concentrate on regions, in which axions are likely to exist. In order to understand the astrophysical constraints, a short overview on the evolution of low-mass stars will be given. They are the main source to constrain the axion parameter space. Following this overview the different limits on the interaction strength of axions with various particles will be discussed. In Fig. 3.12 the astrophysical and cosmological bounds are summarized together with some experimentally studied regions.

3.5.1 Stellar Evolution of Low-Mass Stars

It is essential to understand the different stages of stellar evolution, i.e. how stars live and die, and how these stages can be observed in order to discover new energy loss channels. Although the details of star formation are still not fully understood, it is known that stars are mainly born in the disks of spiral galaxies, where globular clusters, which will be dealt with in more detail in the following section, can be found. These clusters provide a very good laboratory to study stellar evolution, since they contain early generations of stars, which are all of the same age and almost identical regarding their chemical composition. This leaves basically only one free parameter in which the stars differ, namely their initial mass.
In Fig. 3.13, the color-magnitude diagram (Hertzsprung-Russell diagram) of a typical globular cluster is shown. Essentially, in the vertical direction the brightness V in the visible band is displayed, while horizontally the difference between blueness B and brightness V is plotted. The blueness is a measure of the color or surface temperature, where blue (= hot) stars lie towards the left.
The life of a star begins on the so-called main sequence (MS), where stars burn hydrogen in their core. Different masses of the stars are reflected by different locations on the MS in the color-magnitude diagram. More massive stars are shining brighter and have thus a shorter lifetime.

[10]The external magnetic field has to match the missing quantum numbers for photon and axion to mix. Due to the fact that the photon is a spin 1 particle while the axion has spin 0 the magnetic field has to be transversal [32].

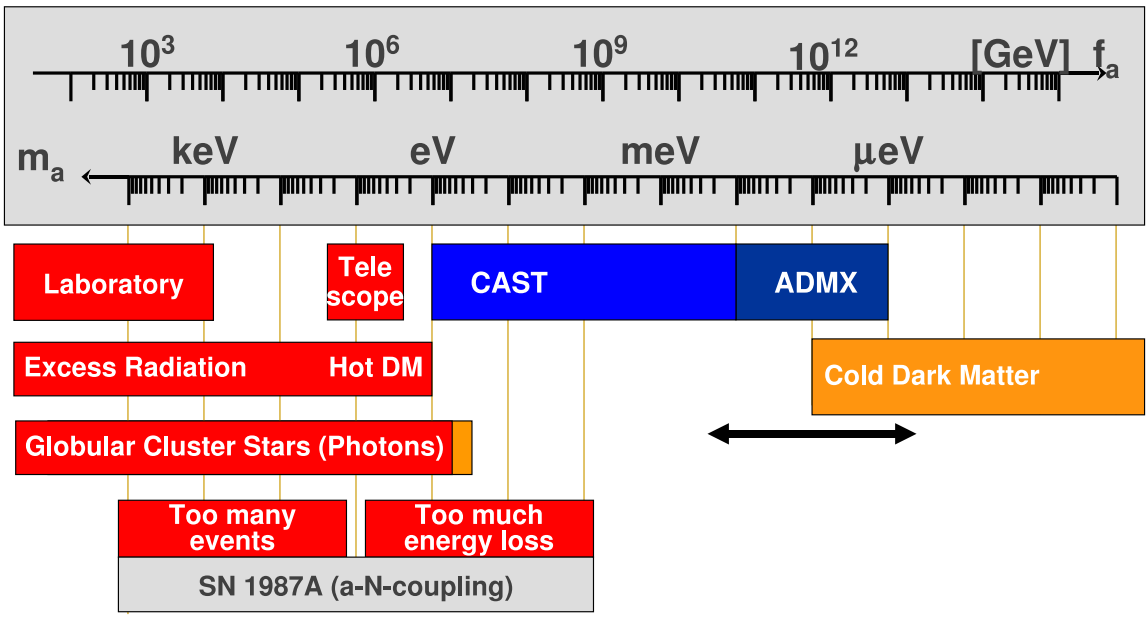

Figure 3.12: Summary of astrophysical and cosmological exclusion ranges and experimental search regions for axions. The various limits are discussed in Section 3.5 and Section 3.6.
The blue bars represent the experimental search ranges of CAST and ADMX, telescope and laboratory searches are included as well. For the theoretical limits, orange bars indicate a strong model-dependence. The cold dark matter (CDM) range in the low-mass region includes only the misalignment mechanism [63], which will be discussed in Section 3.6.

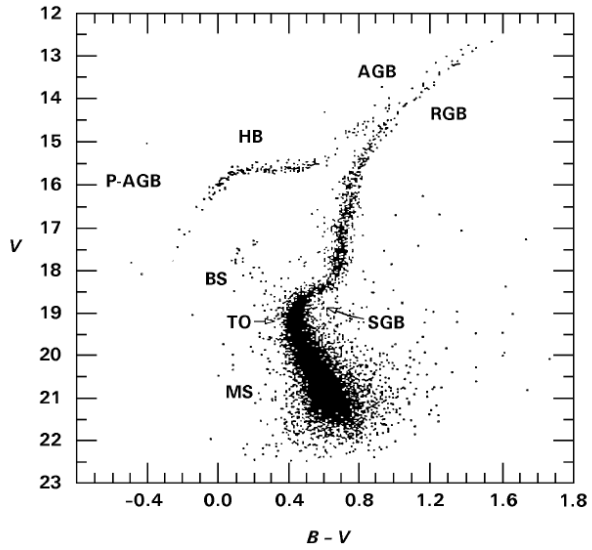

Figure 3.13: Color-magnitude diagram for a typical globular cluster. Essentially the surface temperature of the stars is shown on the x-axis, while the y-axis denotes the surface brightness V. The difference of blueness B (blue meaning hot and lying to the left side) and brightness V is a measure of color and thus surface temperature. The most important evolutionary stages can be classified as follows. In the main sequence (MS) one finds stars with core hydrogen burning. The main sequence turnoff (TO) marks the point where the central hydrogen supply is exhausted. The red giant branch (RGB) follows the previous phase. In these stars hydrogen burning in a thin shell is present, while the core grows until helium ignites. Stars then proceed to the horizontal branch (HB) having a helium burning core and a hydrogen burning shell. Finally the asymptotic giant branch (AGB) is reached in which stars show helium and hydrogen shell burning. Via the post-asymptotic giant branch (P-AGB) a white dwarf state can be reached. Further regions such blue stragglers (BS), sub giant branch (SGB) are not needed in the present discussion. Picture taken from [63].

Once the central hydrogen supply is exhausted, a degenerate helium core with a hydrogen burning shell is developed. This then leads to an increase in surface area and a decrease in surface temperature (red color), turning the star into a red giant. Since the luminosity is determined by the gravitational potential at the outer zone of the helium core, which is growing, the brightness of these stars increases and they climb up the red giant branch (RGB). A high position in the RGB indicates a very massive and compact helium core.
When the core reaches $0.5 M_\odot$[11], it is dense and hot enough to ignite helium. Since the ^{8}Be nucleus consisting of two α-particles is unstable, helium burning proceeds via the so-called triple-α reaction directly to carbon ($3\alpha \rightarrow {}^{12}C$). The brightness of the star decreases, since the energy production rate goes down in the hydrogen shell as the core expands further. These stars proceed to the horizontal branch (HB) in the color-magnitude diagramm. The downwards turn of the HB in Fig. 3.13 towards blue (left) is an artifact of the filter used. If the total luminosity as determined via bolometry is considered, the branch is truly horizontal.
Once the helium supply is exhausted, the star develops a degenerate carbon-oxygen core and climbs the asymptotic giant branch (AGB). Since these low-mass stars cannot ignite the carbon-oxygen core, they finally become white dwarfs. A more detailed description can be found in Ref. [64].

[11] $M_\odot \approx 1.988 \times 10^{30}$ kg is the solar mass.

3.5.2 Globular Cluster Stars

Globular cluster stars are able to provide a restrictive limit on the coupling constant $g_{a\gamma}$ of axions to photons by considering their helium-burning lifetime. Furthermore, a bound on the axion-electron coupling can be derived from observation of helium ignition. Generally speaking, a globular cluster is a gravitationally bound system of about 10^6 stars of low metallicity, which indicates great age. The stars in a globular cluster were formed at the same time, such that the most dominant difference between them lies in their initial mass. Two types of stars in globular clusters are especially interesting to obtain bounds on axionic parameters, namely horizontal branch (HB) stars and red giants (RG), which can both be found in the upper part of the color-magnitude diagram of Fig. 3.13.

Globular Cluster Bounds on the Axion-to-Photon Coupling

The difference between RG and HB stars is that RG have a degenerate helium core and a hydrogen burning shell, while HB stars are found with a helium burning core and a hydrogen burning shell. When RG stars reach their limiting mass, their core becomes dense and hot enough to ignite helium, which makes them proceed to the horizontal branch. In both types of stars, photons can be converted into axions via the Primakoff effect $Ze + \gamma \rightarrow Ze + a$ with the virtual photon of the electromagnetic fields of the electron and proton plasma (see Fig. 3.7). The axion production would be more effective in HB stars, where it could serve as a new energy loss channel, whereas it is negligible for RGs. As a result, one would expect that the HB stars exhaust their nuclear fuel faster and thus their lifetime decreases. If this is true, one should be able to observe that the number of HB stars is reduced in comparison to red giants[12]. From studies of the HB-to-RGB star ratio observed in 15 globular clusters [65] it can be concluded that the helium-burning lifetime agrees within about 10% with expectations. From this, it can be derived [32] that the non-standard energy loss rate integrated over the whole core, L_x, should stay below 10% of the standard helium-burning luminosity $L_{3\alpha}$, i.e.

$$L_x \lesssim 0.1\, L_{3\alpha}. \tag{3.53}$$

The standard value for $L_{3\alpha}$ is about $20 L_\odot$[13]. From the mass of the core of the HB star (roughly $0.5 M_\odot$), it can be calculated that the energy production rate averaged over the core, $\langle \epsilon_{3\alpha} \rangle$, is about 80 erg g^{-1} s^{-1}. From this, one obtains an upper limit on the energy loss rate per unit mass of the non-standard channel as

$$\epsilon_x \lesssim 10 \text{ erg g}^{-1}\text{s}^{-1}. \tag{3.54}$$

In order to obtain an upper limit on the axion-to-photon coupling constant, one needs to consider the axionic energy loss rate per unit mass of a non-degenerate plasma via the Primakoff effect, which is given by [32]

$$\epsilon = \frac{g_{a\gamma}^2 T^7}{4\pi\rho} F\left(\kappa_s^2\right), \tag{3.55}$$

[12] While low-mass stars spend about 10^{10} years on the main sequence, both the RGB and the HB sequence have a duration of about 10^8 years.

[13] $L_\odot \approx 3.84 \times 10^{33}$ erg/s denotes the solar luminosity and 1 erg $\equiv 10^{-7}$ J.

where screening effects, also referred to as Debye-Hückel effect[14], are taken into account via the dimensionless function

$$F\left(\kappa_s^2\right) = \frac{\kappa_s^2}{2\pi^2}\int_0^\infty dx\left[\left(x^2+\kappa_s^2\right) ln\left(1+\frac{x^2}{\kappa_s^2}\right) - x^2\right]\frac{x}{\mathrm{e}^x-1}. \tag{3.56}$$

Here $x = \omega/T$ is the (dimensionless) axion energy and κ_s is related to the so-called Debye-Hückel constant κ via

$$\kappa_s = \frac{\kappa}{2T}, \tag{3.57}$$

where

$$\kappa^2 = \frac{4\pi\alpha}{T}\sum_j Z_j^2 n_j. \tag{3.58}$$

In this equation, the temperature in the plasma is denoted by T, α is the fine-structure constant and n_j represents the number density of charged particles carrying the charge $Z_j e$. Typical values of F for the core of a HB star[15] and the Sun[16] are $F = 0.98$ and $F = 1.84$, respectively. Thus, for typical values of density and temperature in HB stars one obtains an axion energy loss rate of [32]

$$\epsilon = g_{10}^2\ 30\ \mathrm{erg\ g^{-1}s^{-1}}, \tag{3.59}$$

with $g_{10} \equiv g_{a\gamma}/10^{-10}\ \mathrm{GeV}^{-1}$. Since the axionic energy loss rate should not exceed the non-standard energy loss rate as given in Eq. (3.54), an upper limit on the axion-to-photon coupling constant is obtained as

$$g_{a\gamma} \lesssim 0.6\times10^{-10}\mathrm{GeV}^{-1}, \tag{3.60}$$

which is equivalent following Eq. (3.12) to

$$f_a/C_\gamma \gtrsim 2\times10^7\mathrm{GeV}. \tag{3.61}$$

In terms of axion masses this can be expressed as

$$m_a C_\gamma \lesssim 0.3\ \mathrm{eV}, \tag{3.62}$$

where $C_\gamma \approx 0.75$ for DFSZ axions and $C_\gamma \approx 0.08 - 4.08$ for KSVZ models.
This limit obtained from HB stars is often also called the globular cluster limit. Due to uncertainties in its determination, it might however vary by a factor of 2 [63]. Thus, if compared to experimental results, a reasonably conservative limit of $g_{a\gamma} \lesssim 1.0\times10^{-10}\ \mathrm{GeV}^{-1}$ is often used as the horizontal branch limit.

[14]The Debye-Hückel effect is a screening effect. The Primakoff effect involves only the electrostatic Coulomb fields of the target particles. In an environment of freely moving electric charges such fields are screened. This is for example the case in a stellar plasma, such that the axion production cross section will be reduced [66].

[15]Typical conditions in the core of a HB star are $T \approx 10^8$ K and $\rho \approx 10^4$ g/cm^3, which leads to a κ_s^2 of 2.5.

[16]Typical conditions in the Sun yield a κ_s^2 of 12.

Globular Cluster Bounds on Axion-to-Electron Coupling

The helium-burning lifetime is a useful argument to constrain the axion-photon coupling due to the fact that the Primakoff conversion of axions to photons is suppressed in the degenerate core of red giants while enhanced in HB stars. The helium ignition argument on the other hand is more helpful in order to derive a limit on the axion-electron coupling as will be illustrated in the following.
The degenerate helium core of RGB stars has typically a temperature of $T \approx 10^8$ K and a density of around 10^6 g cm^{-3}. At a critical combination of ρ and T, helium ignition takes place. Axion cooling could thus allow the core to grow more, before helium ignition starts, i.e. it could postpone helium ignition, leading to an increase in the brightness of red giants. Theoretical expectations and observations of the core mass at helium ignition match within $5 - 10\%$ [63]. This implies that an additional energy loss rate (with $T = 10^8$ K and average density $\rho = 2 \times 10^5$ g cm^{-3}) should be limited by 10 erg g^{-1} s^{-1}.The helium ignition argument is especially helpful when the emission rates are larger for stars on the red giant branch than on the HB. This is the case for electron-bremsstrahlung $e + Ze \to Ze + e + a$ (see Fig. 3.6). Given the conditions in a red giant core, one finds [67]

$$\epsilon_{\rm brems} \approx g_{ae}^2 \cdot 1.6 \times 10^{26} \text{ erg g}^{-1} \text{ s}^{-1}, \tag{3.63}$$

and this yields the limit

$$g_{ae} \lesssim 3 \times 10^{-13}. \tag{3.64}$$

By using Eq.(3.17) and Eq.(3.45), this corresponds to $f_a/C_e \gtrsim 2 \times 10^9$ GeV and an upper limit on the axion mass of $m_a C_e < 3.5$ meV in the DFSZ model.

Asymptotic Giant Branch Bounds on Axion-to-Electron Coupling

An axion-electron coupling of the order given in Eq. (3.64) would also have a strong effect on the evolution of AGB stars. However, since comparisons of the theoretical expectations with observed data are still missing, no new limits or evidence for signals from axion emission could be obtained.

3.5.3 White Dwarf Cooling

A further bound on the axion-electron interaction can be derived from the cooling of white dwarfs (WD). These compact objects are the remainder of initial low-mass stars (up to several solar masses $M_\odot$). The ignition of their degenerate carbon-oxygen core never takes place and thus the further development consists of cooling, first by neutrino losses and later by surface emission of photons. The axion emission can be constrained by comparing the observed cooling speed via the WD luminosity with calculated expectations. One derives a limit comparable to the one obtained by studying the helium ignition in HB stars

$$g_{ae} \lesssim 3.5 \times 10^{-13}. \tag{3.65}$$

It is furthermore possible to study the cooling speed of single white dwarfs in special cases (ZZ Ceti stars[17]), yielding the most restrictive limit on the axion-electron coupling [63]

$$g_{ae} \lesssim 1.3 \times 10^{-13} \text{ at } 95\% \text{ CL}, \tag{3.66}$$

[17]When white dwarfs appear as ZZ Ceti stars this means that the pulsation is not stable and the cooling speed can be determined via the decrease of the period. A well studied example of such a star is G117-B15A.

which in the DFSZ model translates to $m_a C_e < 1.67$ meV.

3.5.4 Supernova 1987 A

Physics of a Type II Supernova

The supernova SN 1987A provided for the first time the possibility to observe directly the neutrino emission of a newborn neutron star. In this supernova of type II, the star Sandulek-69202 in the Large Magellanic Cloud[18] collapsed. While type I supernovae appear in connection with white dwarfs in a binary system, those of type II are related to the collaps of evolved, massive stars ($M \gtrsim 8\ M_\odot$). These stars are in contrast to white dwarfs able to ignite carbon and oxygen in their center, which leads to heating. After the ashes of carbon burning[19] leave the star with a degenerate core the ignition of neon burning takes place. This processes continues until the star is left with a degenerate core of iron and multiple layers of different burning shells. Once the Chandrasekhar limit[20] of the iron core is reached, no further nuclear energy can be set free by fusion and the iron core becomes unstable ($T = 0.8 \times 10^{10}$ K≈ 0.7 MeV, $\rho \approx 3 \times 10^9$ g cm^{-3}). The following collaps is disrupted only, when the equations of state stiffen, which is the case when nuclear density is reached (3×10^{14} g cm^{-3}) [32] and shock waves form leading to an explosion. The remnants of such a supernova are an expanding nebula and a newborn neutron star (proto neutron star), which is an object of about one solar mass $M_\odot$ with temperatures of some 10 MeV and a high density. Even the very weakly interacting neutrinos are trapped.

Energy-Loss Argument: Free-Streaming and Trapping Scenario

On a larger time scale, energy emission can be explained by diffusive neutrinos transporting energy. Should particles exist which interact more weakly, they can provide a new and more efficient energy loss channel yielding a reduction in the duration of the neutrino burst. In principle this argument can be used to derive limits on many kinds of particles such as for example right-handed neutrinos. In the case of axions, the dominant emission process to be considered is axion-nucleon bremsstrahlung $N + N \rightarrow N + N + a$ as shown in Fig. 3.8. In the following the coupling to nucleons g_{aN} is assumed to be an average of the coupling to neutrons and protons[21].
In Fig. 3.14, the influence of the axion-to-nucleon coupling on the burst duration is illustrated. For very small g_{aN}, the time of the burst is not affected. However, for increasing coupling, the duration gets shorter and finally reaches a minimum (free-streaming regime). If g_{aN} increases further, axions are no longer able to escape (trapping regime) and cooling can only take place via axion diffusion and emission from an *axion sphere* [63], similar to the initial neutrino diffusion. Thus the burst duration increases again and axions are unable to affect the signal duration, once the

[18] The Large Magellanic Cloud is a satellite galaxy of the Milky way. Its distance is about 50 kpc.

[19] The ashes of carbon burning are neon, magnesium, oxygen, and silicon.

[20] The Chandrasekhar limit sets a bound on the mass of objects consisting of nuclei in an electron gas (electron-degenerate matter). It denotes the maximum mass which can be supported by electron degeneracy pressure without suffering a gravitational collaps. Beyond this limit, a stable degenerate system does not exist. The boundary is roughly given by $1.4\ M_\odot$ [32].

[21] As can be seen in Fig. 3.10, axions hardly couple to neutrons in the KSVZ model, but they do interact with protons, while for DFSZ axions the couplings depend on $\cos^2\beta$. In Ref. [32], C_N is thus estimated to be approximatelly 0.2.

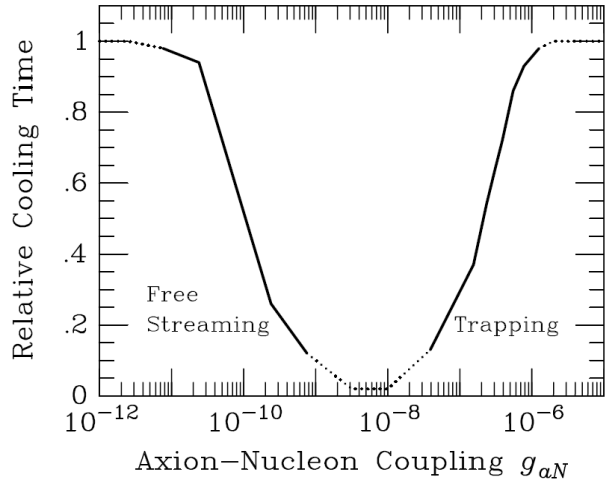

Figure 3.14: Relative duration of the neutrino cooling during SN 1978A depending on the axion-nucleon coupling g_{aN}. In the free streaming regime, the whole core emits axions, while in the case of the trapping regime, axion diffusion causes the emission from an *axion sphere*. While the solid line is based on calculations [68], the dashed line is a continuation by eye [32].

axion sphere moves beyond the *neutrino sphere*.
If axions are this strongly interacting, they would have interacted in the water Cherenkov detectors and thus produced additional events. This yields an excluded coupling constant range of

$$1 \times 10^{-6} \lesssim g_{aN} \lesssim 1 \times 10^{-3}. \tag{3.67}$$

This applies roughly to a range in masses of 20 eV to 20 keV [32]. In any case, there are other reasons (HB limit) by which the trapping regime can be excluded such that the region of interest is the free-streaming regime.
To exclude more values of the axion-nucleon coupling constant, the duration of the neutrino burst can be considered as mentioned above. For the free-streaming scenario, different simulations [63] constrain the additional energy loss rate at typical core conditions of $\rho = 3 \times 10^{14}$ g cm^{-3} and $T = 30$ MeV to

$$\epsilon_a \lesssim 1 \times 10^{19} \text{ erg g}^{-1} \text{ s}^{-1}. \tag{3.68}$$

The authors showed that this divides the neutrino burst duration time[22] in halves. In order to apply Eq. (3.68), Raffelt [32] calculated the non-degenerate energy loss per unit mass due to the axionic bremsstrahlung process (see Fig. 3.8) as

$$\epsilon_a = g_{aN}^2 \, 1.35 \times 10^{34} \text{ erg g}^{-1} \text{ s}^{-1} \, \rho_{15} \, T_{\text{MeV}}^{3.5}, \tag{3.69}$$

[22]Since the mass of the SN core is about $1.5\ M_\odot$, the axion luminosity can be calculated using Eq. (3.68) to be $L_a = \epsilon_a * M_\odot \approx 3 \times 10^{52}$ erg s^{-1}. Thus the axion emission would last about 10 s considering that the gravitational binding energy for a neutron star is roughly 3×10^{53} erg and axion losses would be able to compete with neutrino energy losses.

where $\rho_{15} = \rho/10^{15}$ g cm^{-3} and $T_{\mathrm{MeV}} = T/$ MeV. Comparison with Eq. (3.68) at typical core conditions leads to an excluded range of

$$3 \times 10^{-10} \lesssim g_{aN} \lesssim 3 \times 10^{-7}. \tag{3.70}$$

As mentioned above, the effective nucleon coupling is given by $g_{aN} = C_N m_N / f_a$. Here, an averaged effective PQ-charge for protons and neutrons (for the DFSZ model) as $C_N = 0.2$ is assumed, which is based on the assumption of a proton fraction of 0.3 in the core. One should keep in mind the overall uncertainty involved in the derivation of the excluded range from SN 1987A. A more detailed description can be found in [68].

3.5.5 Observations of the Sun

Further restrictions on the allowed coupling constant range for axions can be derived from observations of the Sun. Even though those might not be the most restrictive bounds, it is still interesting to study them, since solar observations have an experimental accuracy which surpasses that of other stars by orders of magnitude. In the following chapter, which is dedicated entirely to solar axions, the solar age, results from helioseismology as well as the measured solar neutrino flux will be considered briefly.

3.6 Axion Bounds from Cosmology

3.6.1 Thermal Production (HDM)

Axions can be produced in the early universe by interactions with quarks and gluons [58]. Due to the axion-π^0-mixing, the interaction $\pi + \pi \leftrightarrow \pi + a$ is a model-independent process. It is the dominant thermalization process at $T \approx 200$ MeV, i.e. after the QCD phase-transition and before the pions annihilate [69]. Analogous to massive neutrinos, these cosmic axions would be part of the hot dark matter (HDM). Restrictive limits on the possible fraction of HDM can be derived from cosmological precision data (WMAP-5[23]) yielding an axion mass range $m_a < 0.4 - 1.2$ eV, the so-called HDM limit [70]. The different constraints on the axion mass result from the use of various cosmological data. The most restrictive limits are obtained by using Lyman-α forest[24] data which however suffer from poorly controlled systematic uncertainties. The more conservative limit does not take these data into account.
A further, however weaker, upper axion mass bound can be obtained via the so-called excess radiation criterion. If axions were to have masses larger than 20 eV, they could decay into photons more quickly than a cosmic time scale. This would decrease the axion population, but provide radiation, such that limits on this kind of excess radiation can be derived [6, 71]. Even for a very small $g_{a\gamma}$, it is not possible to avoid this limit, since if decays are suppressed, this would lead to an overdomination of the thermal axions in the mass density of the universe.
Both constraints, the HDM limit and the excess radiation bounds, are included in Fig. 3.12.

[23] Wilkinson Microwave Anisotropy Probe

[24] The term Lyman-α forest referes to the total of all absorption lines which arise in the spectra of far away quasars or galaxies due to Lyman-α transitions of neutral hydrogen. The absorption lines appear, when the light from the distant object traverses the interstellar gas.

3.6.2 Misalignment Production

Due to the role axions can play as a cold dark matter (CDM) candidate, they are especially interesting from a cosmological point of view. In addition to thermally created particles, the *misalignment mechanism* [59] can produce axions. After the Peccei-Quinn symmetry $U_{\mathrm{PQ}}(1)$ is spontaneously broken at a temperature of the universe T_{PQ} corresponding to the PQ breaking scale f_a, the axion field relaxes in the Mexican Hat potential (see Fig. 3.15). At this stage the axion is massless and, due to the rotational symmetry of the potential, the value of $\bar{\theta}$ is not yet fixed. The axion can be seen as this massless degree of freedom.

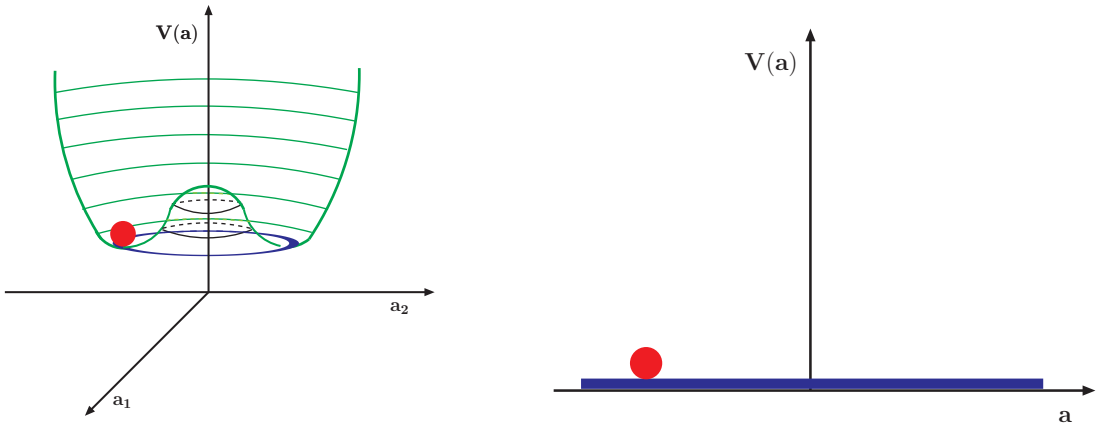

Figure 3.15: After the Peccei-Quinn symmetry $U_{\mathrm{PQ}}(1)$ is spontaneously broken at a temperature T_{univ} corresponding to the PQ breaking scale f_a, the axion field relaxes in the Mexican Hat potential.

Two scenarios have to be distinguished. In the first case, inflation occurs with a reheat temperature[25] $T_{\mathrm{reheat}} < T_{\mathrm{PQ}}$, i.e inflation homogenizes the axion field and basically erases axion strings (Inflation scenario). The second case, on the other hand, assumes that inflation takes place with T_{reheat} larger than the temperature of the PQ-transition, which is in this case equivalent to the scenario that inflation does not occur at all (String Scenario).
Near the QCD phase transition ($T_{\mathrm{univ}} = \Lambda_{\mathrm{QCD}} \approx 200$ MeV), $U_{\mathrm{PQ}}(1)$ is explicitly broken by instanton effects, which is exactly the effect causing the dynamical restauration of the PQ-symmetry and giving mass to the axion. This corresponds to a tilting of the Mexican Hat potential (see Fig. 3.16) such that the axion field moves towards the minimum, where the CP-symmetry is conserved. Coherent oscillations of the axion field form at a critical time t_1 corresponding to a temperature $T_1 \approx 1$ GeV [72] and build a *CDM condensate* [6]. The amplitude of the oscillations depends on how far away from zero the axion field is, when the particle acquires its mass. The contribution of these oscillations is called *vacuum realignment* [72].

[25] At the end of inflation a process called reheating or thermalization occured. Due to the fact that the exact circumstances of inflation are unknown, the process of reheating is also still not well understood.

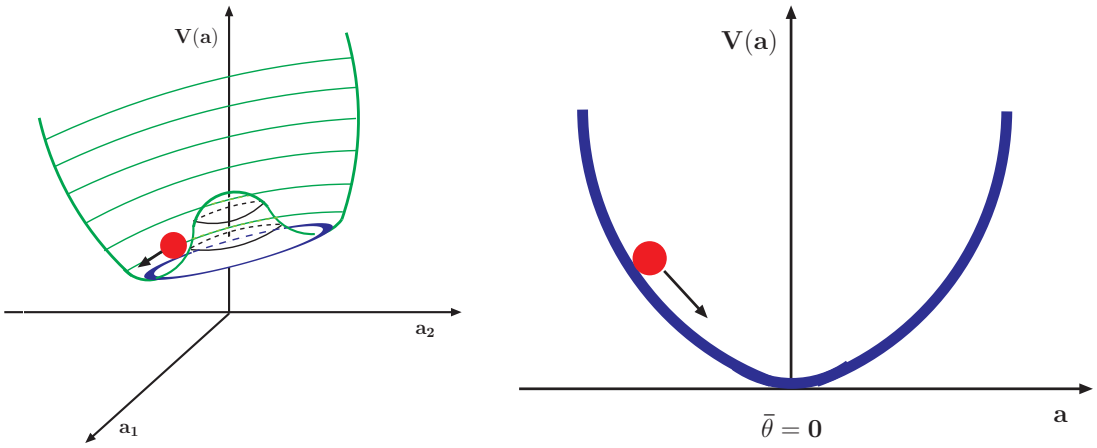

Figure 3.16: $U_{\rm PQ}(1)$ is explicitely broken by instanton effects near the QCD phase transition, which corresponds to a tilting of the Mexican Hat potential. The axion field moves then to the CP-conserving minimum and oscillates around it.

3.6.3 Inflation Scenario

If inflation takes place after the PQ-symmetry breaking, i.e. it occurs with a reheat temperature $T_{\rm reheat} < T_{\rm PQ}$, the only contribution to the cosmic critical density Ω is provided by the misalignment mechanism and is given by [69]

$$\Omega_a h^2 \approx 0.7 \left(\frac{f_a}{10^{12}\ \text{GeV}} \right)^{7/6} \left(\frac{\bar{\theta}_i}{\pi} \right)^2 , \tag{3.71}$$

where the present-day Hubble expansion parameter h is given in units of 100 km s^{-1} Mpc^{-1} and the initial misalignment angle, relative to the position where CP is conserved, is $-\pi \leq \bar{\theta}_i \leq \pi$. Eq. (3.71) shows that this contribution might be accidentally suppressed if the initial misalignment angle happens to be close to 0. If the reheat temperature during inflation is too low to restore the PQ-symmetry, then the axion field exists during inflation and underlies quantum mechanical fluctuations which lead to observable temperature fluctuations in the CMB. These anisotropies in the CMB are severely constrained by precision cosmological data [69]. One consequence is that even for small $\bar{\theta}_i$ the axion population cannot be randomly small. The axion mass would thus be expected to be below $m_a \lesssim 1$ meV [73].

3.6.4 String Scenario

In the second scenario, inflation takes place with $T_{\rm reheat} > T_{\rm PQ}$, which means basically that inflation occurs before the PQ-symmetry breaking or not at all. The consequence of this is that, in addition to vacuum misalignment, axion string[26] decay and axion domain wall[27] decay contribute

[26] Cosmic strings are one-dimensional topological defects which form when an cylindrical or axial symmetry is broken. In case of the PQ-symmetry, these strings are axionic strings.

[27] Domain walls are two-dimensional topological defects. They form when a discrete symmetry is spontaneously broken at a phase transition.

to the cosmological energy density [69].
Axion strings are present after the PQ-transition and decay into axions until the critical time t_1, when the axion acquires mass and every string becomes the boundary of N domain walls. For $N = 1$, the tilting of the Mexican hat potential explains how the axion gets its mass. The fact that $N > 1$ cannot be visualized in this way anymore, since there are then N degenerate CP-conserving minima present. This case leads to the so-called domain wall problem [46]. This problem can be solved ([69] and references therein) but shall not be considered here such that $N = 1$ is assumed in the following. Thus, the contributions to the axion cosmological density result from the initial misalignment effect, the axionic string decay until t_1 and the decay of domain walls (bounded by strings after t_1) into axions. The last contribution can be neglected, yielding a cosmic axion density of [69]

$$\Omega_a h^2 \approx 0.34 \left(\frac{f_a}{10^{12}\ \text{GeV}} \right)^{7/6} . \tag{3.72}$$

Comparing this to the experimentally determined CDM density of $\Omega_{\text{CDM}} h^2 \approx 0.13$ indicates that axions of $m_a \approx 10\ \mu$eV can contribute to the dark matter, while smaller masses are ruled out [6].
In any case, exact results are a controversial issue and Eq.(3.72) is subject to many sources of uncertainty beside the debate about the contribution of axionic string decay to the axion cosmological density.
One more comment on the string scenario would be that here *axion mini clusters* could form, holding a significant fraction of the CDM axions. Since the axion density variations in space during QCD transition are large, free-streaming might not be able to cancel these fluctuations, which leads to the above mentioned mini clusters bound by gravitation, when matter starts to dominate the universe.

Summarizing, the window left open for axions by all considered astrophysical and cosmological constraints reaches from μeV to some meV. Nevertheless, experiments do not only cover this window but also search the "prohibited" regions since neither astrophysical nor cosmological arguments yield absolutely stringent limits. All constraints from astrophysics and cosmology are summarized in Fig. 3.12, where especially for the cold dark matter region the uncertainty is indicated.

3.7 Detection of Invisible Axions

After the rather quick exclusion of visible axions, Pierre Sikivie was the first to accept the challenge of detecting invisible axions and he suggested several experiments, which could serve to find the elusive axions [74]. In his paper, both, haloscopes to look for galactic axions and helioscopes to search for solar axions were suggested. The basic idea is to convert axions into monoenergetic photons by using a strong magnetic field (Primakoff effect, see Chapter 4). This seems to be the most promising approach, since the axion-to-photon coupling is a generic feature of every axion model as a natural consequence of the axion-gluon interaction. Thus, many experiments are making use of the coupling of axions to photons.
In the case of a Coulomb field of a particle carrying charge, the above mentioned conversion can be understood as a scattering process $\gamma + Ze \rightarrow Ze + a$. A strong magnetic field denotes the other

extreme, a macroscopic field. The conversion can be best viewed as an axion-photon oscillation comparable to neutrino-flavor oscillations, since the momentum transfer is small and coherent interaction over a certain length takes place.
The experiments looking for invisible axions can be categorized into three groups according to the origin of the axions: haloscopes and telescope searches looking for galactic axions, laser experiments trying to detect laboratory axions and helioscopes in quest of solar axions. Figure 3.17 provides an overview of the covered axion parameter regions by the various experiments which will be discussed in the following sections.

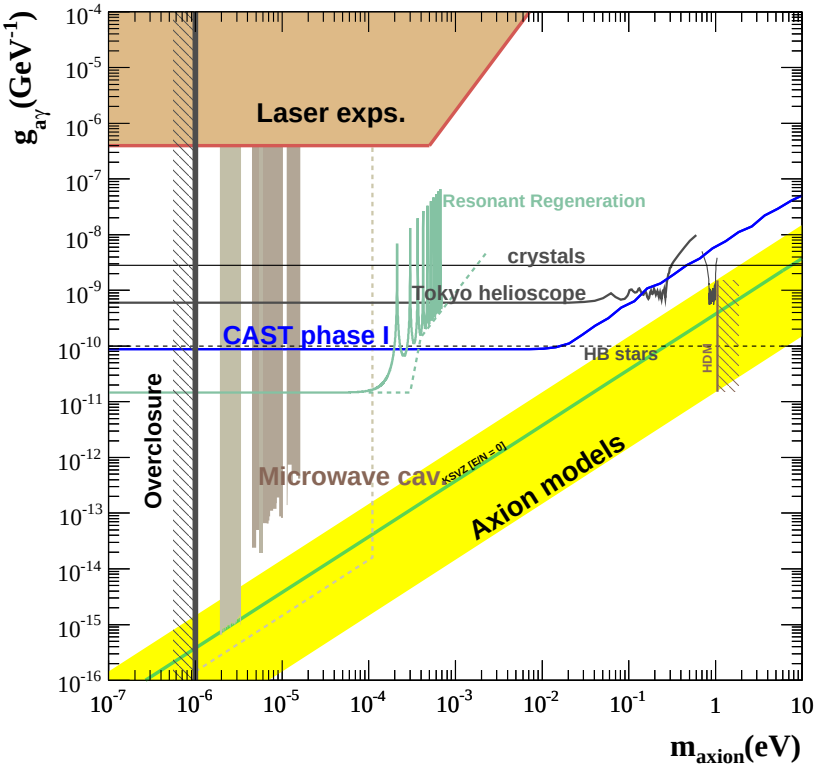

Figure 3.17: Excluded ranges in the axion parameter space by different experiments. A more detailed description of the various types of experimental setups can be found in the text of this section.

3.7.1 Galactic Axion Searches

Haloscopes

In case axions exist, they could provide a significant part or even all of the cosmic CDM, as the astrophysical and cosmological limits in Fig. 3.12 indicate. In a certain range of reasonable axion masses for CDM, galactic halo axions might be detected by microwave cavities, so-called haloscopes. When passing through a strong static magnetic field [74], axions of masses in the μeV

range could be converted resonantly into nearly monochromatic microwave photons (GHz range). The microwave cavity needs to be tunable, since the coupling of axions is only possible to transversal magnetic (TM) modes of the cavity and the axion mass is yet unknown.
The first experiments were done in the 1980s (RBF[28] [75], UF[29] [76]) and yielded upper limits on the axion-photon coupling constant varying from

$$g_{a\gamma}(95\%\ \mathrm{CL}) < 2.4 \times 10^{-14}\ \mathrm{GeV}^{-1} \text{ for an axion mass } m_a = 4.5 \times 10^{-6}\ \mathrm{eV}, \tag{3.73}$$

to

$$g_{a\gamma}(95\%\ \mathrm{CL}) < 4.2 \times 10^{-13}\ \mathrm{GeV}^{-1} \text{ for an axion mass } m_a = 1.6 \times 10^{-5}\ \mathrm{eV}. \tag{3.74}$$

Further experiments followed, applying the same principle but putting a lot of effort in increasing the sensitivity. The ADMX[30] experiment at LLNL[31] so far excluded the mass range of [77]

$$1.98\ \mu\mathrm{eV} < m_a < 2.17\ \mu\mathrm{eV}. \tag{3.75}$$

SQUID[32] amplifiers were used in order to improve the experimental setup by reducing noise and to obtain in this way the above result. At the present time, ADMX is being upgraded by implementing dilution refrigerators in order to further decrease the temperature of the cavity. This increases the speed of the frequency scans even further. The next data taking runs are expected to start in 2009.

Another possibility to detect galactic axions is to utilize the selective ionization of Rydberg atoms and detect the electrons which are produced. This method is applied in the CARRACK[33] experiment located in Kyoto, Japan. While CARRACK I searched around $10\ \mu$eV, CARRACK II investigated the region of $2\ \mu\mathrm{eV} < m_a < 50\ \mu$eV [78]. Since the highly excited atoms need a very good stability of temperature, the CARRACK experiment has been upgraded from stage I to phase II by using a dilution refrigerator. The results achieved so far by haloscopes are included in Fig. 3.18 along with the prospects of the upgraded ADMX experiment.

Telescope Searches

While the two-photon decay rate of axions with masses in the CDM regime is expected to be extremely slow, it could be observable for thermally produced "multi-eV" axions. An almost monochromatic emission line from galaxies and clusters of galaxies [79] should be observable in experiments. An early search (Kitt Peak National Observatory [80]) excluded the mass range of

$$3\ \mathrm{eV} < m_a < 8\ \mathrm{eV}. \tag{3.76}$$

while a more recent search of the same kind [81] led to an excluded range of axion masses of

$$4.5\ \mathrm{eV} < m_a < 7.7\ \mathrm{eV}, \tag{3.77}$$

[28] Rochester-Brookhaven-Fermilab
[29] University of Florida
[30] Axion Dark Matter eXperiment
[31] Lawrence Livermore National Laboratory
[32] Superconducting QUantum Interference Devices
[33] Cosmic Axion Research using Rydberg Atoms in a resonant Cavity in Kyoto

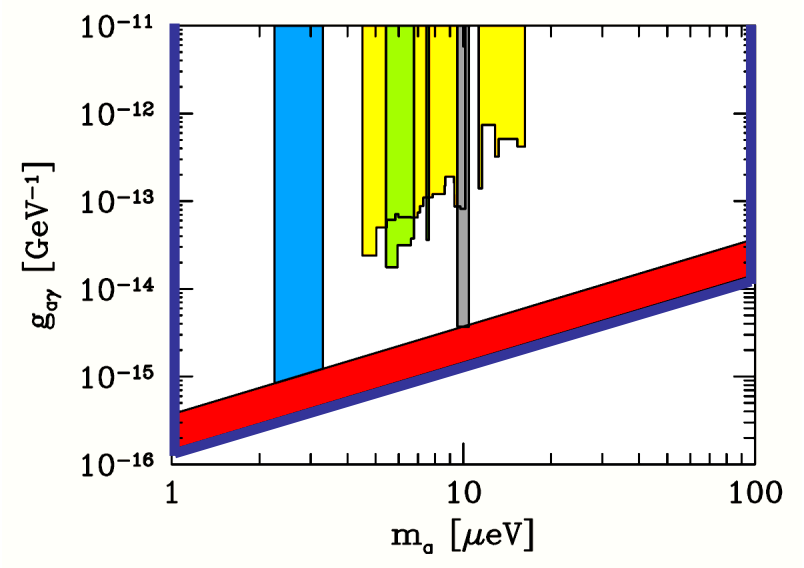

Figure 3.18: Exclusion plot for various haloscope experiments. The yellow region represents the results of RBF [75], and the green area refers to the limits derived by UF [76]. Furthermore, first results of ADMX [77] are included in blue along with the prospects for the upgraded experiment (dark blue frame). The CARRACK I [78] results are shown in grey and the axion model region is indicated in red [62].

unless the coupling of axions to photons is highly suppressed. Thus the range marked as "Telescopes" in Fig. 3.12 could be excluded.
At the Haystack Observatory, a radio telescope was applied to observe nearby dwarf galaxies and derived an upper bound on the coupling constant of [82]

$$g_{a\gamma}(96\%\ \mathrm{CL}) < 1.0 \times 10^{-9}\ \mathrm{GeV}^{-1} \text{ for axion masses } 298\ \mu\mathrm{eV} \lesssim m_a \lesssim 363\ \mu\mathrm{eV}. \quad (3.78)$$

3.7.2 Laboratory Axion Searches

Shining-Light-Through-Walls: Regeneration Experiments

In pure laboratory experiments, no astrophysical or cosmological sources of axions are needed, since the axions are directly produced in the laboratory. Thus, these experiments are independent of models for axion fluxes or densities, which might have to be used in other circumstances.
The basic principle of "Shining-Light-through-Walls" or beam dump experiments is that a strong laser beam is shone through a transverse magnetic field, such that a fraction of the photons is converted into axions. Then a wall or shield is set up to block the photons, while the feably interacting axions are able to pass the barrier. On the other side of the wall, a second transverse magnetic field allows for reconversion of the axions into photons, which can then be detected [83, 84]. Fig. 3.19 illustrates the working principle. It is also possible to use resonanting cavities on both sides [85].
Such an experiment done in the early 1990s [86] resulted in an upper limit on the axion-photon

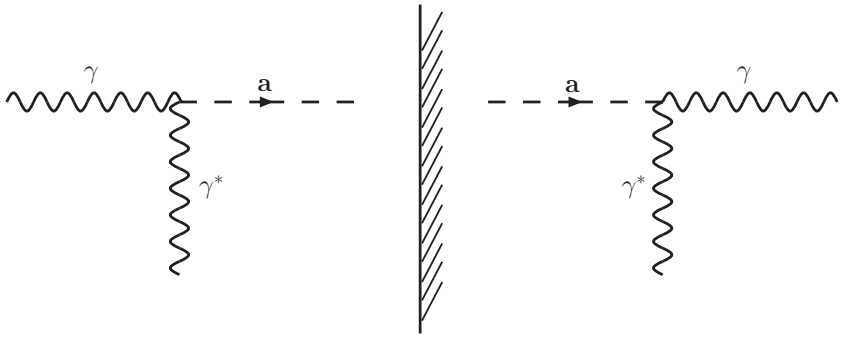

Figure 3.19: Working principle of "Shining-Light-through-Walls" experiments. An incoming photon beam is partly converted into axions in the presence of a transverse magnetic field. A wall keeps the photons from passing to the other side, while the axions are able to pass it unimpededly. Beyond the barrier, a second magnetic field is used to convert the axions back into photons, which can then be detected.

coupling constant of

$$g_{a\gamma}(95\%\ \mathrm{CL}) < 6.7 \times 10^{-7}\ \mathrm{GeV}^{-1} \text{ for axion masses } m_a < 10^{-3}\ \mathrm{eV}. \tag{3.79}$$

More recently, several experiments of this kind have been commissioned in view of an apparent signal claimed by the PVLAS[34] collaboration [87] (for more details see the following section on polarization experiments) in order to confirm it or rule it out.
One of these experiments, the LIPSS[35] experiment at Jefferson Lab, excluded coupling constants larger than 10^{-6} GeV^{-1} for masses around 1 meV [88], thus ruling out the claimed signal.
Another result comes from the BMV[36] collaboration, which also did not see any signal [89].
The same has also been confirmed by the GammeV[37] experiment at FNAL[38] giving a 3σ constraint on $g_{a\gamma} < 3.2 \times 10^{-7}$ in the limit of a massless particle [90].
Also at DESY and CERN experiments have been taking first data. ALPs[39] will need additional upgrades, which are under preparation [56], in order to compete with experiments like GammeV while OSQAR[40] published first results, such that one more experiment excludes the PVLAS signal [91]. In Fig. 3.17, the search region of these experiments in the axion phase space is indicated by the turquoise line labeled "resonant regeneration".

Polarization Experiments

As an alternative to regenerating photons, which have been converted into axions, it is also possible to detect the axion-to-photon conversion induced by a magnetic field directly in the beam itself.

[34] Polarizzazione del Vuoto con LASer (Vacuum Polarization with Laser)
[35] LIght Pseudoscalar or Scalar Search
[36] Birefringence Magnetic du Vide (Magnetic Vacuum Birefringence)
[37] Gamma to milli-eV particle search
[38] Fermi National Accelerator Laboratory
[39] Axion-Like Particle Search/ Any Light Particle Search
[40] Optical Search for QED vacuum magnetic birefringence, Axion and photon Regeneration

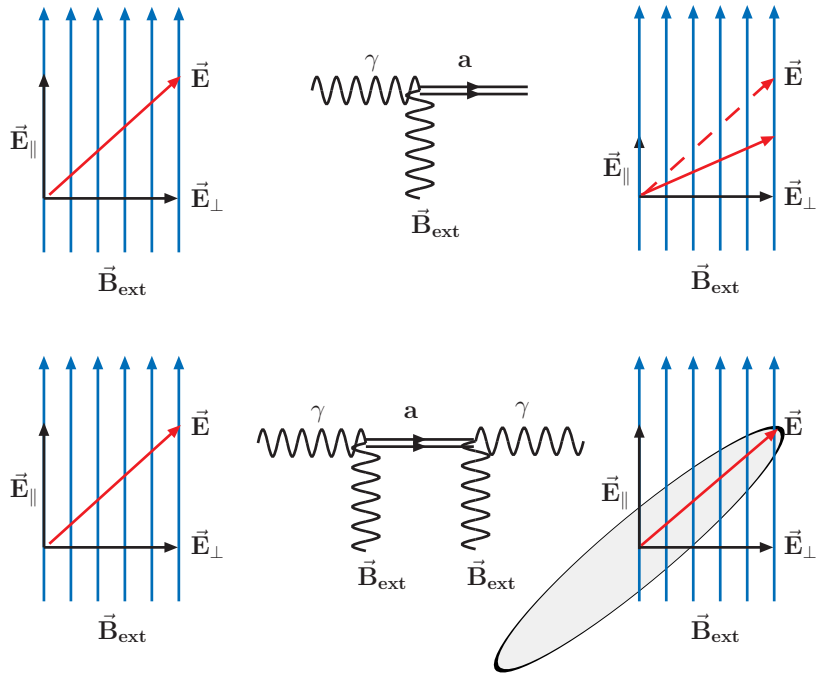

Figure 3.20: Upper image: Basic principle of the development of dichroism (Rotation of the polarization plane), which is induced by the creation of a massive particle coupling to two photons. Lower image: Basic principle of formation of ellipticity, which is induced by the retardation of an electric field component relative to another, when virtual massive particles mix (2-photon coupling).

If polarized light passes through a transverse magnetic field, it experiences both, dichroism and birefringence. Dichroism means that a small rotation of the polarization vector of linearly polarized light is observable. This is due to the fact that the electric field component $E_{\parallel}$, which is parallel to the magnetic field B, is diminished by axion production, while the perpendicular part $E_{\perp}$ stays unaffected (see upper part of Fig. 3.20). Birefringence on the other hand is observable in the fact that initially linearly polarized light becomes elliptically polarized (see lower part of Fig. 3.20). This happens due to the mixing of virtual axions in the $E_{\parallel}$ but not in the $E_{\perp}$ state.
Such an experiment has been performed by Semertzidis et al. [92], yielding

$$g_{a\gamma} < 2.5 \times 10^{-6}\ \text{GeV}^{-1} \text{ for axion masses } m_a < 7 \times 10^{-4}\ \text{eV}, \tag{3.80}$$

as a result for the observed optical rotation.
In 2006, PVLAS, a more recent polarization experiment, reported a signature, which might have been interpreted tentatively as evidence for a light pseudo-scalar particle with a mass of about $1 - 1.5$ meV and a coupling to photons of around 3×10^{-6} GeV^{-1} [87]. The imminent difficulty was to reconcile such a signal with the more stringent limits on the axion-photon coupling constant as obtained from the Sun for example by CAST. Theoretical models to explain this discrepancy were developed and several experiments were launched immediately to test the PVLAS signal (see previous section). More recently, the PVLAS collaboration published a report, withdrawing the

former results. They concluded that the observed effects were instrumental artifacts rather than an indication of new physics [93]. Despite the fact that the excitement turned out to be for no specific reason, the axion community profited from the renewed interest and increased research activity, which had been triggered by the apparent signal.

3.7.3 Solar Axion Searches

Helioscopes

Helioscopes are used to look for axions coming from the Sun. For this purpose either an electric or a magnetic field can provide the prerequisites to convert axions into photons via the inverse Primakoff effect.
Crystalline detectors can provide an electric field in order to convert axions coherently into photons, which is the case when the angle of incident of the axion fulfills the Bragg condition with the plane of the crystal [94]. The three important experiments investigating these Bragg patterns are SOLAX[41], COSME[42] and the DAMA[43] experiment.
SOLAX studied the mass range $m_a \lesssim 1$ keV. It obtained a limit on the axion to photon coupling of [95]

$$g_{a\gamma}(95\%\ \mathrm{CL}) < 2.7 \times 10^{-9}\ \mathrm{GeV}^{-1} \text{ for axion masses } m_a \lesssim 1\ \mathrm{keV}, \tag{3.81}$$

using a Germanium spectrometer.
COSME provided a similar result with a Germanium detector as well. It is independent of the axion mass and yields [96]

$$g_{a\gamma}(95\%\ \mathrm{CL}) < 2.78 \times 10^{-9}\ \mathrm{GeV}^{-1}. \tag{3.82}$$

DAMA gave a limit of [97]

$$g_{a\gamma}(90\%\ \mathrm{CL}) < 1.7 \times 10^{-9}\ \mathrm{GeV}^{-1}, \tag{3.83}$$

with a NaI(Tl) crystal independent of the axion mass. Unfortunately, studies revealed that the capability to detect solar axions using an electric field is limited due to the low conversion probability in available detector materials and thus neither present nor future crystal detectors are able to compete with the globular cluster limit (see Section 3.5.2), unless extremely long exposure times are accepted with very high background suppression [98].
Instead of an electric field, the second type of axion helioscopes uses a transverse magnetic field for the axion-to-photon conversion [74, 99]. The first experiment of this kind by Lazarus and collaborators published their results in 1992 [100]. They derived a limit of

$$g_{a\gamma}(99\%\ \mathrm{CL}) < 3.6 \times 10^{-9}\ \mathrm{GeV}^{-1} \text{ for axion masses } m_a < 0.03\ \mathrm{eV}, \tag{3.84}$$

and the examination of an extended mass range yielded the 3σ upper limit of

$$g_{a\gamma}(99\%\ \mathrm{CL}) < 7.7 \times 10^{-9}\ \mathrm{GeV}^{-1} \text{ for axion masses } 0.03\ \mathrm{eV} < m_a < 0.11\ \mathrm{eV}. \tag{3.85}$$

[41] SOLar AXion search in Argentina
[42] Germanium detector located in the Canfranc Underground Laboratory
[43] Particle DArk MAtter searches with highly radiopure scintillators at Gran Sasso

The Tokyo Axion Helioscope applied the same method with a higher sensitivity and could thus improve the limit to [101]

$$g_{a\gamma}(95\%\ \mathrm{CL}) < 6.0 \times 10^{-10}\ \mathrm{GeV}^{-1} \text{ for axion masses } m_a < 0.03\ \mathrm{eV}. \tag{3.86}$$

Only recently the experiment published the results of its third phase [102], in which the magnet has been filled with a buffer gas to restore coherence, further improving its previously obtained limits to

$$g_{a\gamma}(95\%\ \mathrm{CL}) < 5.6 - 13.4 \times 10^{-10}\ \mathrm{GeV}^{-1} \text{ for axion masses } 0.84\ \mathrm{eV} < m_a < 1.0\ \mathrm{eV}. \tag{3.87}$$

The CERN Axion Solar Telescope (CAST), which is the topic of Chapter 5, where a detailed description can be found, is applying the same principle but has a much higher sensitivity than the Tokyo Axion Helioscope, due to its larger product of magnetic field and length. It achieved in its first phase an upper limit on the axion-to-photon coupling constant of [53, 103]

$$g_{a\gamma}(95\%\ \mathrm{CL}) < 8.8 \times 10^{-11}\ \mathrm{GeV}^{-1} \text{ for axion masses } m_a < 0.02\ \mathrm{eV}. \tag{3.88}$$

The exclusion plot of CAST's Phase I with vacuum inside the magnet can be seen in Fig. 3.21. The first results of the Tokyo helioscope are included as well along with other experimental and theoretical bounds. The results of CAST's second phase with ^{4}He in the magnet bores are the subject of this thesis and will be described in more detail later on.

Big Scale Helioscope

As a closing remark, a possible future experiment to find solar axions is based on the idea to observe the Sun from an X-ray satellite, when the Earth is in between the star and the satellite. Thus, Earth's magnetic field on the side away from the Sun could be used to convert solar axions into photons and these can then be detected by the satellite [104]. Only small axion masses $m_a \lesssim 10^{-4}$ eV could be covered, but the sensitivity could be able to compete with astrophysical limits.

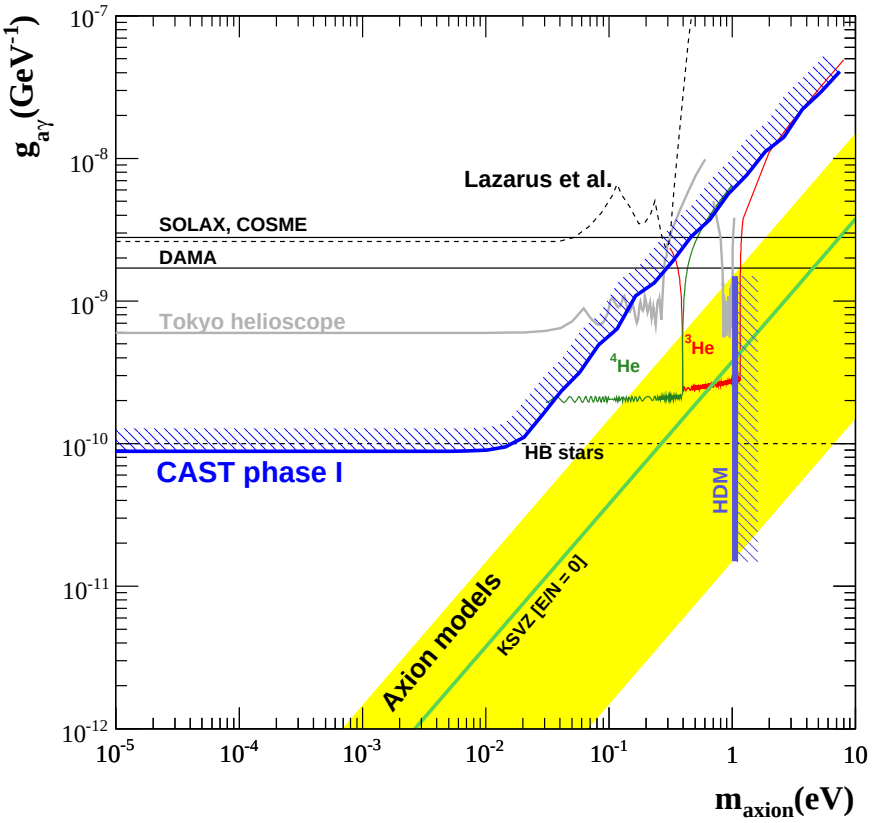

Figure 3.21: CAST exclusion plot of the axion-to-photon coupling constant at 95% CL for all data obtained in Phase I [53]. The achieved limit of CAST is compared with other experimental constraints (Lazarus [100], SOLAX [95], COSME [96], DAMA [97], Tokyo helioscope [101]). The prospects for CAST's Phase II are shown in green (^{4}He) and red (^{3}He). Furthermore, the Horizontal Branch (HB) star limit and the hot dark matter (HDM) limit are included. The yellow band represents the typical theoretical axion models and the green solid line corresponds to the case of the KSVZ model with $E/N = 0$.

Chapter 4

The Solar Axion

CAST is one of the experiments which use the Sun as the closest celestial source of axions in order to proof or rule out the existence of the still hypothetical particle. This chapter is therefore meant to discuss the relevant parameters of solar axion production and detection. First the production of solar axions via the Primakoff effect will be studied and the expected solar axion flux at Earth in the frame of a standard solar model will be discussed. For the detection of axions in magnetic fields, the main factor next to the expected flux is the probability of conversion for axions into photons. Closely connected with this probability is the coherence condition, which determines in which axion mass range efficient conversion can be achieved depending on the given experimental conditions. Having studied the expected axion flux and the conversion probability, it is possible to determine the expected number of photons arising from axion-to-photon conversion. This considerations will be done closing this chapter.

4.1 Production of Axions in the Sun

4.1.1 Solar Axion Production and the Solar Model

As already discussed in Section 3.4, axions can be produced in the core of stars, such as our Sun, which is the closest, brightest and best-known celestial axion source and thus qualifies perfectly for scientific observations. In the extremely hot and dense core of the Sun, the two photon coupling of pseudoscalars allows for the conversion of blackbody photons with energies in the keV-range into axions. The virtual photon is hereby provided by the strong electromagnetic field, originating from the charged particles in the plasma. The Feynman diagram of this so-called Primakoff effect [45] is shown in Fig. 4.1 and can be written as

$$\gamma + Ze \rightarrow Ze + a. \tag{4.1}$$

In non-relativistic conditions, the Primakoff effect turns out to be relevant. In this case, electrons and nuclei can be considered heavy in comparison to the energies of the surrounding photons. Therefore, the differential cross section in this case (not taking into account recoil effects) is given by [32]

$$\frac{d\sigma_{\gamma\rightarrow a}}{d\Omega} = \frac{g_{a\gamma}^2 Z^2 \alpha}{8\pi} \frac{|\vec{p}_\gamma \times \vec{p}_a|^2}{\vec{q}^{\,4}}, \tag{4.2}$$

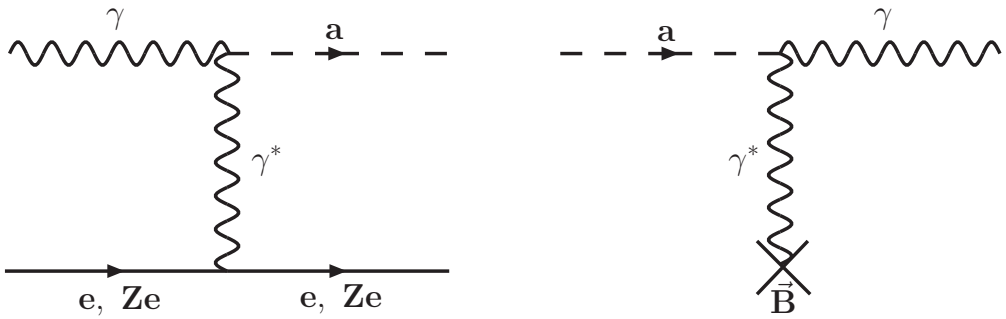

Figure 4.1: Left: Feynman diagram of the Primakoff effect in the Sun. A photon is converted into an axion in the electric field, which originates from the charged particles in the plasma. Right: In a laboratory magnetic field, the axion can couple to a virtual photon provided by the transverse magnetic field resulting in a real photon. This is the so-called inverse Primakoff effect.

where the axion and photon energies are taken to be equal and the momentum transfer is given by $\vec{q} = \vec{p}_\gamma - \vec{p}_a$. The cut-off of the long-range Coulomb potential in vacuum for massive axions is given by the minimum required momentum transfer

$$q_{\min} = \frac{m_a^2}{2E_a}, \tag{4.3}$$

for $m_a \ll E_a$, yielding a total cross section of

$$\sigma_{\gamma\to a} = Z^2 g_{a\gamma}^2 \left[\frac{1}{2}\ln\left(\frac{2E_a}{m_a}\right) - \frac{1}{4}\right]. \tag{4.4}$$

The cut-off of the long-range coulomb potential in a plasma is due to screening effects resulting in an additional factor of the differential cross section such that

$$\frac{d\sigma_{\gamma\to a}}{d\Omega} = \frac{g_{a\gamma}^2 Z^2 \alpha}{8\pi} \frac{|\vec{p}_\gamma \times \vec{p}_a|^2}{\vec{q}^{\,4}} \frac{\vec{q}^{\,2}}{\kappa^2 + \vec{q}^{\,2}}. \tag{4.5}$$

Here, the screening effects are described by the Debye-Hückel scale given by [105]

$$\kappa^2 = \frac{4\pi\alpha}{T_\odot} \sum_j Z_j^2 n_j, \tag{4.6}$$

where $T_\odot$ denotes the temperature in the plasma (solar core), α is the fine-structure constant and n_j represents the number density of charged particles carrying the charge $Z_j e$. Near the center of the Sun, the Debye-Hückel scale κ is roughly 9 keV and the ratio $(\kappa/T) \approx 7$ is approximately constant throughout the Sun. Raffelt [66, 105] calculated the total scattering cross section taking into account this modification. Assuming a non-relativistic medium and neglecting recoil effects, he derived an expression for the transition rate $\Gamma_{\gamma\to a}$ by summing over all target species of the medium

$$\Gamma_{\gamma\to a} = \frac{T_\odot \kappa^2 g_{a\gamma}^2}{32\pi^2} \frac{|\vec{p}_\gamma|}{E_\gamma} \int d\Omega \frac{|\vec{p}_\gamma \times \vec{p}_a|^2}{\vec{q}^{\,2}\,(\vec{q}^{\,2} + \kappa^2)}. \tag{4.7}$$

Performing the angular integration yields in terms of the photon energy E_γ and the absolute value of its momentum $p_\gamma = |\vec{p}_\gamma|$ as well as using $p_a = |\vec{p}_a|$ as the absolute axion momentum [66],

$$\begin{aligned}\Gamma_{\gamma\to a} &= \frac{T_\odot \kappa^2 g_{a\gamma}^2}{32\pi}\frac{p_\gamma}{E_\gamma}\left\{\frac{\left[(p_\gamma+p_a)^2+\kappa^2\right]\left[(p_\gamma-p_a)^2+\kappa^2\right]}{4p_\gamma p_a\kappa^2}\times\ln\left[\frac{(p_\gamma+p_a)^2+\kappa^2}{(p_\gamma-p_a)^2+\kappa^2}\right]\right.\\ &\left.-\frac{\left(p_\gamma^2-p_a^2\right)^2}{4p_\gamma p_a\kappa^2}\ln\left[\frac{(p_\gamma+p_a)^2}{(p_\gamma-p_a)^2}\right]-1\right\}. \end{aligned} \tag{4.8}$$

For the Sun, the effective mass of the photon in the medium, i.e. the plasma frequency[1] ω_p, is small. Typically, it is around 0.3 keV, while the solar core temperature is $T_\odot = 15.6\times10^6$ K $=$ 1.3 keV, leading to typical photon energies of about $3T_\odot \approx 4$ keV. In the following, the plasma frequency will be neglected for this reason and photons will be treated as completely massless. Recoil effects can be ignored, such that $E_\gamma = E_a$ in the photon-to-axion conversion and one can assume $p_\gamma = E_\gamma = E_a$ and $p_a = \sqrt{E_a^2 - m_a^2}$. This turns Eq. (4.8) into

$$\begin{aligned}\Gamma_{\gamma\to a} &= \frac{T_\odot \kappa^2 g_{a\gamma}^2}{32\pi}\left\{\frac{\left(m_a^2-\kappa^2\right)^2+4E_a^2\kappa^2}{4E_a p_a\kappa^2}\ln\left[\frac{(E_a+p_a)^2+\kappa^2}{(E_a-p_a)^2+\kappa^2}\right]\right.\\ &\left.-\frac{m_a^4}{4E_a p_a\kappa^2}\ln\left[\frac{(E_a+p_a)^2}{(E_a-p_a)^2}\right]-1\right\}. \end{aligned} \tag{4.9}$$

For axion masses small against the axion energy, i.e. $p_a \approx E_a$, the next to last term tends to zero and the above equation transforms to

$$\Gamma_{\gamma\to a} = \frac{T_\odot \kappa^2 g_{a\gamma}^2}{32\pi}\left[\left(1+\frac{\kappa^2}{4E^2}\right)\ln\left(1+\frac{4E^2}{\kappa^2}\right)-1\right]. \tag{4.10}$$

The differential axion flux expected at Earth can be obtained by a convolution of the transition rate and the distribution of blackbody photons of the Sun followed by an integration using a standard solar model as

$$\frac{d\Phi_a\left(E_a\right)}{dE_a} = \frac{1}{4\pi d_\odot^2}\int_0^{R_\odot} d^3\vec{r}\,\frac{1}{\pi^2}\frac{E_a^2}{\mathrm{e}^{E_a/T}-1}\Gamma_{\gamma\to a}, \tag{4.11}$$

where the average distance to the Sun is $d_\odot = 1.50\times10^{13}$ cm. Van Bibber *et al.* derived a well-approximated formula [99], using the standard solar model developed by Bahcall *et al.* [106] in 1982

$$\frac{d\Phi_a(E_a)}{dE_a} = 4.02\times10^{10}\left(\frac{g_{a\gamma}}{10^{-10}\mathrm{GeV}^{-1}}\right)^2\frac{\left(E_a/\mathrm{keV}\right)^3}{\mathrm{e}^{(E_a/1.08\mathrm{keV})}-1}\left[\mathrm{cm}^{-2}\mathrm{s}^{-1}\mathrm{keV}^{-1}\right]. \tag{4.12}$$

The average axion energy is $\langle E_a\rangle = 4.2$ keV and its maximum[2] is around 3 keV. From this, the

[1] See Appendix A.

[2] This is the case for KSVZ axions (hadronic axions), for which only the Primakoff production mechanism is relevant. For DFSZ model axions, for which bremsstrahlung processes are dominant, the peak position would be shifted to lower energies.

total axion flux can be calculated as

$$\Phi_a = 3.54 \times 10^{11} \left(\frac{g_{a\gamma}}{10^{-10}\ \mathrm{GeV}^{-1}} \right)^2 \ \mathrm{cm}^{-2}\,\mathrm{s}^{-1}. \tag{4.13}$$

Thus, the axion flux is proportional to g_{10}^2, which corresponds to the square of the coupling constant $g_{a\gamma}$ in units of 10^{-10} GeV^{-1}, i.e.

$$g_{10} = \frac{g_{a\gamma}}{10^{-10}\ \mathrm{GeV}^{-1}}. \tag{4.14}$$

The axion luminosity using this standard solar model is

$$L_a = 1.7 \times 10^{-3} \left(\frac{g_{a\gamma}}{10^{-10}\ \mathrm{GeV}^{-1}} \right)^2 L_\odot, \tag{4.15}$$

where $L_\odot$ is the solar photon luminosity[3].
In 2004, Bahcall and Pinsonneault [107] published an updated solar model, such that the axion parameters could be re-evaluated [108] as

$$\begin{aligned} \Phi_a &= 3.75 \times 10^{11} \left(\frac{g_{a\gamma}}{10^{-10}\ \mathrm{GeV}^{-1}} \right)^2 \ \mathrm{cm}^{-2}\,\mathrm{s}^{-1}, \\ L_a &= 1.85 \times 10^{-3} \left(\frac{g_{a\gamma}}{10^{-10}\ \mathrm{GeV}^{-1}} \right)^2 L_\odot, \\ \langle E_a \rangle &= 4.20\ \mathrm{keV}, \end{aligned} \tag{4.16}$$

with the average axion energy $\langle E_a \rangle$. Figure 4.2 shows a comparison of the differential solar axion flux for the solar model from 1982 (dotted black line) and the one from 2004 (solid red line). It can be seen that the influence of the changes in the solar model is fairly small. The same can be said for the total axion flux prediction. Since the flux calculation is only accurate within a few percent, the changes have been expected to be not severe.
An analytic approximation for the differential axion flux of the 2004 model can be obtained by fitting the function

$$\frac{d\Phi_a(E_a)}{dE_a} = A \left(\frac{E_a}{E_0} \right)^\alpha \mathrm{e}^{-(\alpha+1)E_a/E_0}. \tag{4.17}$$

with the three parameters A, E_0 and α to solar data. While A is a normalization factor, E_0 corresponds to the average energy $\langle E_a \rangle$ and α is related to higher moments of energy. The best fit can be obtained for the function

$$\frac{d\Phi_a(E_a)}{dE_a} = 6.020 \times 10^{10} \left(\frac{g_{a\gamma}}{10^{-10}\mathrm{GeV}^{-1}} \right)^2 \frac{(E_a/\mathrm{keV})^{2.481}}{\mathrm{e}^{((E_a/\mathrm{keV})/1.205)}} \left[\mathrm{cm}^{-2}\mathrm{s}^{-1}\mathrm{keV}^{-1} \right]. \tag{4.18}$$

The provided fit accuracy is at the 1% level for energies from 1 to 11 keV.
If an imaging device is used for detecting photons from axion-to-photon conversion, as it is the

[3] $L_\odot = 3.84 \times 10^{33}$ erg/s

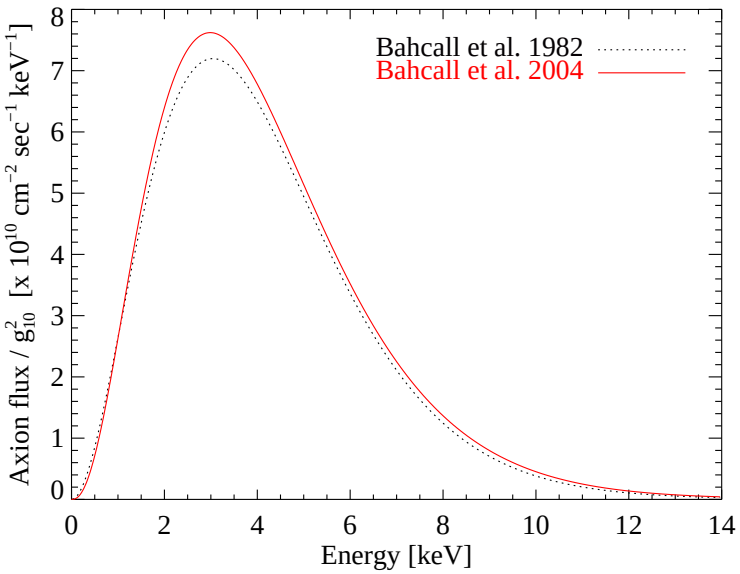

Figure 4.2: Comparison of the differential axion flux from the Sun at Earth for two different solar models. The dotted black line shows the flux for an early solar model from 1982 [106], while the solid red line uses a modern solar model [107].

case for the CAST experiment with its X-ray telescope (see Chapter 5 and 6), it is of advantage to consider the differential axion flux as an apparent surface luminosity $\varphi_a\left(E_a, r\right)$ of the solar disk [108]. This means that the flux is calculated per unit surface area of the apparent 2-dimensional solar disk and it is a function of the dimensionless radial coordinate $0 \leq r \leq 1$, which represents the radius normalized to the radius[4] of the Sun $R_\odot$. The apparent surface luminosity $\varphi_a\left(E_a, r\right)$ can be determined by

$$\varphi_a\left(E_a, r\right) = \frac{R_\odot^3}{2\pi^3 d_\odot^2} \int_r^1 ds \frac{s}{\sqrt{s^2 - r^2}} E_a \; k \; f_B \Gamma_{a\to\gamma}, \tag{4.19}$$

and is given in units of cm^{-2} s^{-1} keV^{-1} per unit surface area, which is dimensionless, due to the fact that the radial coordinate r does not have a dimension. Here, $d_\odot$ is the average distance of the Earth from the Sun as in Eq. (4.11), s represents the radial position in the Sun, which determines the physical quantities to be considered, e.g. the temperature and density. Finally, $f_B = \left(\mathrm{e}^{E_a/T_\odot} - 1\right)^{-1}$ is the Bose-Einstein distribution. In Fig. 4.3, the axion surface luminosity as seen from Earth is shown as a function of axion energy E_a and radial coordinate r. The color scale is given in units of axions/ (cm$^2 \cdot$ s $\cdot$ keV) per unit surface area on the solar disk. It can be seen that most axions are expected to originate from the inner 20% of the solar radius. Furthermore, the axion flux is expected to be largest at energies around 3 keV. Figure 4.4 illustrates the energy dependence of the axion surface luminosity for several radial coordinates. It has been derived by integrating up to different values of r.

[4] $R_{\mathrm{Sun}} = R_\odot = 6.9598 \times 10^{10}$ cm

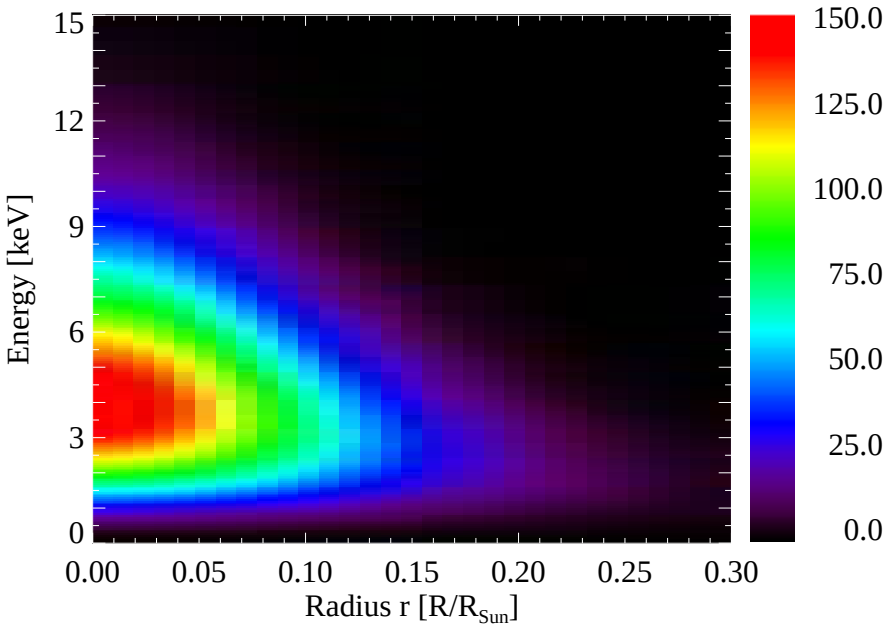

Figure 4.3: Contour plot of the axion surface luminosity of the Sun as a function of energy and dimensionless radial coordinate r. The units, in which the flux is given, are axions/ (cm^2 · s · keV) per unit surface area on the solar disk.

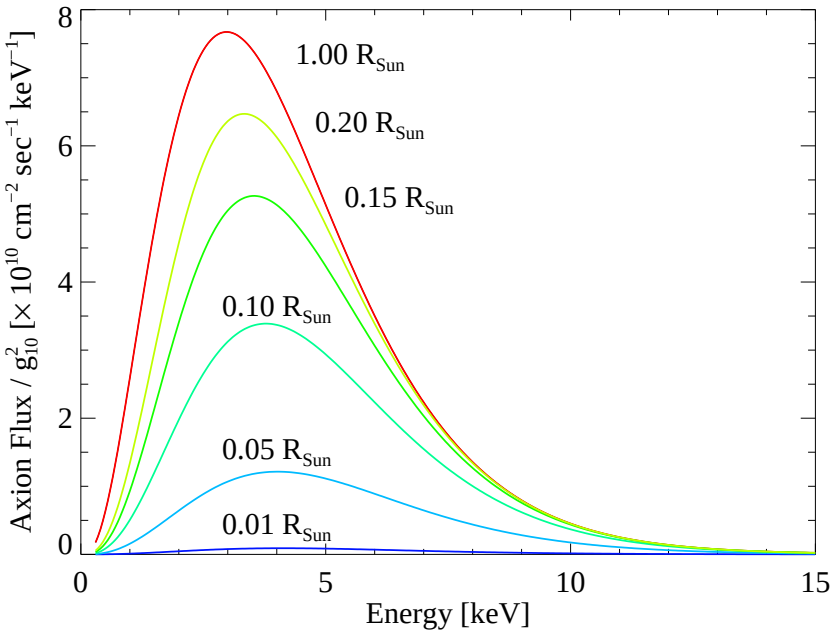

Figure 4.4: Solar axion surface luminosity depending on energy for various values of the radial coordinate r. It has been derived by integrating up to different values of r. Here the same units as in Fig. 4.3 have been used.

The total axion flux at Earth can be obtained from the apparent surface luminosity $\varphi_a\left(E_a, r\right)$ by

$$\Phi_a = 2\pi \int_0^1 dr\, r \int_{\omega_p}^{\infty} dE\, \varphi_a\left(E_a, r\right), \tag{4.20}$$

where ω_p is the plasma frequency.

4.1.2 Constraints on the Solar Axion Flux

As already mentioned in Chapter 3, the knowledge about solar properties can be used to constrain the solar axion flux.
Since axion losses would increase the consumption of nuclear fuel and the standard Sun has lived through half of its helium burning phase, its solar axion luminosity should not exceed the solar photon luminosity. From this, one can conclude, for example, that a PVLAS-type "signal" as discussed in Section 3.7.2 would require an axion luminosity of

$$L_a > 10^6 \times L_\odot, \tag{4.21}$$

such that the Sun would only live about 1000 years [63].
Furthermore, precision helioseismology can be used to investigate the interior of the Sun. The seismic model and all modern variations of the standard solar model are well compatible within seismic uncertainties, thus strongly disfavoring axionic solar models with $g_{a\gamma} > 1 \times 10^{-9}$ GeV^{-1}. This implies that the axion luminosity L_a should not exceed $10 - 20\%$ of the solar luminosity $L_\odot$ [109].
Another constraining factor makes use of the measured solar neutrino flux. The enhanced burning of nuclear fuel due to axion emission would lead to a rise in temperature and an increase of neutrino fluxes. Thus, only a coupling constant $g_{a\gamma} \lesssim 5 \times 10^{-10}$ GeV^{-1}, which corresponds to $L_a \lesssim 0.04 L_\odot$, yields self-consistent solar models with axion losses compatible with the observed neutrino fluxes from the Sun. However, one should keep in mind that the uncertainties of the neutrino flux predictions from solar models are quite large.
Concerning the consistency of the results of the CAST experiment and standard solar models, it can be said that the solar axion flux, which corresponds to the CAST limits, is too small to significantly affect the above mentioned observations. Axion losses can thus be seen as minor perturbations of solar models, such that CAST limits and these models are completely consistent.

4.1.3 Do Axions Escape from the Sun?

Solar axions can only be detected, if they are actually able to escape from the Sun. If their mean free path (MFP) λ_a is less than the solar radius, they cannot leave the Sun. In natural units, the photon-axion conversion rate given in Eq. (4.10) and the inverse MFP of a photon of energy E_γ considering the Primakoff effect are identical. Thus the MFP can be obtained from Eq. (4.10) in the static limit (no recoil, screening included). With a temperature $T \approx 1.3$ keV and $\kappa \approx 9$ keV at the solar center, one calculates the MFP λ_a for 4 keV axions as

$$\lambda_a \approx 6 \times 10^{24} \left(\frac{g_{a\gamma}}{10^{-10}\mathrm{GeV}^{-1}}\right)^{-2} \mathrm{cm} \;\approx 8 \times 10^{13} g_{10}^{-2} R_\odot, \tag{4.22}$$

where $g_{10} = g_{a\gamma}/10^{-10}\mathrm{GeV}^{-1}$. Thus, the coupling constant $g_{a\gamma}$ would have to be larger than the observed CAST limit by a factor of 10^7 in order to have re-absorption of axions in the Sun.
In the extreme case of such a strong coupling, axions would influence the solar structure. They would be responsible for the bulk of the energy transport within the Sun which is otherwise carried by the photons. In order to be trapped in the Sun, axions would have to interact strongly enough to have a MFP smaller than that of photons, which is around 1 mm in the solar core. The solar structure will only remain unaffected, if the MFP of axions would not be much larger than this. Otherwise, the energy transfer rate in the Sun would be extremely accelerated and the solar structure would be dramatically altered. This condition is so stringent that re-absorption is not a possibility worth considering for particles like axions [63].

4.2 Probability of Axion-To-Photon-Conversion

In a laboratory magnetic field, solar axions can be converted into real photons via the inverse Primakoff effect (see right part of Fig. 4.1). The virtual photon is hereby provided by the magnetic field. The conversion process can be treated in a similar way as neutrino oscillations [32].
Although the photon has spin 1 and the axion is a spin-zero particle, they can mix provided that the mixing agent, which can be an external magnetic or electric field, matches the missing quantum numbers. The conversion from a free photon into a spin-zero axion requires a change in the azimuthal quantum number of angular momentum (J_z). For the photon $J_z = \pm 1$, while for the axion $J_z = 0$ holds. A longitudinal field, i.e. a field providing an azimuthal symmetry, cannot allow for these transitions since it cannot change J_z. A transverse field however allows for mixing of a photon with an axion.
The determining wave equation for particles propagating along the z-axis in a transverse magnetic field B has been derived by Raffelt and Stodolsky [110] as

$$\left[\begin{pmatrix} \omega - \frac{m_\gamma^2}{2\omega} - i\frac{\Gamma}{2} & g_{a\gamma}\frac{B}{2} \\ g_{a\gamma}\frac{B}{2} & \omega - \frac{m_a^2}{2\omega} \end{pmatrix} - i\partial_z\right] \begin{pmatrix} A_\parallel \\ a \end{pmatrix} = 0, \tag{4.23}$$

where $A_\parallel$ denotes the amplitude of the photon field component parallel to the magnetic field B, the amplitude of the axion field is a and ω represents the frequency. Furthermore, damping is incorporated by the inverse absorption length Γ of photons. A first-order solution using a perturbative approach can be found up to a global phase as

$$\begin{aligned} \langle A_\parallel(z)|a(0)\rangle &= \frac{1}{2} g_{a\gamma} \exp\left(-\int_0^z dz' \, \frac{\Gamma}{2}\right) \\ &\quad \times \int_0^z dz' B \, \exp\left(i \int_0^{z'} dz'' \left[\frac{m_\gamma^2 - m_a^2}{2\omega} - i\frac{\Gamma}{2}\right]\right). \end{aligned} \tag{4.24}$$

The conversion probability[5] $P_{a\to\gamma}$ of axions into photons at a length $z = L$ of the magnetic field is then

$$P_{a\to\gamma} = |\langle A_{\parallel}(z)|a(0)\rangle|^2 = \left(\frac{Bg_{a\gamma}}{2}\right)^2 \frac{1}{q^2+\Gamma^2/4}\left[1+\mathrm{e}^{-\Gamma L}-2\mathrm{e}^{-\Gamma L/2}\cos\left(qL\right)\right], \tag{4.25}$$

where q is the absolute momentum transfer between the real photon in the medium and the axion and is given by

$$q = \left|\frac{m_\gamma^2 - m_a^2}{2E_a}\right|. \tag{4.26}$$

Here, m_γ is the effective photon mass in the gas, while m_a and E_a are mass and energy of the axion, respectively. It is possible to obtain the momentum transfer q by considering the axion energy, which is

$$E_a^2 = m_a^2 + p_a^2. \tag{4.27}$$

Thus, the momentum of the axion can be derived as

$$p_a = E_a\sqrt{1-\frac{m_a^2}{E_a^2}}, \tag{4.28}$$

where the development for $m_a \ll E_a$ yields

$$p_a \approx E_a - \frac{m_a^2}{2E_a}. \tag{4.29}$$

Analogous, one obtains

$$p_\gamma \approx E_\gamma - \frac{m_\gamma^2}{2E_\gamma}, \tag{4.30}$$

and with this the momentum transfer q follows as

$$q = |p_a - p_\gamma| = \left|\frac{m_a^2}{2E_a} - \frac{m_\gamma^2}{2E_\gamma}\right|, \tag{4.31}$$

which is Eq. (4.26) if $E_a = E_\gamma$.
It is possible to differentiate between two cases for the probability of conversion, which will yield slightly different results. First an evacuated conversion region will be studied, followed by an investigation of the influence of a buffer gas used to fill the conversion volume.

4.2.1 Coherence Condition and Conversion Probability in Vacuum

The probability for converting an axion into a photon in a magnetic field in vacuum can be obtained from Eq. (4.25) by considering the limit $m_\gamma \to 0$. Under the assumption that the absorption is then

[5] For the expression given in Eq. (4.25), Heaviside-Lorentz units have been used. A short explanation can be found in Appendix B.

negligible ($\Gamma \approx 0$), this yields

$$P_{a\to\gamma} = \left(\frac{BLg_{a\gamma}}{2}\right)^2 \left(\frac{\sin\left(\frac{qL}{2}\right)}{\left(\frac{qL}{2}\right)}\right)^2 . \tag{4.32}$$

Here, B is the magnetic field and the momentum transfer q given in Eq. (4.26) between axion and real photon reduces to

$$q = \frac{m_a^2}{2E_a}, \tag{4.33}$$

since $m_\gamma = 0$. This yields a condition under which coherence is assured, i.e photon and axion wave are in phase, and it is possible to obtain a conversion probability significantly different from zero. This coherence condition is provided by

$$\frac{qL}{2} < \pi, \tag{4.34}$$

which is illustrated in Fig. 4.5. Here, the $(\sin(x)/x)^2$ term of Eq. (4.32) with $x = qL/2$ is plotted as a function of x and it can be seen that the largest contributions are found for values $x < \pi$. Expressing this in terms of axion masses, one obtains

$$m_a < \sqrt{\frac{4\pi E_a}{L}}, \tag{4.35}$$

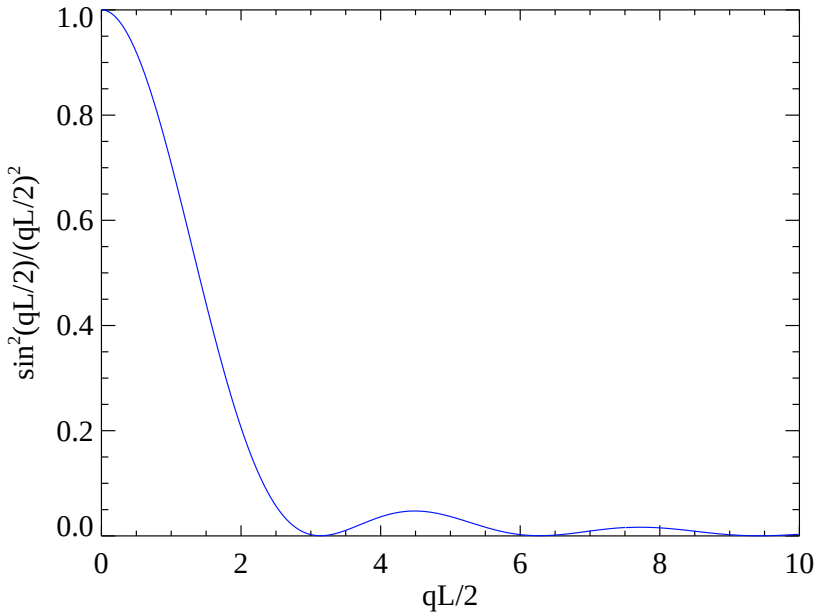

Figure 4.5: Dependence of the coherence term on different values of its argument $qL/2$. The major contributions to the probability function result from values of $qL/2$ which are smaller than π.

such that the coherence condition is fulfilled for axion masses smaller than 0.02 eV, if a magnetic length of about 10 m and an axion energy of $E_a \approx 4.2$ keV are assumed. In the limit $x \to 0$, the $\sin^2(x)/x^2$ term tends to 1 and Eq. (4.32) can be reduced to

$$P_{a\to\gamma} = \left(\frac{BLg_{a\gamma}}{2}\right)^2, \tag{4.36}$$

which is then the simplified probability of conversion in vacuum.

4.2.2 Coherence Condition and Conversion Probability in a Buffer Gas

In order to access higher axion masses than those observable with an evacuated conversion volume in a given experiment, the magnetic field region can be filled with a buffer gas. The requirement for this gas is to have a low[6] atomic number Z, such that basically only helium and hydrogen qualify. In this case however, the full formula for the conversion probability given in Eq. (4.25) has to be considered using the momentum transfer provided by Eq. (4.26) as

$$q = \left|\frac{m_\gamma^2 - m_a^2}{2E_a}\right|, \tag{4.37}$$

with effective photon masses different from zero.

The Effective Photon Mass In order to calculate the momentum transfer q, the effective mass of photons in a gas has to be known. While in vacuum photons are massless and travel with the speed of light c, they acquire an effective mass when passing through a transparent medium, which they traverse at a speed smaller than c. In the classical wave picture, this slowing down can be understood as a delaying of the photon wave due to interference of the original light with photons coming from matter polarized by the initial photons. In the context of a particle picture, one might consider it as an effect of mixing between the initial photon and quantum excitations of the traversed matter, which results in a particle with effective mass which thus cannot travel at speed c. The photon energy is given by $E_\gamma^2 = m_\gamma^2 = \hbar^2\omega_p^2$, where ω_p is the plasma frequency. It can be derived following Ref. [111] as

$$\omega_p^2 = 4\pi n_e \frac{e^2}{m} = 4\pi n_e r_0, \tag{4.38}$$

with n_e being the electron density, and $r_0 = e^2/m$ the classical electron radius.
Using that $n_e = N_e/V$, where N_e is the number of electrons in volume V, the plasma frequency can be expressed as

$$\omega_p^2 = 4\pi \frac{N_e}{V} r_0. \tag{4.39}$$

[6] One reason to use low Z gases is that the absorption of photons in a gas increases with the atomic number Z. Furthermore in an experiment like CAST, which is operated at 1.8 K, only low Z gases like helium and hydrogen are still gaseous at the pressures which are required.

The effective photon mass follows then as

$$m_\gamma^2 = 4\pi \frac{N_e}{V} r_0. \tag{4.40}$$

In the case of helium, the number of electrons corresponds to twice the number of atoms N_a, i.e. $N_e = 2N_a$. And thus, applying the ideal gas law

$$pV = nRT, \tag{4.41}$$

with pressure p, volume V, gas constant R, temperature T and the amount of gas n given in mol, it follows that

$$\frac{N_e}{V} = \frac{2pN_A}{RT}. \tag{4.42}$$

It has been used that $n = N_a/N_A$ and N_A is Avogadro's constant. Inserting Eq. (4.42) into Eq. (4.40) leads then to

$$m_\gamma^2 = 8\pi \frac{r_0 N_A}{R} \frac{p}{T} = 5.130 \times 10^{11} \frac{p}{T} \frac{\mathrm{K}}{\mathrm{mbar\ m^2}}. \tag{4.43}$$

Taking into account natural units ($\hbar c = 0.197$ GeV fm), yields straightforward

$$m_\gamma = \sqrt{0.01997 \frac{p/\mathrm{mbar}}{T/\mathrm{K}}}\,\mathrm{eV}, \tag{4.44}$$

which is the effective photon mass in helium.

The Momentum Transfer Having determined the effective photon mass, it is now possible to calculate the momentum transfer between the axion and the real photon as given in Eq. (4.37). In Fig. 4.6, q is visualized depending on the axion energy and mass for an exemplary pressure of ^{4}He, which is in this case 5.49 mbar at a temperature of 1.8 K and corresponds to an effective photon mass of 0.25 eV. The color scale represents the size of q in units of eV. It can be seen that the momentum transfer becomes minimal for axion masses close to the corresponding effective photon mass of the considered helium pressure. Since the momentum transfer has to be small in order to fulfill the coherence condition of Eq. (4.34), only a narrow range of axion masses can be studied at a specific helium gas pressure.
To demonstrate the influence of the pressure on the momentum transfer, Fig. 4.7 diplays q versus the axion mass for all energies from 1 to 7 keV at various pressures of ^{4}He at 1.8 K. For each pressure setting, the momentum transfer is close to zero only for a narrow mass range. With increasing pressure of the gas, the minimal value of q shifts to higher axion masses. For the smallest plotted pressure of 0.08 mbar, q is small enough to fulfill the coherence condition for masses up to 0.03 eV.
In Fig. 4.8, the energy dependence of the momentum transfer is visualized for different axion masses at a helium pressure of 5.49 mbar (at 1.8 K). It can be seen that q is smallest for an axion mass of 0.25 eV, which corresponds to the effective photon mass at the considered pressure. For axion masses higher or lower than this photon mass, the momentum transfer increases, i.e. the coherence condition cannot be fulfilled. From Eq. (4.37) it is obvious that the momentum transfer decreases with increasing energy, as can be also seen in Fig. 4.8.

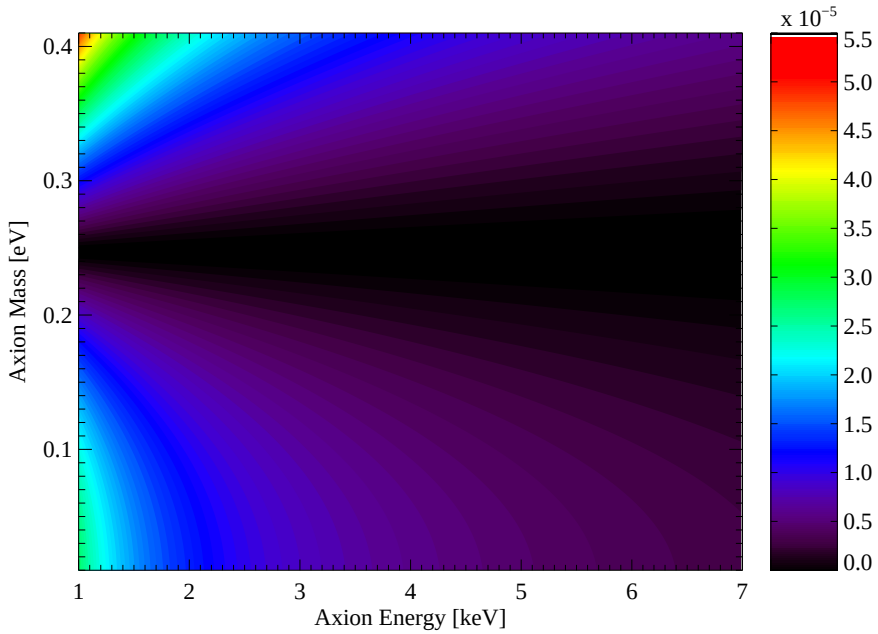

Figure 4.6: Momentum transfer depending on axion energy and mass for an exemplary pressure of 5.49 mbar at 1.8 K, which corresponds to an effective photon mass of about 0.25 eV. The colorbar represents the size of q in units of eV.

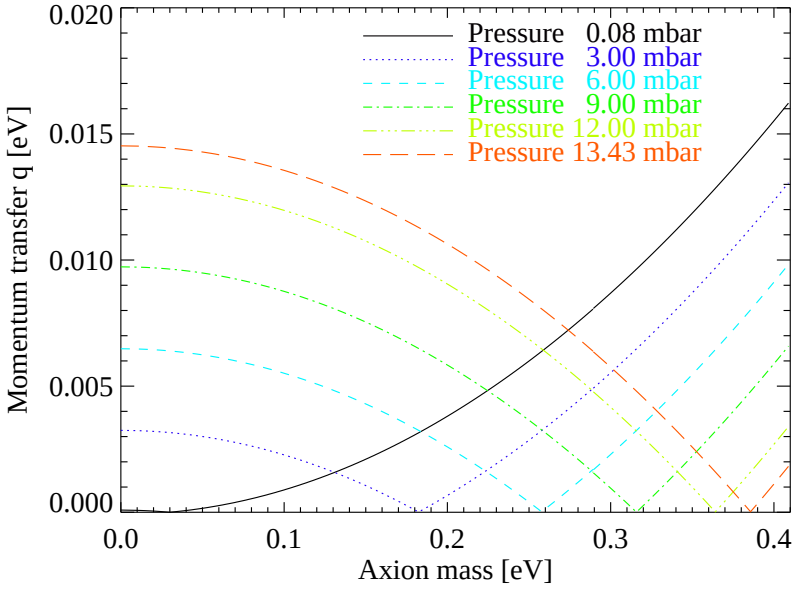

Figure 4.7: Momentum transfer depending on axion mass for all energies from 1 to 7 keV at various pressure settings. The temperature here is 1.8 K.

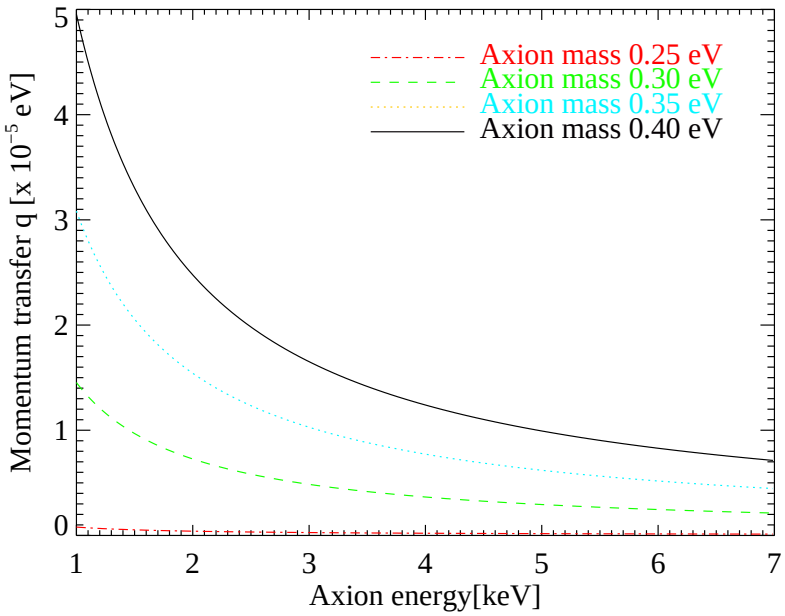

Figure 4.8: Momentum transfer depending on axion energy for different axion masses at a pressure of 5.49 mbar at 1.8 K, which corresponds to an effective photon mass of about 0.25 eV.

The Absorption of Photons in a Buffer Gas Another important factor influencing the conversion probability is the absorption of the photons originating from axions via the Primakoff effect in a gas. In general, the absorption Γ of these photons in a gas is defined as the inverse of the absorption length λ:

$$\Gamma(E_a) = \frac{1}{\lambda(E_a)} = \rho\mu(E_a), \tag{4.45}$$

where ρ is the density of the gas and $\mu(E_a)$ represents the energy-dependent mass absorption coefficient, which is given by

$$\mu(E_a) = \frac{N_A}{A}\sigma_A(E_a), \tag{4.46}$$

with Avogadro's constant N_A and mass number A. The scattering cross section σ_A

$$\sigma_A(E_a) = \sigma_{\mathrm{PE}}(E_a) + \sigma_{\mathrm{coherent}}(E_a) + \sigma_{\mathrm{incoherent}}(E_a) \tag{4.47}$$

takes into account photoelectric, coherent and incoherent contributions[7]. At standard temperature and pressure[8] (STP), the ideal gas equation yields for helium gas

$$\lambda_{\mathrm{STP}} = \lambda\frac{T_{\mathrm{STP}}p_{\mathrm{He}}}{p_{\mathrm{STP}}T_{\mathrm{He}}}, \tag{4.48}$$

[7]The coherent scattering cross section corresponds to Rayleigh scattering, while the incoherent contribution is due to Compton effect.

[8]$T_{\mathrm{STP}} = 273.15$ K and $p_{\mathrm{STP}} = 1013.25$ mbar

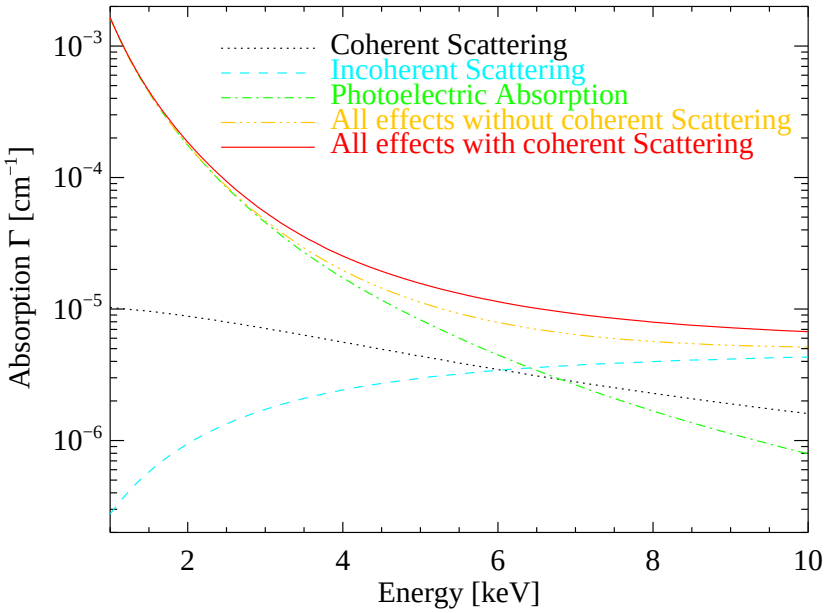

Figure 4.9: Absorption Γ for different physical effects as calculated using the NIST database with helium at a pressure of 1 mbar ($T = 1.8$ K).

and thus Eq. (4.45) turns into

$$\Gamma(E_a) = \mu(E_a)\rho_{\mathrm{STP}}\frac{T_{\mathrm{STP}}p_{\mathrm{He}}}{p_{\mathrm{STP}}T_{\mathrm{He}}}, \tag{4.49}$$

for helium. The density under standard conditions ρ_{STP} for ^{4}He is 0.1786 g/L.
The NIST database [112] provides the mass absorption coefficient depending on energy, such that for a given temperature T_{He} and pressure p_{He} the absorption can be calculated. Hereby, different effects can be included as it is illustrated in Fig. 4.9. The absorption including all effects is shown in Fig. 4.10 for different pressures of helium at a temperature of 1.8 K.

Mass Range of Coherence Re-establishing coherence by filling the magnet field region with a buffer gas makes small axion mass ranges around the effective photon mass accessible as can be seen from Eq. (4.26) together with the coherence condition of Eq. (4.34), namely

$$\sqrt{m_\gamma^2 - \frac{4\pi E_a}{L}} < m_a < \sqrt{m_\gamma^2 + \frac{4\pi E_a}{L}}. \tag{4.50}$$

Since the effective photon mass depends on the pressure, an axion mass range of up to about 0.43 eV can be scanned with ^{4}He at 1.8 K with an experiment like CAST[9]. For higher masses (up to about 1 eV) ^{3}He has to be used, since at the magnet operating temperature of 1.8 K ^{4}He reaches

[9]The CAST experiment will be introduced in Chapter 5.

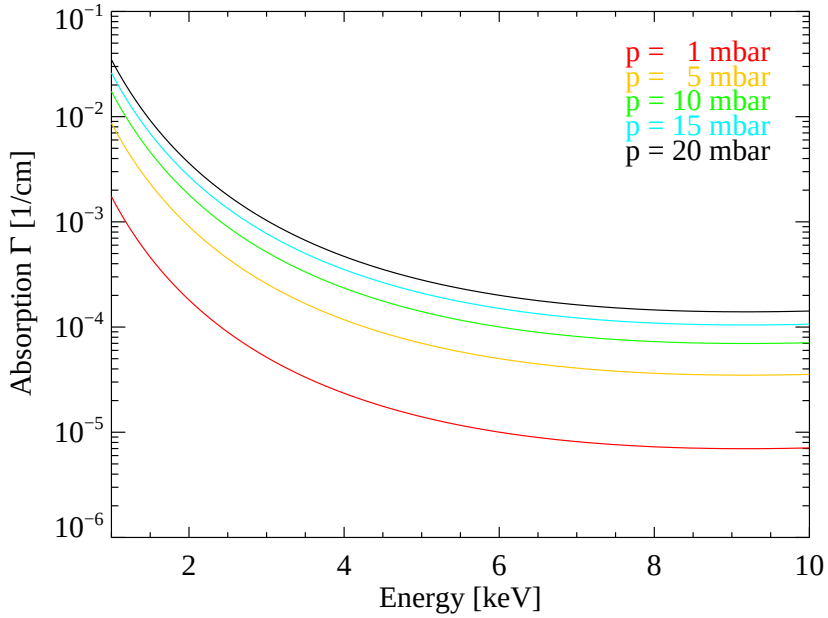

Figure 4.10: Absorption Γ in helium including all effects for various pressure settings at $T = 1.8$ K. Calculations have been done using the NIST database [112].

its saturation vapor pressure at 16.405 mbar (about 0.43 eV in axion mass). Depending on the used gas, the length of the magnetic field region and the operating temperature, other experiments might be able to access slightly different mass ranges.

4.3 Expected Number of Photons

The expected number of photons N_γ from axion-to-photon conversion in a magnetic field can be calculated depending on the axion mass and the pressure of the buffer gas by

$$N_\gamma = \int_E \frac{d\Phi(E_a)}{dE_a} P_{a\to\gamma}(E_a)\, \epsilon(E_a)\, \Delta t\, A\, dE_a, \tag{4.51}$$

where A and $\epsilon(E_a)$ are the detector area and efficiency, respectively, and Δt is the exposure time. An example for the number of expected photons from conversion of axions in vacuum and at an exemplary pressure p of the helium at 1.8 K in the magnetic field region is shown in Fig. 4.11 for the experimental conditions of the CAST experiment to give an idea of the general principle. Here, an exposure time of 90 min has been considered not taking into account any detector efficiency ($\epsilon = 1$). The sensitive area has been assumed to be of the size of the CAST magnet bore (14.522 cm^2). A more detailed study of the expected number of photons in the case of the CAST experiment can be found in Chapter 8.

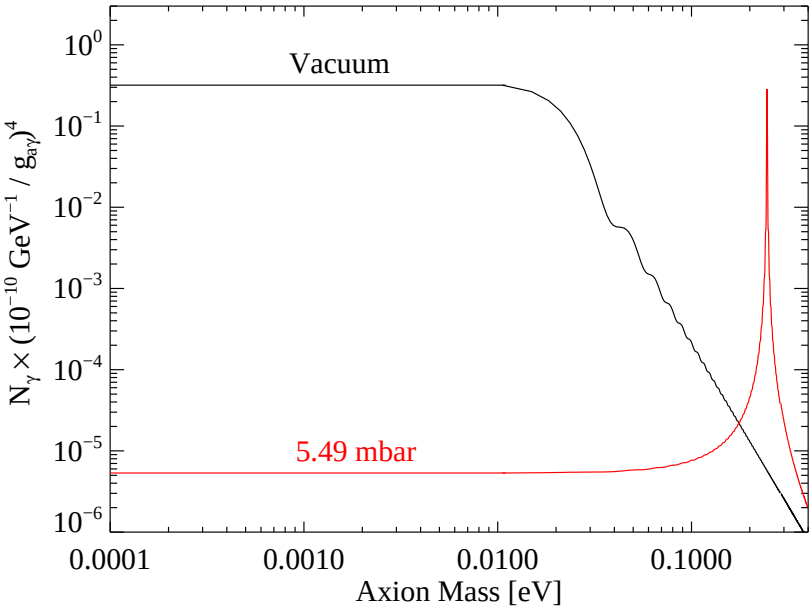

Figure 4.11: Expected number of photons from axion-to-photon-conversion in a magnetic field of $B = 8.8\ T$ with a length of $L = 9.26$ m. The exposure time is 90 min. Detector efficencies have not been taken into account and as sensitive area the size of a CAST magnet bore (14.52 cm^2) has been assumed. The pressure is given at 1.8 K.

Chapter 5

The CAST Experiment

In this chapter, the CERN Axion Solar Telescope (CAST) experiment shown in Fig. 5.1 will be presented. It is located above ground at Point 8 of the Large Hadron Collider (LHC) at CERN in Geneva, Switzerland. Being a helioscope, it uses a strong magnetic field in order to reconvert axions produced in the solar core into X-ray photons. Since a transverse magnetic field with respect to the direction of the incoming axions is required, CAST has been built to follow the Sun very accurately, in order to maximize the time during which magnet axis and Sun are aligned.
In the first section, the division of the experiment into basically two phases will be explained. Following this, the experimental setup will be introduced starting with the key piece of the experiment, which is a 9.26 m long LHC prototype magnet able to provide a field of up to 9 Tesla. Since the

Figure 5.1: Experimental setup of the CERN Axion Solar Telescope. The magnet (blue) is installed on a platform (green), which is supported on the right hand side by a turntable (olive green) allowing horizontal movement. On the other end (left in image), it is carried by two lifting screws at a girder (yellow) for enabling vertical movement. The yellow girder also allows for the horizontal movement along the rails visible on the floor of the experimental hall. Part of the cryogenics plant to cool the superconducting magnet is visible on the right side.

accuracy of the solar tracking is crucial for a successful running of the CAST experiment, both, hardware and software to follow the Sun will be considered in more detail in the third section of this chapter. To assure the accuracy of CAST in tracking the Sun, twice a year an optical cross-check is performed, the solar filming, which will be subject of the fourth section. After this, both vacuum and gas systems for ^{4}He and ^{3}He will be introduced being the biggest and most important upgrade from Phase I to Phase II. The changes of the system were necessary to extend the axion mass range which can be studied. As during Phase I, the three X-ray detectors used for CAST's Phase II were a conventional Time Projection Chamber (TPC), a novel MICROMEsh GAseous Structure (MICROMEGAS, MM) and an X-ray mirror optics in combination with a Charge Coupled Device (CCD) as a focal plane detector, which both had been originally developed for satellite space missions. Closing the chapter, the results of Phase I will be shortly summarized.

5.1 CAST Physics Program: Phase I and II

For the time being, CAST is the most sensitive helioscope in the world. In order to investigate a wide range of masses, the experiment has been designed to consist of two phases: Phase I with vacuum in the magnet bores and Phase II, during which the magnetic field region is filled with helium.
During Phase I, the magnetic field region was kept under vacuum allowing to search for axions in the mass range up to 0.02 eV with very high sensitivity. For higher masses, the coherence condition is not fulfilled anymore in evacuated magnet bores and thus, the sensitivity decreases rapidly. In order to restore the coherence between the axion and the photon wave, a buffer gas can be filled inside the magnet as it was explained in Section 4.2. By systematically changing the density of the gas at a constant temperature and thus its pressure inside the magnet, different axion masses can be studied, since each density setting restores the coherence in a narrow mass range (see Fig. 4.11). The stepsize in density inside the cold bore has been chosen in a way that consecutive settings overlap and thus an excellent coverage of the accessible mass range is provided. This basic concept has been implemented in CAST's Phase II by using helium as a buffer gas. The second phase of the CAST experiment can be subdivided in two stages: the ^{4}He and the ^{3}He part.
During the years 2005 and 2006, the cold bore has been filled with ^{4}He. This enables to scan axion masses with high sensitivity up to about 0.42 eV, since the saturation pressure of ^{4}He at 1.8 K is 16.41 mbar. In order to stay within safety limits of the setup, CAST did not go up to this highest pressure. To reach higher masses, ^{3}He can be used, which has been done at CAST starting in 2008. Here, the saturation pressure at 1.8 K is 135.58 mbar, which extends the mass range to search for axions up to about 1.2 eV. Since the natural abundancy of ^{3}He is rather small and purification processes are quite demanding, the gas system of CAST used for ^{4}He had to be upgraded when changing to ^{3}He as buffer gas.

5.2 Magnet and Cryogenics

The main component of the CAST experiment is a decommissioned prototype magnet built for LHC [113]. The superconducting dipole is one of the first generation bending magnets designed to be used in the accelerator (see Fig. 5.2). It has two straight beam pipes of 9.26 m length each. Both

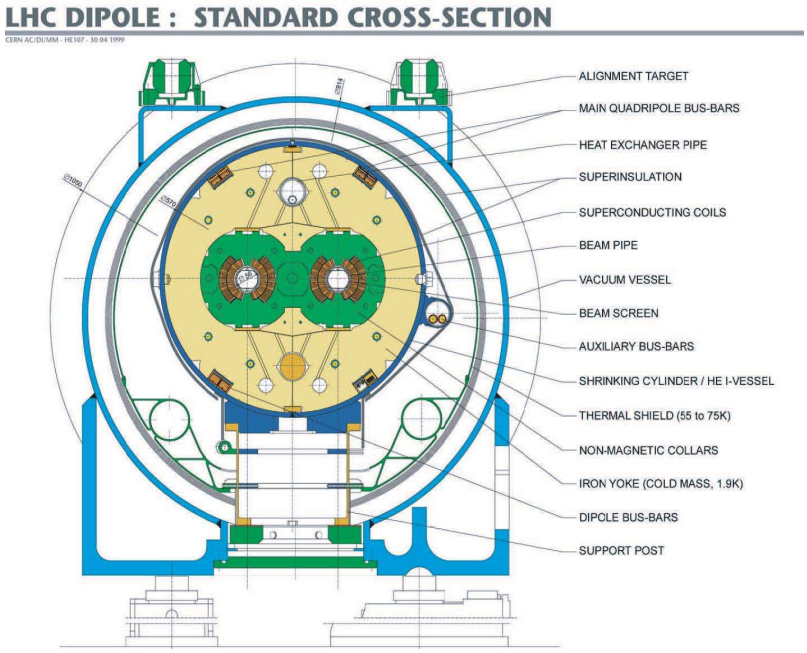

Figure 5.2: Cross section of a twin aperture LHC dipole prototype magnet. Its two straight bores have a length of 9.26 m each. The superconducting magnet is operated at a temperature of 1.8 K [114].

bores have a diameter of 43 mm, resulting in a total cross-sectional area A of about 2×14.52 cm^2. The twin aperture magnet is able to provide a field of up to 9 Tesla over its full length, while its nominal field required for the LHC running is 8.4 T. In Fig. 5.3, the orientation of the magnetic field and its strength depending on the position inside the magnetic cross section are shown. The

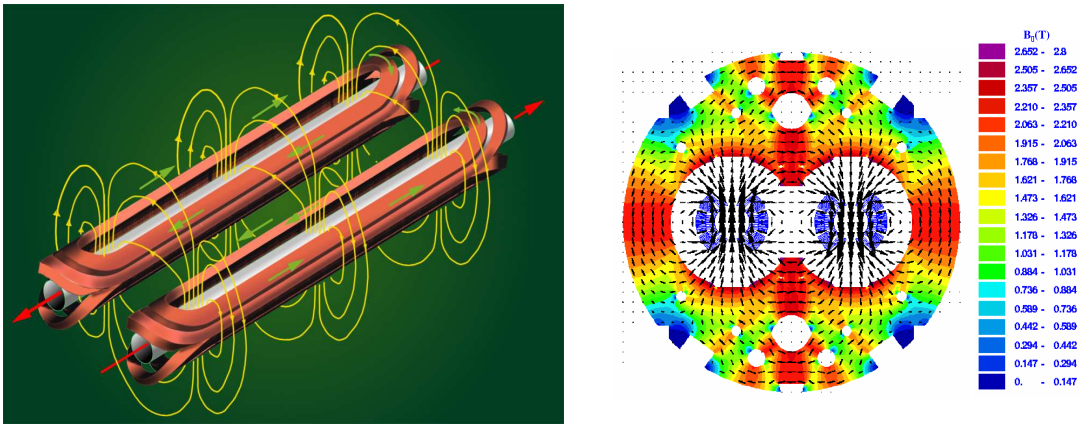

Figure 5.3: Left: Orientation of the magnetic field over the length of the magnet for both magnet pipes. Right: Contour plot of the magnetic field in the magnet cross section. For this plot, the maximal magnetic field was 2.8 T [114].

Table 5.1: Correspondence between current and magnetic field for the CAST magnet [115]

Current [A]	Magnetic field [T]
0	0
4988	3.40
8981	6.12
10977	7.46
12000	8.13
12808	8.66
13330	9.00

correspondence between current and magnetic field is given in Tab. 5.1.

The magnet is made of superconducting Niobium-Titanium (NbTi) and operated at 1.8 K to obtain the maximum field of 9 T, which corresponds to 13330 A. During routine operation at the CAST experiment in Phase II, a field of 8.8 T corresponding to 13000 A has been used to ensure a stable performance of the setup.

A cryogenic system to cool and operate the magnet with superfluid helium has been installed [116] using no longer needed cryogenics of the former Large Electron Positron collider (LEP) and its experiment DELPHI[1]. The Magnet Feed Box (MFB, see Fig. 5.4) supplying the magnet with all needed cryogenic and electrical feeds is mounted on top of the magnet towards its western end while the other side of the dipole is closed by the Magnet Return Box (MRB, see Fig. 5.4). It has been a major engineering challenge to setup the system allowing for sufficient movement of the magnet to follow the Sun. Transfer lines for the liquid helium, gaseous helium pumping and the quench recovery system as well as the current supply for the magnet operation had to be constructed very flexible.

An important part of the cryogenic system is the quench recovery system. In case of a sudden change of the magnet from its superconducting to normal-conductive state, in which an electric resistance occurs, the magnet temperature increases quickly, resulting in a rapid increase of the pressure inside the dipole (quench, see also Fig. 5.5). In order to protect the cryogenic plant and the magnet, a fast discharge of the current is triggered along with the closing of the liquid helium supply valve. Generally, the helium is recovered, but if the pressure reaches the preset safety limits, the helium is released to prevent damage of the magnet and the cryogenic plant. Besides real quenches also fake quenches might occur, triggered by false warning signals of monitored quantities to detect real quenches. The overall performance of the cryogenic system at the CAST experiment has been extremely stable over all data taking periods so far.

[1] DEtector with Lepton, Photon and Hadron Identification

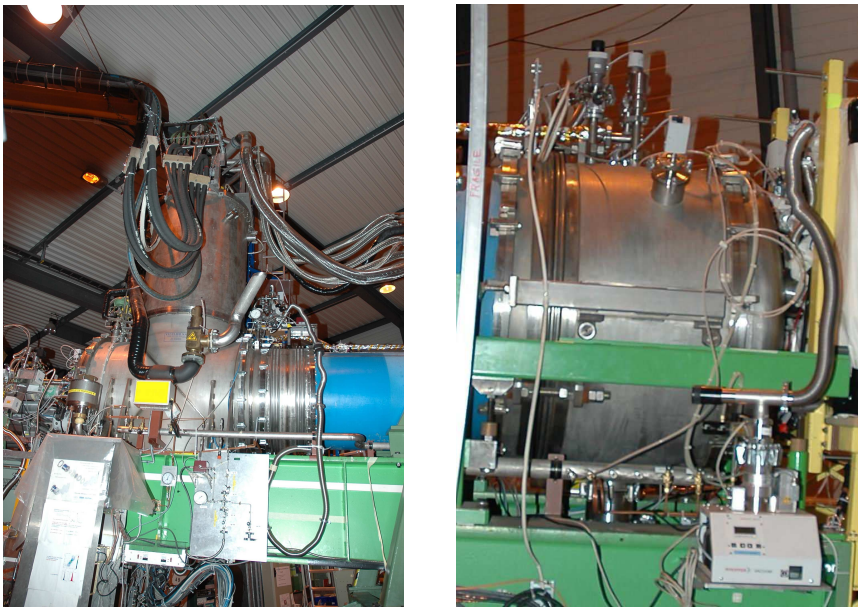

Figure 5.4: Left: The Magnet Feed Box (MFB) of CAST supplies the magnet with all the necessary cryogenic and electrical feeds. In Fig. 5.1, its location is towards the right side of the magnet. Right: The Magnet Return Box (MRB) closes the other end of the magnet. In Fig. 5.1, it can be found at the left end of the magnet.

Figure 5.5: Quench of the CAST magnet. In case of a sudden change of the magnet from its superconducting to normal-conductive state, the cooling helium is released to protect the system.

5.3 Tracking System

In order to track the solar core with an accuracy of better than 0.01°, an extremely precise system is absolutely essential to move the whole CAST setup with its weight of over 40 tons. A reliable software to guide the movement is needed. Hardware and software of the tracking system have been carefully designed and upgraded where necessary. Various checks, such as the so-called GRID measurements[2] by the CERN surveyors and optical filming of the Sun, have been performed frequently. Thus, the tracking accuracy has been shown to satisfy the determined needs of CAST.

5.3.1 Hardware

The supporting structure to move the magnet is composed of two major parts: a girder with two lifting screws to enable vertical movement of $\pm 8^\circ$ and a turntable to allow horizontal motion in a range of $\pm 40^\circ$. The combination of these two components optimizes the time, during which the magnet can be aligned with the Sun during sunrise and sunset, such that the maximal possible statistics in axion sensitive conditions can be obtained.
In Fig. 5.1, the girder (yellow) with its two black lifting screws can be seen at the left side. On one hand, it guides the magnet movement along the horizontal by following the installed rails on the floor, on the other hand it moves the whole magnet up and down along the big screws. Most of the weight is located on the opposite side of the magnet, close to the MFB, where the turntable is situated. It is the pivot of the whole setup and enables the horizontal movement. The design of the CAST movement system is shown in Fig. 5.6.
The limitation of the magnet movement to a range of about 80° is due to the surrounding infrastructure such as control room and cryo plant. The constraints on the vertical range of $\pm 8^\circ$ is on one hand due to mechanical constraints and on the other due to restrictions resulting from cryogenics. The mechanical constraints are the weight of the magnet and its support, which does not allow for higher values than $+8^\circ$, and the position of the floor, which prevents from reaching lower magnet positions, while the cryogenic restrictions are due to the fact that cooling is no longer efficient at larger vertical angles, thus increasing the risk of quenches dramatically.
As a consequence, the magnet can be aligned with the solar core for approximately 1.5 hours during sunrise and the same period of time during sunset. In the best case, this adds up to a total possible alignment time during a full year of about 45 days.

5.3.2 Encoders

The connection between the hardware parts, which are the motors driving the magnet movement horizontally and vertically, and the guidance software are the encoders, which are shown in Fig. 5.7. Both hardware and software stops are implemented to prevent the magnet from jumping off the rails or tilting too much. A precise calibration of the encoders is fundamental for an accurate tracking of the solar core. It has been established at the very beginning of the experiment and regularily checked ever since by surveyors.

[2] GRID measurements consist of independent checks of the magnet position in a set of reference coordinates, which had been previously defined and cover the complete range of movement of the CAST magnet. A potential drift in the pointing ability of the setup with respect to the initial calibration in 2002 can thus be efficiently detected.

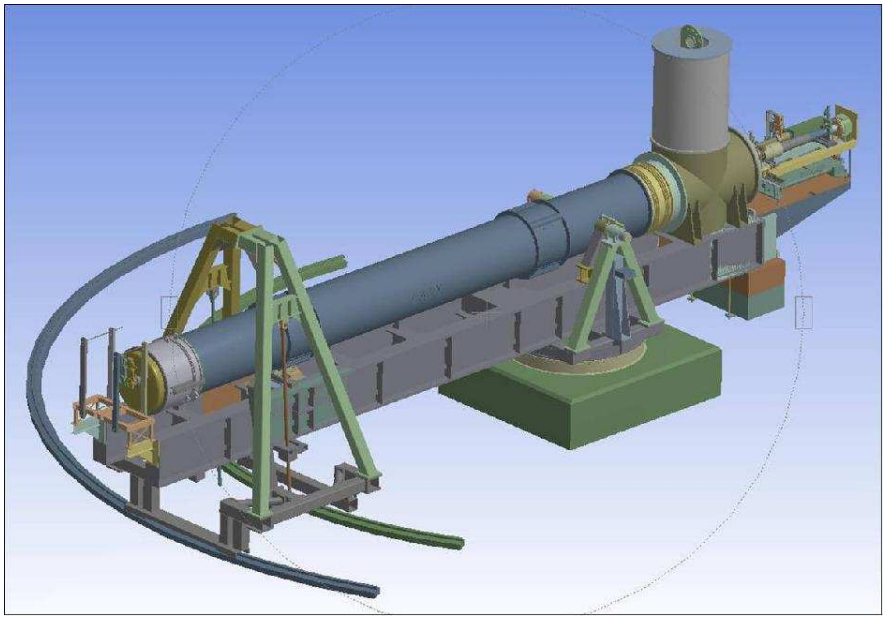

Figure 5.6: Design of the CAST movement system.

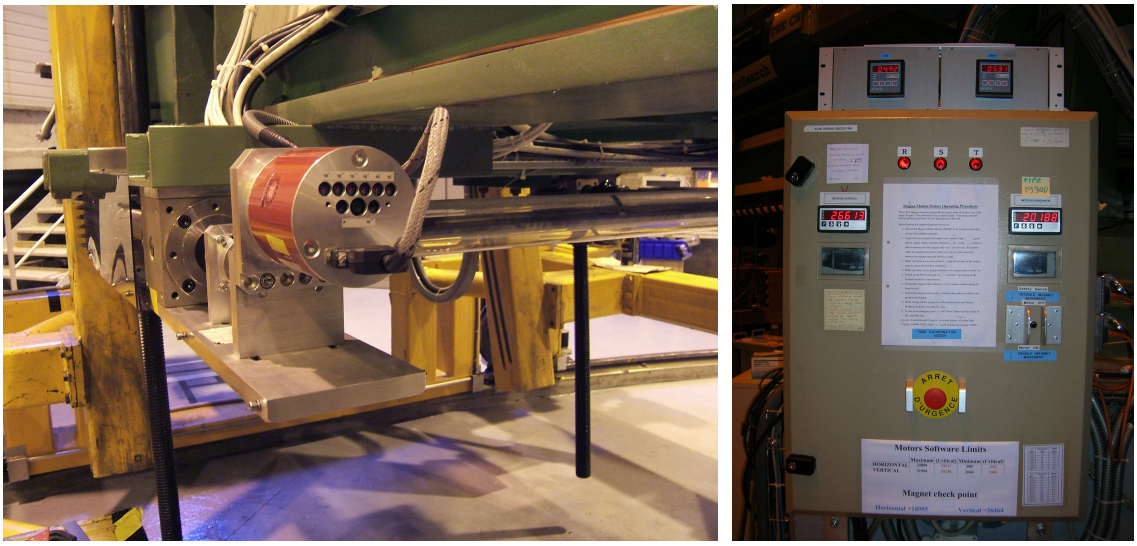

Figure 5.7: Left: The motor encoders convert input values for the motors into angular coordinates and vice versa. Right: Via the motor control box, hardware and software of the tracking system are connected and the magent can be moved from here.

5.3.3 Software

The guidance of the magnet movement is provided by the tracking software. It also logs relevant physical quantities, such as for example tracking precision, to be used later in the data analysis. The general operation scheme of the magnet movement with all relevant components is pictured in Fig. 5.8. The LabView control software is based on NOVAS[3], which is a package of subroutines

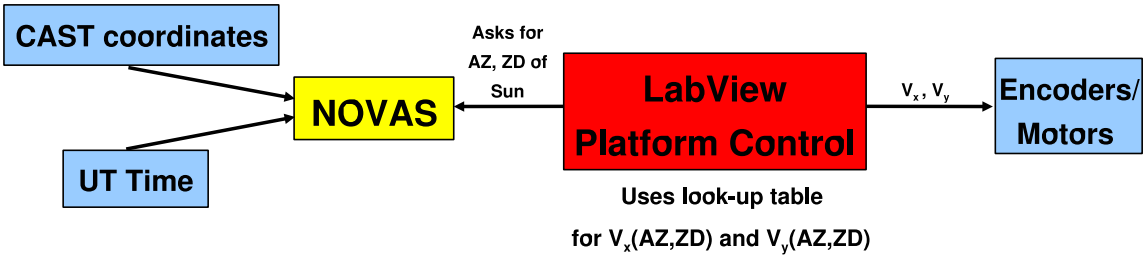

Figure 5.8: Schematic view of the tracking software based on NOVAS. Using the coordinates of the experiments along with Universal Time (UT), NOVAS provides the azimuth (AZ) and the zenith (ZD) angle of the Sun. These values are then converted by the Labview Control program into horizontal and vertical encoder values used to guide the motors. To accomplish this, tables are applied which were obtained with the help of the EST division of CERN.

provided by the U.S. Naval Observatory [117] and can be used to calculate various astrometric quantities. Given the Universal Time (UT) and the coordinates of the CAST experiment[4], NOVAS provides the azimuth (AZ) and the zenith (ZD) angle of the Sun one minute into the future. These can then be converted into motor encoder values by making use of look-up tables for the encoder numbers $V_x(\mathrm{AZ}, \mathrm{ZD})$ and $V_y(\mathrm{AZ}, \mathrm{ZD})$. Following this, the magnet is steered to the calculated position. The expected and actual tracking position are constantly monitored and controlled, yielding the above mentioned tracking precision, such that in case of any discrepancy the magnet movement can be corrected and its speed adjusted accordingly.
The two crucial inputs are the time (UT) and the tables used to correlate AZ and ZD with encoder values for the motors. The time of the tracking PC is continuously synchroniced with two CERN time servers. The second critical input, the tables, has been created with the help of CERN's EST[5] division. For this, the surveyors measured ninety magnet positions and correlated them with the corresponding encoder values. The accuracy of these $V_x(\mathrm{AZ}, \mathrm{ZD})$-$V_y(\mathrm{AZ}, \mathrm{ZD})$-tables is very high ($\mathcal{O}(0.001^\circ)$). Gaps between neighboring values were filled by using a spline interpolation method. Thus, the overall accuracy is always better than 0.01°, however typically around 0.002° [118]. In Tab. 5.2, an overview of all possible errors is shown, demonstrating the very high overall pointing accuracy of CAST. Regularly repeated GRID measurements confirm the stable and accurate operation of the movement system. In addition to this, twice per year an optical crosscheck can be performed (solar filming), which will be described in the following section.

[3] Naval Observatory Vector Astrometry Subroutines
[4] $46^\circ 15'$ N, $6^\circ 5'$ E, 330 m above sea level.
[5] Engineering Support and Technology

Table 5.2: Summary of possible error sources of the solar tracking precision [118].

Source of Error	Typical Error	Maximal Error
Astronomical Calculations	$0.0020°$	$0.006°$
Uncertainty of Coordinates (CAST)	$0.0010°$	
Clock Time	$0.0000°$	
GRID Measurements (0.02 mm precision)	$0.0010°$	
Interpolation of GRID Measurements	$0.0020°$	$< 0.01°$
Horizontal Encoder Precision	$0.0014°$	
Vertical Encoder Precision	$0.0003°$	
Deviation of Motor Speeds from Linearity	$< 0.0020°$	
TOTAL	$< 0.01°$	$< 0.01°$

5.4 Solar Filming

Through a window in the experimental hall, it is possible to directly observe the Sun for about two weeks in spring and fall each year. The experiment takes advantage of this, using it as an optical crosscheck of the magnet movement when following the Sun.

5.4.1 Importance of the Magnet Alignment

The field of view (FOV) provided by the magnet bore as limiting optical element can be expressed as an opening angle α. It is illustrated in Fig. 5.9 and given by

$$\alpha = 2 \arctan \frac{d}{L}. \tag{5.1}$$

L signifies here the length of the magnet ($L = 9.26$ m) and d stands for its diameter ($d = 43$ mm), such that α can be obtained as $0.53°$. Since none of the sensitive regions of any detector is directly

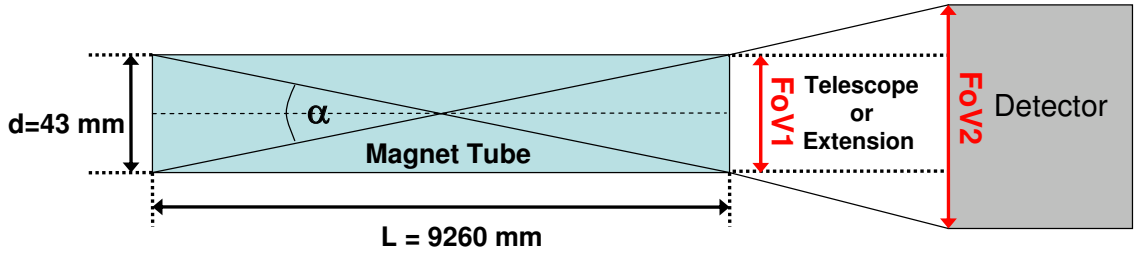

Figure 5.9: Field of view α of the magnet. While the fully illuminated field of view is represented by FOV1, for the detectors a partly vignetted field of view, FOV2, is obtained due to the distances between the bore and the sensitive part. α can be calculated and is about the size of the Sun ($0.5°$).

and without extension connected to the bore, vignetting effects will occur. Thus, not the full FOV is visible for the detectors. For the CCD chip the FOV would be about $0.34^\circ \times 1.06^\circ$ such that more or less 64% of the entire Sun (0.53°) would be covered. Using the telescope, the potential signal from the magnet aperture is focused to a spot of 23 pixel diameter, i.e. it covers a disk of about 20% of the Sun from which 82.6% of the axions are expected to come. Thus, a very high pointing accuracy of the experimental setup is crucial, if one is aiming to detect axions from the solar core (10%-20% of the solar radius).

5.4.2 Filming of the Sun

Atmospheric Refraction Unlike axions, photons are changing their direction, when passing through the atmosphere of the Earth, due to refraction.This refraction R can be defined as

$$R \equiv z - z', \tag{5.2}$$

with z and z' being the true and the apparent zenith distance, respectively (see Fig. 5.10).

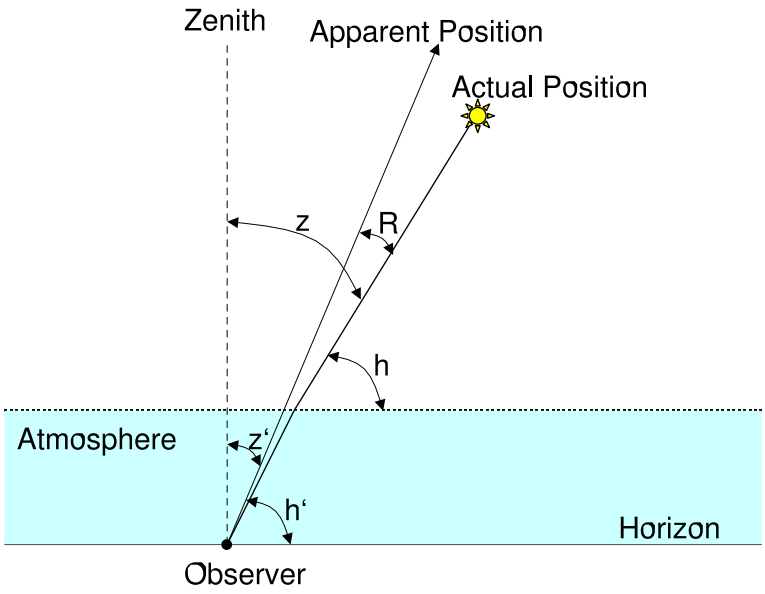

Figure 5.10: Schematic of refraction R in the atmosphere. The variables h and z denote the true altitude above the horizon and the zenith distance, respectively, while h' and z' represent the apparent height and zenith distance. The incoming ray is bent towards the surface in the atmosphere of Earth.

One may also define the refraction via the true and apparent altitude above the horizon, h and h' as

$$R \equiv h - h', \tag{5.3}$$

which is equivalent due to the fact that $z^{(\prime)} = 90^\circ - h^{(\prime)}$. Since the density of the atmosphere is decreasing with altitude, an incoming ray is bent towards the surface of the Earth. The refraction

is large (about 0.6°) for objects close to the horizon ($z = 90^\circ$) and decreases to zero for the zenith position ($z = 0^\circ$), since it depends on the distance travelled in the atmosphere. Beside that, various other factors influence the refraction R, such as geographic latitude and altitude or atmospheric conditions. Since R depends on the refraction index n, it also varies with temperature and atmospheric pressure. For exact predictions, ray tracing simulations are used, but there also exist some very accurate approximative formulae, such as [119]

$$R = \frac{p}{60 \cdot T}\, 3.4303 \left[z' - \arcsin\left(0.9986\ \sin\left(0.9968 z'\right)\right)\right] - 0.0112 z' \,, \tag{5.4}$$

which only needs the temperature T and the pressure p, both at the place of observation, as input along with the apparent zenith distance in units of degree.

Software At CAST, the normal tracking software as described in Section 5.3 has an additional extention, the filming mode. Here, the local pressure and temperature can be entered and since the zenith distance z is provided by the tracking program based on NOVAS, the refraction of photons can be taken into account in real time, when guiding the magnet. Thus, the experiment follows the apparent position of the Sun, rather than its real location as during axion tracking. The error of the refractive correction given the input of pressure and temperature is less than 0.00025°, even at low altitudes, i.e. positions close to the horizon, where the filming at CAST takes place. The change in refraction for a variation of ± 5 K in temperature and 3% in pressure is less than 5%.

System to Film the Sun The first solar filming has been performed in Fall 2002, after a window had been installed in the experimental hall, such that the Sun could be observed twice a year in March and late September for 1 to 2 weeks each. Since then, the filming has been performed 11 times altogether, in Fall 2002-2008 and in Spring 2003/05/06/08, although in a few filming runs both, weather conditions and disturbing trees, did not allow for quality pictures.
The first setup consisted of a standard webcamera connected to a little telescope and indicated that the CAST magnet was pointing to the solar center. However, since better resolution and accuracy were wanted, a new setup consisting of a SBIG ST-7 CCD camera with optics of 200 mm focal length was used together with two targets for the alignment of the system (see Fig. 5.11). The targets were a disk with pointers and crosshairs mounted inside a Taylor-Hobson sphere as used by the surveyors. They were used to align the setup with the help of the surveyors as shown in the upper part of Fig. 5.12. The principle of the alignment corresponds to the aiming with a rifle via rear and front sight. To simplify and improve the alignment procedure the targets have been replaced from spring 2008 onwards by the use of a laser mounted together with a theodolite (see lower part of Fig. 5.12). By adjusting the laser parallel to the magnet axis and shining it to the camera, the expected solar center could be marked and the targets became obsolete. Furthermore, in the same year, a second filming system was used in parallel for the first time, cross-checking and confirming previous results. A detailed description of the different systems can be found in [120].

Results Summarizing, it has been shown that the CAST magnet is pointing to the solar core within the desired accuracy of 0.02°. There is a slight tendency of the magnet being ahead in tracking, but the observed deviation is completely within acceptance limits taking into account the

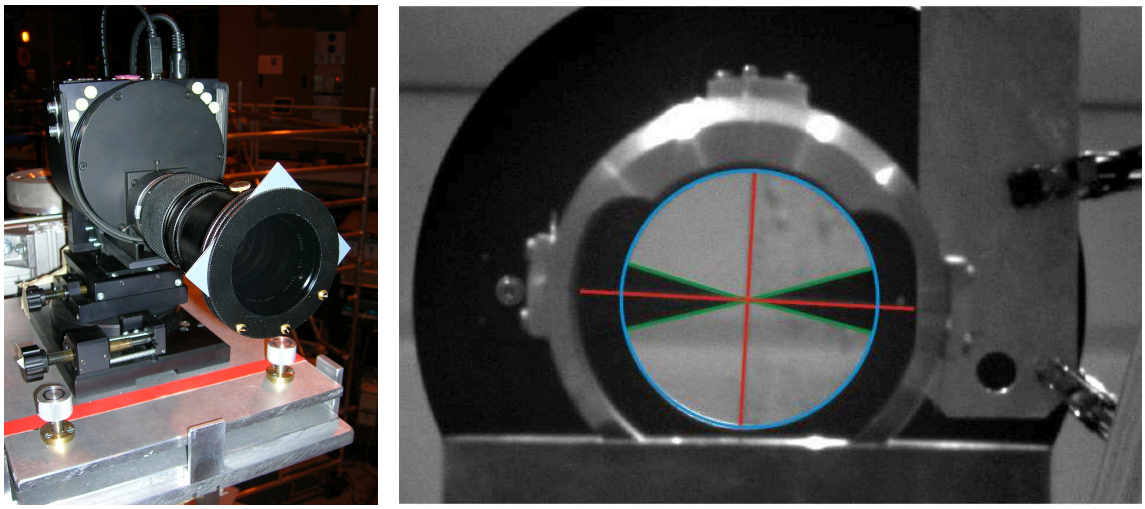

Figure 5.11: Left: Camera used for the solar filming. Right: Two targets are used to align the system. A sphere with crosshairs is situated about 5 m away from the camera. A disk with two pointers forms the second target at a distance of 7.6 m from the camera.

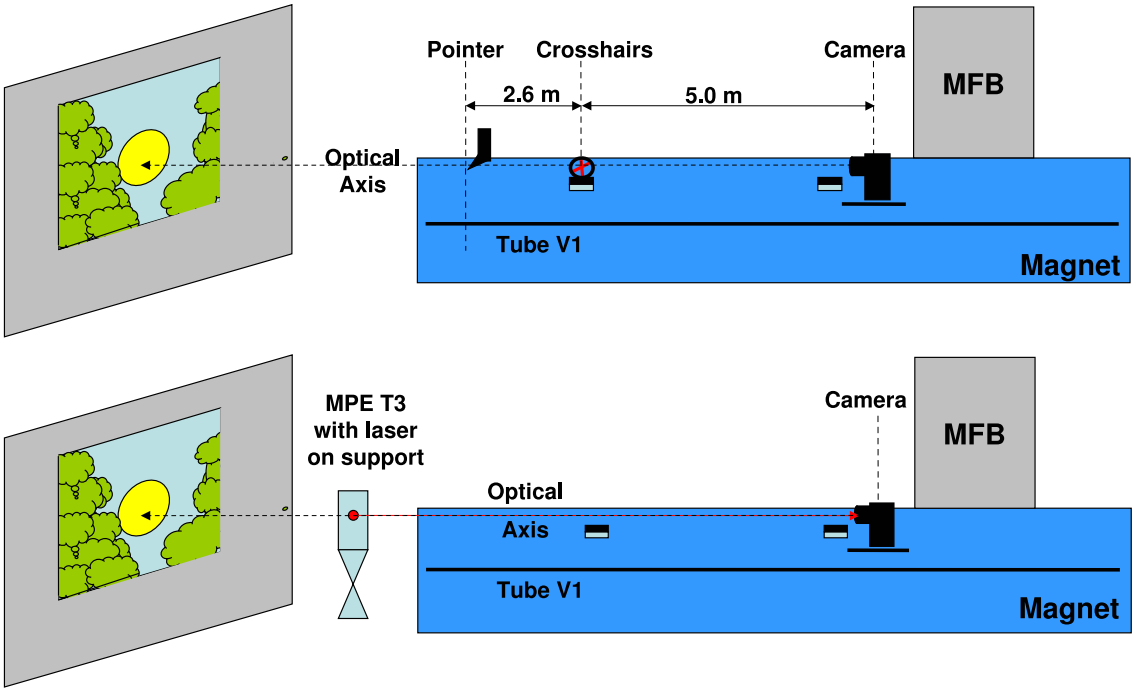

Figure 5.12: Top: Setup of the filming system using two targets to align. The camera is aligned with the magnet axis by using crosswires at a distance of 5 m and a pointer at 7.6 m. Bottom: Setup of the filming system using a laser. The camera is located at the same position as during former filmings. No targets such as previously used crosshairs or the disk with two pointers were needed, since the T3-theodolite with its laser was used for the alignment of the system.

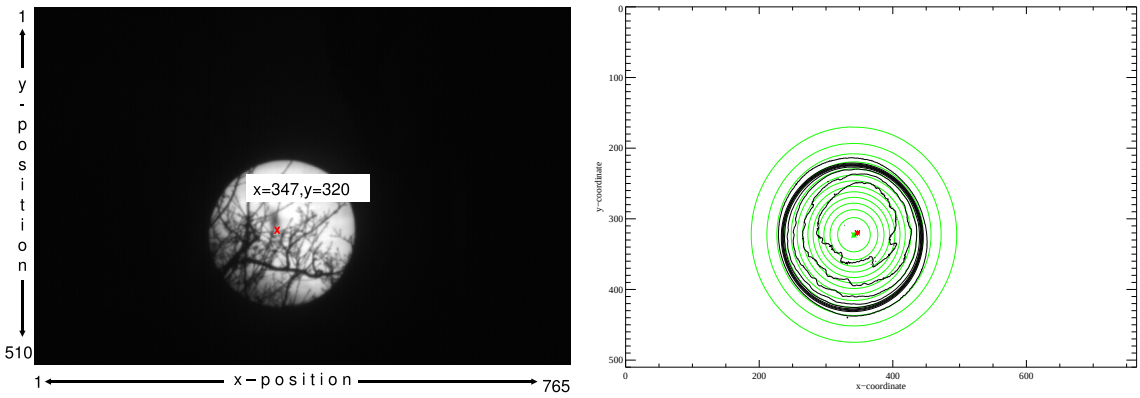

Figure 5.13: Left: Example of an image obtained during solar filming. Right: Fit of a Gaussian to the combined data of a complete filming run. The red cross indicates where the magnet is pointing, while the black lines are the contour of the data. The fit is displayed in green. As can be seen, the magnet seems to be slightly ahead of the Sun in tracking.

errors of the measurements. In Tab. 5.3, an overview of the solar filming data acquired since 2005 is given and Fig. 5.13 shows an exemplary result of the filming in March 2008. Detailed reports are available for the filming from 2005 onwards and the interested reader is referred to Ref. [120].

5.5 The Vacuum and Gas System for ^{4}He and ^{3}He

During CAST's Phase I in 2003 and 2004, both beam pipes of the magnet were kept under vacuum of the order of 10^{-7} mbar. The system of pumps and valves was then extended, such that ^{4}He at various pressures could be inserted into the cold bore to enlarge the axion mass range under investigation during Phase II. The saturated vapor pressure for ^{4}He at 1.8 K is 16.41 mbar, such that for higher pressures, ^{3}He has to be used. Therefore, the gas system had to be further upgraded, after reaching 13.4 mbar with ^{4}He in 2006. The improvement of the gas system was especially necessary to garantee the pureness of the ^{3}He avoiding any contamination and at the same time preventing the loss of the precious gas.

Year	Deviation horizontal/vertical	Statistical Error	Systematic Error
Spring 2005	$0.018°/0.020°$	$0.002°/0.001°$	$0.026°/0.028°$
Fall 2005	$0.023°/0.019°$	$0.001°/0.001°$	$0.054°/0.025°$
Spring 2006	$0.023°/0.011°$	$0.003°/0.007°$	$0.015°/0.015°$
Fall 2007	$0.047°/0.004°$	$---/--$	$0.021°/0.020°$
Spring 2008	$0.014°/0.008°$	$0.007°/0.011°$	$0.020°/0.020°$

Table 5.3: Summary of solar filming results since 2005 [120].

Since the initial vacuum system forms the basis for the gas systems implemented for Phase II, it will shortly be described here, followed by an introduction to the gas systems.

5.5.1 The Vacuum System

To evacuate the cold bore of CAST, an assembly of pumps and valves forms the vacuum system. As sketched in Fig. 5.14, four gate valves permit to separate the cold bore volume of the magnet from the detectors, which are attached to the four ends of the bores. The detectors will be treated in Section 5.6. The gate valves are labeled VT1 and VT2 for the TPC, VT3 for the MM detector and VT4 for the X-ray telescope. In case of occuring problems they can be closed automatically by an interlock system, which controls the status of all valves. Various pressure probes and the corresponding gauges are installed in the experiment and are able to send alarms to the interlock system in case of any irregularity observed in pressure or even a possible vacuum breakdown. In such a case, the interlock system can react appropriately, closing valves and thus protecting the whole setup. Further alarms are sent by the cryogenics system such as a quench alarm for example. Besides protecting the magnet and the vacuum system from damage, the gate valves can also be used to manually decouple one or more detectors from the system, such that interventions on parts of the equipment can be accomplished without interrupting the data taking process of other detectors.
To protect the most sensitive detector system of CAST, the X-ray telescope (see Chapter 6), two more valves are installed, namely V14 and V13. While V14 separates the magnet from the mirror optics, V13 is situated between the X-ray optics and the CCD detector. A more detailed description of the vacuum system for the X-ray telescope can be found in Section 6.2.2.
In order to observe X-ray photons from axion conversion in the magnet, it is essential that the gate valves of the measuring detectors are open, since X-ray photons from axion conversion would otherwise be absorbed in the material of the valve. In case of the X-ray telescope, V13 and V14 have to be open in addition to the gate valve VT4, when acquiring tracking data.

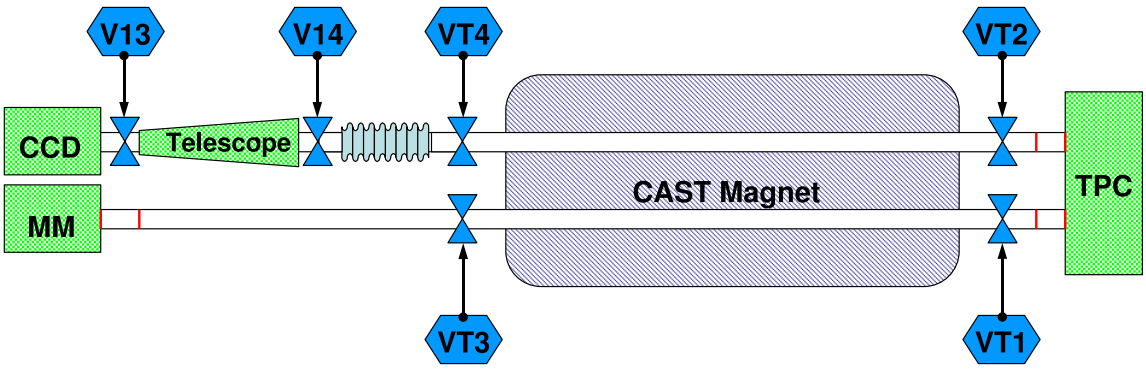

Figure 5.14: The vacuum system of the CAST experiment as used during Phase I. It provides the framework for the gas systems for ^{4}He and ^{3}He. The gate valves separating the cold bore from the detectors are shown in blue and labeled VT1 to VT4. The vacuum system of the X-ray telescope has two additional valves (V13/V14) to protect the optics and the focal plane detector. The connecting bellow between the telescope and the magnet is shown between V14 and VT4.

5.5.2 The ^{4}He Gas System

During the shutdown of the experiment after Phase I in 2005, a gas system was designed and installed in order to insert a precise amount of ^{4}He gas into the magnet and thus control the pressure or equivalently the density inside the cold bore. The philosophy of the system was to change the buffer gas density by increasing the density in steps. These steps corresponded to 0.08 mbar at 1.8 K in the cold bore. Like this, an overlap of the axion-to-photon conversion probability distribution at FWHM for two neighboring steps can be achieved. To provide the required overlap, the system has to determine accurately the quantity of gas to be inserted into the cold bore of the magnet. The achieved accuracy and reproducibility (at a temperature of 1.8 K) was better than 0.01 mbar and 0.1 mbar, respectively [121]. An efficient thermal coupling of the superfluid helium used to cool the magnet garanteed the density homogeneity along the cold bores. A schematic drawing of the implementation of the gas system in the former vacuum system is shown in Fig. 5.15, while Fig. 5.16 shows a more technical drawing of the ^{4}He system as it was used in the first part of Phase II with ^{4}He.

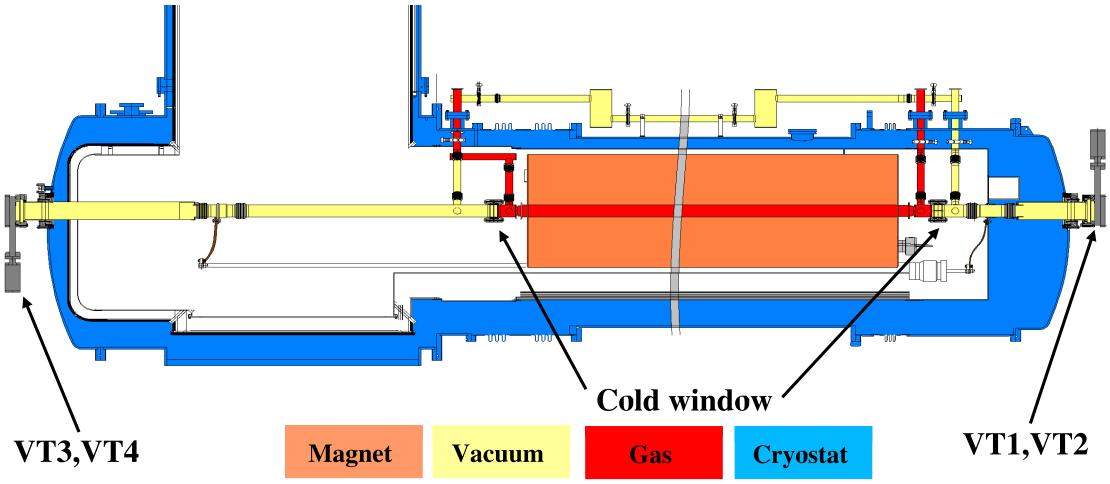

Figure 5.15: Integration of the gas system for Phase II into the existing vacuum system of Phase I. The magnet is shown in orange placed inside the cryostat (blue). The vacuum system (yellow) and the additional gas system (red) are separated by a cold window at each end of the magnet bore. Note that the schematic is not to scale, i.e. the grey vertical cut in the middle of the magnet signifies that the size of the cold bore has been shortened here.

Cold Windows An essential part for the integration of the gas system into the existing vacuum system at CAST are the so-called cold windows specifically developed for the CAST experiment [122]. The four X-ray windows are designed to confine the helium to the cold bore and to withstand a high pressure difference between the inside of the magnet bore and the outer volumes, i.e. the detector systems. During a quench, the pressure inside the cold bore can rapidly rise up to 2.7 bar and the windows must be strong enough to withstand the resulting forces. On the other

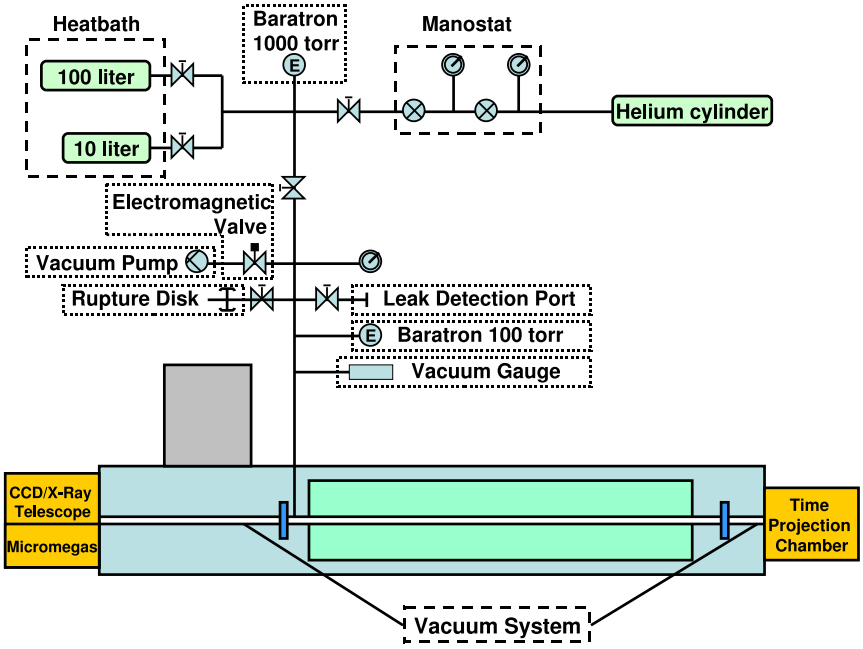

Figure 5.16: Schematic drawing of the ^{4}He system of the CAST experiment.

hand, the windows have to allow X-rays in the keV range to pass, so they cannot be chosen to be arbitrarily thick. Further requirements were low permeability to helium and transparency in the range of visible wavelengths in order to allow for laser alignment of the X-ray telescope and visual crosschecks of the cold windows.

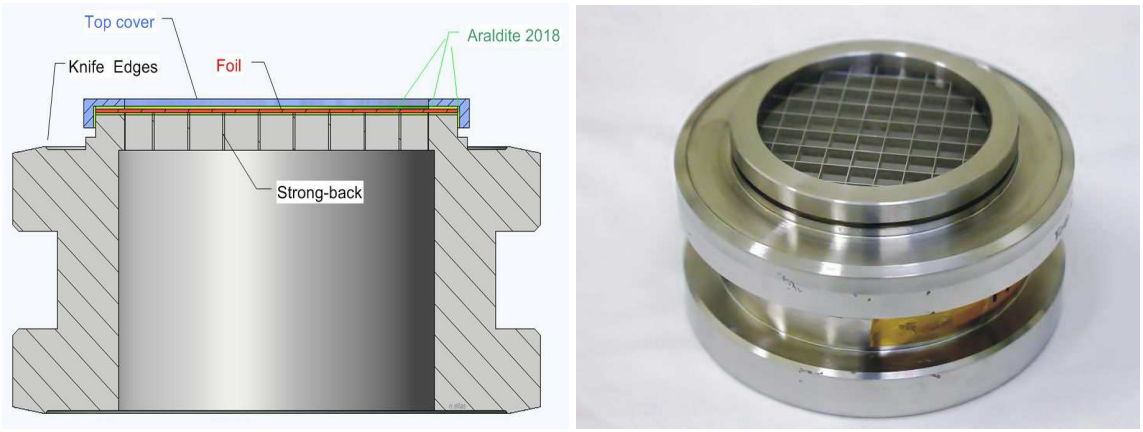

Figure 5.17: Left: Schematic drawing of the cold windows designed for the CAST experiment to confine the helium to the cold bore. Right: Image of one of the cold windows used at CAST. The supporting strongback is clearly visible.

In order to fulfill all the requirements, a foil of 15 μm polypropylene has been mounted on a stainless steel strongback for support (see Fig. 5.17). The strongback support structure covers 12.6% of the geometric area. Taking the components of the windows together, this results in a transmission of $\approx 87\%$ in the energy range of 1 to 7 keV. In tests, it could be proven that the leak rate is below 1×10^{-7} mbar liter/sec. In addition, the windows have been pressure tested to assure their reliability in case of a quench.

Density Profile along the Magnet The density profile along the magnet axis has been simulated taking into account convectional effects at the ends of the magnet (see Fig. 5.18) and the computational fluid dynamics modeling agreed with experimental test measurements done at the CAST experiment. This shows that the temperature of the helium in the cold bore is homogeneous within the magnetic field regions indicated by the blue color in Fig. 5.18 [123].

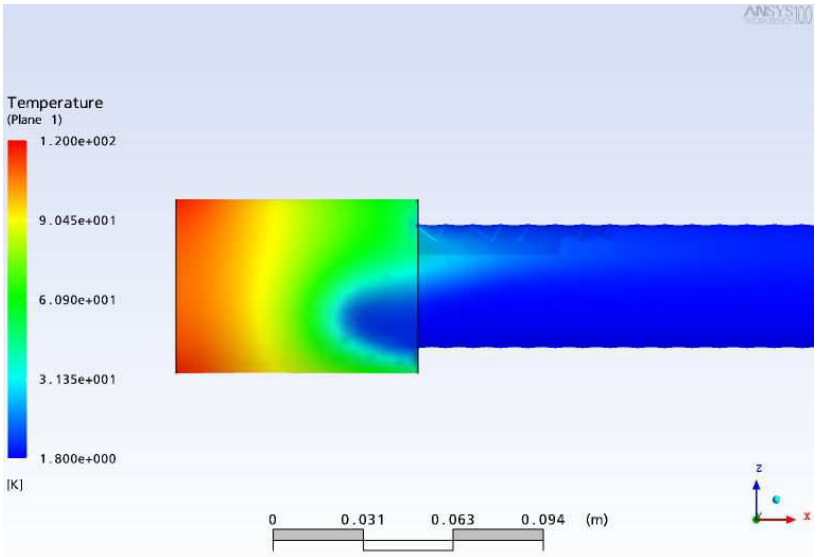

Figure 5.18: Simulation of the temperature profile of the helium in the coldbore. Displayed is one end of the cold bore, where connections to warmer parts create a temperature gradient. Only a small part of the cold bore (with stable temperature, blue) of about 10 cm is shown as indicated by the scale below the image. Picture courtesy of [123].

Furthermore, the influence of gravity on the pressure along the magnet bore has been studied. When the magnet is at its extreme position of $\pm 8^\circ$, gravitational effects causing a density gradient have been found to be negligible for pressures used with ^{4}He, i.e. up to 13.6 mbar at 1.8 K [124]. For higher pressures with ^{3}He, however, these effects might have to be taken into consideration [125].

Thermoacoustic Oscillations Initial tests revealed potential problems due to spontaneous thermoacoustic oscillations[6] (TAOs) [126] which were observed for pressure settings above 2 mbar. As

[6]Thermoacoustic Oscillations appear in cryogenic systems for the case that a long tube (open at its cold end) is extended to a closed end at a warm boundary. TAOs need to be carefully studied since they are often connected with a non-negligible conduction of heat along the tube.

a consequence, the gas density in specific locations of the cold bore can vary strongly with time. Initially observed TAOs had an amplitude of about 6% of the total pressure measured at room temperature. Extensive studies showed that the oscillations could be eliminated by installing damping devices in the gas line, which hence were included in the experimental setup.

Routine Operation During the first part of Phase II, the pressure was changed once per day by trained personnel in steps of 0.08 mbar covering a pressure range from 0.08 mbar to about 13.4 mbar. Altogether, 160 density settings were done. Two intermediate pressure settings corresponding to steps of 0.04 mbar were taken leading to a total of 162 covered settings. In this way, axion masses up to 0.39 eV could be scanned.
Some pressure settings have been repeated, since the detector with the highest discovery potential (X-ray telescope) had missed a few tracking runs. Further settings were checked again in order to rule out possible candidates for an axion signal. In the course of the first part of Phase II, a protocol has been developed in order to determine if a setting should be considered as a possible candidate and thus had to be repeated. This protocol has been tested and was partly applied during the measurements with ^{4}He and was fully operational for the beginning of the ^{3}He phase allowing for an average fraction of repetitions of density settings for 10% of the total available time.

5.5.3 The ^{3}He Gas System

In order to use ^{3}He inside the conversion region of the CAST magnet to access higher axion masses once the saturation pressure of ^{4}He is reached, the existing ^{4}He gas system had to be significantly upgraded. This was necessary in order to fulfill the following requirements, which were partly based on experience collected with the first gas system:

- Prevention against loss of ^{3}He, which is more expensive than ^{4}He due to its small natural abundance and demanding purification processes
- Accurate metering of the helium in the conversion volume and good reproducibility
- Suppression of thermoacoustic oscillations
- Protection of the thin X-ray cold windows
- Safety release procedure for the ^{3}He gas to garantee operational safety

A schematic drawing of the final system can be found in Fig. 5.19. A very detailed description of this system, which has been used at CAST since late 2007, can be found in Ref. [123].

Routine Operation During the second part of Phase II, the pressure is changed once per tracking, i.e. twice per day, by trained personnel. By filling the cold bore with the additional gas, corresponding to one extra setting, in the middle of each tracking, all detectors can measure every setting. Thus, the possibility to overlook a potential axion signal is minimized. Only about 3 min are needed to change the pressure in the cold bore and allow its stabilization. It has also been implemented in the gas system for ^{3}He that the pressure can be changed several times during one single tracking. It is even possible to ramp the pressure continously over maximal 10 settings,

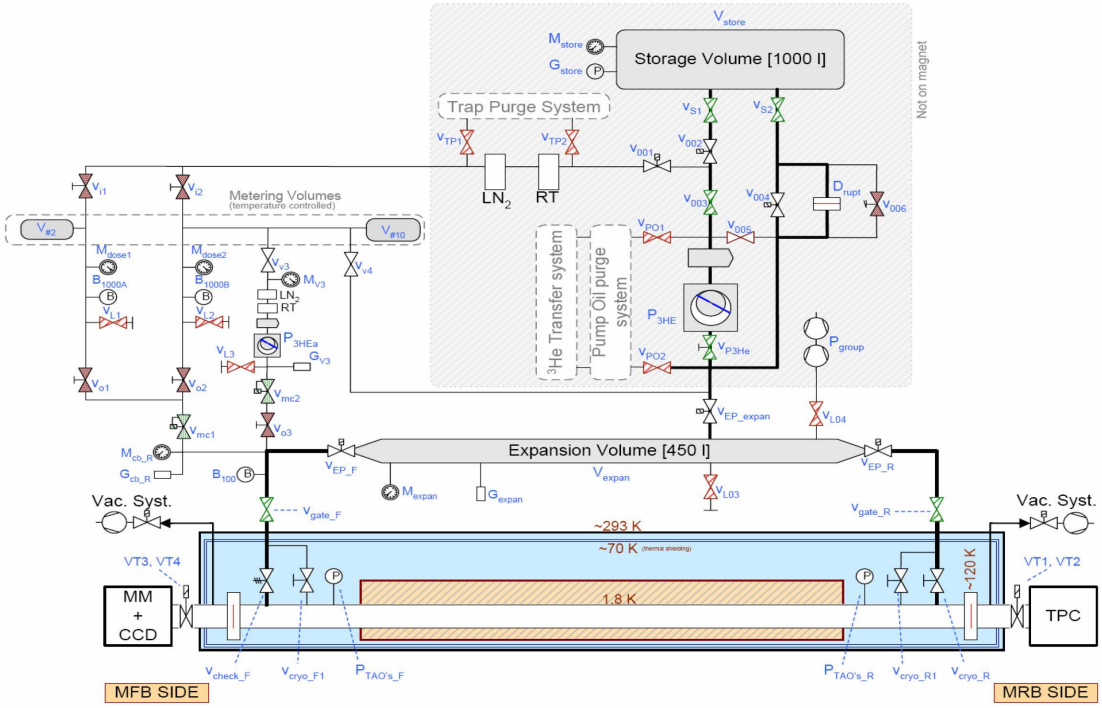

Figure 5.19: Schematic drawing of the ^{3}He gas system. It is much more sophisticated than the previously used system for ^{4}He due to the stricter performance requirements [123].

while following the Sun. In Fig. 5.20, the pressure changes for ^{4}He and ^{3}He are visualized. The light blue area indicates the time of the shift, the red area the solar tracking and the dashed line represents the middle of tracking. Note that the time scale is not in due proportion. In blue, the change of pressure during the measurements with ^{4}He is shown with one step per day, while in green the ^{3}He procedure with one change per tracking is displayed. Furthermore, the yellow curve represents one of the possible ramping modes[7], which might be applied in the course of the remaining time in Phase II.

Status and Schedule During the second part of Phase II, the pressure is changed once per tracking, i.e. twice per day by trained personnel in steps of 0.086-0.114 mbar covering a pressure range from 13.25 mbar to currently 38.91 mbar. Altogether, 412 density settings have been covered in CAST's Phase II (157 with ^{4}He only, 252 with ^{3}He only, and 3 settings have been measured with both isotopes). So far axion masses up to about 0.66 eV have been scanned. The goal is to reach a pressure of 120 mbar at 1.8 K corresponding to an axion mass of 1.15 eV. Depending on the available time and resources, the step size might be increase further to reach the designated goal.

[7]There are several possibilities of using the ramping mode. One might ramp down during every tracking instead of up or change between two trackings, e.g. ramping up in one tracking and down in the next or vice versa. More details on the different modes can be found in [123].

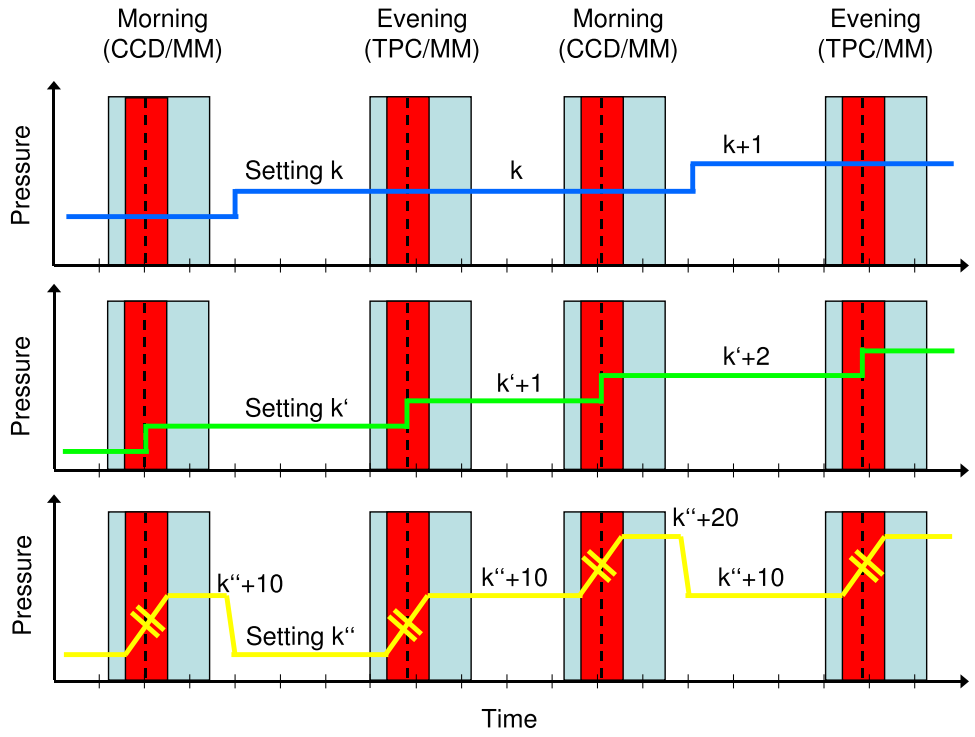

Figure 5.20: The three different modes of changing the pressure setting in the cold bore of the CAST magnet. Note that the time scale is not in due proportion. Top: Pressure change during the ^{4}He phase. Once a day between morning and evening tracking the pressure was increased to the next higher setting (blue line). Middle: Pressure change during the ^{3}He phase. The pressure is increased in the middle of each tracking, i.e. twice per day, by one step (green line). Bottom: Possible ramping mode to change the pressure during one tracking continously over up to 10 density settings (yellow line). This mode has been tested but not yet used in tracking runs.

5.6 Detectors of CAST's ^{4}He Phase

During the ^{4}He phase of the CAST experiment, three different types of detectors have been mounted on both ends of the magnet to search for photons from axion conversion via the Primakoff effect. These detectors had already been used during the vacuum phase of CAST. Some additional upgrades have however been done. Installed on the eastern end of the magnet, ready to search for axions during sunset, a conventional Time Projection Chamber (TPC) has been used covering both bores. A second gaseous detector, a MICROMEsh GAseous Structure device (MICROMEGAS, MM), has been mounted on the other side of the magnet to be able to detect photons originating from axions during sunrise. Next to it, covering the second sunrise bore, an X-ray telescope with a Charge Coupled Device (CCD) as a focal plane detector is ready to look for axions. This detector system provides the most sensitive setup of the CAST experiment with the highest discovery potential.

5.6.1 The Time Projection Chamber

The detector mounted on the eastern end of the magnet covering both of its bores is a conventional Time Projection Chamber, which is exposed to converted photons from axions arriving during the tracking of sunset. The design of this gas detector follows a well-known concept and combines elements of both Multiwire Proportional Chambers (MWPC) and drift chambers. The primary interaction of the photons takes place in the central piece of the detector which is a large gas volume. There, free electrons can be produced via an ionization process. The electrons can then drift towards a plane of anode wires. Due to the strong electric field, an avalance process takes place, resulting in an amplification of the signal. While the first coordinate can be obtained from the anode wire giving the signal, cathode pads provide the second coordinate. From the drift time it is eventually possible to determine the third coordinate, which gives the detector its name. A schematic of the TPC working principle can be seen in Fig. 5.21.

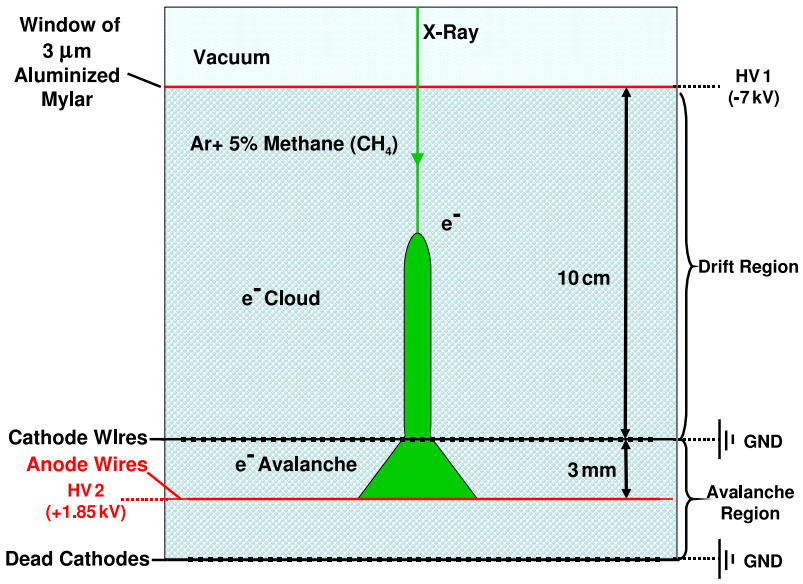

Figure 5.21: Working principle of a time projection chamber. Incoming photons can produce free electrons via ionization, which then drift towards the anode wires. In the strong electric field, an avalance process takes place.

Detector Setup

In total, the conversion volume of the TPC detector covers $10 \times 15 \times 30$ cm^3. The drift region of 10 cm is parallel to the axes of the magnet tubes, while the cross-section of 15×30 cm^2 is perpendicular to it and covers both magnet bores, which have a diameter of 43 mm each and are separated by 18 cm. The gas mixture in the volume consists to 95% of argon and 5% of methane (CH_4) at atmospheric pressure. For photons up to 6 keV traversing the chamber parallel to the magnet axes, this allows basically for total conversion (99%). At higher energies (11.5 keV) the conversion rate drops to about 50%. In order to avoid contaminations, the gas is permanently

renewed.
The basic setup of the detector is displayed in Fig. 5.22. It is formed by a drift electrode of aluminum, which is located close to the magnet, and a combination of 3 planes. While the anode plane has 48 wires (each with $\varnothing = 20$ µm) and is set to $+1.85$ kV, the two cathode planes at ground have a total of 96 wires (each with $\varnothing = 100$ µm). In one plane, the distance between two neighboring wires is 3 mm. The gap between the anode and the first cathode is 3 mm, while the distance is 6 mm between the anode and the second cathode plane (dead cathodes in Fig. 5.21), which is further away from the drift electrode than the first cathode plane.
Most pieces of the detector are made of plexiglass, which is of advantage, due to the low natural radioactivity of this material, while only few metallic pieces (e.g. wires/screws) have been used.

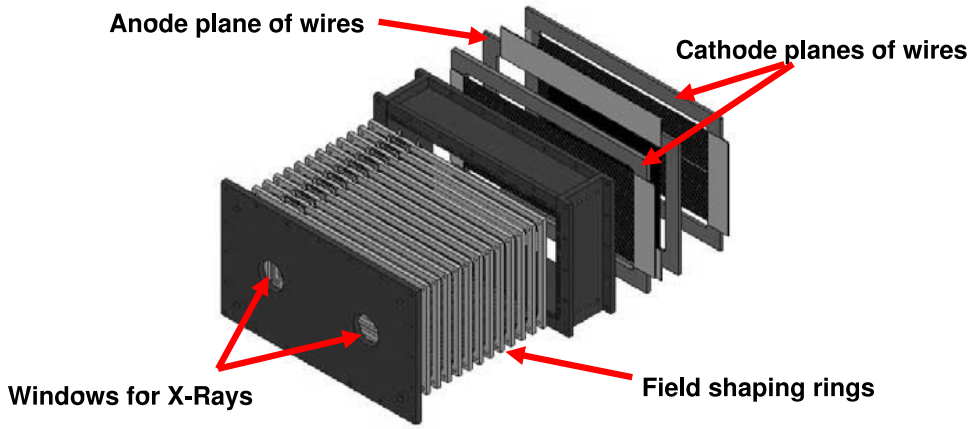

Figure 5.22: Blow-up view of the TPC. The openings to be connected to the magnet bore via windows can be seen along with the field shaping rings. They are followed by the structures holding the wires for the first cathode, the anode plane and finally the second cathode plane.

Concept of Windows and Differential Pumping

The connection of the gaseous detector at 1 atm to the vacuum of the magnet is achieved by the use of thin windows. The first one separates the vacuum in the magnet (5×10^{-7} mbar) from a vacuum buffer region, while the second window cuts off this buffer from the gas-filled detector volume. The windows consist of 3 or 5 µm mylar foil glued to a metallic strongback on the vacuum side of the foil. The geometrical opacity of the strongback is about 8%, whereas the foil is practically transparent for X-rays in the desired range ($\approx 30\%$ at 1 keV, $\approx 85\%$ at 2 keV, and $\approx 95\%$ at 3 keV [127]). In order to serve as drift electrode, the inner side of the mylar foil is aluminized (40 nm). The differential pumping system has been in use since 2004. It protects the windows efficiently and avoids gas leaks towards the magnet.

Shielding

The shielding of the TPC can be divided into an active and a passive part. Background inducing muons can be rejected by an installed active veto shielding. The passive shielding consists of different layers able to stop various passing particles. The innermost layer, the plexiglass vessel of the TPC (17 mm) itself, is able to block X-ray fluorescence of the copper (5 mm), which is used as a Faraday cage to reduce electronic noise and to absorb low energy X-rays produced by environmental γ-rays in the outer part of the shielding. The next layer consists of lead bricks (2.5 cm) and is able to reduce γ-radiation from the experimental environment in the low and medium energy range. Surrounding the lead, Cadmium (1 mm) is used to stop thermal neutrons, which have been reduced in speed, when passing the circumjacent layer of polyethylene (22.5 cm) and originate from medium energy neutrons in the environmental surrounding. Furthermore, a PVC bag is used to cover the entire shielding mentioned above. It is tightly closed and constantly flushed with radiopure N_2-gas reducing radon in the volume. A factor of 4.7 for the reduction in background between 1 keV and 10 keV as compared to no shielding could be achieved. A schematic drawing of the shielding setup is shown in Fig. 5.23. It has been installed since 2004.

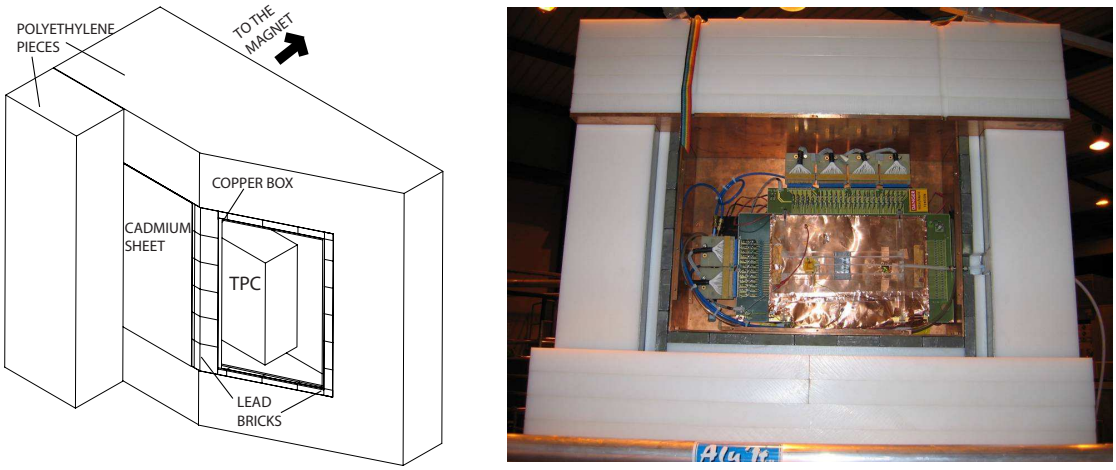

Figure 5.23: Left: Scheme showing the different layers of the TPC shielding. These layers are (from inside to outside): copper (5 mm), lead (2.5 cm), cadmium (1 mm) and polyethylene (22.5 cm). The PVC bag used to enable flushing the complete volume with N_2 is not included in the picture. Right: Photo of the different layers of the TPC shielding.

Requirements and Advantages

The requirements for the TPC detector of the CAST experiment are quite stringent. It needed to have a low threshold (keV-level), high gain and it should be position sensitive, in order to recognize which events originate from the magnet bore. Like this, background rejection via pattern recognition becomes effective. Furthermore, it was desirable to have a high efficiency in the keV energy range along with low background at the energies of interest. Another issue is that the operation should be stable and robust over the full data taking period. The CAST TPC allowed a very

stable performance due to its robust and well-known conventional design along with an optimized shielding to suppress background.

Calibration and Data Taking

During the ^{4}He phase in 2005 and 2006, calibrations of the TPC detector were taken four times a day using a low-energy X-ray source. The TPC covered 154 out of 160 pressure settings and acquired 304.1 hours of tracking and 4346.6 hours of background data corresponding to a 96.3% data taking efficiency with an average detector efficiency of 48% and a dead time of 2%. Throughout the whole data taking period, the TPC showed a stable performance.
The analysis of the complete set of ^{4}He data is finished [128]. It considers the energy range from 1 to 12 keV for pressures up to 13.4 mbar which corresponds to an axion mass of 0.39 eV. No excess of signal over background could be observed and therefore an upper limit on the coupling constant $g_{a\gamma}$ was obtained applying the same technique as for the other detectors (see Section 8.2).

Upgrades for Phase II

The TPC detector used for Phase II is the same as during Phase I with some minor upgrades in order to reduce electronic noise. A detailed description of the Phase I configuration and performance can be found in [129]. For the ^{3}He Phase, which started in March 2008, the TPC has been replaced by two novel Micromegas detectors (bulk and microbulk detector).

5.6.2 The Micromegas Detector

One of the magnet bores on the western end (sunrise end) of the magnet is covered by a MICROMEsh GAseous Structure detector in order to look for reconverted photons from axions during sunrise data taking. This second gas detector in the CAST experiment has been developed rather recently [130] and has a more compact design than the TPC. Instead of wires like in the TPC, the MM detector uses a micromesh to separate the conversion region from the amplification region.
The operation principle of a MM detector is shown in Fig. 5.24. After crossing a buffer space of vacuum between two windows, a photon entering the detector from the magnet aperture can produce a photoelectron via the photoelectric effect in the conversion-drift region. This volume is filled with a gas mixture of argon (95%) and isobutane (5%). The generated photoelectron can then drift for a short distance creating further ion-electron pairs. When the electrons reach the micromesh, they can enter the amplification region, where an avalance process is started due to the strong field. The grid will stop ions produced in the avalance process from reentering the conversion region. It collects the charges of the ions and thus provides one of the readout signals. The electrons travel further till they reach the anode plane, where their signal is then collected by a structure of x-y-strips.

Detector Setup

The material used to built the detector frame is plexiglass and serves to support the electrodes and two windows of 4 μm polypropylene foil. The second window is aluminized and is used as the drift cathode. The gas volume is separated by a copper-made micromesh (4 μm) into a conversion

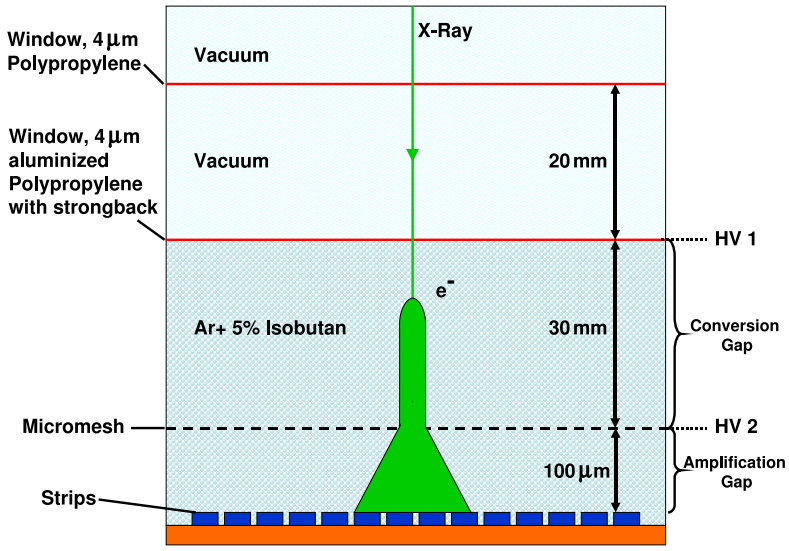

Figure 5.24: Working principle of a Micromegas detector. Photoelectrons can be produced in the conversion drift region and cause an avalanche process in the strong electric field present due to the micromesh.

region of 30 mm and an amplification gap of 100 µm. In order to separate the mesh from the readout plane, pillars spaced 1 mm apart with a diameter of 100 µm each are attached to either the micromesh (initial setup) or the readout (upgraded version with reduced crosstalk). There are 192 X- and 192 Y-strips with a pitch of 350 µm providing the detector with an active area of about 45 cm^2. A schematic drawing of the MM detector is shown in Fig. 5.25.

Concept of Windows and Differential Pumping

The same principle of using two windows (4 µm each) and differential pumping as for the TPC detector is applied for the MM. The first window is used to separate the vacuum of the magnet bore (5×10^{-7} mbar) from a vacuum buffer (5×10^{-4} mbar). No strongback is needed to support this window. In a distance of 20 mm from the first foil, a second window is installed to separate the vacuum buffer region from the gas-filled conversion region (1 bar). The strongback this window is glued on in order to withstand the pressure difference has a transparency of 94.6%. As for the TPC, the aim is to obtain maximal transparency for X-rays of low energies and minimize the leak rate toward the vacuum in the magnet as much as possible.

Requirements and Advantages

Similar requirements as for the TPC had to be fulfilled. And therefore, the MM detector design has been continuously developed and several improved versions have been installed at CAST since 2003. The major advantages of a Micromegas detector are its high stability and efficiency, along with its good resolution in both position and energy. Furthermore this kind of detector has a fast response and a dead time of only 14 ms.

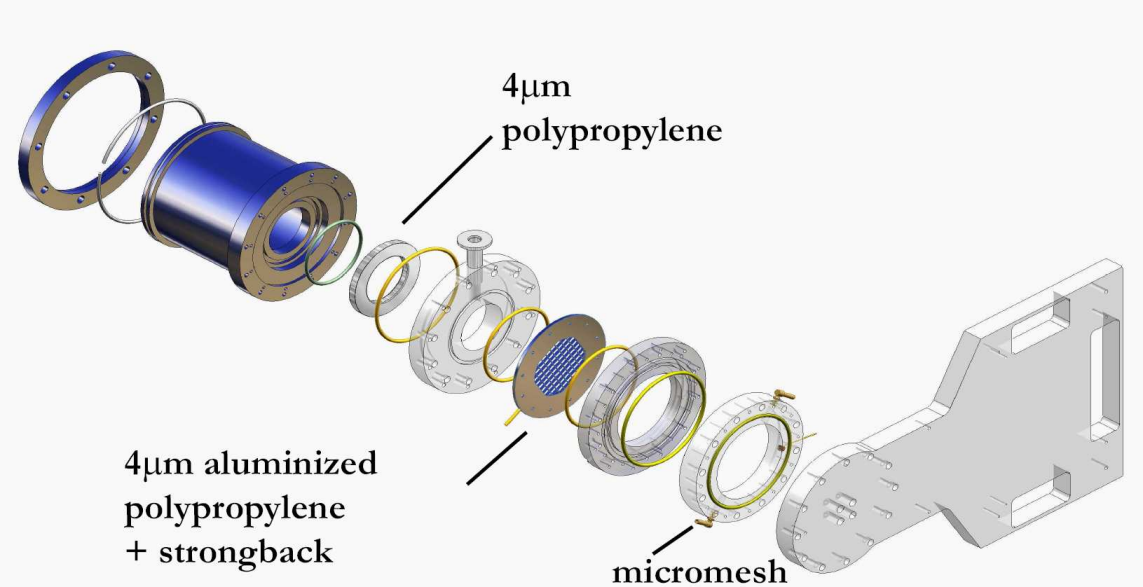

Figure 5.25: Blow-up view of the Micromegas detector. The connection to the magnet bore, which would be to the left side of the displayed components, is accomplished via an extension by an aluminum tube of roughly 1 m, such that both, the X-ray telescope with the CCD and the MM detector, fit on the available platform.

Calibration and Data Taking

Calibrations and pedestal runs have been taken throughout the whole ^{4}He data taking phase on a daily basis using a ^{55}Fe source. The MM detector has been operated continously during Phase II covering 159 out of 160 density settings with ^{4}He. A total of 336.6 hours of tracking data and 3115.0 hours of background data have been acquired during this time. The integrated detector efficiency including all relevant effects amounts to 44% in the range from 2 to 7 keV. The performance of the detector has been stable throughout the complete data taking period.
The analysis of the complete set of ^{4}He data for the MM is finished. It considers the energy range from 2 to 7 keV. No excess of signal over background could be observed and an upper limit on the coupling constant $g_{a\gamma}$ has been extracted from the data by applying the same technique as for the other detectors (see Section 8.2).

Upgrades for Phase II

The MM detector used for Phase I had to be replaced by a new one due to an installation incident. This new detector was working reliably and it was possible to achieve a lower background than before, since the Cu-fluorescence line originating from the detector materials could be reduced by gold coating the amplification mesh. Beside this feature implemented for improved background conditions, the design of the MM detector used during the ^{4}He data taking phase is identical with the one which was working in Phase I. A detailed description of the Phase I configuration and performance can be found in [131].

5.6.3 The X-Ray Mirror Optics and the CCD Detector

The X-ray telescope [132] consisting of a combination of X-ray mirror optics with a Charge Coupled Device (CCD) as a focal plane detector (see Fig. 5.26) will be discussed in detail in the next chapter.

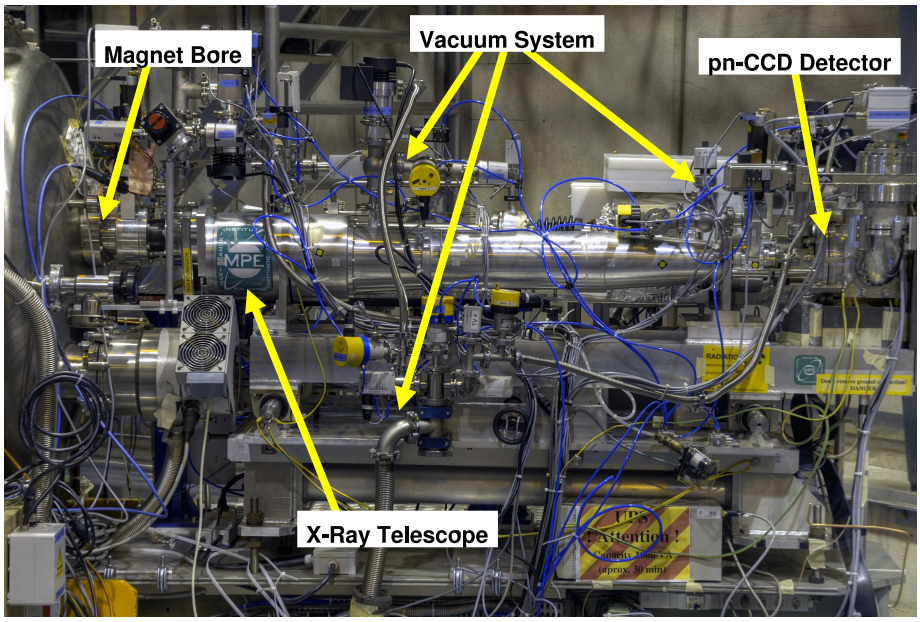

Figure 5.26: The X-ray Telescope of the CAST experiment. The vacuum setup of the detector is shown together with the X-ray optics and the focal plane detector, which is a pn-CCD.

5.7 Results of CAST Phase I

During its first phase with evacuated magnet bores, CAST has been able to provide the best experimental upper limit on the coupling constant in a wide axion mass range. In the mass region up to 0.02 eV it supersedes the theoretical horizontal branch star limit (HB limit). The obtained limit for $g_{a\gamma} \lesssim 8.8 \times 10^{-11}$ GeV^{-1} at 95% C.L. has been published in Ref. [53]. Details concerning the analysis of the Phase I data can be found in Refs. [133, 134]. In Fig. 5.27, the upper limit on the coupling constant as achieved using all data acquired in Phase I is shown along with the expectations for ^{4}He and ^{3}He.

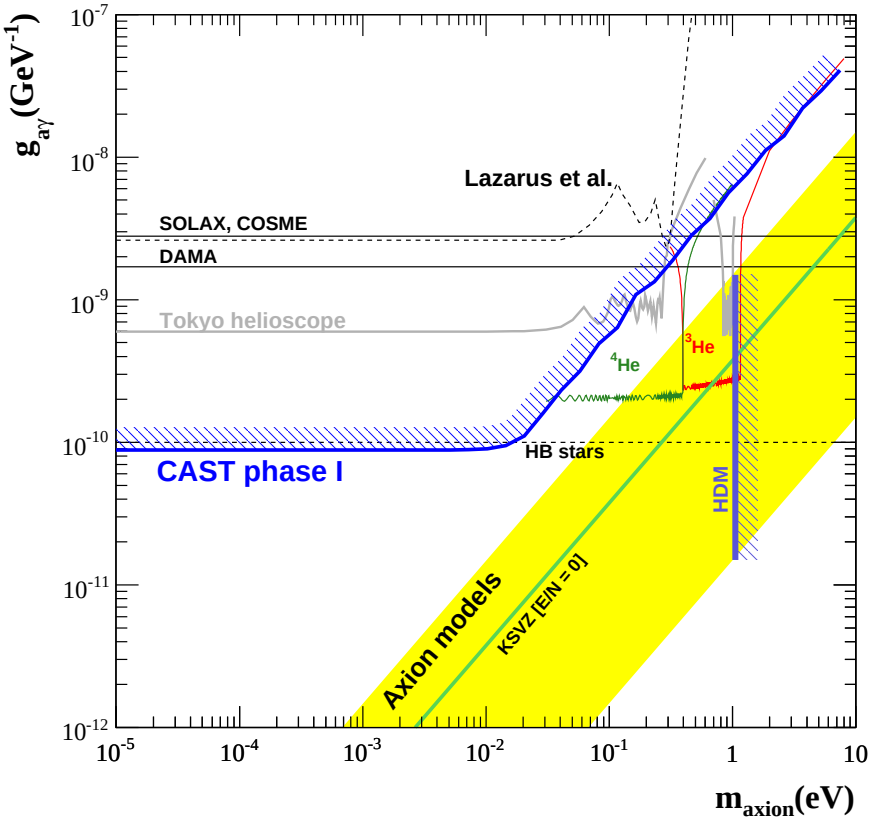

Figure 5.27: CAST exclusion plot of the axion-to-photon coupling constant at 95% CL for all data obtained in Phase I with expectations for Phase II [53]. The achieved limit of CAST's first phase is compared to other experimental constraints (Lazarus [100], SOLAX [95], COSME [96], DAMA [97], Tokyo helioscope [101]). Furthermore, the Horizontal Branch (HB) star limit and the hot dark matter (HDM) limit are included. The yellow band represents the typical theoretical axion models and the green solid line corresponds to the case of the KSVZ model with $E/N = 0$.

Chapter 6

The X-Ray Telescope of CAST

The most sensitive detector system used at CAST is the X-ray telescope. It is a combination of X-ray mirror optics and a Charge Coupled Device (CCD), which is located in the focal plane of the mirror optics. Both instruments were originally built for satellite space missions and provide CAST with an X-ray telescope able to exhibit a very high axion discovery potential along with an excellent imaging capability. In this chapter, first the two major components of the CAST X-ray telescope, i.e. the mirror optics and the CCD detector will be introduced. For both, the general working principle and their implementation in the CAST experiment will be discussed. Following this, the alignment of the X-ray telescope with the help of a parallel laser beam and an X-ray source will be treated, since it is a crucial issue for the imaging device. The chapter will be closed by the consideration of the experimental background of the X-ray telescope and performed simulations to better understand its behavior.

6.1 The X-Ray Mirror System

The mirror system used to focus the potential signal from the magnet bore of 43 mm diameter to a spot of about 1.7 mm radius is a Wolter type I telescope. It is a prototype for the ABRIXAS[1] mission [135] launched in April 1999, which was meant to map the sky in the X-ray range for energies between 0.5 keV and 15 keV. It's purpose was thus to complete the ROSAT[2] mission towards higher energies.

6.1.1 Working Principle

The basic physical concept used to focus X-rays is the principle of total reflection for an incident angle θ_1 larger than a critical angle θ_c. Total reflection occurs, when a beam of light traveling through an optically dense material (large refractive index) is incident on a medium with a smaller index of refraction, i.e. on a medium which is optically less dense. Snell's law for such a beam

[1] A BRoad Imaging X-ray All-sky Survey

[2] The missions name originates from the abbreviation of the German word for X-ray satellite (Röntgensatellit)

going from a medium with refractive index n_1 to one of n_2 where $n_1 > n_2$ yields

$$\frac{\sin\theta_1}{\sin\theta_2} = \frac{n_2}{n_1}, \tag{6.1}$$

where θ_1 is the incident angle and θ_2 the angle of refraction. Since θ_2 cannot be larger than $90°$, one obtains the critical angle of incidence as

$$\theta_c = \arcsin\left(\frac{n_2}{n_1}\right). \tag{6.2}$$

If one is far from any absorption edges

$$\theta_c^2 \propto \lambda^2 r_0 N_e, \tag{6.3}$$

holds [136], with λ being the wavelength of the incident light, r_0 the classical electron radius and N_e the electron density. Thus, the critical angle depends on the energy of the beam E_γ and the atomic number Z of the mirror material, since

$$\begin{aligned} \theta_c &\propto \lambda \propto \tfrac{1}{E_\gamma}, \\ \theta_c &\propto \sqrt{N_e} \approx \sqrt{Z}. \end{aligned} \tag{6.4}$$

Therefore it can be concluded that materials with a higher atomic number Z are better reflectors, since low grazing angles[3] are desirable, when constructing X-ray optics. The most popular material used is gold.

Wolter Type Optics

If an optical system is supposed to produce a sharp image for both, on-axis and off-axis objects, the Abbe sine condition [137] has to be (at least approximatively) fulfilled. This implies that

$$f = \frac{h}{\sin(\theta)}, \tag{6.5}$$

must hold for a constant focal length f on the side of the image with h being the distance of the ray from the optical axis and θ representing the angle between the final path of the ray and the optical axis as shown in Fig. 6.1. A first approach by Giacconi and Rossi [138] of using a simple parabolic mirror did not succeed in satisfying the Abbe sine condition and off-axis objects were strongly blurred in this case. In 1952, Wolter [139] proved that by combining two mirror elements, namely a parabolic and a hyperbolic mirror, which are placed confocal and coaxial, the required condition can be approximately fulfilled. He proposed three different types of mirror configurations, which are nowadays known as Wolter type I, II and III optics. All three types are depicted in Fig. 6.2. In telescopes of type I (see upper panel of Fig. 6.2), which provide the mechanically simplest solution, the X-rays are reflected first on the inside surface of a parabolic mirror surface and then

[3] The grazing angle is defined as the angle between the incident ray and the surface of the material, i.e. as $90° - \theta_1$. Grazing angles are often used, when large angles of incident are discussed. They are generally measured in milliradians.

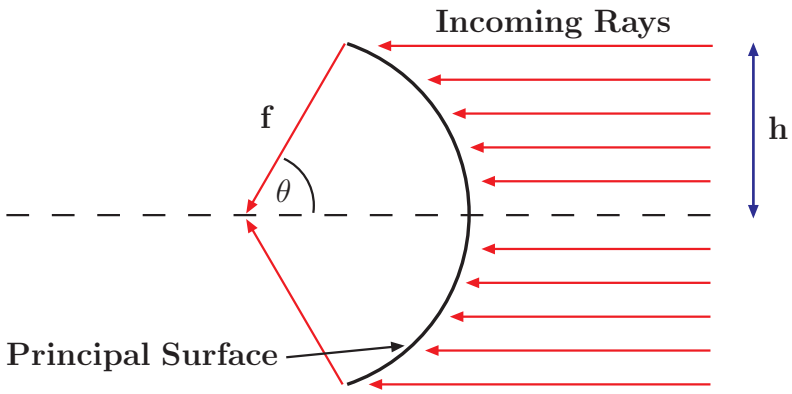

Figure 6.1: Schematic view of the Abbe sine condition, which has to be fulfilled in order to produce sharp images of on-axis as well as off-axis situated objects.

on the inside of a hyperbolic one. Furthermore, several mirror shells can be nested into one another, which presents a big advantage, since it increases the reflective area and thus the light collecting efficiency rises. This is especially useful, since most astronomic X-ray sources tend to be rather weak.
For type II (see middle panel of Fig. 6.2), the first reflection is analog to type I on the inner surface of a paraboloid, while the second reflection is on the outside of a hyperboloid. This results in a higher focal plane magnification, since longer focal lengths are allowed in this case. A disadvantage in comparison to type I is, however, that off-axis images are more blurred for type II, which limits its applications mainly to narrow field imaging.
In the third type of Wolter optics (see lower panel of Fig. 6.2) finally, the first reflection is taking place on the outer surface of a parabolic mirror and the second on the inner side of an elliptic shell. This type is not suitable for X-ray astronomy.
The most popular and widely used Wolter optics are those of type I. This is also the case for the ABRIXAS telescope used at the CAST experiment.

6.1.2 The ABRIXAS Mirror System at CAST

The CAST X-ray telescope [132, 141] consists of 27 nested shells. The parabolic and hyperbolic nickel shells of the Wolter type I telescope are coated with gold for optimized reflectivity. The mirror shells are arranged coaxial and confocally with a focal length of 1600 mm. While the innermost mirror shell has a radius of 38 mm, the maximum shell radius is 81.5 mm. A spider-cob like structure supports the nested shells and divides them into 6 identical sectors (see left part of Fig. 6.3). At the CAST experiment, only one of the mirror sectors is used, since the diameter of the magnet aperture is 43 mm. It is indicated in the left part of Fig. 6.3 by the white circle. Due to this off-axis mounting, no shadowing effects from the support structure are observed at CAST.

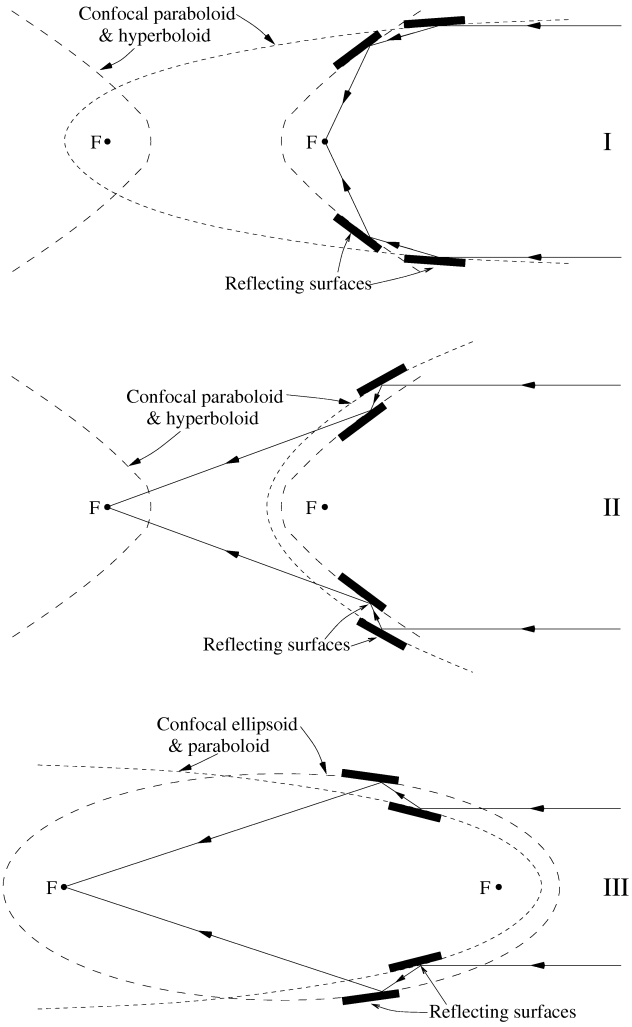

Figure 6.2: Schematic working principles of the Wolter-type I, II and III optics. Type I and II both use parabolic and hyperbolic mirrors, while for type III parabolic and elliptic reflector shells are employed. A more detailed description of the various types can be found in the text. Image courtesy Ref. [140].

Overall Performance The determining parameters for a mirror system like the one for CAST at a given focal length are the effective area and the point spread function (PSF). While the effective area of a telescope can be defined as the unrestricted collecting area after considering all obstructions in the optical path, the PSF provides the spatial resolution.
For a specific coating, the effective area depends mainly on the off-axis angle, the photon energy and the micro-roughness of the mirror surfaces. Here, a growing micro-roughness results in a reduced effective area. The effective area also decreases with larger incident angles of the photon, because this corresponds to a reduction in reflectivity. Furthermore, the efficiency can be diminished by geometrical effects such as vignetting[4].

[4]Vignetting is the decrease of brightness or saturation of an image in its outer region.

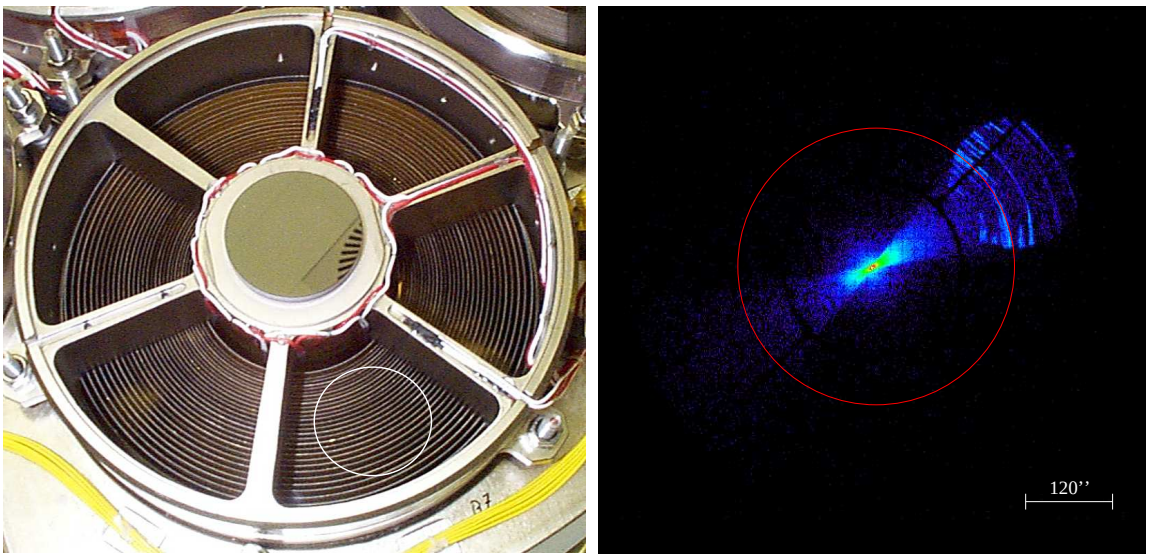

Figure 6.3: Left: Mirror system in front view. The mirror shells can be seen along with the support structure dividing the telescope into six sectors. At CAST, one sector is used and the approximate size of the magnet aperture is marked by the white circle [132]. Right: Intensity image of the point spread function in logarithmic intensity scale obtained by illuminating one sector with an almost parallel X-ray beam of 1.5 keV at the PANTER X-ray test facility in Munich. The red circle indicates the expected solar axion image. Single reflections on the shells are observable as circular structure towards the upper right edge due to the finite source distance.

In case of ideal imaging optics, a point source should be imaged as a point-like signal. But since the used optics are not perfect, the image will be spread over a certain area. This spatial resolution is taken into account for the PSF by considering the measured full width at half maximum (FWHM) of a point source image.
The six sectors of the ABRIXAS telescope used at CAST have been calibrated at the PANTER test facility of the MPE[5] in Munich [142]. For this purpose, monoenergetic X-rays at various energies were used. The result of these measurements showed an on-axis resolution of 34.5 arcsec (HEW[6]) at 1.5 keV and 44.9 arcsec at 8.0 keV. Thus, the resolution is much better than the size of the expected axion image of the Sun ($\approx 0.1°$). An exemplary image of the intensity distribution of one mirror sector illuminated with a point-like source at about 130 m distance is shown in the right part of Fig. 6.3. Since the mirror system has not been illuminated symmetrically, an apparent asymmetry is observable in the picture. It should be noted that the PSF depends on the size of the source as well as on the off-axis angle.

Determination of Effective Area and Point Spread Function The energy dependence of the effective area has been measured for all six sectors of the telescope at PANTER. The results for each sector, when fully illuminated, are summarized in Tab. 6.1. At CAST, the sector with the best

[5]Max-Planck-Institut für extraterrestrische Physik/ Max Planck Institute for Extraterrestrial Physics
[6]Half Energy Width

Sector	Effective area [cm^2]			
	0.93 keV	1.49 keV	4.50 keV	8.04 keV
1	13.5	13.4	8.2	3.9
2	13.5	13.4	8.2	3.8
3	8.9	13.6	8.3	3.9
4	13.9	13.9	8.4	4.0
5	12.6	12.8	7.9	3.4
6	13.1	13.4	8.5	4.0

Table 6.1: Results of the measurements of the effective area for the individual mirror sectors of the CAST telescope at the PANTER test facility.

effective area is used, which turned out to be sector 4. In Fig. 6.4, the measured on-axis effective area of sector 4 is shown (black crosses). It was obtained with a telescope aperture of 48 mm, which formed the setup of the PANTER calibration measurements. In order to use these results for the 43 mm opening of the CAST magnet, a ray-tracing algorithm developed for the ABRIXAS mirror system to predict the effective area has been applied to simulate a 48 mm and 43 mm aperture (black and red line, respectively). The mirror system along with its support structure as well as the magnet geometry are included in the simulations. A perfectly straight beam pipe has been assumed.

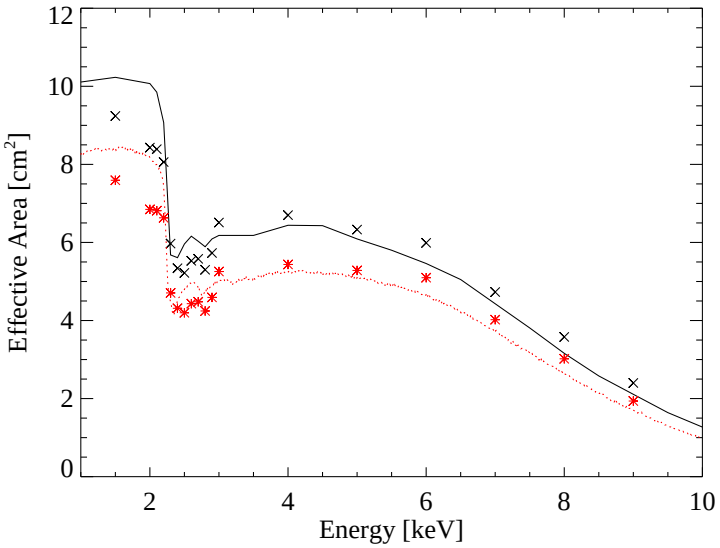

Figure 6.4: On-axis effective area of the X-ray telescope. The PANTER measurements with a 48 mm aperture are marked by the black crosses. Furthermore, the simulated curves for 48 mm and 43 mm apertures are shown (black solid line and red dotted curve, respectively). The expected values for CAST (red stars) have been obtained by scaling the PANTER results with the ratio of the simulations for the two different aperture sizes. For the simulation, point-like sources have been assumed [132].

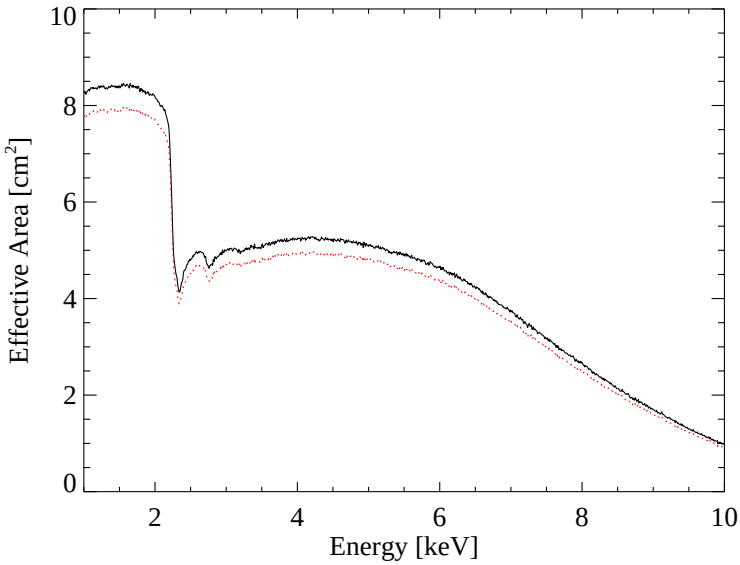

Figure 6.5: Comparison of the simulations for the CAST magnet aperture (43 mm) using a point source (black) and a realistic extended axion source as the Sun (red) [132].

The expected effective area for CAST (red stars) is then obtained by scaling the PANTER results with the ratio of the simulations for the two different apertures. Shown in Fig. 6.4 are the results for simulations assuming point-like sources. The difference in the on-axis effective area between point-like sources at infinity and a realistic extended axion source as the Sun is shown in Fig. 6.5. The upper line (black) is the CAST effective area for a point source, while the red curve has been obtained for an extended source as the Sun.
The influence of off-axis angles on the effective area is displayed in Fig 6.6. Both, the behavior of radial and of tangential off-axis angles relative to the surface of the mirror shells is shown. The telescope is situated on-axis, i.e. not tilted with respect to the line of observation[7]. There is a difference in the two directions due to the asymmetric setup, in which only one sector is illuminated. This yields an asymmetry in the PSF and also in the efficiency loss due to geometric effects (vignetting). The non-symmetry of the PSF can be seen as well in the right part of Fig. 6.3, but it is of no importance for CAST, since the expected size of the axion signal spot is much larger as marked by the red circle.
To point out the influence of geometric effects on the effective area of the telescope, Fig. 6.7 shows transmission losses in percent as separate contributions from the magnet geometry (straight tube of diameter 43 mm) and the telescope structure as well as the combined deficit. One should note that in this case, the telescope has been tilted[8]. It can be seen that for a slight misalignment of the telescope, the off-axis effective area of the mirror system and the additional effects caused by vignetting from the magnet bores result in a non-neglegible reduction of the detector sensitivity. In

[7] This was the situation for the CAST telescope during the data taking period in 2003.

[8] This has been the situation for the CAST telescope during the data taking period in 2004 and during the ^{4}He part of Phase II.

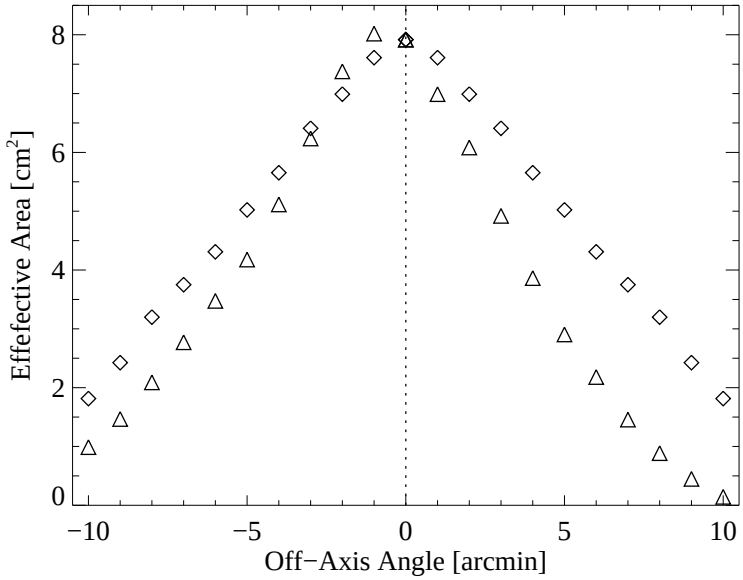

Figure 6.6: Influence of off-axis angles on the effective area for the mirror optics. Triangles mark the radial off-axis angles, while the diamonds represent tangential off-axis angles relative to the surface of the mirror shells for the telescope which is not tilted with respect to the line of observation. The difference between radial and tangential off-axis angle is due to the asymmetric setup with only one illuminated sector at the CAST experiment [132].

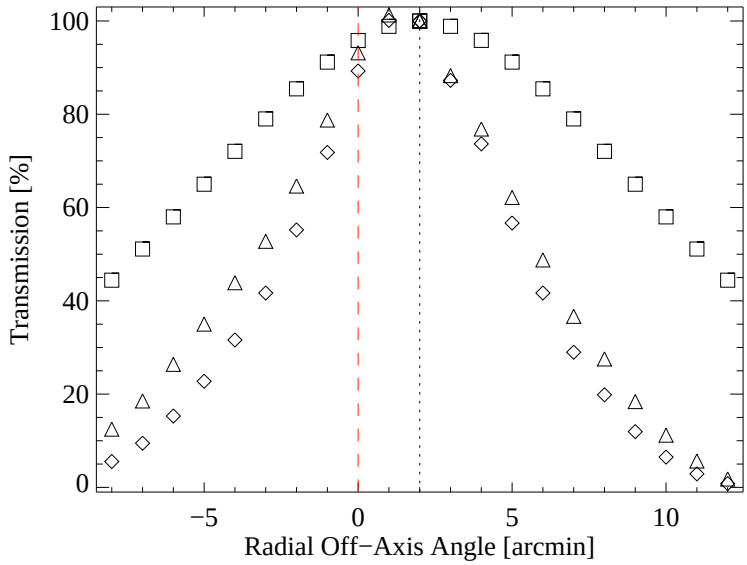

Figure 6.7: Transmission losses depending on radial off-axis angle are shown for the individual components. The reduction of the transmission due to the magnet pipe (squares) and the mirror system (triangles) as well as their combination (diamonds) for the tilted telescope are illustrated. The tilt of 2 arcmin (red dashed line) corresponds to a loss of 10 % of the effective area [132].

numbers, for a misalignment of about 2 arcmin, losses of approximately 10% in efficiency have to be expected.
In all simulations for PSF and effective area, which have been done, energy and off-axis angle dependent, a micro-roughness of 0.5 nm was assumed. This value is typical for the ABRIXAS mirrors. It turned out that the scattering effects due to the micro-roughness can be neglegted.

Relative Efficiency for Phase I and Phase II The effective area of the telescope not including the quantum efficiency of the CCD detector, which will be treated in more detail in Section 6.2, differs for the two data taking periods of Phase I, i.e. 2003 and 2004, since the telescope has been permanently tilted by 2 arcmin during 2004. The motivation for this tilt and the resulting reduction in efficiency by $\approx 10\%$ was to center the axion signal spot on the CCD chip. The data taking with ^{4}He has been performed with the same setup as used in 2004, i.e. with a slightly tilted telescope. The relative efficiency for the telescope not taking into account the CCD detector or the cold windows for Phase II is shown in Fig. 6.8.

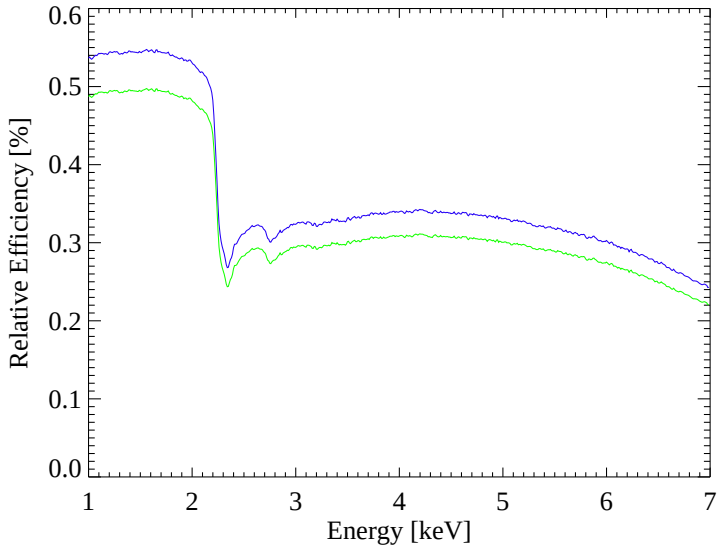

Figure 6.8: Relative efficiency of the mirror system only. Two cases are displayed: for the 2003 data taking run (blue) and for the tilted optics in 2004 and the ^{4}He part of Phase II (green).

6.2 The pn-CCD

The detector used at the CAST experiment in the focal plane of the X-ray mirror optics is a Charge Coupled Device (CCD). It is constructed in the same way as those used onboard the ESA[9] satellite mission XMM-Newton[10] [143]. X-rays arising from axion-to-photon conversion are focused on

[9] European Space Agency
[10] X-ray Multi-mirror Mission named Newton in honor of Sir Isaak Newton.

the fully depleted pn-CCD, which is a 280 μm thick device. The backside illumination through an extremely thin entrance window of 20 nm on the back of the chip is especially advantageous. Together with the thick depletion region, it provides an excellent quantum efficiency of $\gtrsim 95\%$ in the energy range of 1-7 keV, which is particularly interesting for axion searches.
This kind of detector is an advancement of silicon drift detectors suggested initially by Gatti and Rehak [144] and has a size of about 3×1 cm^2. It consists of 200×64 pixels with a size of 150×150 μm^2 each. In the following, the basic working principle of such a device will be introduced and the pn-CCD used at the CAST experiment will be characterized in more detail.

6.2.1 Working Principle

The Physics of Semiconductors

Basic Semiconductor Properties Materials can be classified as conductors, insulators and semiconductors depending on their electrical conductivity. Metalls are conductors with free electrons available to transport the charge, while nonmetals and hydrocarbons are representants of insulators. The most commonly used semiconductors are single crystals with diamond or zinc blende lattice type as illustrated in Fig. 6.9. The former structure can be found with elemental semiconductors

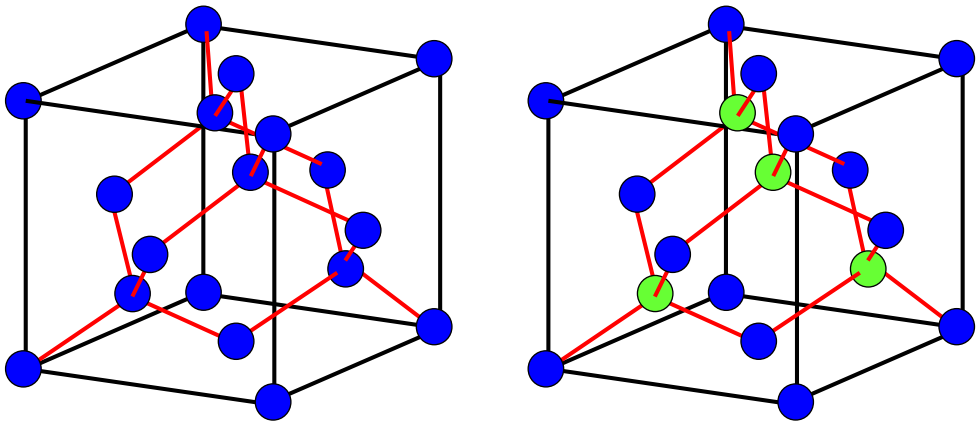

Figure 6.9: Left: Diamond lattice structure. In case of pure silicon or germanium, every blue sphere represents one silicon or germanium atom, respectively. Right: Zinc blende lattice structure. For the example of gallium arsenide every blue sphere represents a gallium ion, while the green ones are the arsenic ions.

such as silicon (Si) and germanium (Ge), while the latter type, which is also referred to as sphalerite structure, is common with compound semiconductors such as gallium arsenide (GaAr). Both structures are face centered cubic (fcc).
In so-called intrinsic or pure semiconductors, no impurities are present and thus the number of holes and free electrons is equal. Extrinsic semiconductors, on the other hand, can be obtained via doping processes, in which the material properties are intentionally altered by introducing specific impurities.
In general, semiconductors can be understood by studying their energy band structure as illustrated

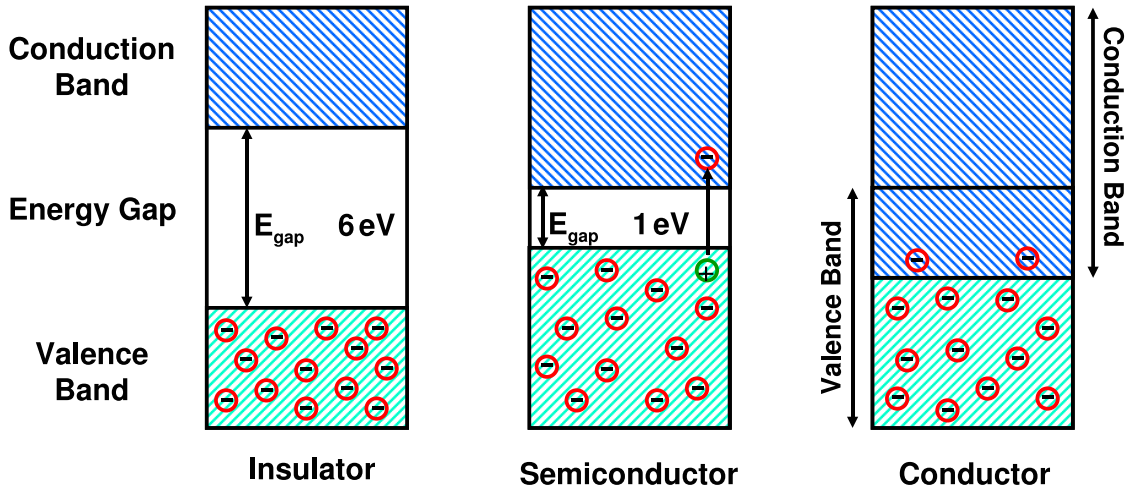

Figure 6.10: Energy band model for insulators, semiconductors and conductors. In insulators, the energy gap between valence band and conduction band is too wide to allow electrons to cross it and so the conduction band is empty. In case of a conducting material, both bands overlap, such that electrons are able to move quasi-free. In semiconductors, the forbidden energy region is small and electrons can be rather easily excited into the conduction band.

in Fig. 6.10. A forbidden energy gap separates the valence band with positive holes from the conduction band containing free electrons. Thus, transport of electric charge can be due to movement of electrons or holes in the respective band. For comparison, also the energy band structures of conductors (no forbidden gap) and insulators (large forbidden gap) are shown in Fig. 6.10.

Doped Semiconductors Being an element of the fourth main group, silicon has four valence electrons, such that it is able to form four covalent bonds. The conductive properties of the semiconductor can be improved by replacing a few silicon atoms in the silicon crystal by either pentavalent atoms or trivalent atoms. This process is generally referred to as doping. The emerging semiconductors can be categorized as n-type, if atoms of the fifth main group are added, and p-type for extra atoms of the third main group.
In case the dopant is an element of the fifth main group, an extra electron is provided, which can be easily excited at room temperature into the conduction band. In addition, these extra electrons might fill up existing holes in the semiconductor and thus decrease the standard hole concentration. In this so-called n-type semiconductors, the current is mainly flowing due to movement of electrons, while holes are minority carriers. Typical donor elements used for this kind of doping are phosphorus, arsenic and antimony.
If on the other hand the introduced impurity is trivalent, the electrons will not be numerous enough to fill up the valence band resulting in an excess of holes. The initial number of free electrons can be decreased by the increased number of holes, since they will be filled up. This leads to the fact that the holes will be the majority carriers of charge, while the electrons only contribute as minority transporters. Such a material is referred to as p-type semiconductor. The most commonly used acceptor impurities are gallium, boron and indium.

A typical introduced impurity concentration is of the order 10^{13} atoms/cm^3, which leads to a doping concentration of a few parts in a billion (10^9), taking into account the densities of germanium and silicon, which are about 10^{22} atoms/cm^3.
Electrical contacts of semiconductors are often obtained by using very high impurity concentrations (up to 10^{20} atoms/cm^3) leading to heavily doped semiconductors, which are highly conductive. In order to distinguish these materials from normally doped semiconductors, a plus sign is added after the material type. Heavily doped n-type and p-type semiconductors are thus referred to as n^+ and p^+, respectively.
The conductivity σ and the resistivity ρ of an n-type material can be obtained as [145]

$$\sigma = \frac{1}{\rho} \approx eN_D\mu_e, \tag{6.6}$$

where N_D is the donor concentration and μ_e the mobility of the electrons. An analogous result follows for p-type semiconductors.

The pn-Junction and Depletion Region Semiconductor junctions provide the basic principle of all semiconductor detectors. This can be illustrated by considering the working principle of a pn-junction, which is obtained by joining a p-type with an n-type semiconductor material. Between the two semiconductors, a so-called space-charge region is created as illustrated in Fig. 6.11. There is a diffusion of holes and electrons towards the n-type and p-type material, respectively, due to initial differences in the electron and hole concentrations in the two materials. Like this, holes on the p-side are filled up by diffusing electrons whereas electrons on the n-side are captured by diffusing holes. The recombination processes near the junction build up a charge on either initially neutral side of the junction. At some point, this creates an electric field gradient, which is large enough to stop the diffusion. The charge density profile and the electric field distribution are displayed in the middle part of Fig. 6.11. The contact potential ΔU is the potential difference across the junction and can be seen in the lower part of the same figure. It leads to a deformation of the band structure and is of the order 1 V.
Summarizing, the space charge region or depletion zone is the region of changing potential. Almost no free electrons or holes are present and the electric field ensures that any mobile charge carriers in this region are guided out of the depletion zone. This fact can be used to detect ionization radiation which will create electron-hole pairs, when it enters the space charge region. The created charge will be swept out and by employing electrical contacts on both sides of the pn-junction, a signal can be detected and will be proportional to the occuring ionization.
On one hand, the depletion depth is dependent on temperature, but it can also be varied by applying an external voltage. The initial depletion depth d, which is the sum of the space charge region on the n-side x_n and the p-side x_p, can be obtained as [145]

$$d = x_n + x_p = \sqrt{\frac{2\epsilon\Delta U}{e}\frac{(N_A + N_D)}{N_A N_D}}, \tag{6.7}$$

where ϵ is the dielectric constant, while N_A and N_D represent the acceptor and the donor concentration.

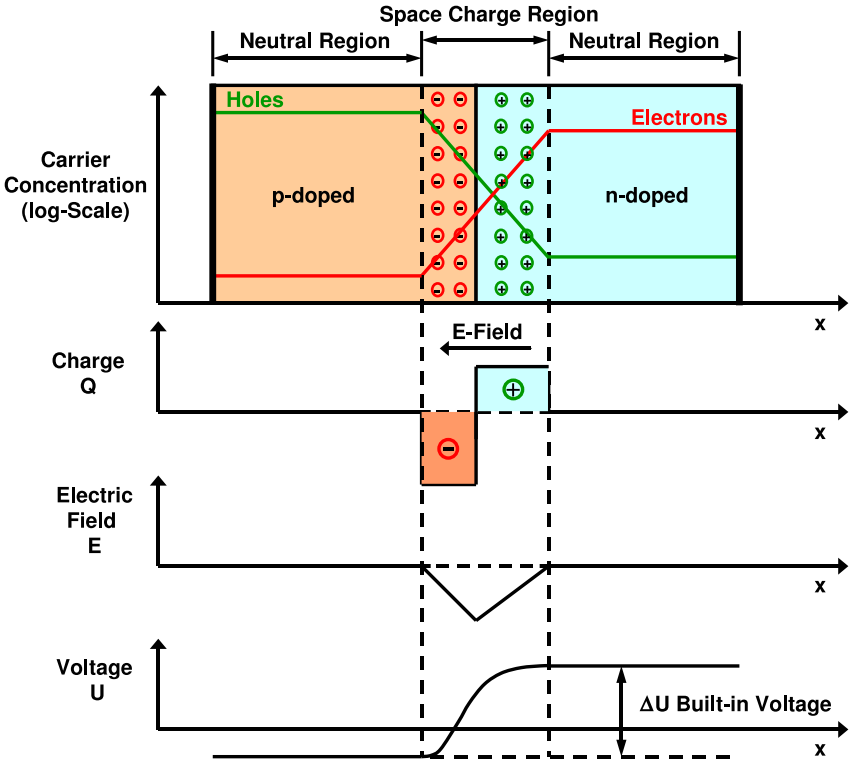

Figure 6.11: Working principle of a pn-junction. The space-charge region is shown in the upper part of the illustration. Initial diffusion takes place here until the emerging field gradient becomes large enough to prevent further movement of charge. The behavior of charge, electric field and voltage are outlined in the region of the pn-junction in the lower part of the schematic.

Detector Characteristics of Semiconductors

There are two important points to consider, when choosing a semiconductor material: the interaction of radiation with the chosen semiconductor and the photon absorption length in the considered material.
The interaction of radiation with a semiconductor is crucial, since this is the process that leads to the creation of electron-hole pairs yielding a detectable electrical signal. As far as charged particles are concerned, low-recoil collisions with electrons along the flight path can result in ionization. Photons on the other hand have to interact first via e.g. the photo or the Compton effect with a target electron. A part of the energy will always go into ionization, while the rest can excite lattice vibrations. Which fraction of energy can be converted into ionization depends mostly on the detector material, while the energy and the type of radiation play a minor role, except at low energies. The mean number of signal counts N of the entering radiation at a given energy is [146]

$$N = \frac{E}{E'} \tag{6.8}$$

where E is the energy absorbed in the semiconductor device and E' the average energy needed to create an electron-hole pair. The statistical variance of the signal counts is proportional to E/E' and thus given by

$$\langle (\Delta N)^2 \rangle = F \frac{E}{E'}, \tag{6.9}$$

with the Fano factor F, which is a material specific constant. This factor is difficult to determine exactly for silicon and germanium. It depends on the energy of the absorbed radiation as well as on the detector temperature. In any case F should be small, i.e. of the order 0.12 at room temperature for these materials. The Fano factor depends on all fundamental energy transfer processes in the semiconductor, including those which do not lead to ionization. Since it requires exact knowledge of all occuring processes in a detector, the accurate determination of F is challenging. Since the energy resolution is proportional to $\sqrt{FE'}$, semiconductors profit of the smallness of both, F and E', which is the small energy needed to create free charge carriers.

A second important aspect in choosing detector materials is the photon absorption length. An absorption length, which is too short, will result in the creation of a signal charge close to the surface, such that it may be completely or partially lost due to specific surface treatment or insensitive covering material. If otherwise the absorption length is too large, the photon may pass the detector without any interaction at all and the signal will be lost. In Fig. 6.12, the absorption length in silicon and silicon dioxide is shown depending on the energy of the incoming photon. Especially

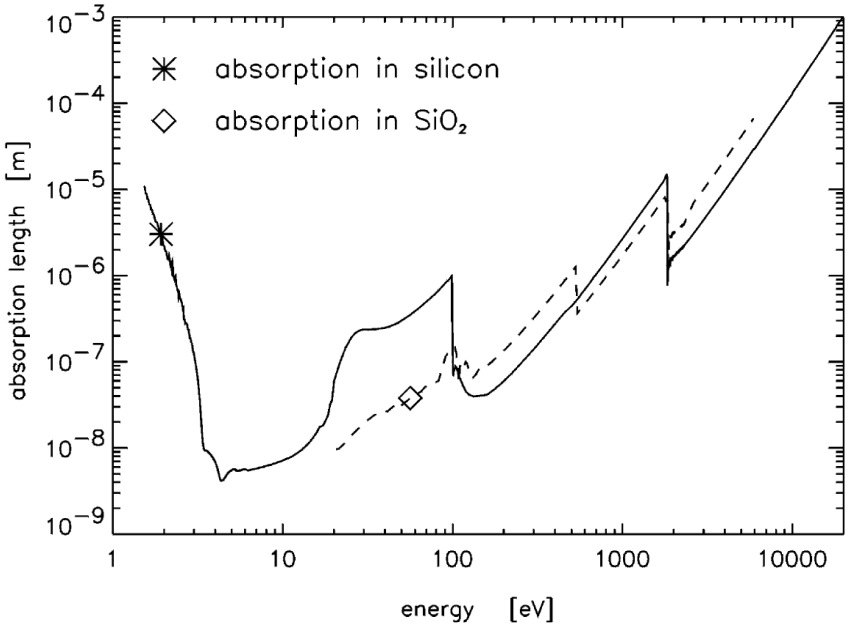

Figure 6.12: Photon absorption length in Si and SiO_2 [143] depending on the initial photon energy.

around the M-, L- and K-edges (at 20, $100 - 115$ and 1830 eV), the absorption is very efficient[11] for silicon.

Fully Depleted Backside Illuminated pn-CCDs

The physics of pn-CCDs and silicon drift detectors (SDD) are closely related, but while in an SDD the charge is drifted out continuously, the CCD moves the packets of charge to the readout in discrete time intervals, such that a CCD could be referred to as a "discrete SDD" [143]. The

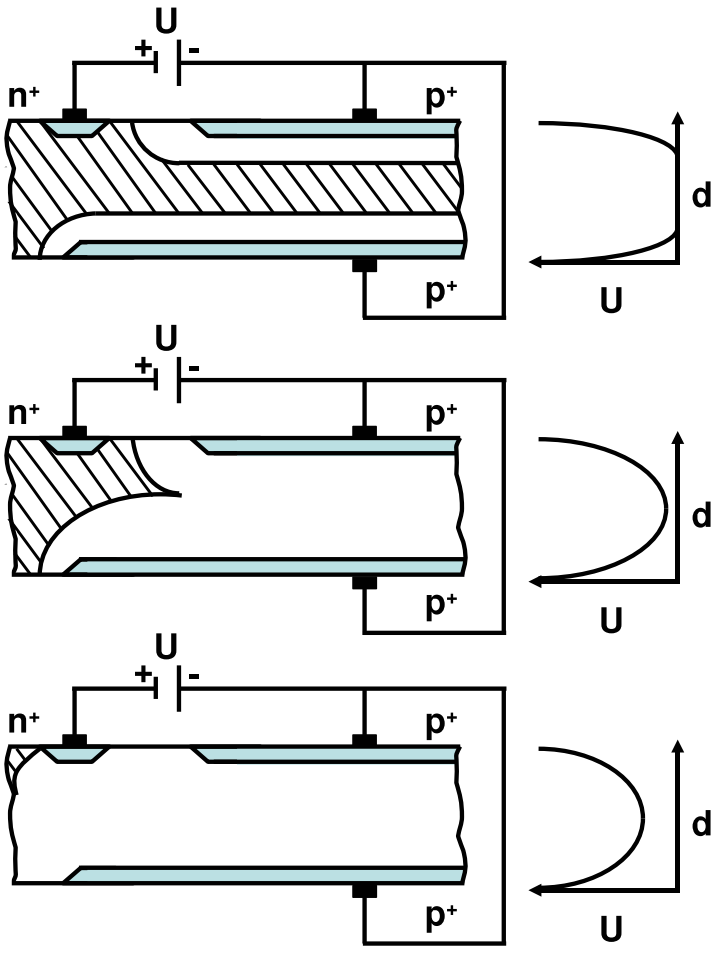

Figure 6.13: Principle of sidewards depletion. The shaded area represents the undepleted n-silicon, while white areas show the depleted n-silicon region. In the uppermost sketch, no reverse voltage is applied, such that only the intrinsic depletion zones are present. The middle image shows full depletion, which starts from both rectifying junctions on the top and bottom surface of the wafer. The lowermost depiction finally shows the state of "overdepletion" for completeness. On the right side, the potential U is shown for the different situations depending on the position d in the wafer (see also Ref. [143]).

[11] The energy range considered with the CAST experiment reaches from 1-7 keV.

basic principle used is sideward depletion, which means the removal of mobile charge carriers as described in the following.
An n-type silicon wafer can be depleted via a small n^+-ohmic contact, which is positively biased relative to the p^+-implants located on both sides of the wafer. As shown in Fig. 6.13, an expansion of the depletion region from both rectifying junctions at the same time can be observed, given that the ohmic connection from the n^+-readout anode to the whole (non-depleted) bulk is not interrupted. The two separated depletion zones get into contact at a specific voltage causing the previously existent electron channel in the middle of the substrate between the p^+-implants to disappear. This completes the depletion at a voltage which is about a forth of the one needed to fully deplete a diode of the same thickness. As can also be seen in Fig. 6.13, the electron potential has a parabolic shape in a plane perpendicular to the wafer, and the minimum of the potential can be found in the middle of the wafer. Shifting this minimum towards either surface can be accomplished by simply applying different voltages to the p^+-contacts on different sides. The advantages of this scheme, namely the possibility to determine the position of the potential minimum externally and the capability for low noise performance given by a small capacitance of the n^+-contact, are used to operate fully depleted pn-CCDs.
A basic scheme of such a detector is shown in Fig. 6.14, where due to a negatively biased p^+-contact on the backside in reference to the top electrodes, shifts the minimum of the electron potential towards the upper surface.

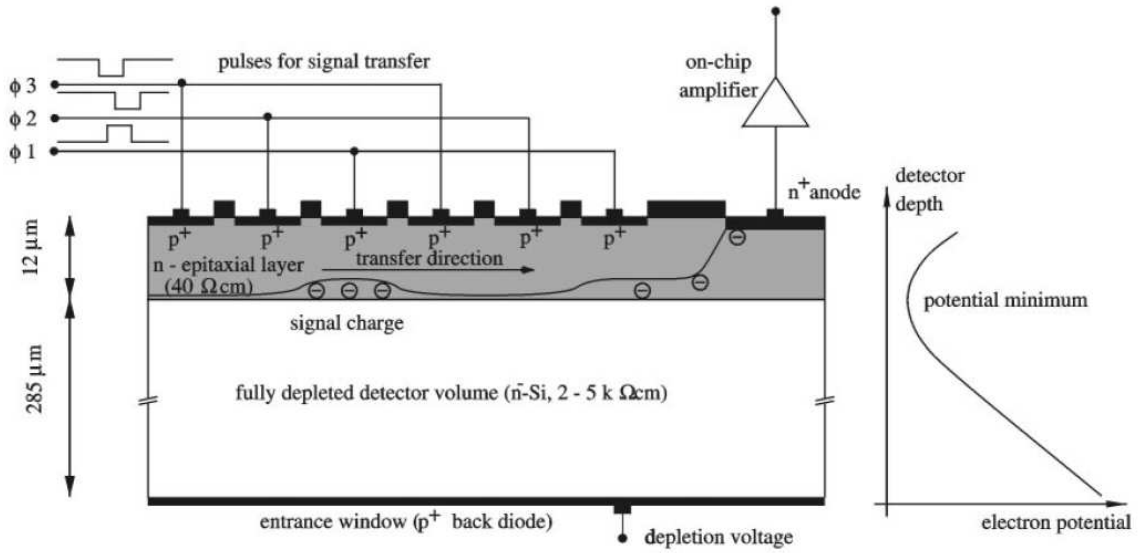

Figure 6.14: Schematic view of the cross section through a pn-CCD. The cut is along the transfer channel. The device is illuminated from the bottom (backside) and fully depleted over about 300 μm [143].

By choosing the voltages of the p^+-transfer registers Φ_1, Φ_2 and Φ_3 adequately, local potential minima for electrons in a distance of about 10 μm from the surface can be formed, such that the just mentioned three shift registers cover together one pixel. By changing the applied voltages with time, charges in the potential minimum can be shifted towards the n^+-readout anode. This

operation is demonstrated in Fig. 6.15. The size of a pixel is here 150×150 μm^2 and the p$^+$-back contact is not shown.

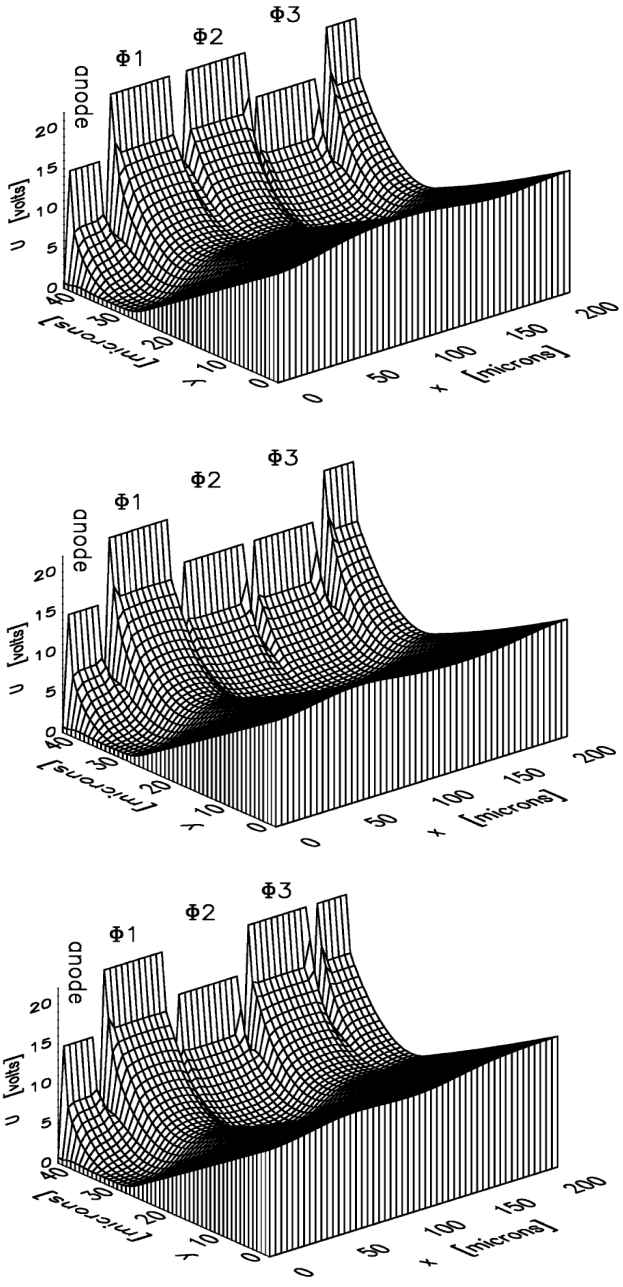

Figure 6.15: Working principle of the charge transport in the shift registers Φ_1, Φ_2 and Φ_3. At $t = 0$, the charge is stored in Φ_3 (top). For a short time, the signal charge is then kept in Φ_2 and Φ_3 together by adjusting Φ_2 accordingly (middle). Finally, the transfer to Φ_2 is completed (bottom). As can be seen from the x-axis, the charge has been transported over 50 μm. This corresponds to a third of a pixel [143].

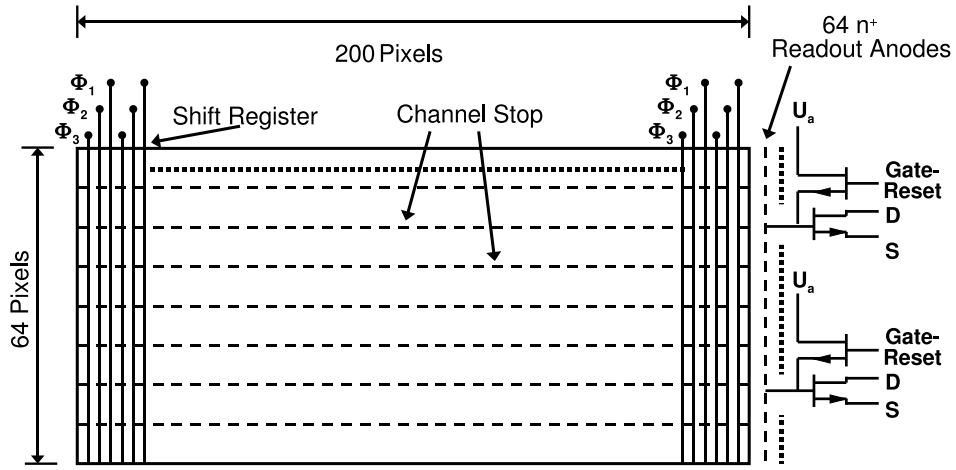

Figure 6.16: Pn-CCD subunit of 64 pixels width (about 1 cm) and 200 pixels length (roughly 3 cm). On the chip, 64 preamplifiers are included as indicated in the schematic [143]. The channel stops, which are narrow gaps between the single strips can be seen along with the shift registers used to transport the collected charge towards the readout.

To obtain the pixel structure, the doping is increased in the surface zone with channel guides, i.e. strips being perpendicular to the gate direction. Narrow gaps between the strips are referred to as channel stops (see Fig. 6.16). The doped zones produce space charge regions acting as potential barriers for the electrons, and thus, the charges are constrained in all directions.

Integrated Electronics and Readout

In Fig. 6.16, the basic readout principle of the pn-CCD is shown schematically. The chip consists of 200 pixels in the direction of the signal transfer (lines) and 64 pixels perpendicular to the transfer direction (columns). The usual serial multiplexing CCD register has been substituted by 64 parallel output anodes. Each anode signal is preamplified directly on the chip via a JFET[12] source follower. The 64 identical JFET-preamplified CCD channels are bonded to a 64-channel CMOS[13] amplifier chip, the CAMEX64[14], which amplifies, shapes, samples and multiplexes in parallel all 64 analogue input signals. The electronics of one of these channels are shown in Fig. 6.17. They consist of two charge sensitive amplifiers, which are both succeeded by a source follower each, and a fourfold capacitive coupling between the amplifiers. The main steps displayed are

1. Input: JFET on CCD chip biased with JFET current source on CAMEX64

2. Voltage amplification: Amplification as ratio of coupling capacitor to feed-back capacitor.

3. Shaping: Capacitor limits high frequency bandwidth

[12] Junction Field Effect Transitor
[13] Complementary Metal Oxide Semiconductor
[14] CMOS Amplifier and MultiplEXer chip, formerly: CMOS Analog MultiplEXing readout chip

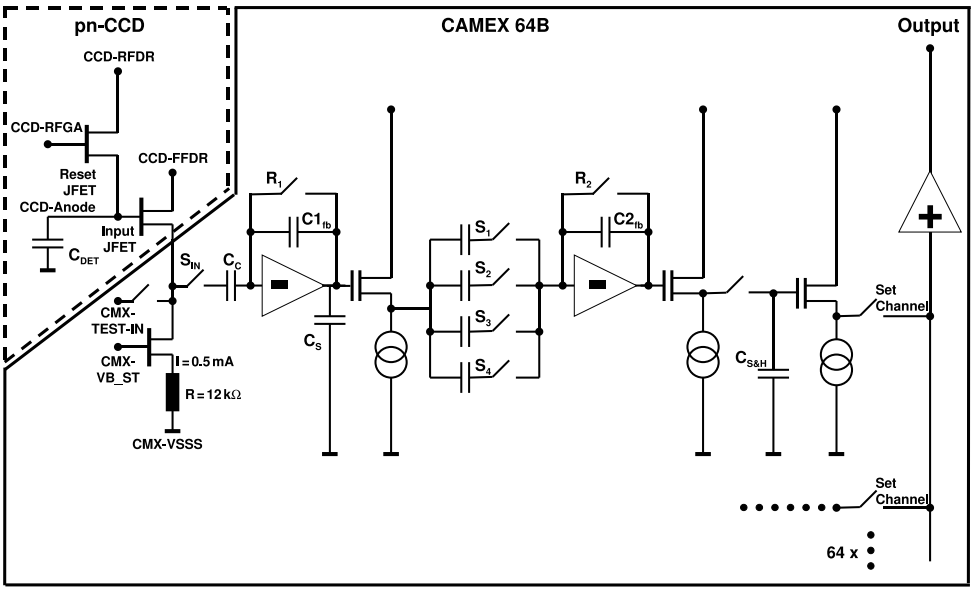

Figure 6.17: Readout schematics of the pn-CCD and the CAMEX64. The sensitive area of the CCD and its on-chip electronics are shown in the upper left part of the schematics. For the CAMEX64, one of the 64 identical readout channels is depicted in detail.

4. Sampling: Four capacitors and switches take samples before and after signal passed in order to suppress noise

5. Sample-and-Hold/ Multiplexing: Former data are multiplexed to output while new data are read in parallel.

The signals are then given by the multiplexer to an Analog-to-Digital Converter (ADC) and like this, readout and digitalization can be done in parallel for the 64 channels.
Using the full sensitive area, a total readout time of ≈ 70 ms is needed. The time control of the CAMEX switches is done by a digital control unit, the TIMEX[15] chip. Further details can be found in Refs. [143, 146, 147].

Properties of the CCD Signal

The properties of the pn-CCD detector signal play a crucial role in understanding the data taken with this device. For this reason, the most important characteristics of the CCD will be shortly discussed covering offset and noise as well as partial, pile-up, split and out-of-time events. Furthermore, other aspects are important to be considered, such as bad pixels and the charge transfer efficiency (CTE).

Offset The physical offset of the CCD detector is the so-called dark current. Even if the chip is not illuminated, there is still a small signal observable, which is the dark current. It is extremely

[15] TIme MultiplEXer

affected by the chip temperature. At room temperature enough thermally generated electrons can be produced in both the extended depletion region and the silicon bulk to fill up the pixels. Further contributions to the offset can result from the on-chip electronics, the CAMEX chip and the rest of the readout electronics. By cooling the chip to $\approx -130°\mathrm{C}$, the dark current is minimized.

Common Mode Due to the fact that the supply voltage of the First-FETs is slightly varying with time, the value of every pixel in a line is shifted by a constant value when leaving the CAMEX. Since always all pixels of a complete line are treated simultaneously by the First-FETs, the effect is the same for each whole line. It is referred to as Common Mode (CM) and contributes to the overall energy resolution.

Noise The noise of a CCD detector has mainly two different origins and can thus be separated into detector intrinsic noise and electronic noise.
The noise contribution of the single CCD pixels, which makes up for the intrinsic noise, results from impurities of the detector material or leaks. A quantitative description is provided by the Fano factor F, as discussed in Eq. 6.9, limiting the energy resolution ΔE due to intrinsic noise to

$$\Delta E_{\mathrm{Fano}} = 2.35\sqrt{F \cdot \frac{E'}{E}}, \tag{6.10}$$

where the factor 2.35 relates the standard deviation of a Gaussian to its FWHM. For silicon $F \approx 0.12$ and the mean energy to create an electron-hole pair is $E' = 3.65$ eV. Thus the intrinsic Fano noise for a typical absorbed energy of Mn-K$_\alpha$ (5.9 keV) limits the energy resolution to about 2% or 120 eV at this energy.
The main components of the electronic noise are thermal noise, noise originating from the leakage current of the readout anode and low frequency noise. The first contribution results from thermal fluctuations of electrons, even with no external power applied. The leakage current noise originates from currents flowing to the electronics. The largest share to the electronic noise is produced by the CAMEX readout chip. Amplifiers and ADCs contribute to the low frequency noise. By cooling the detector, the noise can be reduced, however not completely removed, since it is basically random.

Energy Resolution An estimation of the overall energy resolution can be derived by considering all noise contributions, i.e. intrinsic and the electronic noise, as well as the share of offset and common mode. Therefore, the total energy resolution can be estimated as

$$\begin{aligned} \Delta E_{\mathrm{Total}} &= \sqrt{\Delta E^2_{\mathrm{Noise}} + \Delta E^2_{\mathrm{Offset}} + \Delta E^2_{\mathrm{CM}}} \\ &= \sqrt{\Delta E^2_{\mathrm{Fano}} + \Delta E^2_{\mathrm{CAMEX}} + \Delta E^2_{\mathrm{ADC}} + \Delta E^2_{\mathrm{Offset}} + \Delta E^2_{\mathrm{CM}}}\,, \end{aligned} \tag{6.11}$$

which corresponds to 170-180 eV at typical energies in the keV range and is within acceptable limits. A more detailed discussion of the noise and its estimation can be found in Refs. [148, 149].

Table 6.2: Percentages of split events for a pixel size of 150×150 μm^2.

Event Type	**Percentage**
Single Events	$\approx 80\%$
Double Events	$\approx 19\%$
Triple and Quadruple Events	$\approx 1\%$

Partial Events If an incident photon interacts with the detector material in the dead zone close to the surface, part of the generated charge is able to recombine, before the pixel layer is reached. Such an event is referred to as a partial event and it is most likely to appear for low photon energies between 100 eV to 500 eV. The amount of partial events is strongly dependent on energy. They can be described by the so-called charge collection efficiency (CCE), which is the ratio of deposited electrons N as a function of absorption depth x and the number of generated electrons N_g by the incident photon

$$CCE(x) = \frac{N(x)}{N_g}. \tag{6.12}$$

Partial events are an effect on the percent level, and since this process is known, it can on average be modelled and taken into account.

Pile-Up Events If more than one photon hit the same pixel during a single integration cycle, they are registered as one count with an energy corresponding to the sum of the two photon energies. Such events are called pile-ups and can be reduced by shortening the accumulation period. Furthermore, models to describe pile-up events can be used to estimate the percentage of this type of events.

Split Events Split events appear due to the fact that the charge cloud composed of photon-generated electrons spreads when propagating through the drift region towards the pixel plane. The dispersion of charge happens as a result of diffusion or coulomb repulsion. As a result, the extended charge cloud can hit one or more pixels. The different possible signal patterns are illustrated in Fig. 6.18. If only one pixel is hit, a single event is detected, while if the charges are within the reach of two pixels' potential minima and they are split between both pixels, it is referred to as a double event. Analogously three and four hit pixels form triple and quadruple events, respectively. The fraction of different split events depends only on the pixel size and the radius of the charge distribution. Thus, for a given size of the charge cloud, which depends on the energy of the initial photon, the probability for single and other events can be approximatively determined from the ratio of the areas sensitive for split events to the overall area of one pixel. In general, the splitting ratio is energy dependent and strongly related to the geometry of the drift field within a pixel. A typical distribution for a pixel size of 150×150 μm^2 can however be determined as shown in Tab. 6.2, demonstrating that single events are the most common type.

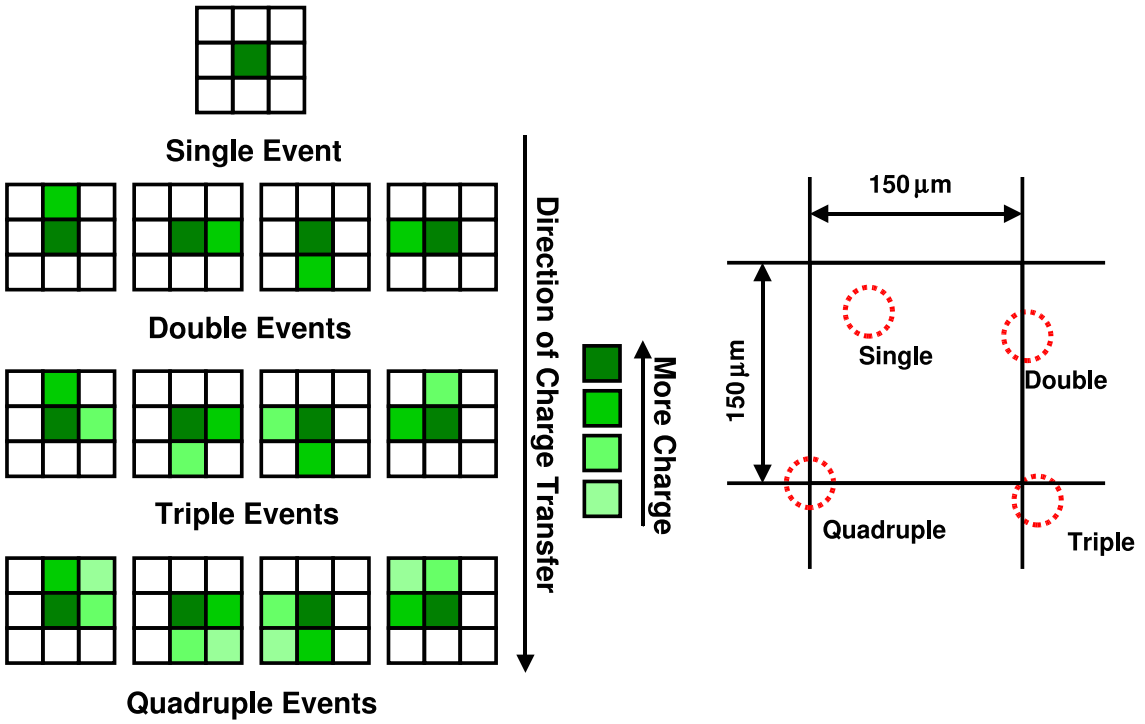

Figure 6.18: Left: Possible signal patterns of split events in the pn-CCD. Due to the extended charge cloud, up to 4 pixels can be hit resulting in single, double, triple and quadruple events. Darker color indicates more deposited charge in a pixel. Right: Schematic of one pixel of the CCD chip illustrating the different possible pattern types.

Out-of-Time Events Since the CCD detector has no physical dead time and stays sensitive also during readout, it might happen that a photon hits the detector, while the charges are shifted out. This means that the incident photon is detected, but it will be tagged with a wrong line number. Such events are called Out-of-Time events (OOT-events). Due to the shift of charges along a column, these events are spread over each readout channel. The fraction of OOT-events f_{OOT} can be calculated as the ratio of the readout time t_{read} and the integration time t_{int}

$$f_{\mathrm{OOT}} = \frac{t_{\mathrm{read}}}{t_{\mathrm{int}}} = \frac{t_{\mathrm{read}}}{t_{\mathrm{cycle}} - t_{\mathrm{read}}}, \tag{6.13}$$

where the time of a full cycle (integration and readout) is $t_{\mathrm{cycle}} = 71.77$ ms and $t_{\mathrm{read}} = 6.06$ ms for all 200 lines. Thus, for an ideal point source, a fraction of OOT-events of 9.2% is found. For a potential axion signal area of 11.5 pixel radius, this fraction f_{OOT} is obtained as 8.1%.

Bad Pixels Pixel defects can cause faulty signals. In general, one classifies bad pixels in dead pixels, hot pixels, and stuck pixels. While a dead pixel is always off, defects which are hot or stuck are pixels with higher noise than average. Hot pixels just appear if the exposure time is long enough, stuck pixels are present in all images. Any pixel defect might originate from the manufacturing process, but temperature effects can worsen the situation. However, the position of

bad pixels is fixed, such that they can be eliminated from the raw data and pose no further problem for the analysis.

Charge Transfer Efficiency When the electrons are transferred from line to line, charges can be lost for various reasons. The charge transfer efficiency (CTE) describes this behaviour. For the transfer of the charge q from line $j+1$ to line j, the CTE can be defined as

$$\mathrm{CTE} = \frac{q_{j+1}}{q_j}, \tag{6.14}$$

such that the charge that reaches the readout anode q_a, when a charge q_j was generated in line j and shifted over the chip is

$$q_a = q_j \cdot \mathrm{CTE}^j. \tag{6.15}$$

Reasons for a CTE smaller than 1 (generally around 0.9996) are for example impurity atoms in the semiconductor, which act as trapping center.

6.2.2 The XMM-Newton pn-CCD at CAST

Detector Design and Characteristics

The focal-plane detector used at CAST together with the X-ray optics is a fully depleted EPIC[16] pn-CCD of the type which has been sucessfully operated on-board the ESA[17] X-ray satellite XMM-Newton [143] for more than 8 years up to now. The key benefits of this detector are its extended depletion region of 280 μm and its extremely thin and homogeneous entrance window of 20 nm, located on the backside of the chip. The thin window makes it possible to achieve a quantum efficiency of $\gtrsim 95\%$ in the photon energy range of 1 to 7 keV, which is the interesting region for the axion search with the CAST experiment.
The full chip provides a sensitive area of 2.88 cm^2. This area is divided into 200×64 pixels. Each pixel covers an area of 150×150 μm^2, which corresponds to an angular resolution of 19.3×19.3 arcsec^2/pixel, if the focal length of the X-ray optics (1600 mm) is taken into account. Therefore, the sensitve area of the CCD chip is larger than the solar core ($\approx 0.2\ R_\odot$), from which most axions are expected to come[18].
In order to obtain an optimal performance, the pn-CCD chip at CAST is operated at a temperature of -130°C. A Stirling cooler system is used to guarantee stable conditions. Flexible copper leads thermally couple the cold finger of the Stirling cooler to the gold-plated cooling mask of the chip (see Fig. 6.19). The detector is installed in a vacuum vessel made of aluminum and it has a passive shielding of copper and lead to reduce external γ-ray background. In Fig. 6.20, the detector in its housing without (left image) and with (right image) copper shield is shown. In order to protect both, CCD chip and X-ray mirror optics from possible contamination, the whole system is operated in vacuum. It is possible to pump the vessel containing the CCD chip and the X-ray optics independently. Furthermore, the different parts of the system, such as for example pumps, can be

[16] European Photon Imaging Camera

[17] European Space Agency

[18] A spot on the chip of 23 pixels diameter corresponds to the solar core and contains 82.6% of the total expected solar axion flux.

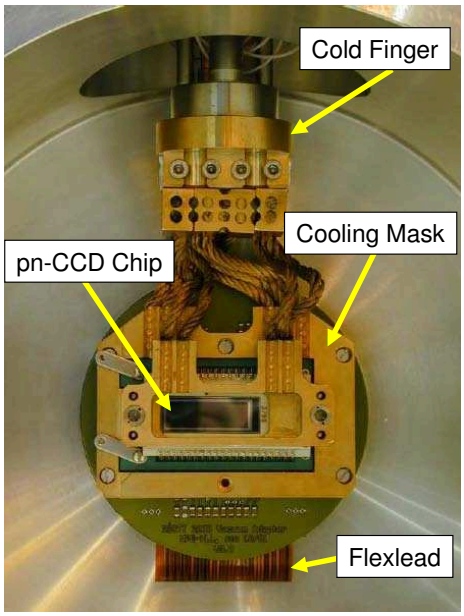

Figure 6.19: CCD chip with gold-plated cooling mask. The mask is thermally coupled to the cold finger of a Stirling cooler via flexible copper leads [141].

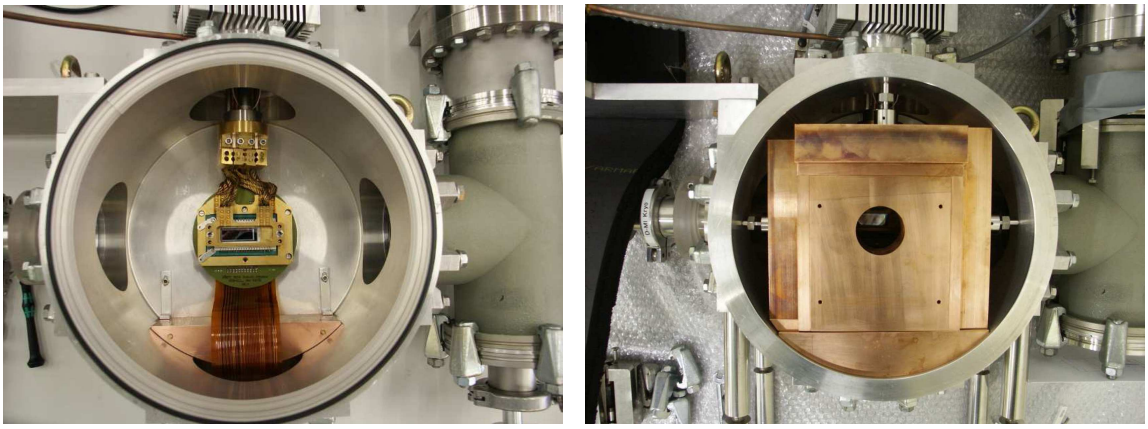

Figure 6.20: Left: Front-view of the pn-CCD detector installed at the CAST experiment in its aluminum vacuum vessel with vacuum components connected on the right hand side. Right: The CAST pn-CCD with inner shielding consisting of 2 cm low-activity, oxygen-free copper and 2.2 cm ancient lead. The additional 2.5 cm lead outside the vacuum vessel are not present in the picture [141].

separated from the rest of the setup for repair works. In order to protect the X-ray telescope in case of a quench, additional valves exist that can close off the system from the cold bore of the CAST magnet. A schematic of the telescope vacuum system is shown in Fig. 6.21 and displays all important components.

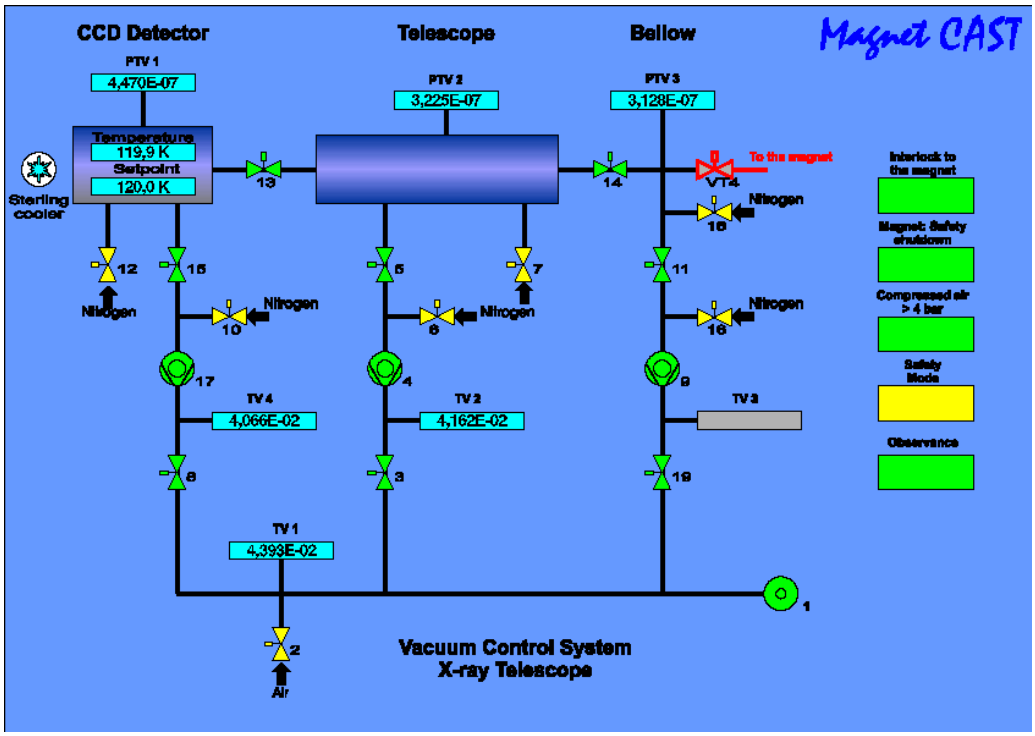

Figure 6.21: Schematic representation of the vacuum system for the X-ray telescope. The roughing pump is labeled 1, while the turbo pumps are numbered 4, 9 and 17. Green color signifies a running pump or an open valve. Yellow indicates for a pump that it is stopped and for a valve that it is closed. The valves labeled as either air or nitrogen can be used to vent the detector.

Quantum Efficiency

The quantum efficiency (QE) of a photo-sensitive device, like a CCD, is the percentage of incoming photons that actually produce an electron-hole pair in the sensitive region and can thus be detected. It is therefore a measure for the sensitivity of the detector to photons. Determining factors for the QE are characteristic features of the used material as well as the production process to manufacture the detector. For the EPIC pn-CCD used in the XMM-Newton mission, the QE has been measured at synchrotron radiation facilities in Berlin and Orsay in reference to a calibrated solid state detector.
In Fig. 6.22, the QE as measured for the fully depleted pn-CCD of the EPIC camera is shown [143]. At an energy of 0.525 keV, the QE drops due to absorption losses at the oxygen edge in the SiO_2 layers on the detector surface, which are meant to passivate the material (see also Fig. 6.12). The inserted picture in Fig. 6.22 shows the typical X-ray absorption fine structure (XAFS) in the region of the Si-K edge at 1.84 keV. The solid line represents a detector model fit obtained by using photo absorption coefficients given by atomic data tables. It can be seen that the QE is higher than 90% in the whole energy range between 0.3 keV and about 10 keV. More details concering the QE can be found in Ref. [150].

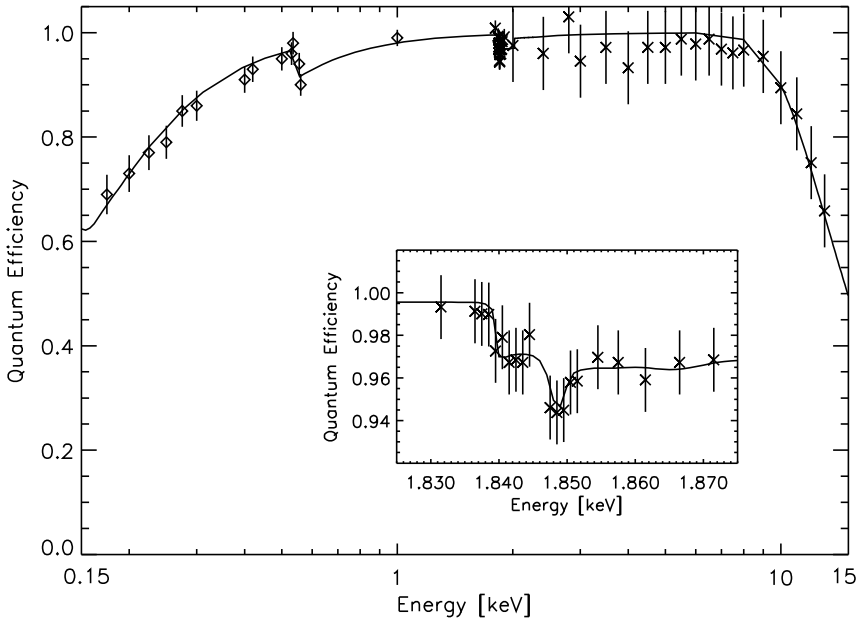

Figure 6.22: Quantum efficiency of the pn-CCD as determined for the EPIC camera onboard XMM-Newton as a function of incident photon energy. Dips in the QE around the oxygen edge (0.525 keV) of SiO_2 and the silicon K-edge (1.84 keV) are apparent. The line represents a detector model for a sensitive volume of 300 μm thickness, which has been fit to the data [143].

Combined Efficiency of X-Ray Mirror Optics and CCD Detector

Knowing the quantum efficiency of the CCD detector, it is possible to obtain the total efficiency for the different stages of the CAST experiment, by combining the efficiency of the X-ray mirror optics, which has been treated in detail in Section 6.1.2, with the QE of the semiconductor device. Considering the total efficiency of the X-ray telescope together with the CCD detector all three data taking periods differ. While the efficiencies for 2003 and 2004 only differ due to the tilt of the telescope, in Phase II the transmission of the cold windows has to be considered in addition to the tilt during the 2004 run. The cold windows were introduced to constrain the ^{4}He within the magnetic field region. They are made of 15 μm polypropylene (PP) mounted on a strongback. This support structure causes a loss of 12.6% in addition to the PP foil as determined at PANTER [151]. In Fig. 6.23, the different efficiencies are shown including the one used for the analysis of the ^{4}He data of Phase II (black line), which varies between about 20% and 30% in the displayed energy range of 1-7 keV.

Calibration and Energy Resolution

Before the detector was installed at CAST, the gain was determined at the X-ray facility PUMA in Munich using an X-ray fluorescence generator. Hereby, X-rays can be directed on different materials in order to determine the factor connecting the detected charges from obtained electrons in the CCD detector and the analog-digital unit (ADU) as given in the readout. In Fig. 6.24, the results

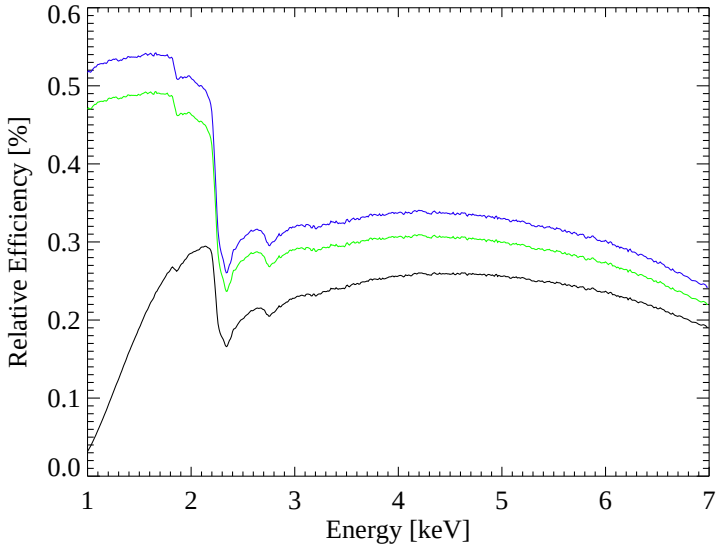

Figure 6.23: Total relative efficiency as used for the analysis of the Phase I and II data taking into account the efficiency of the telescope as well as the quantum efficiency of the CCD detector. The total efficiency for 2004 (green) differs from the one for 2003 (blue) due to the tilt of the telescope. For Phase II (black), the telescope position remained unchanged, but additional windows were installed to keep the helium inside the magnet pipes, lowering the efficiency to values between 20 to 30%.

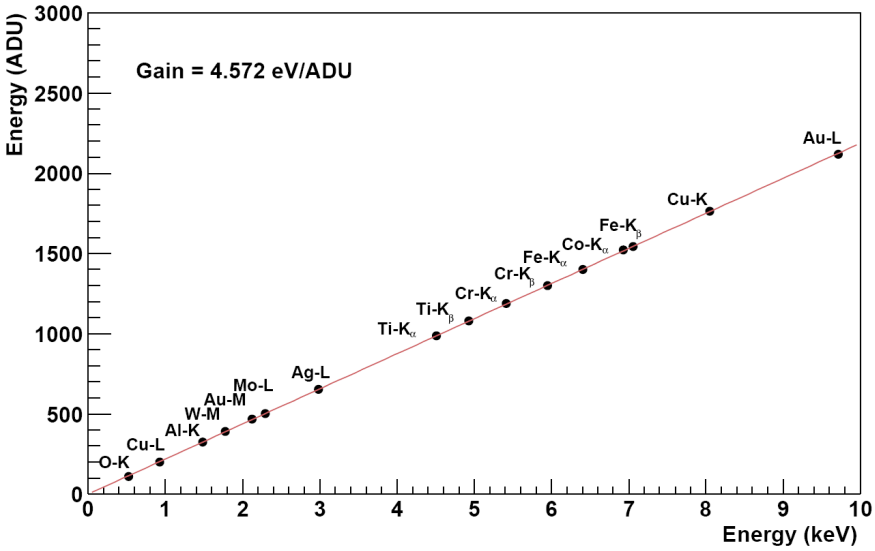

Figure 6.24: Gain calibration of the CCD detector at the PUMA test facility in Munich. The points represent the measurements and the line is a linear fit to the data [133].

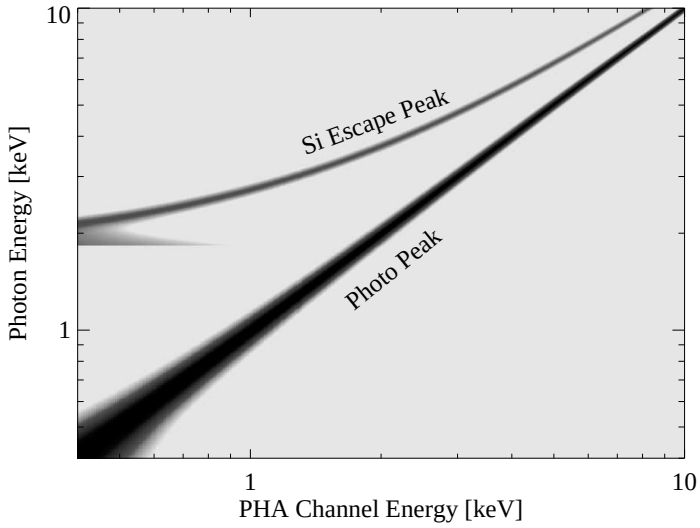

Figure 6.25: Response matrix of the pn-CCD used at CAST displayed in logarithmic grey scale. The contributions of the photon peak and the silicon escape peak can be seen. The finite energy resolution is reflected in the width of the distribution. Second order effects have been neglected [132].

of these measurements are displayed. The gain was determined as 4.6 eV/ADU and it can be seen that it is linear over the full considered energy range of 0.2 to 10 keV.
In order to determine the energy calibration and the detector response on-site at the CAST experiment, a multi-target X-ray tube has been used. The incident binned differential photon spectrum is observed as a (binned) pulse height spectrum given by a pulse height analyser (PHA). As a consequence, the observed spectrum is a convolution of the incident spectrum and a function characterizing the detector features. The detector redistribution matrix R_{ij} provides the probability that an incident photon of energy E_i is detected as a photon of energy E_j. This together with the effective area of the detector leads to the function in question.
In Fig. 6.25, the modeled detector response matrix is shown. Included in the redistribution function are the photo peak and the silicon escape peak[19] as well as the finite energy resolution of the detector. Other effects, such as partial events have not been taken into account, since they are not important for the given situation at CAST.
In addition to this, there is the possibility to test the long-term stability of the energy calibration by using an ^{55}Fe source (see Fig. 6.26) together with several X-ray fluorescent lines in the background spectrum, which can be used to extend the calibration range to energies larger than 10 keV, i.e. energies which were out of range for the X-ray tube. Thus, a conversion of incident photon energy to detector channel can be derived for the energy range from 0.5 to 10 keV by fitting a polynomial to the data [132, 152].
In Fig. 6.27, the energy resolution of the pn-CCD is displayed. Not only does it depend on the

[19] If a photon is absorbed in the silicon of the detector, it generates an electron-hole pair. The hole in the inner shell can be filled by an electron from an outer shell resulting in an emitted photon. If this photon escapes the detector, then its energy is missing and a signal (silicon escape peak) is registered at the diminished energy of $E_{\mathrm{SiEscape}} = E_{\mathrm{Mn-K}_\alpha} - E_{\mathrm{Si-K}_\alpha} \approx 4.15$ keV, i.e. 1.74 keV below the photo peak.

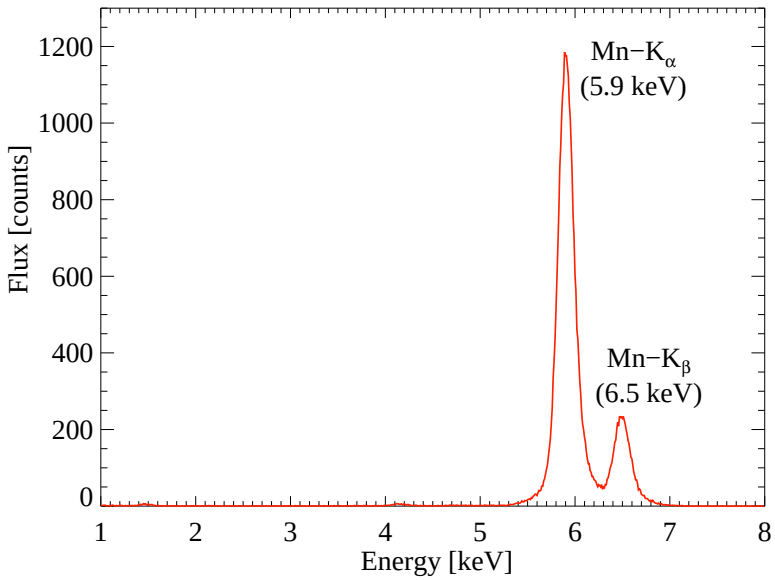

Figure 6.26: Typical calibration spectrum of an ^{55}Fe source for the CCD detector at CAST with an energy resolution of ≈ 170 eV at 5.9 keV. Both, the Mn-K$_\alpha$ and the Mn-K$_\beta$ peaks are apparent.

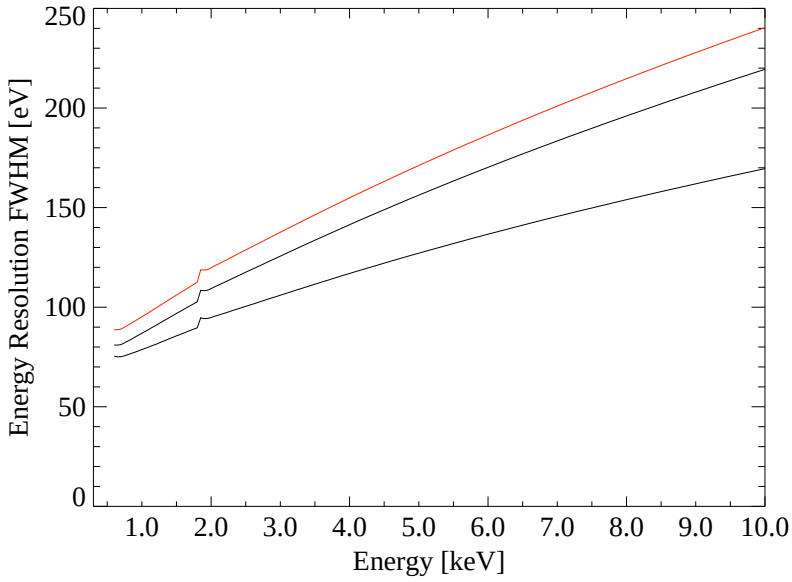

Figure 6.27: Energy resolution of the pn-CCD detector depending on incident photon energy. The lowest curve corresponds to the energy resolution for single events in the EPIC pn-CCD, while the middle line represents double events of the same detector. The uppermost line is the CAST in-situ energy resolution for the combination of single and double events [132].

energy of the incident photon, but also on the type of the split event. These split event patterns have been discussed in Section 6.2.1. For the incident photon energy dependence, the detector response model of the EPIC pn-CCD on-board XMM-Newton has been adopted [153]. Not only is the energy resolution for single and double events of the EPIC pn-CCD shown but also the resulting CAST resolution for combining single and double events. Due to the relatively high noise in the experimental area, the CAST detector resolution is slightly worse than the one obtained for XMM-Newton.
Combining all performed calibration procedures provides an absolute energy calibration of better than 1%.

6.3 The Alignment of the X-ray Telescope

The alignment of the X-ray mirror optics and the pn-CCD detector are critical factors in order to optimize the telescope performance. Therefore, two different methods are used to assure that the telescope is aligned parallel to the magnet axis with an accuracy of better than 40 arcsec. Furthermore, it is possible to monitor the long term stability of this alignment. For the first purpose, a laser system providing a parallel beam is installed on the magnet end opposite to the CCD detector, i.e. instead of the normally installed TPC. The laser is aligned by the surveyors with the theoretical magnet axis and the light can thus be shone through the entire setup. The focal image of the parallel laser beam can be observed on the CCD detector and it can be used to determine the center of the expected axion signal spot. The second method to align, verify and furthermore constantly monitor the telescope alignment is the use of a pyroelectric X-ray source installed between the TPC detector and the magnet. The experimental setup which is used during an alignment is shown in Fig. 6.28, where the mentioned X-ray source is labeled X-ray finger. Laser and X-ray finger alignments have been repeatedly performed before, during and after CAST data taking periods. Since the thesis at hand is concerned with the analysis of the ^{4}He data obtained during CAST's Phase II, the focus will be put on the telescope alignment for this second phase.

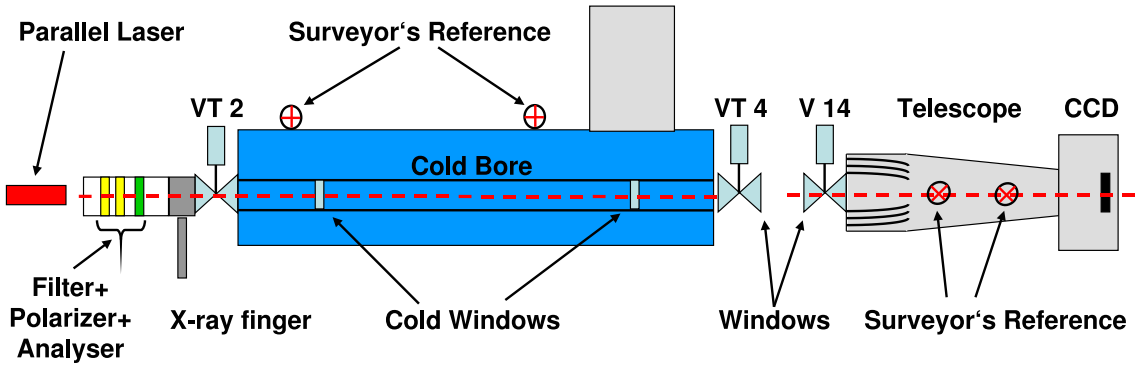

Figure 6.28: Schematic of the experimental setup for laser and X-ray finger alignment of the X-ray telescope. In order to use the laser, the TPC detector has to be dismounted, while X-ray finger measurements can be also performed during normal data taking periods.

6.3.1 Laser Alignment

The laser alignment for CAST's second phase was performed before the data taking period, namely in November 2005, and verified in August 2007 after the completion of CAST's ^{4}He phase. An exemplary image of the parallel laser beam on the CCD chip is shown in the left part of Fig. 6.29. The size of the expected axion signal region containing the image of the inner 20% of the solar radius is indicated by the a white circle.
The procedure to align the laser with the magnet axis for Phase II has been the same as during Phase I of the experiment [154]. The final result of the alignment is visualized in Fig. 6.30 together

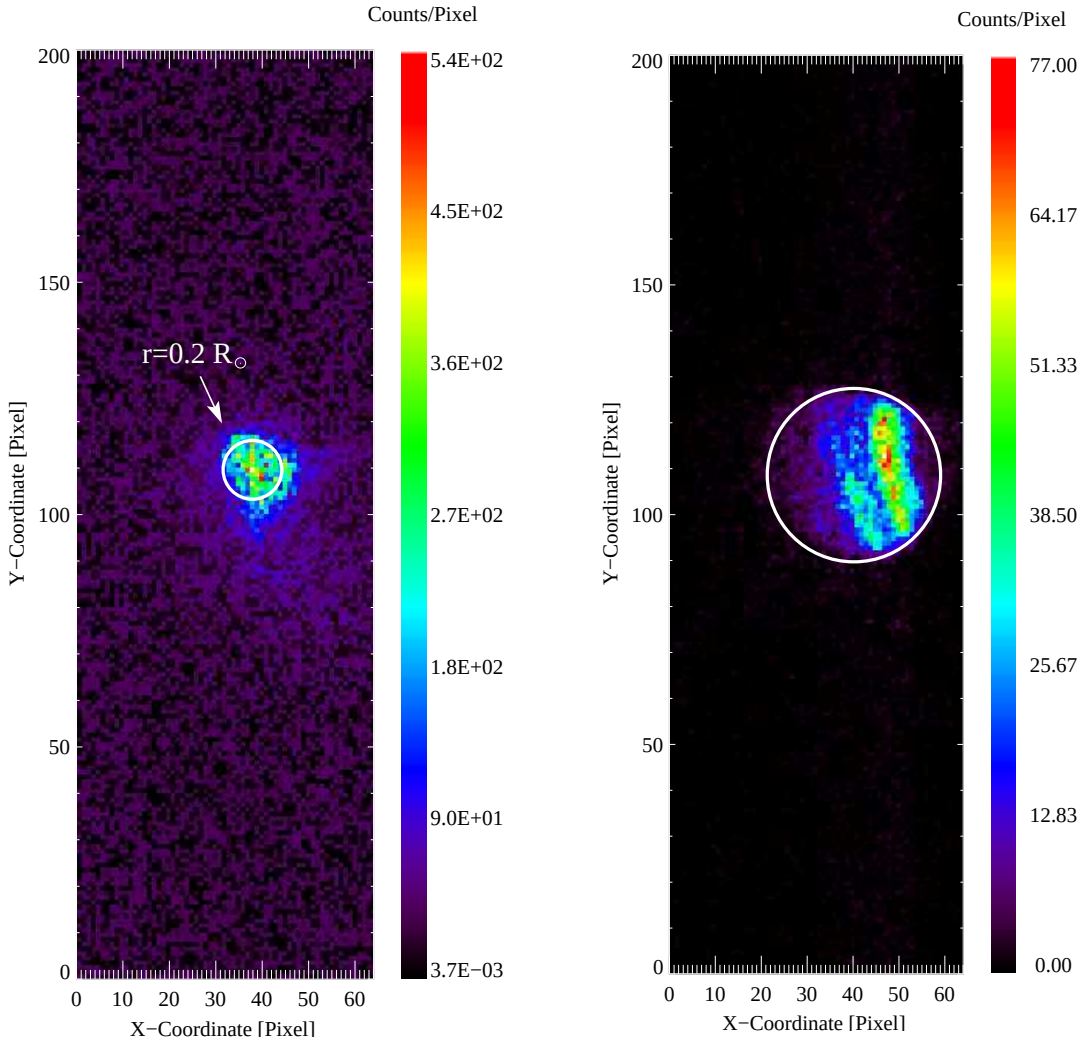

Figure 6.29: Left: Focal plane intensity image of the parallel laser. This image can be used to define the center of the circular region in which the axion image from the solar core ($r = 0.2\ R_\odot$) is expected. Right: Intensity distribution of the 70 MBq X-ray source. Here, the white circle corresponds to the projection of the magnet bore on the focal plane of the telescope. The center of laser and X-ray spot have to coincide [132].

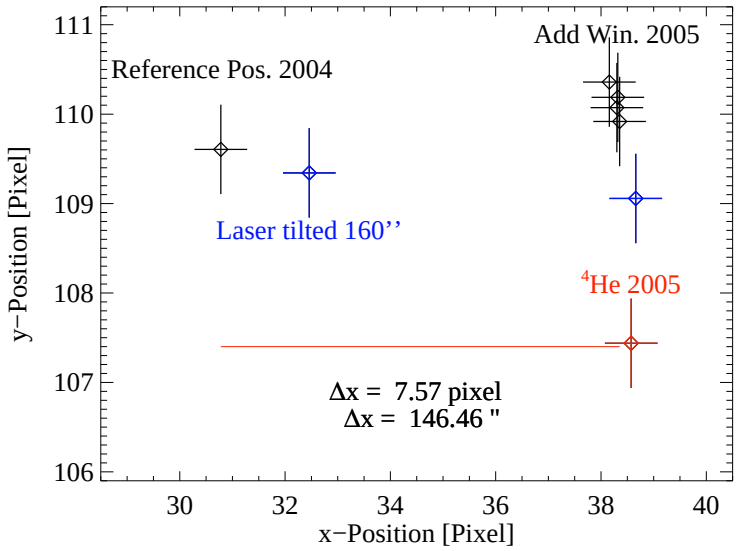

Figure 6.30: Results of the laser alignment in 2004 and 2005. The reference position of 2004 is shown in black. It has been taken with an incorrect alignment. The influence of the helium in the cold bore is reflected in the position of the red symbol, while the effect of an additional window is shown by the black symbols in the upper right part of the plot. The blue symbols show that by tilting the correctly aligned laser in 2005, one can reproduce the 2004 position [154]. The red line is meant to indicate the difference in x-direction between the measurements in 2004 and 2005.

with the results of a previous alignment and the outcome of several performed tests, which will be discussed in the following. These checks were meant especially to study the influence of ^{4}He gas inside the magnet and the effect of the newly added cold windows on the position of the laser spot on the CCD chip. Moreover, different laser intensities were tested.

For the first investigation in 2005, laser images with ^{4}He in the cold bore were acquired. Since some effects, which are still under investigation[20], could be observed when gas was filled inside the magnet bore, all laser alignment measurements have then been performed without gas inside the cold bore. The spot position with gas in the cold bore is shown in red in Fig. 6.30.

Furthermore, the effect of the cold windows on the laser beam have been studied by introducing a third cold window in the optical path. The position of the laser spot remained basically unchanged with and without the additional window in place. Furthermore, the spot position turned out to be independent of a rotation and tilt of the extra window, such that no problems for the alignment have to be expected due to the changes in the CAST setup for its second phase (see black points in Fig. 6.30).

An additional test showed that the laser spot is situated in the same region on the CCD chip for different intensities of the laser light as long as the full magnet bore is illuminated.

It is worth remarking that the linear behavior of the X-ray optics was already checked in the alignment of 2004, demonstrating that there is a linear relation between the observed laser spot on the

[20] A change in position of the laser spot could be observed under certain circumstances, which might be due to either refraction in the helium gas, thermo-acoustic oscillations of the gas or a lens effect of wrinkles on the cold windows. Further details can be found in Ref. [154, 155].

CCD chip and the off-axis angle of the laser in vertical and horizontal direction [154].
The biggest achievement of the 2005 alignment was the discovery that former alignments had been performed using an incorrect theoretical magnet axis. While the X-ray spot could be found in the same position for both 2004 and 2005 measurements, the laser spot using the proper alignment in 2005 shifted as compared to former results. Tilting the laser by 160 arcsec made it possible to reproduce the laser position of 2004 as indicated in Fig. 6.30 by the blue points. As a result of the corrected alignment, the agreement between laser and X-ray data, which will be discussed in Section 6.3.3, improved in comparison to earlier alignments. Phase I data thus had to be re-analyzed using the new spot center obtained in 2005.

6.3.2 X-ray Finger Measurements

The 70 MBq pyroelectric X-ray finger, emitting mostly photons of 8 keV, is particularly suitable to monitor the stability of the alignment during data taking periods, since it does not require the removal of a detector, due to its permanent installation. In contrast to a radioactive source, it has the advantage that it is not disturbing any background measurements in neither the TPC nor the CCD detector, since it can be turned off and parked in a hidden position, when idle. For alignment checks, it can be automatically and accurately positioned in the field of view of the telescope. The precision and functionality of this manipulator has been also veryfied, whenever the surveyors aligned the laser. Except for one single occasion in June 2006, when a software problem was encountered, the positioning of the X-ray finger worked completely reliably. The right part of Fig. 6.29 shows a typical image of the X-ray finger on the CCD chip with the white circle indicating the projected size of the magnet bore. The image is larger than the one of the parallel laser beam, since the X-ray finger is located at a finite distance of the X-ray optics. This results in the fact that the photons of 8 keV are focused to a point about 30 cm behind the CCD chip, and thus one observes a larger image. Furthermore, it is apparent from the intensity image in Fig. 6.29 that the distribution is not uniform. This reflects the characteristics of the X-ray emission of the source[21].
The center of the X-rays can be determined by a Gaussian fit or as the center of a circular envelope of the intensity distribution, which is more accurate especially for determination of the x-coordinate of the center. The long term stability is demonstrated in Fig. 6.31, where the barycenter of the X-ray measurements is shown for 2005, 2006 and 2007. As can be seen, the measurements confirm the stability of the spot position of better than about 20 arcsec corresponding to 1 pixel throughout the Phase II data taking period. The overall pointing precision of the CAST magnet is better than 1 arcmin ($\approx 0.017°$), which is sufficient taking into account that the magnet bore allows a field of view of about 16 arcmin ($\approx 0.27°$).
To obtain the center of the expected axion signal region, the results of the X-ray measurements can be correlated with the findings from the laser alignment.

6.3.3 Correlation between X-ray and Laser Spot

In order to correlate the X-ray and laser spot results, the normalized laser intensity distribution projected on the x- and y-axis were overlaid with those for the X-ray spot. Assuming a circular shape of the X-ray spot, its center must coincide with the one of the laser spot. In Fig. 6.32,

[21] The emission strength depends on the angle of the X-ray source with respect to the optical axis.

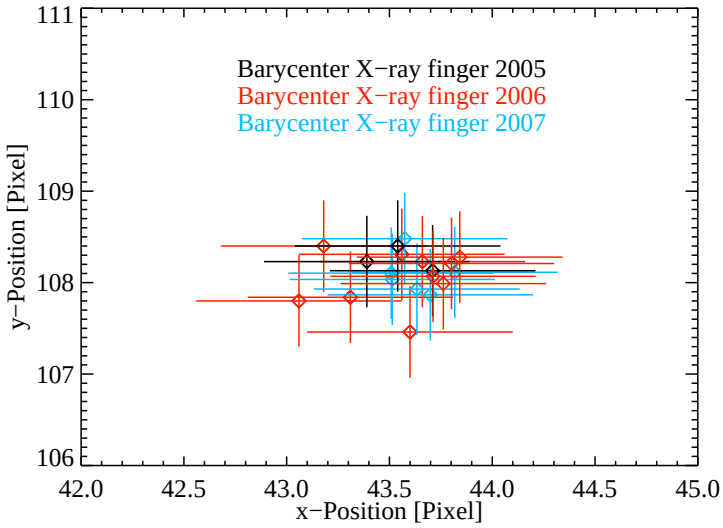

Figure 6.31: Long term stability of the X-ray spot position. The barycenters of each X-ray finger measurement in the alignments taken during 2005-2007 are shown with errors. Note that this method is not suited to determine the spot position in the x-direction. For this the circular envelope method will be used.

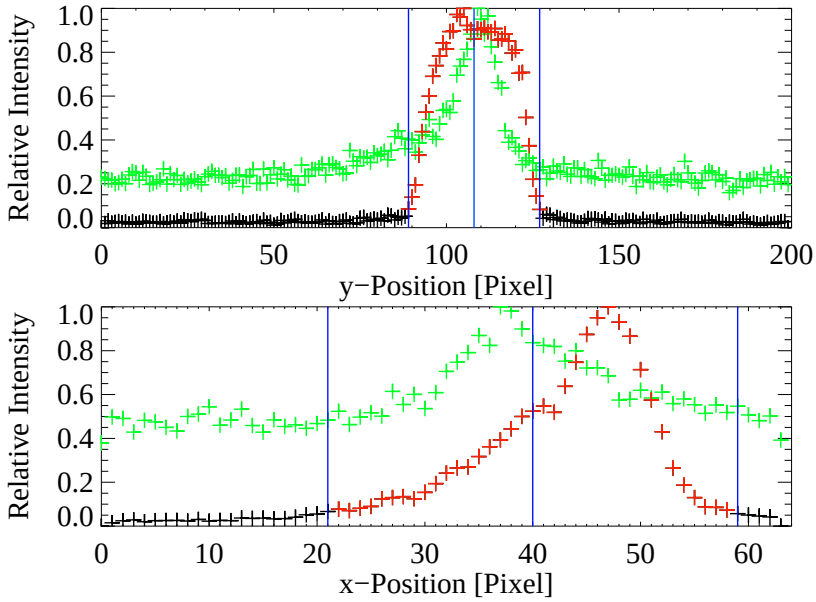

Figure 6.32: Determination of the spot center from laser and X-ray alignment data. For both, x- and y-position, the relative intensity of the laser is shown in green, while the X-ray measurements are displayed in red for intensities higher than 7% of the maximal value and in black otherwise. The outermost blue lines indicate this circular envelope of the Xray spot, and the central blue line shows the determined spot center [154].

this is shown for the 2005 alignment data. The X-ray finger data are displayed as red and black crosses depending on the magnitude of the intensity, while the green symbols represent the laser data. Additionally here, the outermost blue lines mark the circular envelope for the projections of the X-rays, i.e. the coordinate for which the intensity drops below 7% of the maximum, while the center blue line indicates the determined center of the axion signal region. As a result from this, a spot center of $x = 40$ pixels and $y = 108$ pixels was determined and is used in the analysis of the CCD data for ^{4}He in Phase II.

6.4 Background Simulations and Measurements

Since CAST is looking for rare events without having the advantage of being located in a low-background underground laboratory, reduction and detailed understanding of the background are a crucial issue in order to optimize the sensitivity of the experiment and its detectors. Generally speaking, there are different approaches to lower the background originating from cosmic rays and gamma rays as well as radioactive (*non-radiopure*) components inside the detector or the magnet. The first aspect is to choose radiopure materials to build and surround the detector. Furthermore, active and passive shielding can be implemented in the setup. Also a minimization of the active detector volume by using a focusing device is a method to reduce background. In addition to that, pattern recognition algorithms can be applied, thus further lowering the background.
While the materials close to the detector had not been chosen specifically based on high radiopurity, the shielding was optimized during the first phase of CAST. Pattern recognition methods are used to identify minimum ionizing particles (MIPs) very efficiently. Using the X-ray mirror optics suppresses the background by a factor of about 155, which is due to the fact that the magnet aperture area of 14.5 cm^2 is focused to a spot of roughly 9.3 mm^2 on the CCD chip.

6.4.1 Shielding

The implemented shielding of the pn-CCD at CAST consists of inner and outer components. Directly surounding the detector, a copper shield of oxygen-free copper with low activity is installed (10-40 mm). The copper box has an opening above the chip towards the mirror optics. Also inside the vacuum vessel, a layer of 22 mm ancient lead (almost free of ^{210}Pb) covered with a 2 mm layer of copper is included. Like this, the environmental γ-ray background is reduced.
In order to also lower the natural γ-radiation from the walls of the experimental hall, an external shield consisting of additional lead surrounding the detector and especially its backside, which is situated close to the adjacent wall, has been installed. Thus, during magnet movement with different distances between detector and wall, the background level is not changing [132, 133].

6.4.2 Detector Components and Simulations

The materials situated in the adjacencies of the chip were not explicitly chosen to be highly radiopure, but they were tested at the Canfranc Underground Laboratory of the University of Zaragoza. Furthermore, detailed Monte Carlo studies have been performed using GEANT4. As a result it could be concluded that less than 33% of the total background level originates from contaminations of the detector materials (^{238}U, ^{235}U, ^{40}K), while about half of the observed background is

induced by γ-rays from the surroundings of the CCD. ^{222}Rn is not a real problem at the moment since the detector is operated in vacuum. A detailed report is given in Ref. [156].

6.4.3 Typical Background Spectrum

The typical background spectrum for data taken with ^{4}He in the cold bore during Phase II is shown in Fig. 6.33. Considering the energy range for the axion search of 1-7 keV, one obtains a mean normalized count rate integrated over the whole sensitive area of the detector of $(2.39 \pm 0.02) \times 10^{-4}$ counts s^{-1}keV^{-1}. In other terms, this corresponds to a mean differential flux of $(8.66 \pm 0.06) \times 10^{-5}$ counts cm^{-2}s^{-1}keV^{-1}. In the expected axion signal region (≈ 9.34 mm^2) this means a background count rate of 0.175 counts per hour in the energy range from 1-7 keV. The most characteristic background contributions in the displayed energy range of Fig. 6.33 are fluorescence emission lines from materials in the surrounding of the CCD chip.
The copper K_α and K_β photo peaks (at 8.0 keV and 8.9 keV, respectively) as well as the escape peak of copper in silicon (6.3 keV) originate from the cooling mask near the chip. Since this mask is gold-plated, also gold lines are observable: Au-M_α ($\approx$ 2.1 keV), Au-L_α ($\approx$ 9.7 keV), and Au-L_β (≈ 11.5 keV). Furthermore, lead peaks from soldering can be seen for energies above 10 keV, namely Pb-L_α at 10.5 keV and the Pb-L_β at 12.6 keV. Below 7 keV, a quasi-flat Compton

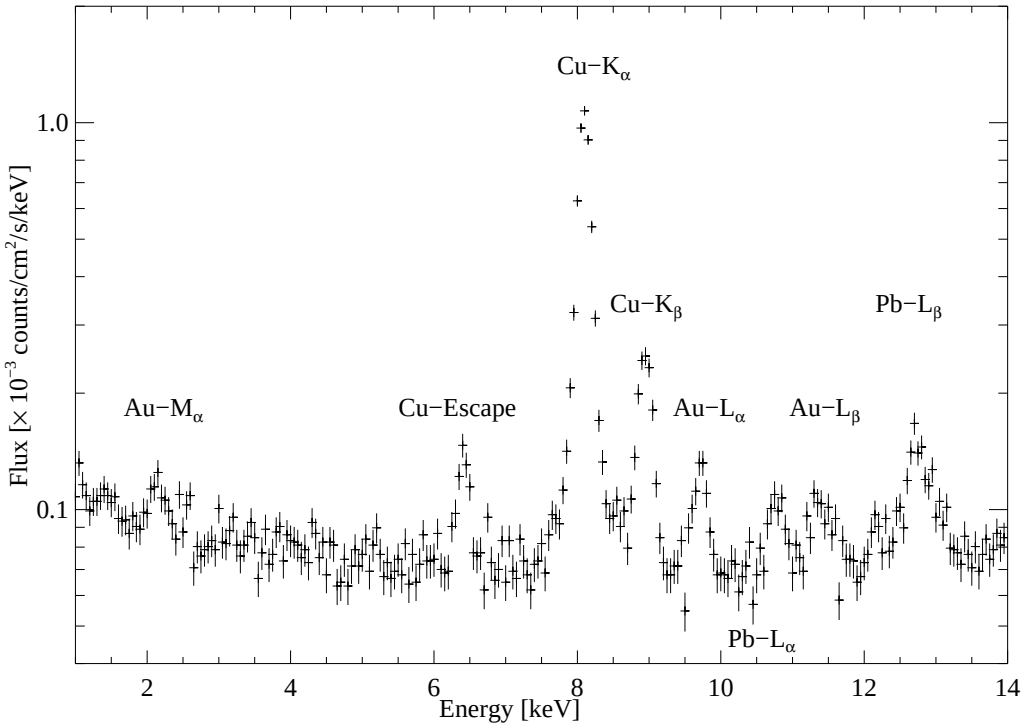

Figure 6.33: In the background spectrum for the data obtained with the CCD detector during Phase II of CAST, characteristic photon lines originating from the materials of the detector and its close surroundings can be observed.

continuum of mainly backscattered photons [153] is observable. This is the region chosen for the analysis of the CAST data acquired with the CCD detector.

Having characterized the X-ray mirror optics and the CCD detector, the following chapter will deal with the data obtained with the X-ray telescope during the ^{4}He part of CAST's Phase II.

Chapter 7

The CCD Data with ^{4}He Gas in the CAST Magnet

During the years 2005 and 2006, the CAST experiment acquired data with ^{4}He gas inside the magnetic field region. During times, when the CAST magnet was pointing towards the Sun, tracking data, i.e. data under axion-sensitive conditions, were taken. In case axions exist, these data correspond then to an expected axion signal plus the experimental background. During all other times, i.e. when the magnet is not aligned with the Sun, background data can be acquired.
In this chapter, the data acquisition with the X-ray telescope will be presented. First, an overview of the data taking is given, followed by data processing details and quality checks of the data on both, a daily and longterm basis. Performed background studies will be discussed before the actual analysis will be presented in Chapter 8.

7.1 Data Taking with ^{4}He Gas in the CAST Magnet

7.1.1 CAST Data Taking Overview

Data acquisition with ^{4}He gas in the cold bore of the CAST magnet started on November 24th in 2005 and lasted until December 8th 2006. From beginning of February 2006 until the end of April 2006, a shutdown of the whole CAST experiment had been scheduled to open the cryostat. The cold windows were checked and different maintenance works were done. Data taking was resumed during the last days of April 2006.
During the full data taking period, the detectors of the CAST experiment covered 160 density steps, each corresponding to a pressure difference of 0.083-0.087 mbar. Furthermore, two additional steps of half size around a potential candidate setting have been performed. The maximum pressure reached with ^{4}He was 13.425 mbar, which corresponds to an effective photon mass of 0.39 eV.

7.1.2 CCD Data Taking Overview

The pn-CCD detector of CAST accomplished to take data on 218 days, during which 187 tracking runs and 207 background runs were recorded. The 187 solar runs covered 149 different density

steps, i.e. 147 out of 160 full steps and the two additionally performed intermediate steps. The density settings not covered by the CCD detector have been investigated by at least one of the other CAST detectors. They were missed by the X-ray telescope system due to different problems. In January and in April 2006, a broken turbo pump in the CCD vacuum system made data taking impossible until the replacement of the pumps. Further reasons for missed settings were software problems due to an extremely long power cut at CERN and difficulties with the vacuum system of the detector, due to a malfunctioning pressure gauge. All defects could be fixed rather quickly, such that no more than 13 settings in total were missed. Summarizing, the total time of acquired tracking data is 294.8 hours, while under background conditions 2758.1 hours of data have been taken.

7.1.3 CCD Data Taking Procedure

The CCD detector has been operated continuously during the ^{4}He part of Phase II, except for the mentioned minor interruptions due to technical problems. Every morning before the solar tracking, the shifters started the automatic Data Acquisition System (DAQ). First, the DAQ takes a dark run of 200 frames[1], lasting about 14 s. Following this, a calibration run with the ^{55}Fe source is performed. It generally consists of 6000 frames and thus requires about 7 min. When the calibration finishes, a continous data taking run of 89 files with 12550 frames each is started, lasting more than 22 hours and thus running till the next morning.
It was ensured that the DAQ was started around 15 min before the tracking of the Sun began, such that the first 6 files would contain the full solar run (about 90 min) and could thus be used for a Quicklook-Analysis (QL). This preliminary analysis provides a first preview of the daily results and will be described in Section 7.2.3.

7.2 Data Treatment and Data Quality Checks

The processing of the CCD data is performed in several steps. The first treatment of the acquired raw data is done directly with the DAQ-PC in the CAST control room. In order to reduce the raw data, empty frames are discarded and only readout intervals with data are kept. The original frame number containing the counts is saved, such that no information, e.g. about the time of the registered event, is lost. After this preprocessing stage, the data are sent to TU Darmstadt for further processing, which is then available online in form of the Quicklook-Analysis. After additional information such as slow control (SC) and tracking relevant information are taken into account, the final data file to be used for further analysis is obtained. For all processed data, a backup file is then produced at the MPE/WHI[2] in Munich and at the University of Freiburg.

7.2.1 Data Processing

While the raw data and the results of the preprocessing at CERN are given in compact binary format for fast access and storage, the next step converts the data into the so-called FITS format[3], which

[1] A frame corresponds to one CCD read-out cycle of 71.77 ms.
[2] Werner Heisenberg Institute
[3] Flexible Image Transport System

is an easy-to-handle, standard astronomical data format, originally introduced by NASA[4] [157]. Not only has it been designed as an image format, but also to store scientific data arranged in arrays of muliple dimensions. Data stored in FITS files can then be further analyzed using the IDL[5] software, which is preferably used in astronomy by institutes, such as NASA or the German Aerospace Center DLR[6].
Once the FITS file containing all the CCD data is produced, several steps follow:

- Conversion of CAST tracking information from ASCII to FITS format,
- Conversion of CAST slow control information from ASCII to FITS format,
- Production of event FITS files from the basic CCD data file for different valid pattern types.

The tracking information provides all necessary parameters of the experiment connected with the magnet movement, such as for example, whether or not the magnet is following the Sun and with which precision. A detailed list of all provided parameters can be found in Ref. [158]. The tracking information is initially provided in the form of ASCII files and transformed into FITS files for the CCD data processing.
Similarly to the tracking PC, the slow control of the CAST experiment logs all parameters relevant to the experiment, such as different pressures in the vacuum and gas systems, conditions of valves, the status of the magnetic field and temperatures (for a comprehensive list see Ref. [159]). Also this information is given in ASCII format and converted into a FITS file.
An important step in the processing of the CCD data is the creation of so-called event files for all valid pattern types from the basic CCD data file. The main point here is the application of a pattern recognition algorithm to sort out events caused by cosmic rays. As illustrated in Chapter 6, when discussing the properties of the CCD signal, only certain types of split events qualify as photons from axion-conversion, such as single, double, triple and quadruple events showing a specific pixel geometry (see also Fig. 6.18). A double with hits in two diagonal pixels, for example, does not provide a valid pattern. Selected event files are obtained from the basic CCD data file, sorted into different valid pattern types.
Additionally, information from the telescope vacuum system can be included. Thus, it can be ensured that the valve connecting the X-ray mirror optics with the magnet (V14) and the one between the telescope and the pn-CCD detector (V13) are both open, allowing photons from possible axion-conversion to reach the detector.

7.2.2 Data Extraction

Having created FITS files containing all necessary information provided by SC and tracking PC as well as the CCD event files of valid patterns, the next step is to combine all these sources of information. This can be accomplished by the use of so-called Good-Time-Interval (GTI) files, which provide the times at which certain conditions are fulfilled. A useful software package to handle and work with FITS files is FTOOLS [160]. It can be employed to extract such good time

[4] National Aeronautics and Space Administration
[5] Interactive Data Language
[6] Deutsches Zentrum für Luft- und Raumfahrt

intervals. At CAST for example, this might be all times, during which the magnetic field has been turned on and the magnet has been tracking the Sun (tracking data). Thus, for all files containing information relevant to the analysis, GTIs can be selected, taking into account all important factors to determine, if tracking or background data have been acquired during the time under consideration. Finally, the different good time intervals for SC and tracking can be merged together with the valid pattern event files of the CCD. In this way, all data qualifying for tracking or background can be obtained.
The conditions taken into account for the selection of ^{4}He tracking and background data from the tracking logfiles are:

- **MAGB**: Magnetic field strength as read by the tracking PC. The correspondence between magnetic field B and current I was given in Tab. 5.1.

- **HMOTV**: Supply voltage of the horizontal motors. Tracking data have to fulfill HMOTV$>$ 10 V. For background measurements HMOTV$=0$ V is required.

- **HPRECIS**: Precision of the horizontal movement, i.e. calculated goal position minus measured position. During tracking, this precision has to be better than 0.01° at any time.

- **VPRECIS**: Same as HPRECIS, but for the vertical movement. Also this accuracy has to be better than 0.01° for the data to be taken into account as tracking.

- **TIME**: Time of the measurement. This criterium can be used to distinguish between the morning and the evening tracking.

- **TRACK**: If the solar tracking switch in the tracking software is turned on, this flag is set to 1. Otherwise, it is 0. In order to take only the morning tracking into account, the TIME criterion is used. Furthermore, by considering HMOTV and HPRECIS, real tracking times can be determined.

From the SC information the following criteria are used:

- **VT4OPEN**: Status of the gate valve VT4 connecting the X-ray telescope to the magnet. If VT4OPEN$=1$, the valve is open. For VT4OPEN$=0$, it is closed.

- **QUENCH**: Flag to mark the start time and duration of a quench. For both, tracking and background, this flag needs to be zero, i.e. no quench.

In Fig. 7.1, the important selection critera and their conditions during Phase II are shown. The upper plot shows the selection of GTIs for tracking, the lower plot the same for background runs.
After all the GTIs are produced and merged, the FITS files containing the final data for the analysis can be extracted in different energy ranges for all types of events. It is then also possible to separate the file containing all data of Phase II into single data taking days. These can then be recombined to obtain files, including the data of each single density setting.

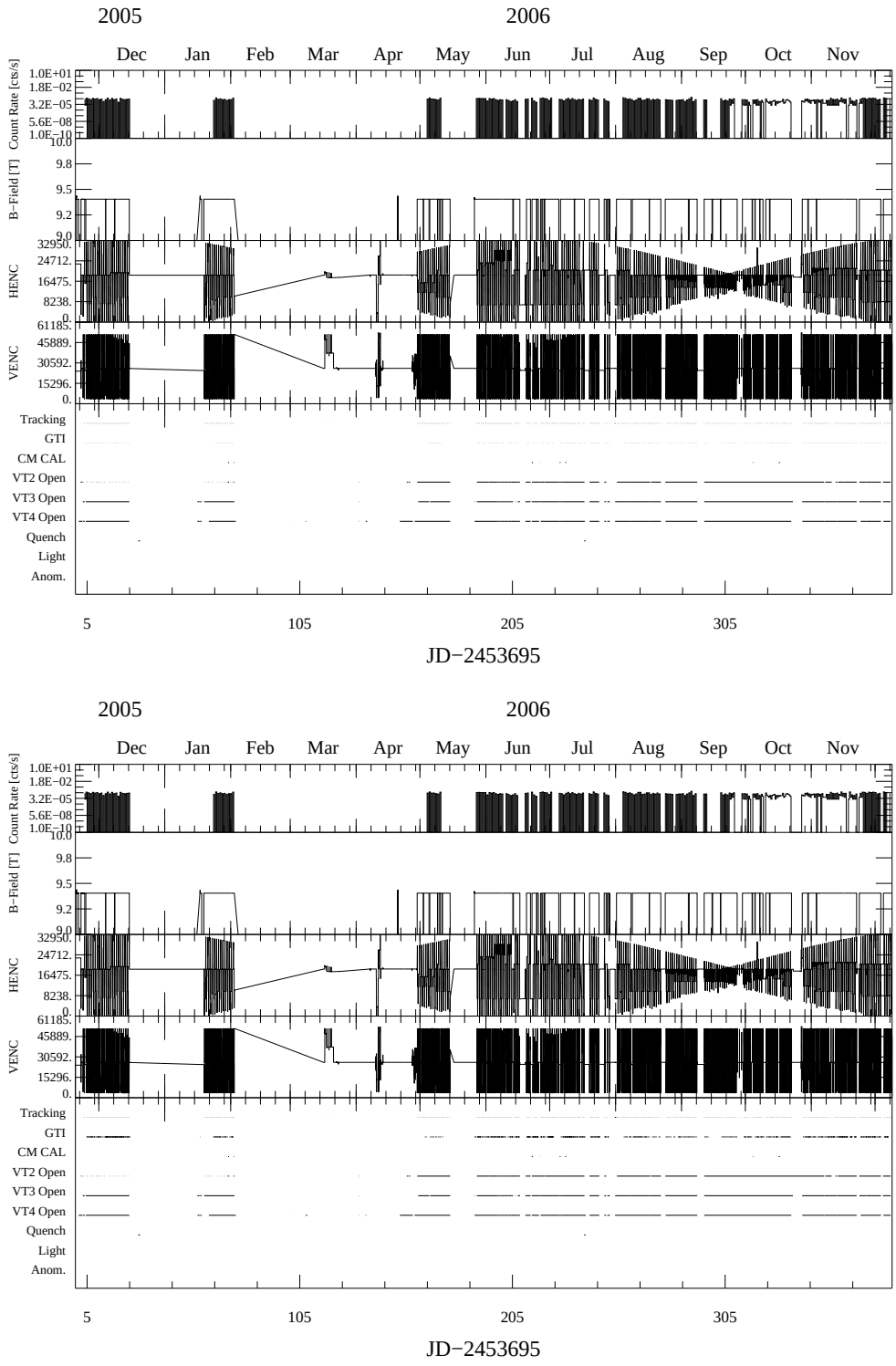

Figure 7.1: Top: Screening of the CCD data to determine the GTIs for tracking data. Different selection criteria are shown in the plot. Proceeding from top to bottom the following parameters are shown: CCD count rate, magnetic field, horizontal encoder value (a change of it indicating movement), vertical encoder value, tracking flag, GTI, flag used for X-ray finger measurements (CM CAL), status of the gate valves VT2, VT3 and VT4 as well as the Quench flag. Light and Anomaly mark periods during which problems occured. All ^{4}He data are shown. Time is given in Julian Day (JD) and Universal Time (UT). Bottom: Same plot for background data.

7.2.3 Daily Data Quality Check of the ^{4}He Data: The Quicklook-Analysis

In order to provide a quick check of the detector performance and the events of the morning tracking, a first analysis is made accessible online[7] automatically around two hours after the end of the tracking run. For every day, a file covering approximately the tracking run (6 first files of a day, i.e. first 90 min of a run) and one for the full day are available at the above mentioned webpage. All important detector parameters can be checked, starting from the raw spectra over noise and offset maps to the point of calibration. In this way, it can be confirmed that the detector is performing as expected. It is important to note that no slow control data or tracking information is included in the QL-Analysis. Therefore, the QL results do not represent a final result but are meant to provide an indication of the daily made observation.
One important file in the QL-Analysis is the so-called true color event image. It shows all the events which occured during tracking on the full chip. Therefore, it can be used to determine roughly, how many counts have been registered during tracking in the axion signal spot region. This information together with the knowledge that the detector has been working properly can be used to determine if the pressure in the cold bore should be changed to the next setting or if a specific setting is worth repeating, since it provides a potential axion candidate. For more information on the quicklook analysis, the interested reader is referred to Ref. [161].
During the ^{4}He phase a protocol has been developed, on how to handle potential candidate steps, i.e. pressure settings, during which more counts than expected were registered. In 2005 and 2006, only the CCD detector was used to determine, whether a repetition should be done, while the fully evolved protocol, now used for the ^{3}He run, can take all four detectors of the CAST experiment into account. The idea behind the protocol is to follow a consistent and homogeneous policy during the whole data taking period and spend about 5% extra time of the total CAST running time to investigate possibly anomalous events. A detailed description of the CAST protocol, which is using Monte Carlo simulations to eliminate candidates, can be found in Ref. [162].

7.2.4 Longterm Data Quality Check of the ^{4}He Data

Overview of Considered Data Set To monitor the longterm stability and the quality of the data, the full ^{4}He tracking and background data set has been used. After the data extraction using the above discussed GTIs, the ^{4}He data consist of 187 tracking runs at 149 different density settings with 207 background runs. The total tracking time has been 1061282.7 s ≈ 294.8 h, while under background conditions 9929245.0 s ≈ 2758.1 hours have been acquired.
The full chip has a total area of $A \approx 2.761$ cm^2 and the expected axion signal area is a circular area with its center at $x = 40$ and $y = 108$ as determined by the laser and X-ray finger alignment. The radius of the spot has been determined by calculating the signal-to-noise ratio depending on the spot radius for different $g_{a\gamma}$. The optimization is then accomplished by determining the value of the radius for which the common maximum for different coupling constants is found. This yields an optimal spot radius of 11.5 pixels corresponding to 82.6% encircled axion flux. The area of the potential signal spot is 9.348 mm^2.
There have been 1508 counts registered on the full chip during tracking and 14223 counts, while taking background data. In the spot, 45 counts were found, when following the Sun and in total

[7] http://astropp.physik.tu-darmstadt.de/projects/cast/data/QL/ql-hefour_ en.php.

Table 7.1: Summary of the ^{4}He data acquired during 2005 and 2006 in the energy range 1-7 keV for background and tracking conditions.

	Tracking	**Background**
Time [hours]	294.8	2758.1
Detected Photons [cts]	1508	14223
Count Rate [$\times 10^{-4}$ cts/s]	14.21 ± 0.37	14.35 ± 0.12
Flux [$\times 10^{-4}$ cts/cm^2/s]	5.15 ± 0.13	5.20 ± 0.04
Mean differential Flux [$\times 10^{-5}$ cts/cm^2/s/keV]	8.58 ± 0.17	8.66 ± 0.07

430 counts were recorded in background data. This includes all valid events, i.e mainly single and double events.
The detector performance as well as the mean differential flux have been stable during background measurements at a level of $(8.66 \pm 0.07) \times 10^{-5}$ cts cm^{-2} s^{-1} keV^{-1} for the full chip in the energy range of 1-7 keV. This translates to 8.13 ± 0.07 counts in an average tracking of 5675.3 s in the energy range of 1-7 keV for the full chip, considering the total available background. In the spot, this corresponds to 0.275 ± 0.002 counts under the same conditions. The corresponding values obtained from tracking data are compatible with these numbers. A summary of the important parameters for the ^{4}He data is given in Tab 7.1. A detailed list summarizing dates on which the CCD took data, the corresponding pressures, tracking time and average background counts can be found in the Appendix C.

Stability of the Detector Performance During the complete data taking phase in 2005 and 2006, the pn-CCD detector and the X-ray telescope revealed an excellent longterm stability, taking into account various operating parameters. This results in the acquisition of a homogeneous and consistent data set over an extended period of time. Constant monitoring of the performance quality and the detector stability is accomplished by performing daily calibrations of the pn-CCD detector with the help of an ^{55}Fe source. Fig. 7.2 provides an overview of the most important parameters monitored throughout the 2005 and 2006 data taking period via the regularly repeated calibrations. One of these parameters is the detector gain. It provides the conversion of analog-digital units (ADU) to eV and has been found to be very stable. Furthermore, the charge transfer inefficiency (CTI) has been monitored. The mean noise level and the mean offset are both averaged over all pixels on the full chip. In addition, the intensity of the Mn-K$_\alpha$ line, its energy resolution (FWHM) and the peak position are recorded. A correlation can be observed between variations in the energy resolution and the mean signal noise, indicating periods with increased noise in the experimental area. These variables do not reflect the achievable perfomance in a laboratory, since the noise level in the CAST experimental hall has been found to be quite high and variating during specific periods. This is due to the fact that the experimental site has never been designed to provide a low-noise environment. At no time, however, did these variations affect the search for axions and the total sensitivity to detect the hypothetical particle. All other parameters have shown high stability during the whole ^{4}He phase, as it has already been the case during Phase I of the CAST experiment.

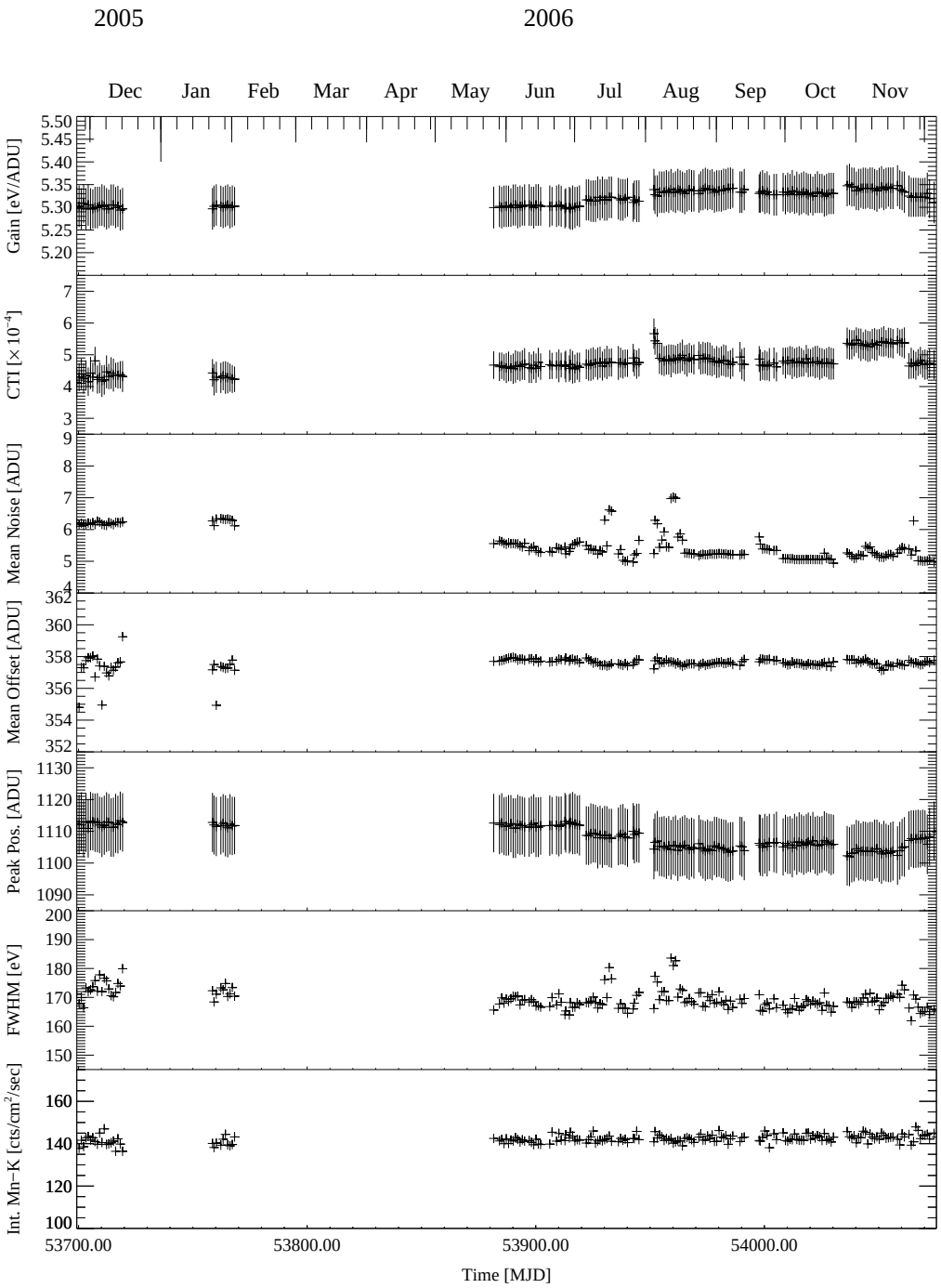

Figure 7.2: Stability of the detector performance of the CAST pn-CCD during the ^{4}He data taking period in 2005 and 2006. The daily calibrations of the pn-CCD detector with an ^{55}Fe source are used to monitor the performance. The gaps indicate shutdown times of the experiment, during which no data have been acquired. From top to bottom are shown: the gain, the charge transfer inefficiency (CTI), the mean noise and offset, which are both averaged over the whole chip. Furthermore,the peak position of the Mn-K$_\alpha$ line, its FWHM and the intensity are displayed. Time is given in standard notation (Universal time, UT) as well as in Modified Julian Day (MJD), which is defined via the Julian Day (JD) by MJD $=$ JD - 2400000.5.

Full Chip Intensity Distribution and Spectrum The spatial distribution of all events on the CCD chip during the ^{4}He data taking phase is shown in Fig. 7.3. The intensity is given in counts per pixel. The left plot shows all tracking data registered in the 64 columns and 200 lines in a total of ≈ 294.8 h. The white circle indicates the size of the expected axion signal region, i.e. the image of the Sun's core containing 82.6% of the total solar axion flux. The plot on the right side is the intensity image for the ≈ 2758.1 h of background data with ^{4}He in the cold bore. It can be seen that the distribution of events is homogeneous over the full chip. The corresponding spectra are

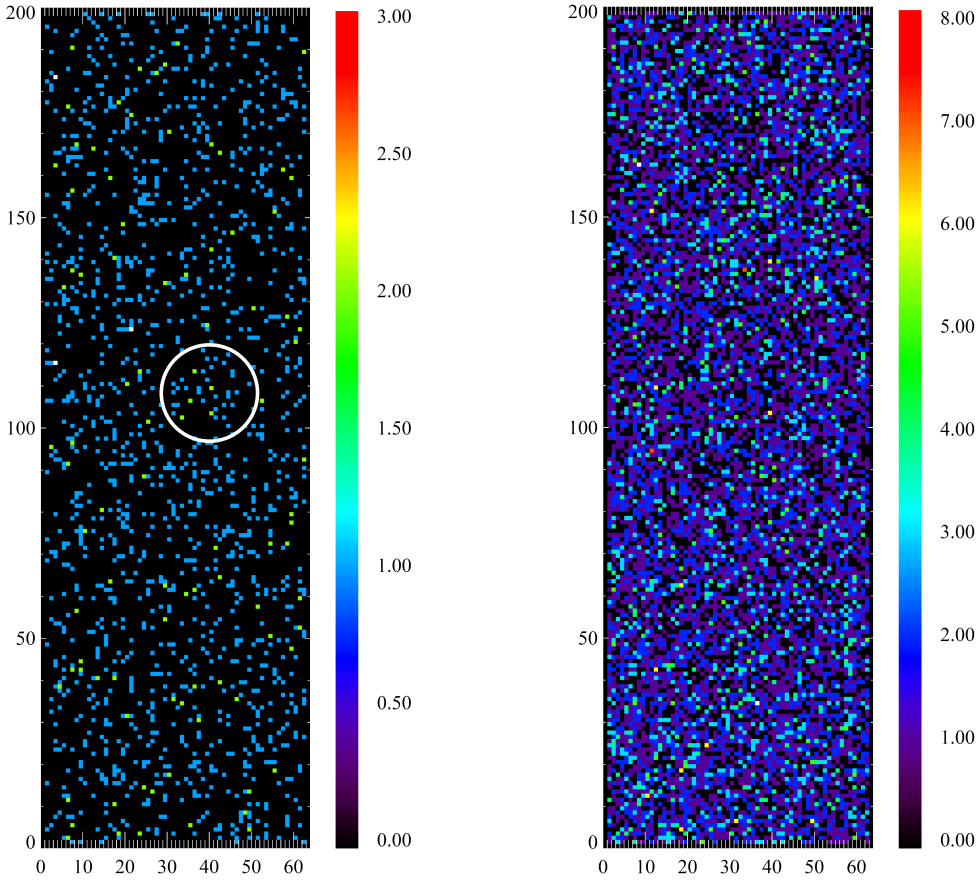

Figure 7.3: Left: Spatial event distribution of all ^{4}He tracking data in the energy range of 1-7 keV. All pressure settings are considered together. The white circle represents the expected axion signal spot with radius 11.5 pixels and its center at $x = 40$ and $y = 108$. It contains the image of the solar core, where most axions are expected to be produced. The intensity is given in counts/pixel. Right: Intensity image of all ^{4}He data acquired under background conditions in the 1 to 7 keV range.

shown in Fig. 7.4 for the energy range of 1-7 keV used as the axion-sensitive range for the CAST experiment (left image) and for the total range of 1-14 keV (right image). The upper part of each plot shows the tracking and background energy spectra in black and red, respectively. They have been normalized with respect to exposure time and correspond to the whole chip area. In the lower part of the plots, the difference between the two spectra is displayed. In the range up to 7 keV only the Au-M$_\alpha$ (2.1 keV) and the escape peak of copper in silicon (≈ 6.3 keV) are slightly apparent.

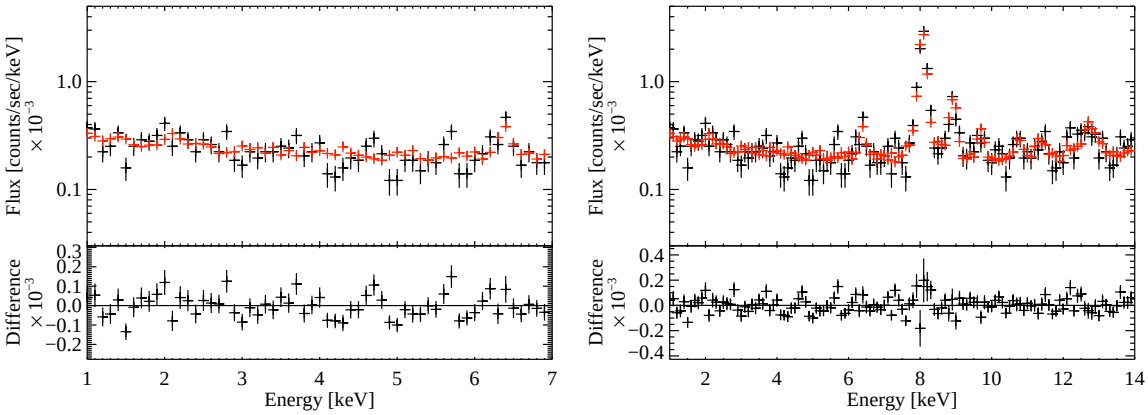

Figure 7.4: Left: Energy spectrum of tracking (black) and background data (red) for the full chip in the energy range of 1-7 keV. All ^{4}He data have been included. The lower part of the graph shows the difference between tracking and background. Right: Equivalent plot for the energy range of 1-14 keV.

For higher energies various peaks of copper, lead and gold are observable with the Cu-K$_\alpha$ peak at 8.0 keV being the most dominant one. The origin and exact position of the peaks have already been discussed in Section 6.4. Both spectra, tracking and background, reveal the same structure, such that both data sets are compatible. For further analysis, only the range between 1 and 7 keV has been used, since this is the axion-sensitive energy range which has the lowest background level and is furthermore free of fluorescent emission lines. Especially the Cu-K$_\alpha$ peak has no disturbing influence.

7.3 Stability of the CCD Background

The stability of the background observed with the CCD detector has been studied. Its behavior is well understood and the background has been shown to be independent of various experimental conditions.
In Section 6.4 the different source of background and a typical background spectrum have been discussed along with performed Monte Carlo simulations. As a reminder, the largest contribution to the background comes from cosmic rays and non-radiopure materials close to the detector, such as copper, lead and gold [156]. Furthermore, electronic noise is present but mainly below the energy threshold of 0.5 keV. X-rays produced in the magnet or the walls of the X-ray mirror optics due to natural radioactive contamination could mimic photons from axion conversion. However, this is negligible, due to the extremely small probability that the X-rays will be emitted parallel to the optical axis of the magnet and the telescope.

7.3.1 Time Variation

In Fig 7.5, the variation of the background with time is shown for all data acquired in 2005 and 2006 with ^{4}He in the magnet. All counts on the full chip in the energy range of 1-7 keV have

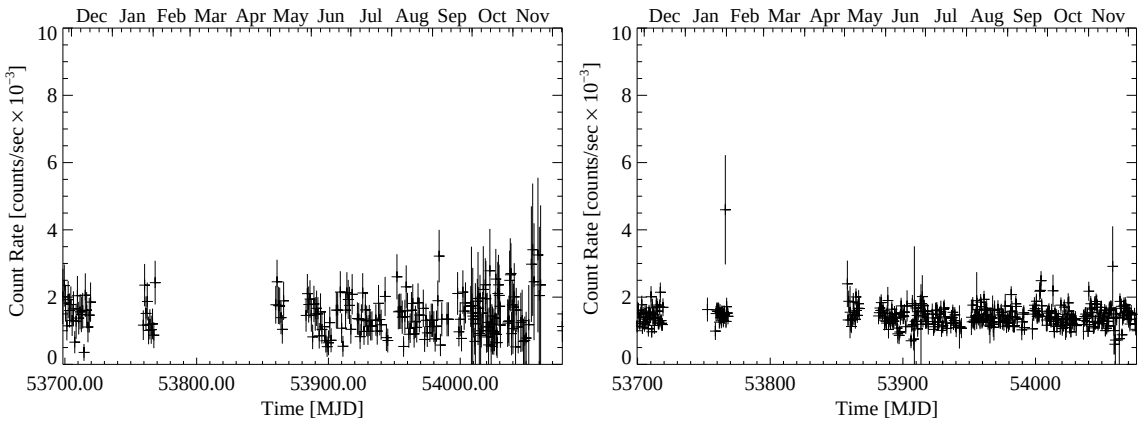

Figure 7.5: Left: Normalized count rate during tracking measurements in the energy range of 1-7 keV depending on time, which is given as Universal Time (UT) and Modified Julian Day (MJD). All counts on the full chip have been taken into account. Right: Normalized count rate during background measurements in the same energy range as a function of time. Also here the full chip has been taken into account.

been considered here. Both, tracking data (see left part of Fig. 7.5) and background data (see right part of Fig. 7.5) reveal no significant dependence on time. Thus, the count rate for tracking and background can be considered stable over the whole data taking period.

7.3.2 Line and Column Distribution

Another possible dependence of the background is a variation of the count rate connected to the line and column number on the chip. Therefore, in Fig. 7.6, the mean intensity per pixel in each of the 200 lines (top plots) as well as in each of the 64 columns (bottom plots) is shown. The line and column distribution is shown for both, tracking (left plots) and background (right plots). The displayed count rates are stable, such that no significant dependence on the line and column distribution can be observed. Note that the error bars for the tracking count rate are larger due to lower available statistics.

7.3.3 Position Dependence

Generally, background and tracking data have not been acquired in exactly the same positions, such that it is necessary to assure that the background is independent of the magnet position in the experimental hall. This might not be the case, for example due to different distances of the detector from the wall resulting in varying strength of natural γ-radiation. While the angular range covered by the CCD detector during tracking reaches from roughly -8° to $+8^\circ$ in the vertical direction (Height H), the horizontal extention (Azimuth AZ) can vary over a range from about 40° to 140° over the course of the year.
During Phase I, the TPC background was strongly sensitive to the position of the magnet and thus the detector location in the experiment. This position dependence had therefore also been studied for the CCD detector. However, no position dependence of the background for the CCD detector was observed and after upgrading the TPC shielding, it was decided that a coverage of the full

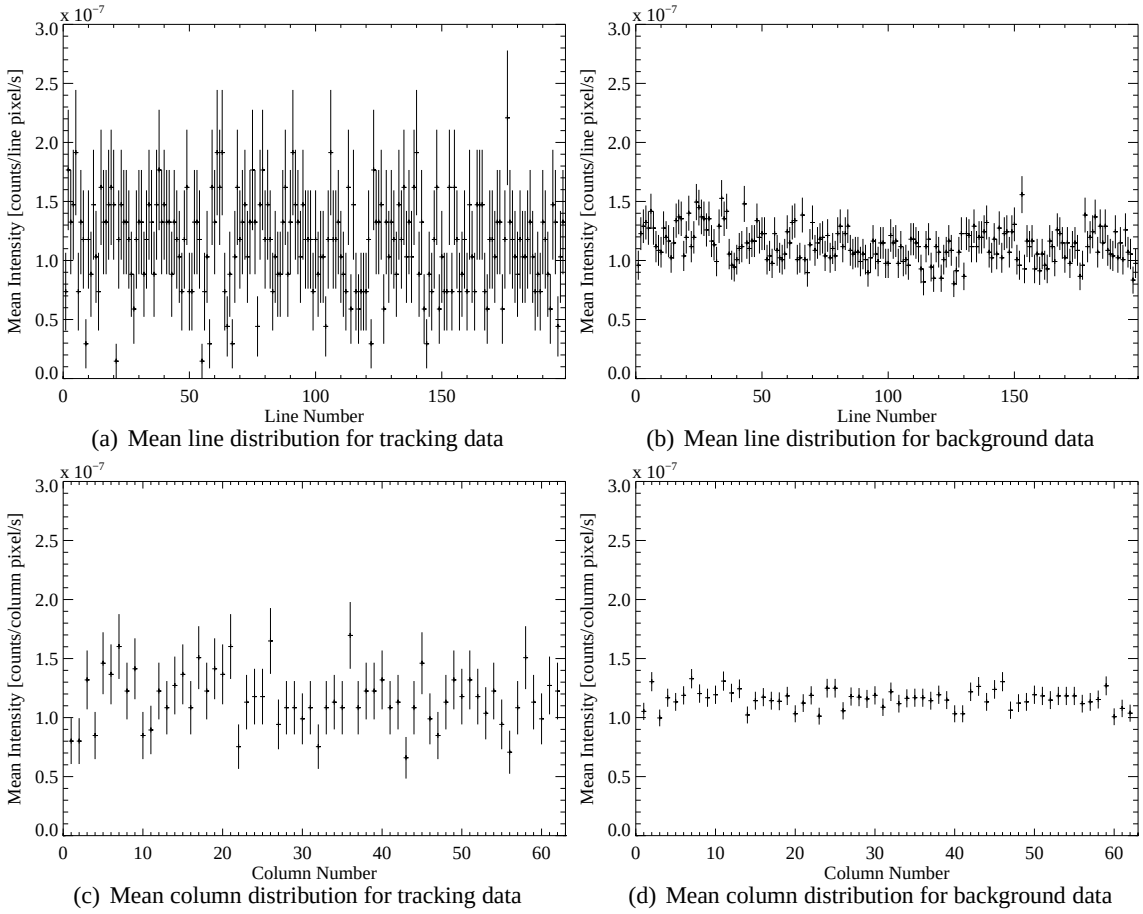

(a) Mean line distribution for tracking data

(b) Mean line distribution for background data

(c) Mean column distribution for tracking data

(d) Mean column distribution for background data

Figure 7.6: The upper two plots show the mean intensity of counts per pixel for each of the 200 lines during tracking (upper left) and background times (upper right) in the ^{4}He phase of CAST. The averaged column distribution per pixel taking into account all 64 columns of the chip can be found in the lower plots for all tracking (lower left) and background (lower right) data.

angular range during background measurements in CAST's second phase was not necessary. Thus, background data were usually acquired in one fixed position, which was slightly varied from time to time, such that the central angular range as passed through during tracking was covered.
To verify former results, the ^{4}He data in the energy range of 1 to 7 keV have been checked for a possible position dependence in the available angular range of background and tracking. This has been done by binning the background data in intervals of 2° in height and 10° in azimuthal angle. The results are displayed in Fig. 7.7. The upper two plots reflect tracking data, while the lower plots correspond to data taken under background conditions. In the images on the left, the actual count rate is indicated by the color of each field. Black fields indicate that no data were available in the respective angular region or that the exposure time in these fields was very small. To determine the count rate, the full chip has been considered. The images on the righthand side of the same figure show the position dependent exposure time during tracking (upper right) and background (lower right) measurements.

The result of this study confirms that the count rates in different locations of the experimental hall during background and tracking measurements are stable in the 1 to 7 keV range within the expected statistical fluctuations, such that the observations of Phase I are confirmed also for CAST's second phase. Thus, no dependence of background on the magnet position in the experimental area has to be taken into account for the analysis.

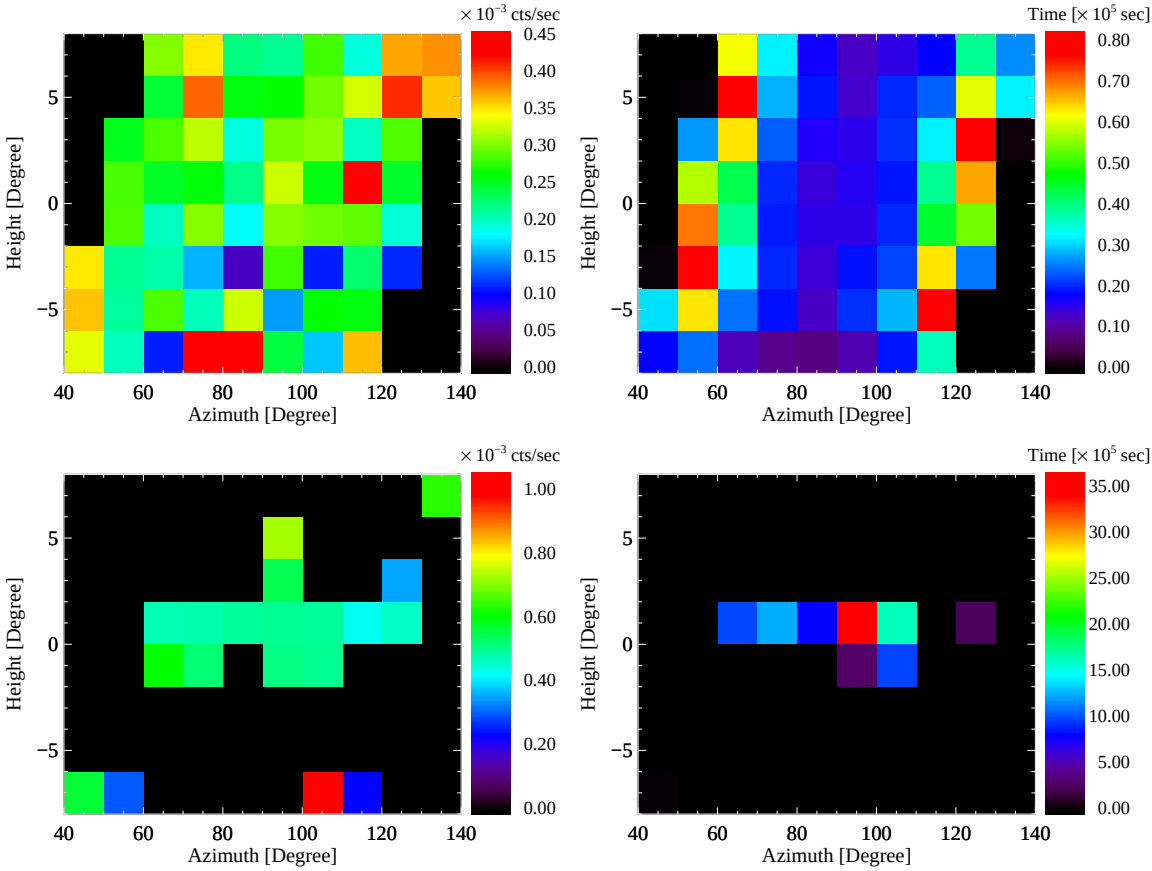

Figure 7.7: Angular position dependence of ^{4}He data. Upper left: Angular position dependence of the tracking data taken in 2005 and 2006 in the energy range of 1 to 7 keV. To determine the count rate, the full chip has been considered. Black fields indicate that no data were acquired in this angular position or that the exposure time in these fields was very small. Upper right: Position-dependent exposure time during tracking measurements. Lower left: Angular position dependence of the background data taken in 2005 and 2006 in the energy range of 1 to 7 keV. This plot includes all the background on the full chip with magnetic field on and gate valve VT4 between detector system and magnet open. Lower right: Position-dependent exposure time during background measurements.

7.3.4 Dependence on Experimental Conditions

While during tracking the magnetic field is always on and the gate valve VT4 connecting the X-ray telescope to the magnet bore is kept open at all times, this is not neccessarily the case during all background measurements. In Fig. 7.8, the CCD count rate as a function of energy is shown. Four

different combinations of the conditions for the magnetic field and the valve are displayed, taking into account the full chip in the 1-7 keV energy range:

- **Magnetic field on and gate valve VT4 open**: Standard definition of background, since these conditions are equivalent to those present during tracking. The normalized count rate of the background defined in this way is shown in the upper left plot of Fig. 7.8. It has the largest exposure time of the four different definitions considered here (2758.1 hours) and thus the smallest statistical uncertainties.

- **Magnetic field on and gate valve VT4 closed**: Sometimes the gate valve has been closed to decouple the detector systems from the magnet and protect both sides. The background taken under this condition and the magnetic field turned on, is shown in the upper right

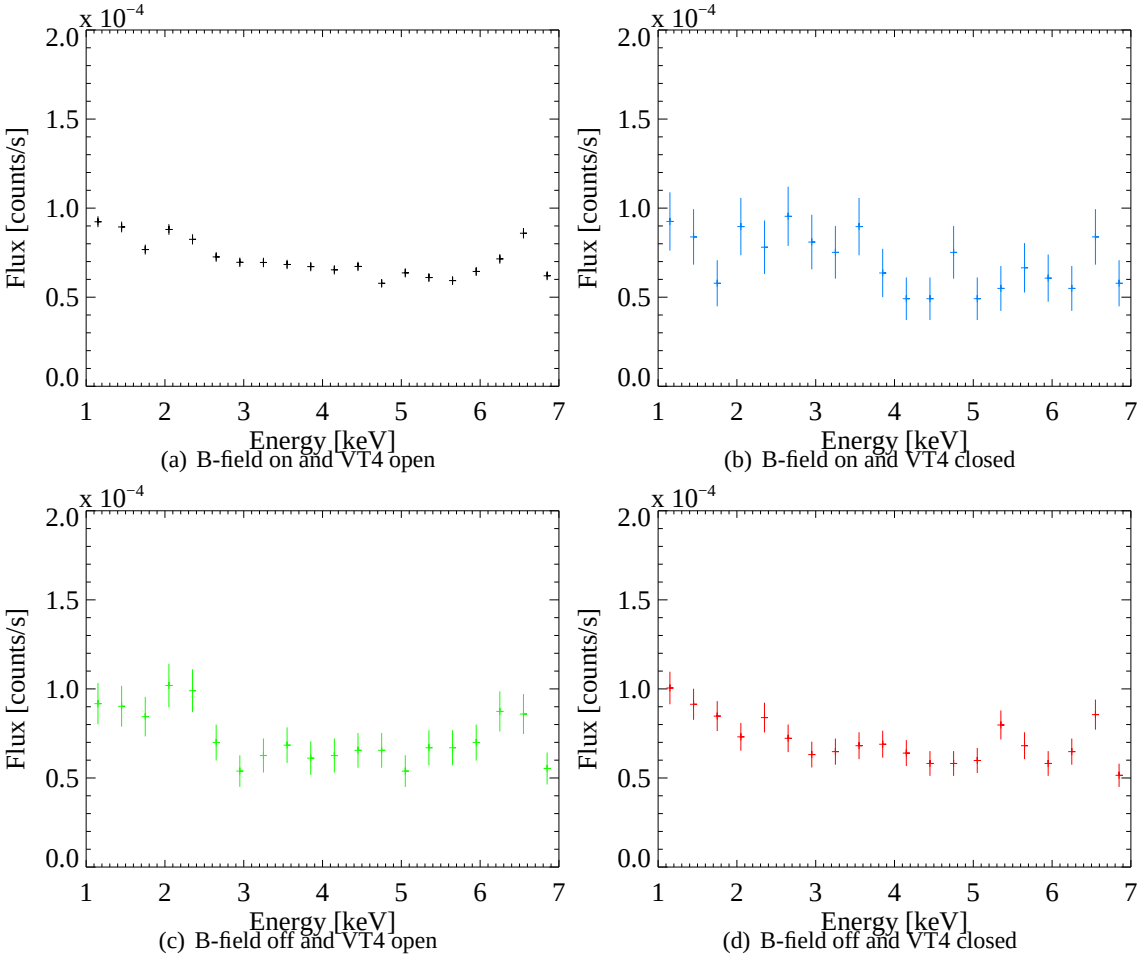

Figure 7.8: Dependence of the ^{4}He data on different experimental conditions. Upper left: Background count rate with magnetic field on and VT4 open. Upper right: Background count rate with magnetic field on and VT4 closed. Lower left: Background count rate with magnetic field off and VT4 open. Lower right: Background count rate with magnetic field off and VT4 closed.

plot of Fig. 7.8. This configuration yields the shortest exposure time of all four possibilities (96.1 hours).

- **Magnetic field off and gate valve VT4 open**: If the magnetic field is turned off, e.g. for works in the experimental area, it is normally not necessary to close the gate valves, since the vacuum generally stays sufficiently good. A total of 190.8 hours background data have been acquired in this condition (lower left plot in Fig 7.8).

- **Magnetic field off and gate valve VT4 closed**: If the magnetic current is ramped down, e.g. due to a quench or an intervention, generally the gate valves are closed to prevent the detectors from any risk of possible damage. Altogether, 334.4 hours have been spent taking background in these conditions, which is displayed in the lower right plot of Fig 7.8.

As a result, no significant variation under the studied experimental conditions of the status of the magnetic field and the gate valve VT4 are apparent. Most of the time for background measurements has, however, been spent in the standard background conditions, i.e. magnetic field on and VT4 open as during tracking.

7.3.5 ^{4}He Gas Pressure Dependence

A further potential background dependence, which is new for Phase II as compared to Phase I, is a possible relation between the pressure of the helium in the cold bore and the background. In order to exclude any significant influence of the helium, the data have been divided into four subsets of increasing pressures. The first set contains all background runs for pressure settings between 0.08 mbar and 3.41 mbar, the second one those from 3.50 mbar to 6.66 mbar. The third and fourth take into account settings from 6.74 mbar to 10.08 mbar and 10.17 mbar to 13.43 mbar, respectively. The count rates obtained from the different subsets in the energy range of 1 to 7 keV taking into account the full chip are shown in Fig. 7.9. The different background spectra are compatible with each other. No distinctive features indicating a dependence of the background on the pressure in the magnet bore are observed within expected fluctuations.

7.3.6 Results of Background Studies

Summarizing all performed background studies, it can be concluded that no dependence of the background on the above mentioned parameters and conditions could be observed. Preferably, for background measurements all conditions except following the Sun should be identical to tracking data, to avoid any dependencies even if of insignificant size. Since background under conditions not corresponding to those during tracking contribute only a small part of additional exposure time, background statistics are not considerably improved by taking the additional data into account. Based on this background set, several definitions of background are possible and will be presented in the following section.

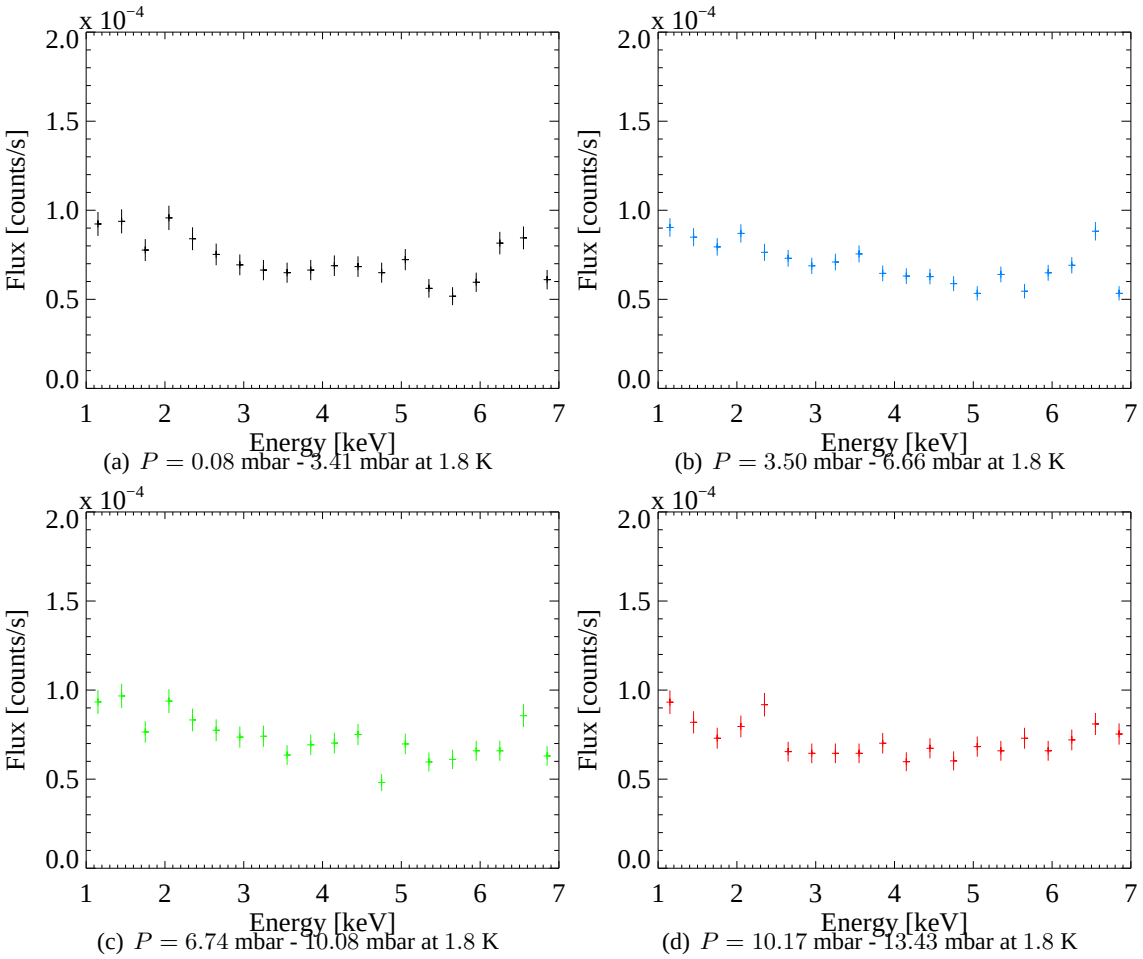

(a) $P = 0.08$ mbar - 3.41 mbar at 1.8 K (b) $P = 3.50$ mbar - 6.66 mbar at 1.8 K

(c) $P = 6.74$ mbar - 10.08 mbar at 1.8 K (d) $P = 10.17$ mbar - 13.43 mbar at 1.8 K

Figure 7.9: Dependence of the ^{4}He data on the pressure of the gas inside the magnet. Upper left: Background count rate with ^{4}He gas pressure from 0.08 mbar to 3.41 mbar at 1.8 K. Upper right: Background count rate with ^{4}He gas pressure from 3.50 mbar to 6.66 mbar at 1.8 K. Lower left: Background count rate with ^{4}He gas pressure from 6.74 mbar to 10.08 mbar at 1.8 K. Lower right: Background count rate with ^{4}He gas pressure from 10.17 mbar to 13.43 mbar at 1.8 K.

7.4 Tracking and Background Definition for the CCD Data

7.4.1 Tracking Data

The tracking data used for the CCD analysis of the ^{4}He phase have been selected to be data acquired during morning trackings of the Sun with magnetic field on and VT4 open. The data cover 149 pressure settings taken in 187 tracking runs and correspond to a total of 294.8 h. Only the counts in the spot region with radius $r = 11.5$ pixel and center $(x, y) = (40, 108)$ have been taken into account from the total of 1508 hits on the full chip in tracking time.
To determine, that a hit was inside the spot, the condition

$$r = \sqrt{(40 - x)^2 + (108 - y)^2} \leq 11.50 \text{ pixels}, \tag{7.1}$$

has to be fulfilled. Here, x and y represent the coordinates of the event, which are determined taking into account the center of the deposited energy. If for example a double event hits the pixels (39,119) and (39,120) and the energy weighted hit coordinates are $x = 39.00$ and $y = 119.46$, then the event is accepted, while if the weighted center is $x = 39.00$ and $y = 119.47$, the event is discarded. In this way, a total of 45 counts in the spot region were found in the tracking data. A detailed list can be found in Appendix D.

7.4.2 Background Definition

Several possibilities of defining the background have been studied using the full background set for ^{4}He as basis. Hereby, the same conditions as during tracking were required (magnetic field on, VT4 open, etc.), without following the Sun. The different definitions have been labeled Background 1, 2, 3 and 4 and are chosen as follows.

Background 1 (Spot during background times) Since the potential signal spot is located in a region of the chip with low background, it is a good choice of background to consider the same area during non-tracking times as background. These data have to be normalized to the time spend in each pressure setting p_k, in order to obtain the background b_{ik} in the energy bin E_i. Sufficient statistics are available for this definition of background.

Background 2 (Full chip during background times) During background times, the full chip can be considered as background, since no signal is expected during these periods. The advantage of this choice is clearly its high statistics as compared to tracking runs, due to its long exposure time. The background obtained in this way has to be normalized to the time spent at each pressure setting as well as to the signal spot area.

Background 3 (Full chip without spot during background times) For comparison, one might also consider the full chip during background times excluding the spot region. As before, normalization to tracking time and signal area are necessary. This will however exclude the most quiet region of the chip (spot region), thus leading to a slightly higher overall background level.

Background 4 (Full chip without spot during tracking times) A special advantage of the X-ray telescope is that background and tracking can be measured simultaneously. This is possible, since the magnet bore is focused to a small spot on the chip. Thus, in principle the rest of the chip is available for background measurements. In order to make use of this fact, the full chip without the signal spot during tracking times can be considered as background. Normalization to the signal area and the time spent in each pressure setting p_k is neccessary. A possible disadvantage of this definition is however, that part of a possible signal would be counted as background, since only the solar core is projected to the spot, while other parts of the Sun are still imaged to the rest of the chip.

The different definitions of background are illustrated in Fig. 7.10. Here, the intensity plots of the CCD chip are displayed for definition 1, 2, 3 and 4 from left to right. The color indicates the counts per pixel.

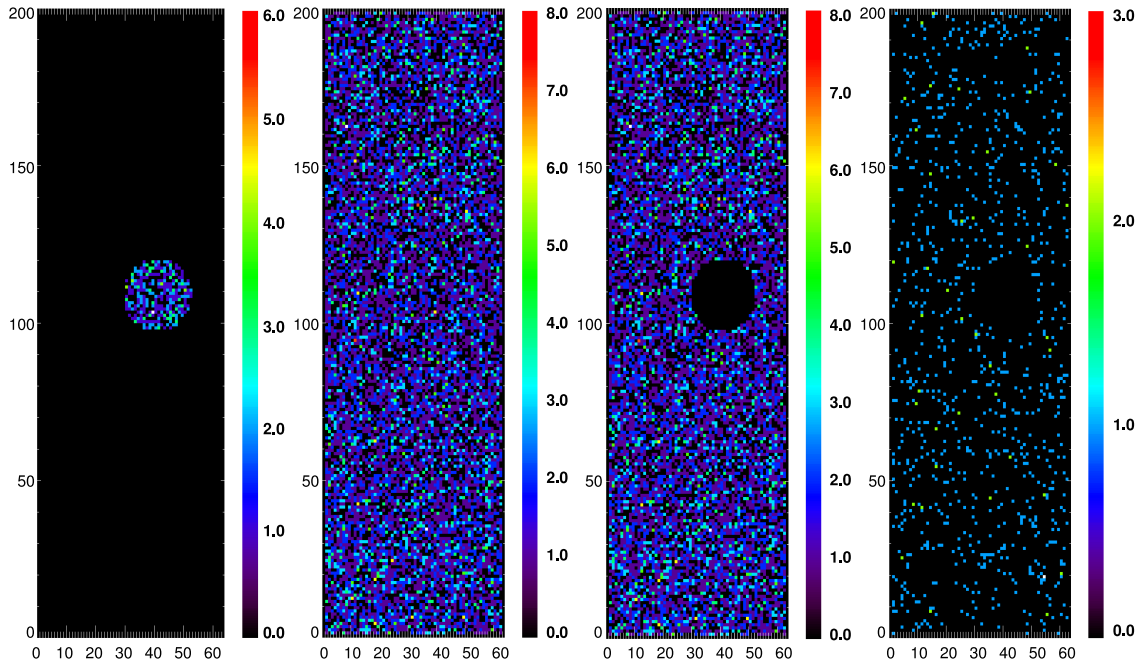

Figure 7.10: Intensity images of different definitions of background. From left to right images of the CCD chip (64 columns, 200 lines) for the following definitions are shown: background 1 (spot during background times), background 2 (full chip during background times), background 3 (full chip without spot during background times) and background 4 (full chip without spot during tracking times). The intensities are given in counts/pixel.

In Fig. 7.11, the spectra of the four different definitions of background are shown. Additionally, the total tracking counts have been included in the spectra (red). Each definition yields a background compatible with the others within statistical fluctuations. For Background 2 and 3 the error in each energy bin is typically of the order 0.1 counts, while for the definitions with lower statistics (Background 1 and 4) typical errors are around 0.5 and 0.3 counts, respectively. Some further definitions of background as used for the other detectors of CAST have been considered[8].They could not be used for the CCD detector, due to extremely low statistics in these cases.
A detailed table for the different background definitions can be found in Appendix E. Here also the statistical errors for each energy bin are provided.

Standard Background As standard background, Background 1 (Spot during background times) has been chosen. It provides both, reasonable statistics and the advantage of using the same region of the chip, in which also a potential signal would be expected. The influence of different definitions of background on the best fit value of $g^4_{a\gamma}$ and on the upper limit will be studied in Section 8.5,

[8]Daily background would be data acquired during non-tracking times of the days with a certain density setting, such that only the background taken under the same ^{4}He pressure conditions is taken into account for each tracking. Nearby background would be non-tracking data, which are close in time to the considered tracking. Off-coherence background uses trackings at pressure settings, which are far away from the considered pressure, such that no significant contribution is expected [128].

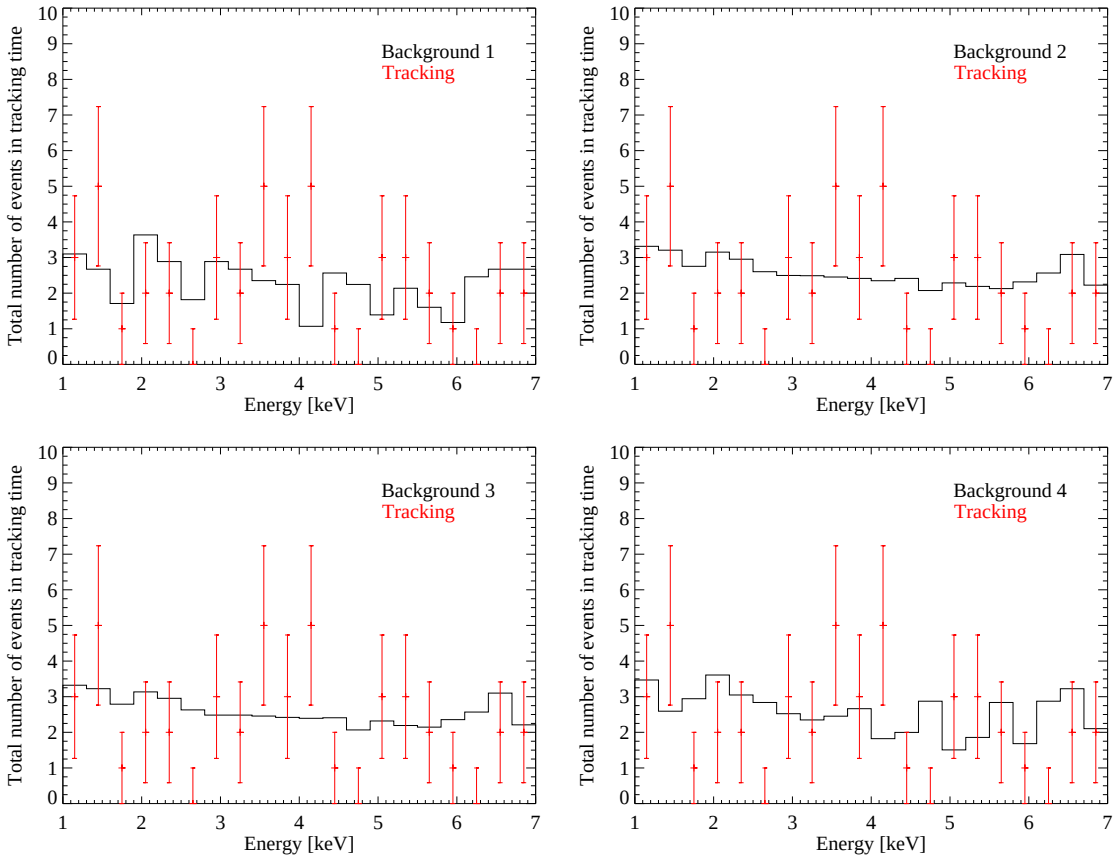

Figure 7.11: Background spectra for different definitions of background, which are compatible with each other within errors. The background spectra have been normalized to the total time of tracking. All counts in the spot during tracking are shown as well.

in which systematic effects will be discussed.

After having confirmed both, data quality and stability, and having defined the data sets to be used as tracking and background, the next step can be taken: the analysis of the CCD data acquired with ^{4}He gas in the cold bore of the CAST magnet.

Chapter 8

The Analysis of the CCD Data with ^{4}He Gas

The second phase of the CAST experiment with ^{4}He gas inside the magnetic field region has been a challenging and exciting extension of the solar axion search into the axion phase-space regions favored by theoretical models. This chapter will present the analysis of the CAST ^{4}He data acquired with the X-ray telescope. To start with, the expectations for a signature of solar axions in the CCD detector will be outlined. The following analysis can be divided into two stages. First, the data are checked for a potential axion signal, and then, in case no signal is observed, an upper limit on the axion-to-photon coupling constant is derived. After a consideration of possible sources of systematic errors, the final results for the ^{4}He phase of the CAST experiment for the CCD detector will be presented.

8.1 Expectations for Solar Axions with the CCD Detector

In order to have a clear idea of what kind of signature is expected from solar axions in the CCD detector, a few basic parameters will be considered. A determining factor is the total efficiency of the X-ray telescope along with the expected solar axion flux in the potential signal spot on the CCD chip. Applying this knowledge, the conversion probability and the expected number of photons in the CCD from axion-conversion can be obtained.

8.1.1 Basic Parameters of the CCD Analysis

Pressure Settings As discussed in Section 7.1, the CCD detector acquired data for a total of 149 out of 160 pressure settings. Each density setting is related to an effective photon mass via Eq. 4.44, which implies that maximal coherence for axion-to-photon conversion is obtained at a specific temperature and pressure for a narrow axion mass range around

$$m_a \approx \sqrt{0.02 \frac{p/\mathrm{mbar}}{T/\mathrm{K}}} \mathrm{eV}. \tag{8.1}$$

To simplify the notation in the following formulae, the settings, at which the CCD took data, have been renumbered according to the table given in Appendix C, such that every CCD setting can be referred to by an index number k with $k = 0, ..., 148$. Pressure values given as settings always refer to the pressure at 1.8 K and will be denoted by p_k.

Magnetic Field Length and Strength The nominal length of the magnetic field region to be used in the analysis is $L = (9.26 \pm 0.05)$ m [115]. The strength of the magnetic field has been obtained by fitting a linear function to the values provided in Tab. 5.1. The applied current of 13000 A during the ^{4}He phase results in a magnetic field with $B = (8.805 \pm 0.037)$ T.

Energy Range The energy range which has been considered for the CCD analysis of the ^{4}He data is 1-7 keV. The energy binning is 0.3 keV. This binning corresponds to approximately twice the energy resolution of the detector.

8.1.2 Total Efficiency and the Expected Solar Axion Flux for the CCD Detector

The Overall Efficiency for the X-Ray Telescope in the ^{4}He Phase As discussed in Chapter 6, the total efficiency for the X-ray telescope includes the efficiency of the mirror optics and the quan-

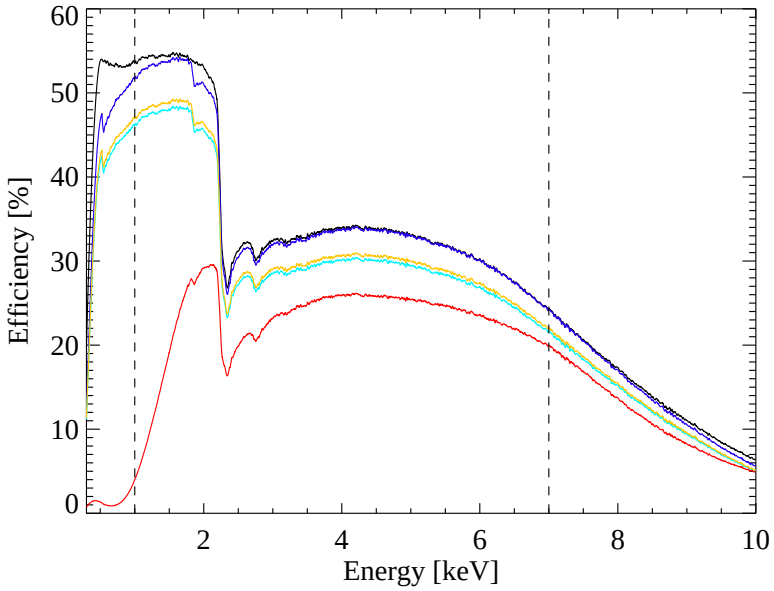

Figure 8.1: The efficiencies of the X-ray mirror optics and the CCD detector taking different conditions into account are shown. The black line represents the efficiency of the mirror optics, while the blue line takes additionally into account the quantum efficiency of the CCD detector. This corresponds to the data taking efficiency during Phase I in 2003. Including the tilt of the telescope yields the green curve. The consideration of the correction for the GRID offset increases the efficiency slightly and one obtains the efficiency for the 2004 data taking period (yellow). The final efficiency for Phase II with ^{4}He is displayed in red, taking into account the cold windows as measured at PANTER. The dashed lines mark the considered energy range for the analysis.

tum efficiency of the CCD detector. Furthermore, the tilt of the telescope relative to the magnet axis which has been introduced in 2004 to center the expected axion signal spot on the CCD chip, has been taken into account. Beside that, the correction for a known offset of the GRID measurements for the CAST magnet position has been considered in the calculations. Finally, the total efficiency also takes into account the cold window[1] and its strongback as measured at PANTER.
In Fig. 8.1, the influence of all different effects is shown. The final efficiency as it is taken into account for the analysis of the CCD ^{4}He data is represented by the lowest red line.
A comparison between the efficiencies using the measured PANTER data for the window and the CXRO[2] database to obtain the transmission, can be found in Fig. 8.2.

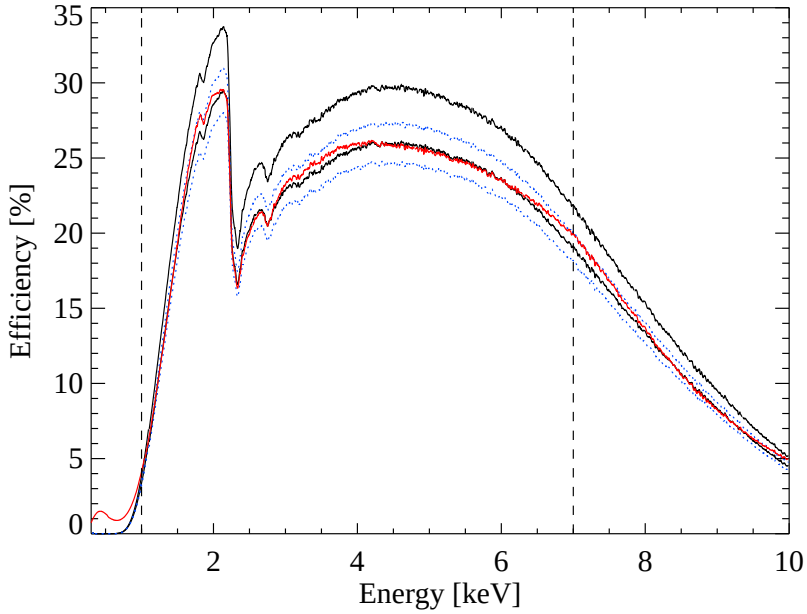

Figure 8.2: The overall efficiency of the X-ray telescope as used for the ^{4}He data is shown in red. It has been obtained using the PANTER results for the windows. The two black curves show the efficiency applying the CXRO database to determine the effect of the window (upper curve: without strongback, lower curve: including strongback). In blue, the estimated error range resulting from the CXRO data is added. The dashed lines mark the considered energy range for the analysis.

Here, the overall efficiency for the ^{4}He phase is shown. The upper black curve has been obtained using the CXRO database for the windows not taking into account the geometric effect of the strongback. The lower black curve takes also this effect into consideration. For the database, an error of 5% has been assumed (blue lines) due to the fact that the structure of the polypropylene used for the windows is not known. The overall efficiency as calculated using the PANTER measurements of the windows is shown in red. Taking into account the errors, the results are compatible. For the analysis, the red curve has been used.

[1] In case of the CCD this is the cold window F8 [151].
[2] Center for X-Ray Optics at Lawrence Berkley National Laboratory

Axion Flux The expected differential axion flux at Earth originating from the full Sun has been derived in Section 4.1.1 (Eq. (4.18)). Due to the use of mirror optics as an X-ray focusing device, the solar core is imaged to a circular region of 23 pixel diameter on the CCD chip. Thus, not the total solar axion flux has to be taken into account for the analysis of the CCD data. It has to be adjusted to the imaged region. In Fig. 8.3, both the total expected solar axion flux (black line) and the reduced flux as expected in the spot region of 11.5 pixel radius (solid red line) are shown.

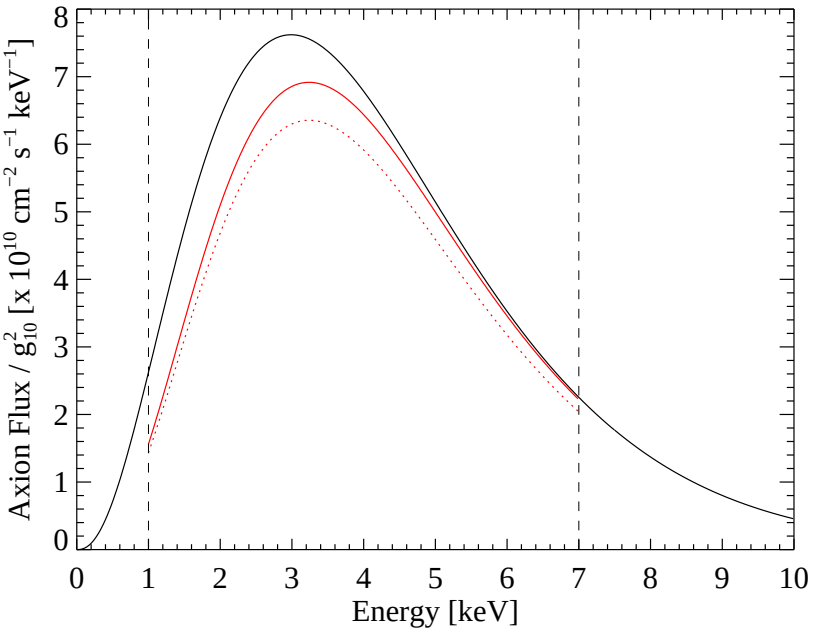

Figure 8.3: Expected solar axion flux at the Earth. The uppermost curve (solid black) shows the differential axion flux as calculated by Raffelt (see Eq. (4.18)) using the standard solar model of Bahcall et al. [107]. The solid red line represents the expected axion flux in the signal spot on the CCD chip of radius 11.5 pixel. The dashed red line takes into account the expected 8.12% Out-Of-Time events (see Section 6.2.1) considering this spot.

The reduced flux has been obtained by considering the energy dependent solar axion surface luminosity (see Eq. (4.19)) for the radial coordinate r which corresponds to the size of the signal spot. Furthermore, the influence of the Out-of-Time (OOT) events on the flux is shown as well in the same figure indicated by the dotted red line. This yields the expected axion flux as used for the ^{4}He analysis of the CCD data. The percentage of OOT events for the optimized spot size of 11.5 pixels radius is 8.12%.

Combined Axion Flux and Detector Efficiency The final expected solar axion flux in the signal spot of the CCD, which takes into account OOT events, can be compared with the expected axion flux for the whole Sun. This is illustrated in Fig. 8.4. Here, the black line shows the axion flux as calculated by Raffelt (Eq. (4.18)), while the red curve represents the axion flux as expected for the signal region on the CCD chip including the total detector efficiency as well as OOT events.

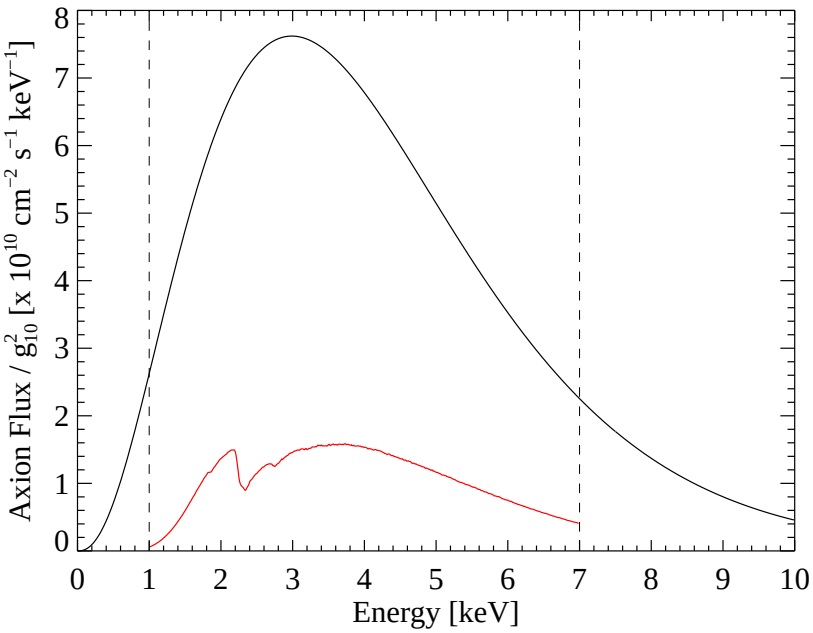

Figure 8.4: Differential axion flux on Earth as expected for the CCD detector. While the black line represents the calculated differential axion flux expected at Earth from the entire Sun, the red line shows the expectations for the CCD detector system. All relevant factors are included: reduced flux in signal region, total efficiency of the X-ray telescope and Out-Of-Time events.

8.1.3 Conversion Probability

The general function describing the axion-to-photon conversion probablility for the Primakoff effect has been derived in Section 4.2 (Eq. (4.25)). It takes into account a buffer gas present in the magnetic field region. For each pressure setting p_k, the probability of conversion depends on the axion mass m_a and the axion energy E_a, if the magnetic field B and its length L are given. Furthermore, it is proportional to the square of the axion-photon coupling constant $g_{a\gamma}$. For the k-th density setting p_k, the probability is given by

$$P_{a\to\gamma,k} = P_{a\to\gamma}(p_k, E_a, m_a, g_{a\gamma}^2) = \left(\frac{B g_{a\gamma}}{2}\right)^2 \frac{1}{q_k^2 + \Gamma_k^2/4}\left[1 + \mathrm{e}^{-\Gamma_k L} - 2\mathrm{e}^{-\Gamma_k L/2}\cos\left(q_k L\right)\right], \tag{8.2}$$

where $q_k = q_k(E_a, m_a) = q(p_k, E_a, m_a)$ represents the momentum transfer between the axion and the real X-ray photon and $\Gamma_k = \Gamma_k(E_a) = \Gamma(p_k, E_a)$ is the absorption of converted photons in ^{4}He gas.

Momentum transfer The momentum transfer has been discussed in detail in Section 4.2. For a specific pressure setting p_k it is given by

$$q_k = q(p_k, E_a, m_a) = \left|\frac{m_{\gamma,k}^2 - m_a^2}{2E_a}\right|, \tag{8.3}$$

where the effective photon mass $m_{\gamma,k} = m_\gamma(p_k)$ is provided by

$$m_{\gamma,k} = \sqrt{0.020 \frac{p_k/\text{mbar}}{T/\text{K}}} \text{eV}, \tag{8.4}$$

as can be seen from Eq. (4.44).
The product $qL/2$ must be small to fulfill the coherence condition. Since the length of the magnetic field L is fixed at the CAST experiment, the momentum transfer q determines the axion mass range which can be studied with high sensitivity. Due to the fact that a higher gas pressure at a constant temperature leads to a larger effective photon mass, higher axion masses become accessible, if more and more helium gas is put inside the cold bore of the CAST experiment.

Absorption The second important physical quantity contributing to the conversion probability function in presence of a buffer gas is the absorption Γ_k of photons in ^{4}He gas. It depends on the axion energy and the pressure of the gas in the magnet at a given temperature. The detailed derivation of the formula for the absorption of photons in ^{4}He gas can be found in Section 4.2.2. Using the NIST database [112], a fit formula describing the absorption at different energies has been determined. For each pressure setting p_k, it includes all relevant effects such as the photo-electric effect, coherent and incoherent scattering.
The fit formula is provided by

$$\begin{aligned} \log_{10}(\Gamma(p_k, E_a)) \quad = \quad & 0.014 \log_{10}^6 E_a + 0.166 \log_{10}^5 E_a + 0.464 \log_{10}^4 E_a \\ & + 0.473 \log_{10}^3 E_a - 0.266 \log_{10}^2 E_a - 3.241 \log_{10} E_a \\ & - 0.760 + \log_{10} p_k. \end{aligned} \tag{8.5}$$

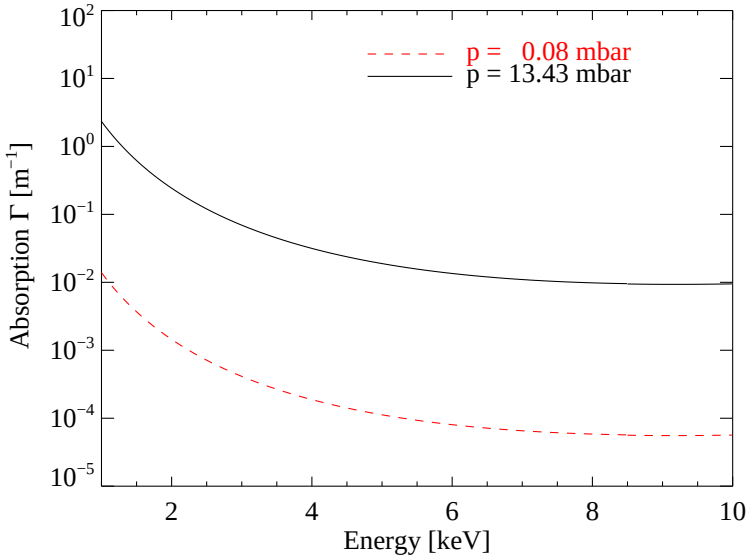

Figure 8.5: Absorption function Γ in ^{4}He for the lowest ($k = 0$, $p_0 = 0.08$ mbar) and the highest ($k = 148$, $p_{148} = 13.43$ mbar) pressure setting as taken with the CCD detector.

In Fig. 8.5, the absorption function for the lowest ($k = 0$, $p_0 = 0.08$ mbar) and the highest ($k = 148$, $p_{148} = 13.43$ mbar) pressure setting of the ^{4}He data taking run are shown. The pressure is given at a temperature of 1.8 K.

Probability of Conversion Taking into consideration the just discussed facts, the conversion probability can be determined for each pressure setting k as a function of axion mass, energy and the square of the axion-photon coupling constant $g_{a\gamma}$. Figure 8.6 illustrates this dependence for a specific pressure setting, namely $k = 60$, which corresponds to a pressure of $p_{60} = 5.49$ mbar or an effective photon mass of 0.247 eV. The conversion probability is maximal around the corresponding axion mass and drops fast for masses far away from the coherence. Some minor contributions to the probability originate from masses close to the corresponding effective photon mass of the considered pressure setting. Furthermore it can be seen that the probability increases with energy. To illustrate the dependence of the conversion probability on the axion mass for specific energies, Fig. 8.7 can be used. It shows the conversion probability for four different axion energies at the same pressure setting ($p_{60} = 5.49$ mbar). As can be seen from Eq. (8.2) and Eq. (8.3), the FWHM of the probability distribution increases for larger energies E_a. Furthermore, since the absoption Γ is inversely proportional to the axion energy E_a, the probability is larger for higher energies, due to decreasing absorption.

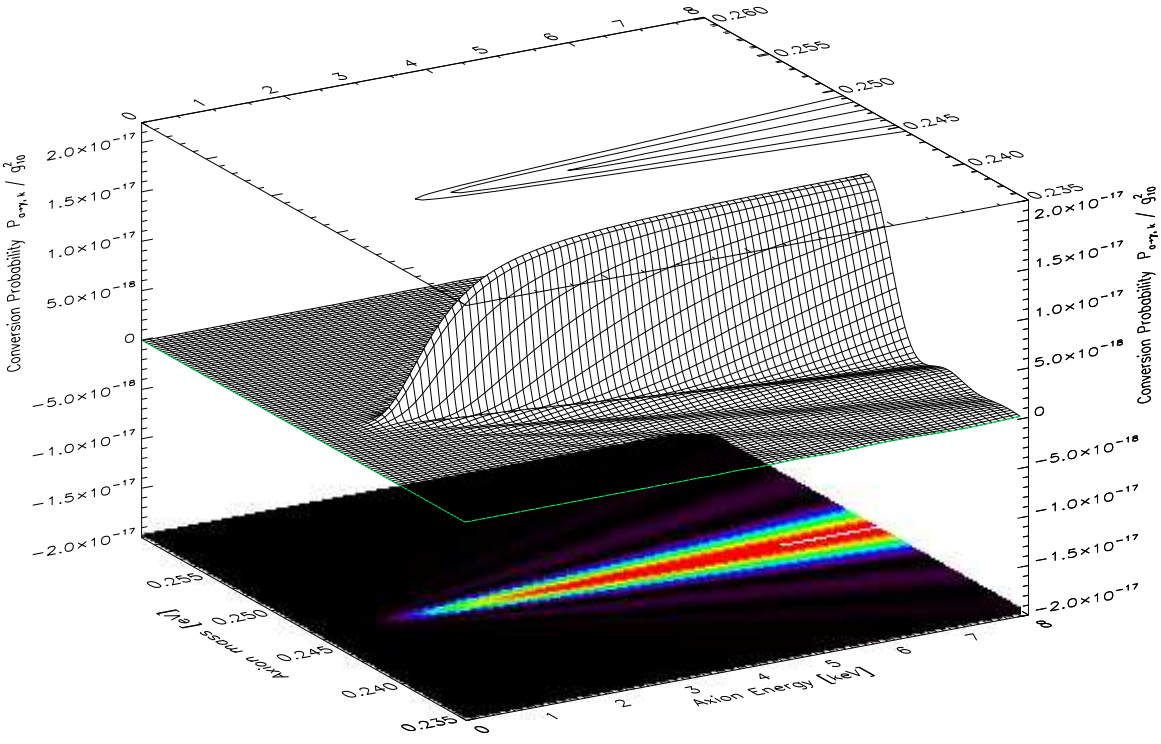

Figure 8.6: Conversion probability as function of axion mass and energy. The plot is for pressure step $k = 60$ of the CCD, which corressponds to $p_{60} = 5.49$ mbar in pressure or 0.247 eV in effective photon mass.

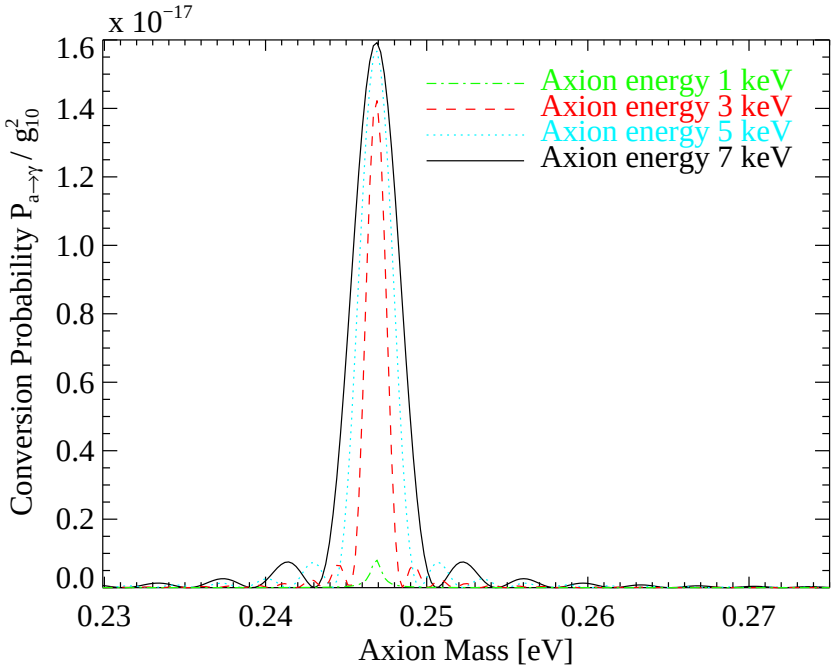

Figure 8.7: Conversion probability as function of axion mass for axion energies E_a of 1, 3, 5 and 7 keV. The curves are given for pressure step $k = 60$ of the CCD, which corressponds to $p_{60} = 5.49$ mbar in pressure at 1.8 K or 0.247 eV in effective photon mass, respectively.

The energy dependence of the conversion probability for different axion masses, on the other hand, is displayed in Fig. 8.8. The pressure at $T = 1.8$ K is kept fixed as $p_{60} = 5.49$ mbar. It can be seen that the main contributions to the conversion probability originate from axion masses close to the effective photon mass corresponding to 5.49 mbar. Thus, only masses around $m_\gamma = 0.247$ eV contribute significantly to the overall conversion probability.

8.1.4 Expected Number of Photons in the CCD Detector

At a given pressure, the expected number of photons $N_{\gamma,k}$ in the CCD from axion-to-photon conversion in the helium-filled magnet bore of CAST can be derived using Eq. (4.51), which has been discussed in Section 4.3. At the k-th pressure setting p_k, one obtains

$$N_{\gamma,k} = N_\gamma(p_k, m_a, g^4_{a\gamma}) = \int_E \frac{d\Phi'(E_a, g^2_{a\gamma})}{dE_a} P_{a\to\gamma,k}(E_a, m_a, g^2_{a\gamma})\, \epsilon(E_a)\, \Delta t_k\, A\, dE_a, \qquad (8.6)$$

which depends on the forth power of the coupling constant $g_{a\gamma}$. The differential solar axion flux expected in the CCD detector, $d\Phi'(E_a, g^2_{a\gamma})/dE_a$, takes into account that only the solar core is imaged to the signal spot and considers Out-of-Time events. The total efficiency of the detector $\epsilon(E_a)$ has to be taken into account. Furthermore, the area of the magnet bore $A = 14.522$ cm^2 is included as well as the exposure time Δt_k at the considered pressure setting p_k.
The expected number of photons depending on the axion mass m_a for specific energies is depicted

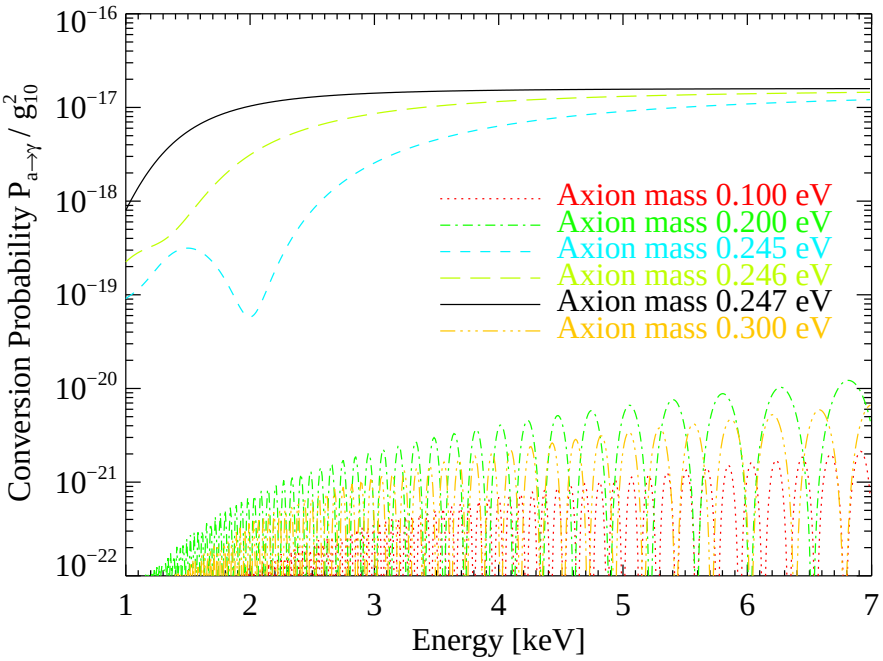

Figure 8.8: Conversion probability as function of axion energy for different axion masses. The curves are given for pressure step $k = 60$ of the CCD, which corressponds to $p_{60} = 5.49$ mbar in pressure at 1.8 K or 0.247 eV in effective photon mass.

in Fig. 8.9 for the 60th pressure setting ($p_{60} = 5.49$ mbar). Here, the exposure time at this setting for the CCD detector of $\Delta t_{60} = 5641.0$ s has been used. While in the upper part of Fig. 8.9 the detector efficiency is not taken into account ($\epsilon = 1$), the expected photon number for the CCD detector system is displayed in the lower part of the same figure. In order to assure that the expected number of photons is calculated with sufficient accuracy, energy steps of 0.01 keV have been used in the determination of N_γ. For the analysis, it is necessary to rebin this expected counts to obtain reasonable energy intervals for the detector. For the i-th energy bin E_i, the expected number of photons at the k-th setting can be obtained as

$$N_{ik} = \int_{E_i}^{E_{i+1}} \frac{d\Phi'(E_a, g_{a\gamma}^2)}{dE_a} P_{a\to\gamma,k}(E_a, m_a, g_{a\gamma}^2)\, \epsilon(E_a)\, \Delta t_k\, A\, dE_a, \tag{8.7}$$

where $\Delta E_a = E_{i+1} - E_i = 0.3$ keV. The expected N_γ for a pressure of $p_{60} = 5.49$ mbar can be found in Fig. 8.10.
The total N_γ integrated over all energies from 1 to 7 keV is shown in Fig. 8.11 for several pressure settings as acquired during the ^{4}He data taking run. The efficiency of the CCD detector system has been taken into account and for each of the displayed pressure settings the average tracking during the ^{4}He phase, i.e. 5675.3 s, has been used as exposure time. The influence of the absorption with increasing pressure can be observed in the plot, since the maximum number of expected photons from conversion drops with increasing density of helium in the magnet.

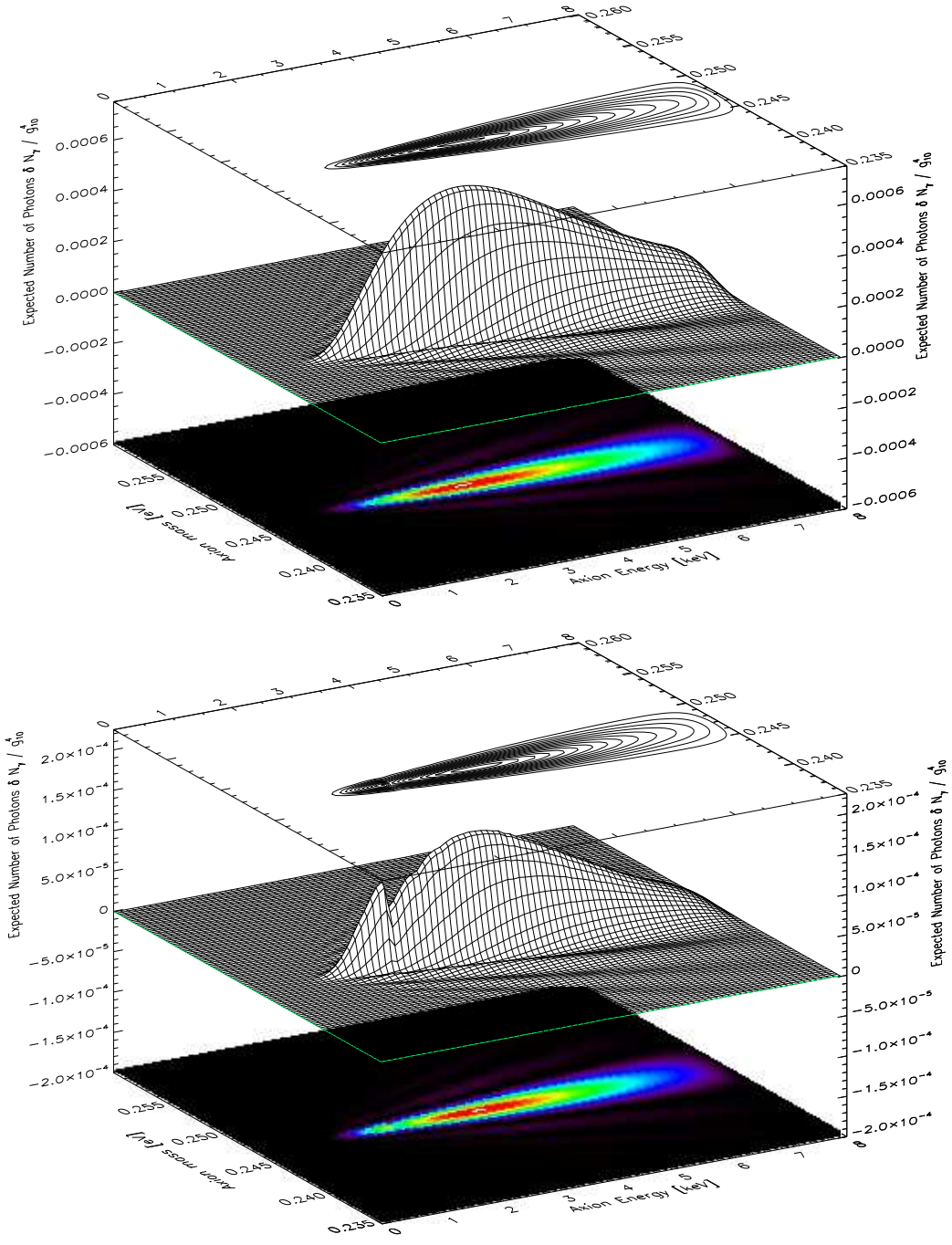

Figure 8.9: Top: Expected number of photons at pressure setting $p_{60} = 5.49$ mbar with efficiency $\epsilon = 1$ at 1.8 K as a function of axion energy and mass. Bottom: Equivalent plot taking into account the efficiency of the X-ray mirror optics and the CCD detector. In both plots, the exposure time at this setting for the CCD detector of 5641.0 s has been used.

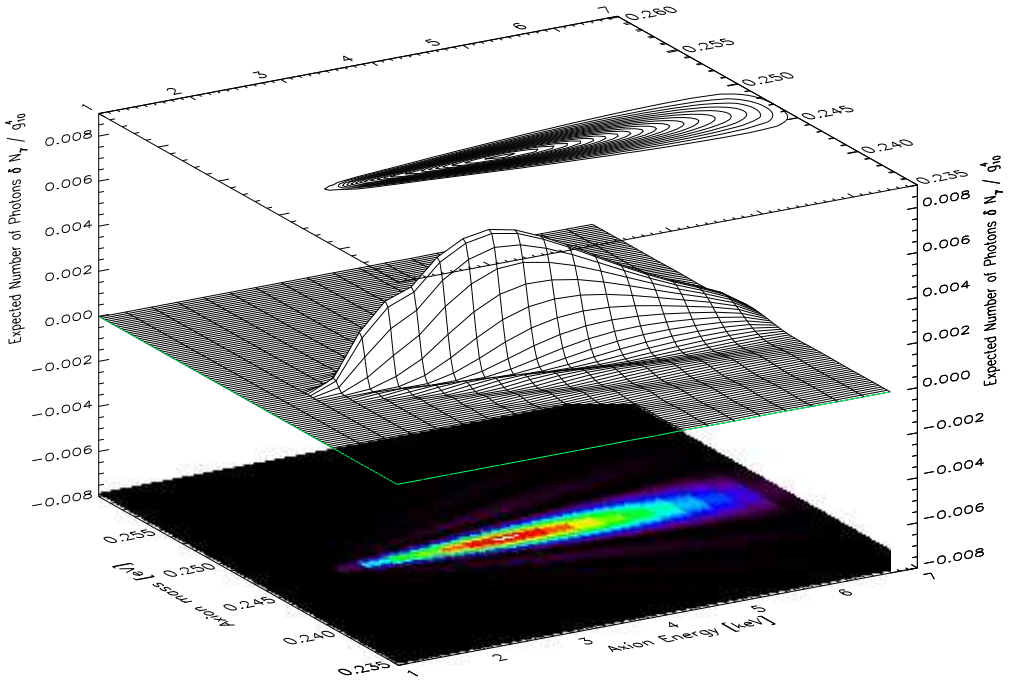

Figure 8.10: Expected number of photons at pressure setting $k = 60$. The plot takes into account the appropriate energy binning and the total efficiency of the X-ray mirror optics and the CCD detector at a ^{4}He pressure of $p_{60} = 5.49$ mbar at 1.8 K. The exposure time at this setting for the CCD detector of $\Delta t_{60} = 5641.0$ s has been used.

8.2 Analysis Procedure for the CCD Data

8.2.1 Basic Concept of the Analysis

The analysis of the CAST CCD data can be divided into two different stages. In a first step, the data are checked for a signal from axion-to-photon conversion via Primakoff effect. In case there is no signal observable, when comparing background and tracking data, the second stage of the analysis is to extract an upper limit on the axion-to-photon coupling constant $g_{a\gamma}$ dependent on the axion mass m_a.
Since the tracking data of Phase II are divided into density steps, the statistics for each step are very small, such that a likelihood method needs to be applied. This has already been done for the CCD data during CAST's first phase [133]. In Phase II, it is necessary for all detectors of CAST.
The extended maximum likelihood method, which will be used in this analysis and which will be discussed in the following section, does not incorporate a possibility to include the uncertainties of the background. However, it has been checked that in the case of the CCD, this does not pose a problem.
Even though the analysis is done in a way, such that it is possible to look at every single density setting separately, in the end the information of all pressure settings must be combined to obtain a single final result for Phase II. Each pressure setting enables to study a certain narrow axion mass

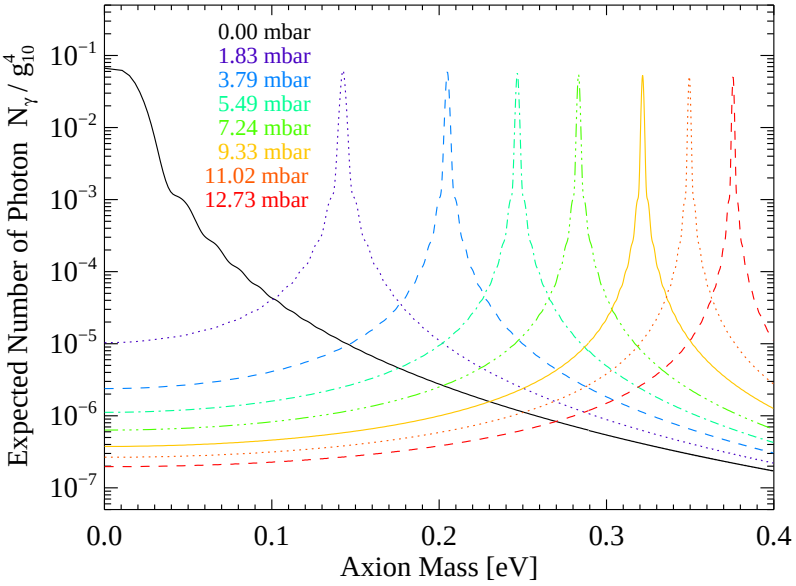

Figure 8.11: Expected number of photons N_γ including the CCD efficiency at several different pressure settings in the 1-7 keV range. The considered time corresponds to that of an average tracking, i.e. 5675.3 s.

range with high sensitivity (see Fig. 8.11). Neighboring density steps, however, will provide additional information about the same masses. To combine all pressure settings, likelihood functions are used.

8.2.2 The Maximum Likelihood Method

The expected number of photons from axion-conversion N_{ik} at a specific density setting p_k in the energy bin E_i can be obtained as Eq. 8.7. The total expectation of counts μ_{ik} in the i-th energy bin E_i at the k-th pressure setting p_k is given by

$$\mu_{ik} = b_{ik} + N_{ik}. \tag{8.8}$$

Here, b_{ik} is the expected background in the i-th energy bin at density step k. It has to be appropriately normalized.
Due to low statistics, one has to deal with Poissonian statistics and the extended Maximum Likelihood (ML) Method can be applied [6]. By applying this method for a single pressure setting p_k, the ML ratio $\mathcal{L}_k$ rather than the standard likelihood function $\mathcal{L}_{\text{std}}$ is maximized. Generally, the standard likelihood function for poissonian statistics is given by

$$\mathcal{L}_{\text{std}} = \prod_i \mathrm{e}^{-\mu_{ik}} \frac{\mu_{ik}^{n_{ik}}}{n_{ik}!}, \tag{8.9}$$

where n_{ik} is the number of counts during tracking in the i-th energy bin and the k-th pressure setting for CAST and the index for the energy bins i runs from 1 to 20 in case of the CCD. For the

ML ratio of the k-th density setting one obtains then

$$\mathcal{L}_k = \frac{\mathcal{L}_{\rm std}}{\mathcal{L}_{0k}} = \frac{\prod_i \mathrm{e}^{-\mu_{ik}} \left(\mu_{ik}^{n_{ik}}/n_{ik}!\right)}{\prod_i \mathrm{e}^{-n_{ik}} \left(n_{ik}^{n_{ik}}/n_{ik}!\right)}, \tag{8.10}$$

where $\mathcal{L}_{0k}$ represents the normalization term. The advantage of defining the ML function in this normalized form is that it yields information about the goodness-of-fit. The expression $-2\ln\mathcal{L}_k$ behaves asymptotically as a χ^2-function, such that from Eq. (8.10) follows

$$\chi^2_k = -2\ln\mathcal{L}_k = \sum_i \left[2\mu_{ik} - n_{ik}\ln\left(\mu_{ik}^2\right) - 2n_{ik} + n_{ik}\ln\left(n_{ik}^2\right)\right]. \tag{8.11}$$

Therefore, maximizing the likelihood function (or its logarithm) is equivalent to minimizing the χ^2-function.
In absence of a signal, the minimal value $\chi^2_{\rm min}$ is expected to be close to $\chi^2_{\rm Null}$, i.e. the value of χ^2 for which $g^4_{a\gamma} = 0$. In case $g^4_{a\gamma} = 0$, tracking and background data can be directly compared, since no photons from conversion are expected. The difference between $\chi^2_{\rm min}$ and $\chi^2_{\rm Null}$ can be used to confirm the absence of signal.
When all pressure settings have been considered separately and the individual ML functions per density setting are calculated, the global likelihood function $\mathcal{L}$ can be obtained by multiplying the individual likelihoods[3]

$$\mathcal{L} = \prod_k \mathcal{L}_k, \tag{8.12}$$

with $k = 0, ..., 148$. Before deriving an upper limit, which takes into account the information of all pressure settings, the global ML function has to be maximized or equivalently, its χ^2-function

$$\chi^2 = -2\ln\mathcal{L}, \tag{8.13}$$

must be minimized to determine the best fit value for the axion-photon coupling constant $g^4_{a\gamma}$ at each axion mass m_a.
The confidence interval for the l-th axion mass can be estimated using

$$\left[\ln\mathcal{L}(g^4_{a\gamma})\right]_l = \left[\ln\mathcal{L}_{\rm max}(g^4_{a\gamma})\right]_l - \frac{\sigma^2}{2}, \tag{8.14}$$

with $\left[\ln\mathcal{L}_{max}(g^4_{a\gamma})\right]_l$ being the maximal value at the l-th mass. The statistical error of the best fit value for $g^4_{a\gamma}$, i.e. $g^4_{a\gamma,\rm min}$, can therefore be obtained as

$$\left[\chi^2(g^4_{a\gamma})\right]_l = \left[\chi^2_{\rm min}(g^4_{a\gamma})\right]_l + \sigma^2. \tag{8.15}$$

Here, $\left[\chi^2_{\rm min}(g^4_{a\gamma})\right]_l$ represents the minimal χ^2 at the l-th axion mass. Since the χ^2-distribution is not symmetric in case of the CCD, the statistical error will also be asymmetric.

[3]Equivalently, one can add up all individual log-likelihood functions to obtain the global log-likelihood.

The upper limit at 95% confidence level can be derived by the integration of the Bayesian probability, which is equivalent to the likelihood function, over the physical region[4] of $g_{a\gamma}^4$ up to 95% of the total (physical) area, i.e.

$$\int_0^{g_{a\gamma}^4(95\%)} P(g_{a\gamma}^4) dg_{a\gamma}^4 = 0.95, \tag{8.16}$$

where the probability $P(g_{a\gamma}^4)$ is given by

$$P(g_{a\gamma}^4) = \mathrm{e}^{-\chi^2/2} = \mathcal{L}(g_{a\gamma}^4). \tag{8.17}$$

Repeating this step for all considered axion masses, one obtains an exclusion plot for the axion phase space[5].
In order to combine all three detectors one can proceed equivalently, i.e. multiplying the global likelihoods of each detector

$$\mathcal{L}_{\mathrm{CAST}\ ^4\mathrm{He\ Phase}} = \mathcal{L}_{\mathrm{TPC}} \cdot \mathcal{L}_{\mathrm{MM}} \cdot \mathcal{L}_{\mathrm{CCD}}, \tag{8.18}$$

to obtain a global CAST likelihood function and derive an exclusion plot for Phase II with ^{4}He in the magnet bores. This result can then also be combined with the achievements of Phase I.

8.3 Absence of a Signal

The first step of the analysis is to check for a possible signal in the tracking data. Unfortunately, no evidence of a signal could be found in the ^{4}He data acquired with the CCD detector as will be shown in this section.

8.3.1 Comparison of Observed Events with the Theoretically Expected Distribution

Since the axion search at CAST is a rare event search, Poissonian statistics should apply. This is especially expected for the CCD detector, since its background level is very low. During a total of 187 tracking runs with an average duration time of 5675.3 s, zero events in the expected axion signal region have been registered in 148 of all runs. One event was observed on 35 of the tracking days. Moreover, in two runs a double hit was found, and the rather rare case of 3 hits in the spot occurred twice. More than 3 photons have not been registered inside the circular signal area during any single tracking run.
Comparing this observation with the expected distribution assuming Poissonian statistics, it turns out that observation and expectation are compatible within statistical fluctuations. The mean background level of two different background definitions has been used for this comparison. Taking into account events in the spot region during background times (Background 1), an average of 0.246 ± 0.012 counts per average tracking is expected in the energy range of 1-7 keV. Using Background 2 (full chip during background times) normalized to the spot region, 0.275 ± 0.002 counts

[4] The physical region refers to positive values of $g_{a\gamma}^4$.

[5] Note that in principle, it is also possible to calculate the upper limit for each single pressure setting in this way, but since neighboring pressure settings contribute to the same masses, one loses information in comparison to the combined limit.

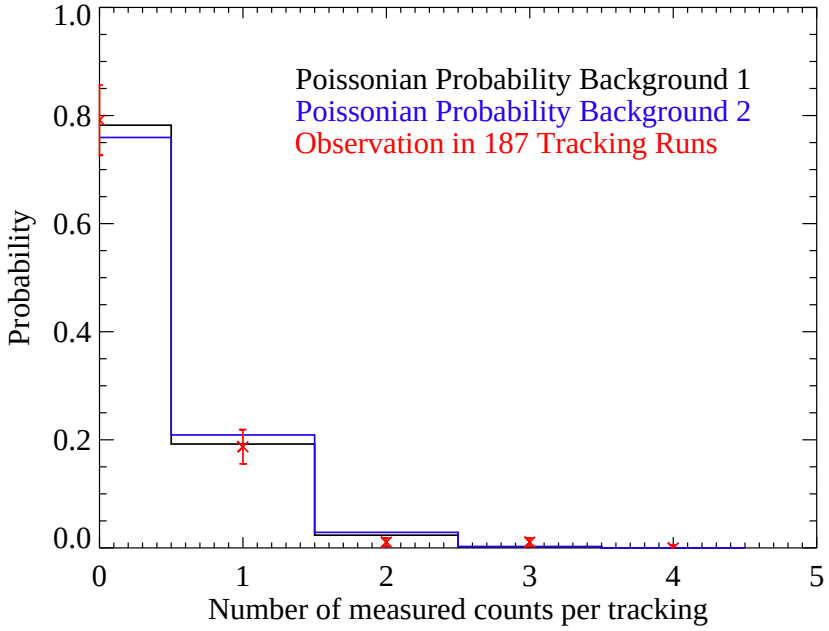

Figure 8.12: Comparison of observed counts per tracking and poissonian expectation. The black and blue line represent the theoretical occurences of 0, 1, 2, 3 and 4 events during an average tracking for two different but compatible definitions of background. In red, the observation in CAST Phase II with ^{4}He is shown. The indicated errors result from statistical uncertainties.

per average tracking should be registered in the considered energy range. This is also visualized in Fig 8.12, where the theoretical expectation has been calculated for the two different compatible background definitions. The black line represents the poissonian distribution for Background 1 normalized to the time of an average tracking. The blue line, on the other hand, takes into account Background 2, which has to be normalized with respect to time of the tracking and the signal area. The actual observation in the CAST experiment is plotted in red. While two events in one tracking have been observed slightly less often than expected, for three events it is the opposite case, however, still within the expected statistical fluctuations.

8.3.2 Hypothesis Testing and Goodness-of-Fit

In order to confirm the compatibility between background and tracking, a goodness-of-fit test has been performed. All tracking runs have been considered separately, i.e. without taking into account the different density settings. Then, the value of χ^2_{Null} has been determined. In a "good" experiment, the mean of a χ^2-distribution should correspond to the number of degrees of freedom N. However, the probability distribution function of the reduced χ^2, i.e. χ^2 over N, depends on the number of degrees of freedom N, such that in order to provide a meaningful statement, one has to provide N along with the reduced χ^2.
The goodness-of-fit can be characterized using the so-called $\mathcal{P}$-values as defined in Ref. [6]. Generally, the $\mathcal{P}$-value represents the probability of obtaining a result which is at least as extreme as

the one that was actually observed under the assumption that the Null hypothesis is true. If x is a function of the data, showing in some way the degree of consistency between the data and the hypothesis H_{Null}, then the $\mathcal{P}$-value can be obtained by integrating the probability distribution function $g(x|H_{\text{Null}})$ from the value of the statistic obtained in the real experiment (x_{obs}) to infinity

$$\mathcal{P} = \int_{x_{\text{obs}}}^{\infty} g(x|H_{\text{Null}})dx, \tag{8.19}$$

if x is defined in such a way that large values correspond to poor agreement with the hypothesis. In Fig. 8.13, the reduced χ^2_{Null} is plotted over the number of degrees of freedom N. The solid lines represent the $\mathcal{P}$-values corresponding to the percentages given. The data points for the 187 tracking runs are added color-coded, black representing zero-event runs, red one-event-runs and green and blue indicating runs with 2 and 3 events, respectively. The percentages given here correspond to the fraction of the 187 tracking runs, in which the specific events have been observed. Fig. 8.13 can be understood as follows: assuming the Null hypothesis holds, the probability of obtaining a result, which is at least as extreme as the observed one, can be obtained from the lines representing the p-values. For the cases of zero events (black symbols) this means for example that, in case tracking and background are compatible, the probabilitity to obtain these events at least to the observed degree is larger than 99%. When one event was observed in a tracking (red symbols), which happened in about 19% of all cases, the $\mathcal{P}$-value is larger than 95% assuming compatibility

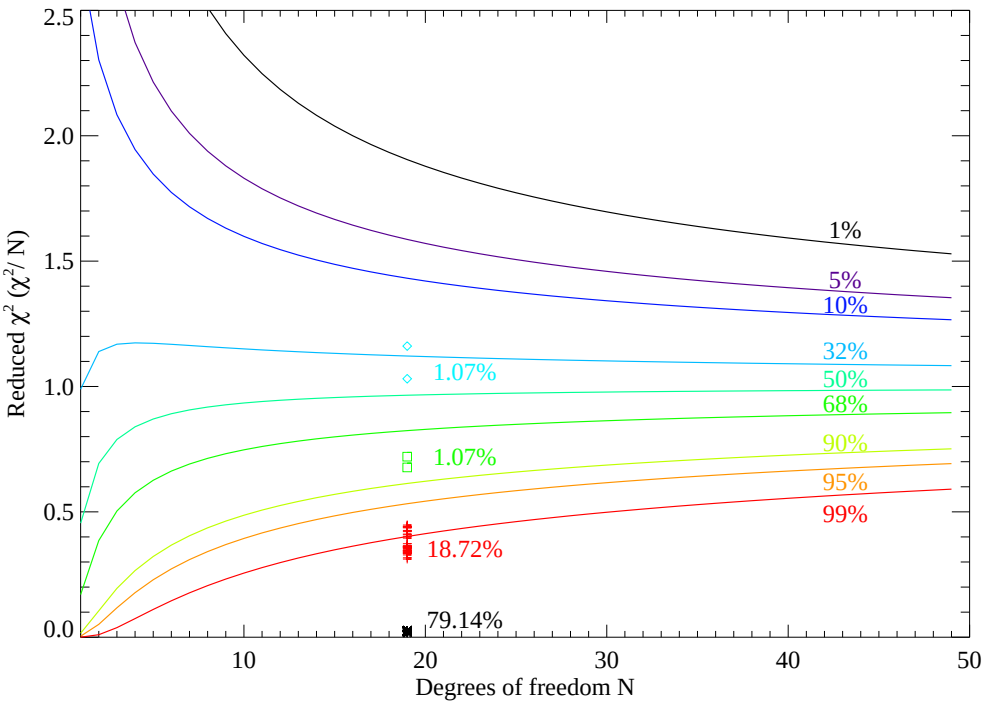

Figure 8.13: Reduced χ^2_{Null} versus degrees of freedom for all tracking runs taken in the ^{4}He phase of CAST with the CCD detector. The curves represent the $\mathcal{P}$-values, while the points indicate the observations.

of tracking and background. For the cases of two and three events the $\mathcal{P}$-values decrease further, yielding probabilities of obtaining a scenario as extreme as the observed one or more extreme of larger than 68% and 25% for two and three events, respectively. Summarizing, it can be said that assuming the compatibility of tracking and background (Null hypothesis), no significant deviations from the Null hypothesis could be observed on the 25% level.

8.3.3 Scan of the Chip

Since the signal spot provides only a fraction of the chip surface, it is advisable to study the compatibility of background and tracking in different locations on the chip. This will, on one hand, show that the expected signal region is located in a low background surrounding, which justifies the choice of the standard background (Background 1: spot during background times). On the other hand, it will become obvious, which regions on the chip might be considered as areas of higher background level, thus increasing the overall background. Moreover, it can be studied, if the background is Poissonian distributed for all possible circular regions on the chip.
The procedure to extract this kind of information is the following: a spot of the size of the expected axion signal region is shifted over the whole chip. As a possible center, a pixel on the full chip qualifies, if it is at least 12 pixels away from any border. In this way, a complete spot with a radius of 11.5 pixels can always be considered. For every one of these potential center points, all 187 tracking runs are then taken into account. It is studied, how often 0, 1, 2, 3 etc. events would be registered, if this spot was the real signal region.
In Fig. 8.14 the results have been visualized. Each plot is an image of all possible spot centers. The color indicates for each pixel the frequency, with which a certain event (0 counts in tracking, 1 count in tracking etc.) appeared in a spot with this specific center during all tracking runs. For the real signal spot, for example the color of the pixel $(x/y) = (40/108)$ will yield 148 times zero events (from left image in Fig. 8.14), 35 times one count (from second image in Fig. 8.14), twice two and three events (from third and fourth image in Fig. 8.14, respectively). For comparison, the expected occurances of the different events assuming Poissonian statistics and a mean background per average tracking of 0.246 ± 0.012 counts (Background 1) and 0.275 ± 0.002 counts (Background 2) are given in Tab. 8.1. The expected axion spot region is relatively quiet in comparison to the rest of the chip. In Tab. 8.2, the mean observed multiplicity of zero, one, two and three events of all possible spots is provided. It has been derived from the results of Fig. 8.14. Furthermore, this table also includes the actually observed multiplicity in the real signal region, such that it can be seen that it is more quiet than average, besides being compatible with Poissonian expectations.
It should be noted that no single tracking had 4 or more events in the real signal spot. Considering all possible spots, not more than 4 events have been registered during a single tracking in a circular region. It might appear, that the observed frequency of 3 events in the real signal spot is rather high as compared to expectations and mean observation of all possible spots. These "suspicious" events will be considered in the following.

8.3.4 Potential Candidate Pressure Settings

For two different density settings, three counts have been observed in the spot during a single tracking.These pressures were $p_{39} = 3.75$ mbar and $p_{70} = 6.33$ mbar. At the 39th setting, a total

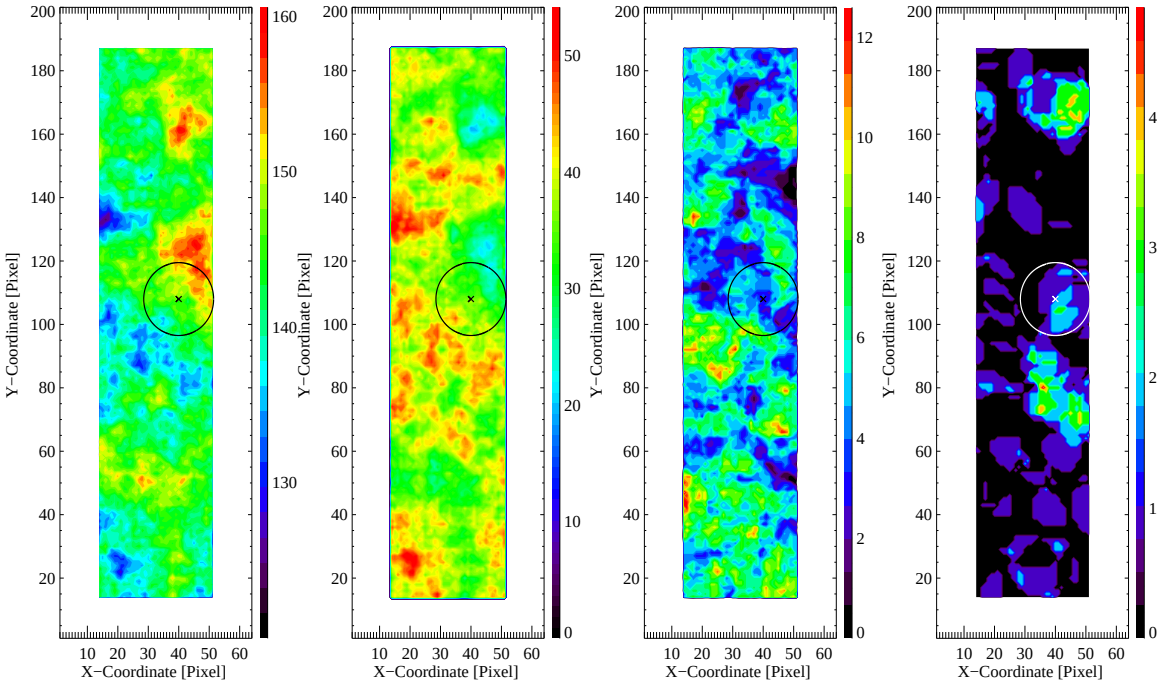

Figure 8.14: Results of scanning the chip. All possible centers for a circular region of the same size as the expected axion signal spot. The color scale indicates, how often a certain number of events has been observed during all 187 tracking runs in a circle of 11.5 pixel radius, if the considered pixel is taken as a center of this circle. In the first plot from left the frequency of zero events in all ^{4}He tracking runs is shown. The second plot from left represents the multiplicity of one event during 187 tracking runs. The third and fourth plot are the corresponding ones for two and three events, respectively.

Background 1: 0.246 cts/average tracking	**Probability [%]**	**Multiplicity in 187 trackings**
0 events	78.21	146.25
1 event	19.22	35.95
2 events	2.36	4.42
3 events	0.19	0.36
4 events	0.01	0.02

Background 2: 0.275 cts/average tracking	**Probability [%]**	**Multiplicity in 187 trackings**
0 events	75.94	142.01
1 event	20.90	39.08
2 events	2.88	5.38
3 events	0.26	0.49
4 events	0.02	0.03

Table 8.1: Expected Poissonian probability and expected occurance of different number of events in 187 tracking runs for two different background definitions (Background 1 and 2).

Number of Events	**Mean Multiplicity**	**Multiplicity in Axion spot**
0	143.43	148
1	37.57	35
2	5.34	2
3	0.60	2
4	0.07	0

Table 8.2: Mean observed occurence of different number of events in 187 tracking runs averaged over all possible circular regions on the chip and actually observed multiplicity in the real signal region.

of 14 tracking runs were done, to determine the significance of the observed effect. For the 70th pressure, the tracking has not been repeated with the CCD detector, but the other detectors did not show any increase in counts. A detailed list of the dates, tracking times and energies of the events can be found in Tab. 8.3.
While the three counts in the spot would correspond to 2.9-3.0 sigma depending on the background definition for May 30 (3.0-3.1 sigma on August 21), the potential signal washes out to a 2.2-2.4 sigma after 14 trackings. Thus, it can be seen as an expected fluctuation within statistical uncertainties. The development of the significance with increasing number of trackings at the same density step is shown in Fig. 8.15 for two different background definitions, namely the normalized background from the spot region during non-tracking times (Background 1, black triangles) and the normalized background obtained from the full chip during background times (Background 2, red squares).

Pressure [mbar]	Date [dd/mm/yy]	Tracking Time [s]	No. of counts	Energy [keV]
3.75	30/05/06	6180.5	3	4.40, 5.66, 6.88
3.75	01/06/06	6179.5	1	5.16
3.75	02/06/06	6120.5	0	–
3.75	03/06/06	6120.5	0	–
3.75	04/06/06	6001.0	1	3.93
3.75	05/06/06	6000.5	1	4.07
3.75	27/06/06	5580.5	1	4.06
3.75	28/06/06	5640.5	0	–
3.75	29/06/06	5701.5	0	–
3.75	30/06/06	5701.5	0	–
3.75	01/07/06	5761.5	0	–
3.75	02/07/06	5760.5	1	1.01
3.75	06/07/06	5865.5	0	–
3.75	07/07/06	5941.5	0	–
6.33	21/08/06	5460.5	3	3.58, 1.32, 1.52

Table 8.3: Summary of potential candidate settings and their repetitions.

8.4 The Determination of the Upper Limit on $g_{a\gamma}$

8.4.1 Upper Limit for Individual Pressure Settings

Since there is no signal present in the ^{4}He data of the CCD detector, it is now possible to build the likelihood and χ^2-functions for each individual pressure setting. The χ^2-distributions can then be minimized, and the best fit value for $g^4_{a\gamma}$, or equivalently for the dimensionless axion-to-photon coupling constant $g^4_{10} = (\frac{g_{a\gamma}}{10^{-10}\mathrm{GeV}^{-1}})^4$, can be obtained.

Axion Parameter Space

The axion mass m_a and the coupling constant g^4_{10} provide the axion parameter space. The highest sensitivity is reached for axion masses close to the effective photon mass of a specific pressure setting, due to the coherence condition. Thus, the best upper limits on the coupling constant for a specific pressure setting can be derived for the mass region corresponding to the covered density settings.
The covered range of pressure settings reaches from 0.08 mbar to 13.43 mbar at 1.8 K and thus axion masses corresponding to pressures from 0-14.5 mbar have been considered for the analysis. In terms of effective photon mass, this includes the region from about 0.0-0.4 eV. In total, 1500 steps in mass, each corresponding to a pressure step of 0.01 mbar, have been taken into account. This means that for each density step, 1500 χ^2-curves were calculated.

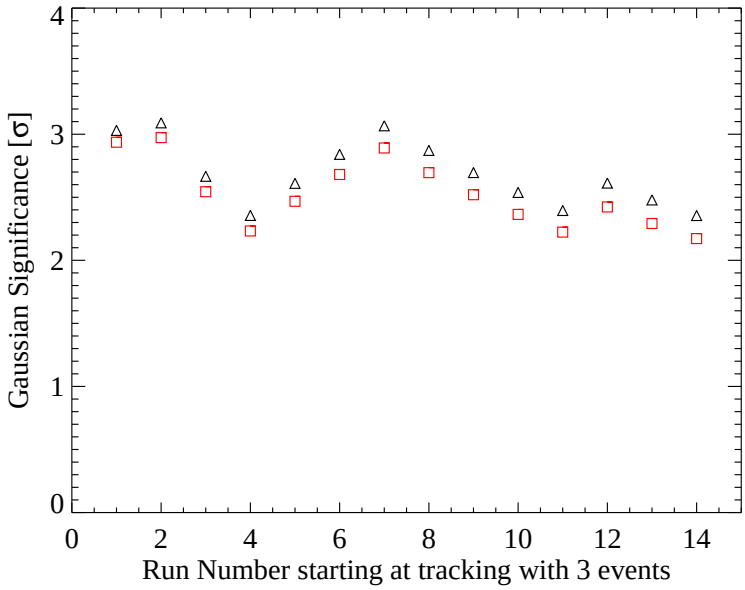

Figure 8.15: Development of observed significance with number of tracking runs at the same density setting p_{39}. The significance in sigmas is given for two different (compatible) background definitions: the normalized background obtained from the full chip during background times (red squares) and the normalized background from the spot region during non-tracking times (black triangles).

The steps of the other axion phase space parameter, i.e. g_{10}^4, have been chosen differently in various ranges. This makes it possible to determine the upper limit on the axion-to-photon coupling constant accurately in the sensitive mass range[6]. On the other hand, the upper bound can be computed also for higher masses, where coherence is lost and the limit increases rapidly. Thus, it is assured that more than $\chi^2_{\min} + 3\sigma$ are covered.

χ^2-Functions for the Individual Density Settings

Since all pressure settings can be treated in the same way, the expectations for the χ^2-curves of one specific density setting p_k will be considered in the following. The χ^2-function can be obtained for a given mass using the likelihood function $\mathcal{L}_k$ given in Eq. (8.10) as

$$\chi^2_k = -2\ln\mathcal{L}_k = \sum_i \left[2\mu_{ik} - n_{ik}\ln\left(\mu^2_{ik}\right) - 2n_{ik} + n_{ik}\ln\left(n^2_{ik}\right)\right], \tag{8.20}$$

where $i = 1...20$ refers to the energy bins in the 1 to 7 keV range, μ_{ik} is the sum of background and expected signal at the k-th setting and in the i-th energy bin (see Eq. (8.8)). n_{ik} are the observed events in the i-th energy bin and pressure step p_k during tracking, i.e in axion-sensitive conditions. One should keep in mind that for one density setting, 1500 χ^2-curves will be obtained, one for each

[6]Sensitive mass range refers to axion masses around the effective photon mass, which corresponds to a covered pressure setting and its surroundings.

considered axion mass in the later obtained exclusion plot.
There are two cases to be considered in order to explain the behavior of the χ^2-curves. They depend on the number of events n_k in the total considered energy range, which have been observed at the k-th density step[7]. The two cases are $n_k = 0$ and $n_k > 0$:

χ^2-curve for n_k=0: If zero counts have been registered during tracking at a certain density setting, Eq. (8.20) simplifies to

$$\chi^2_k = \sum_i 2\mu_{ik}, \tag{8.21}$$

since $\mathcal{L}_k$ turns into

$$\mathcal{L}_k = \prod_i \mathrm{e}^{-\mu_{ik}}. \tag{8.22}$$

Due to the fact that μ_{ik} is linear in g^4_{10} since N_{ik} is proportional to g^4_{10}, the χ^2-curves for all masses will be straight lines. The value of χ^2_{Null} will be the same for all masses at one pressure setting p_k. The slope of the straight line, however, will change, since the expected number of photons N_{ik} depends on the axion mass, i.e. it is only of significant size for a narrow axion mass range around the effective photon mass corresponding to the pressure setting. Thus, for masses close to the coherent mass, where N_{ik} is rather large, the slope will be bigger than for masses far away from it, where the slope approaches a value of zero. There is obviously no minimum and the most likely physical value of g^4_{10} will be zero ($g^4_{10,\mathrm{min}} = g^4_{10,\mathrm{Null}}$). An example of a χ^2-curve in such a case is shown in the left part of Fig. 8.16. While the solid line is the χ^2-curve for an axion mass close to the effective photon mass corresponding to the pressure p_k, the dotted line corresponds to an axion mass far away from the coherence.

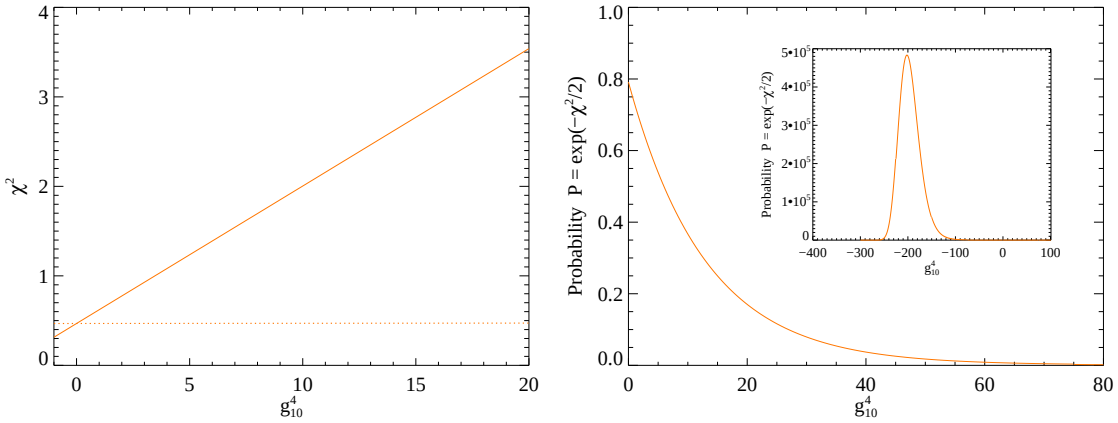

Figure 8.16: Left: χ^2-curve for the 16th pressure setting ($p_{16} = 1.42$ mbar), for which zero events have been registered during tracking. The solid line corresponds to an axion mass $m_a = 0.125$ eV, which is close to the effective photon mass m_γ at this pressure, while the dotted line is for a mass far away from m_γ. Right: Corresponding probability function $P = \exp\left(-\chi^2/2\right)$ for $m_a = 0.125$ eV.

[7] One density setting may comprise one or more tracking runs.

χ^2-curve for n_k>0: If there have been one or more events observed during tracking with a specific pressure setting p_k, the situation changes slightly. For masses close to the effective photon mass of the considered density setting, a χ^2-curve as shown in the left part of Fig. 8.17 (solid line) will be observable. This can be calculated from Eq. (8.20). For example, in the case of one event at the pressure setting p_k ($n_k = 1$), w.l.o.g. $n_{1k} = 1$, it can be written as

$$\chi^2_k = \sum_{i=1}^{20} 2\left(b_{ik} + N_{ik}(g^4_{10})\right) - \ln\left(b_{1k} + N_{1k}(g^4_{10})\right)^2 - 2, \tag{8.23}$$

which can be minimized with respect to g^4_{10}, since $N_{ik} \propto g^4_{10}$. The minimum of χ^2_k will indicate the most likely value for g^4_{10}. If tracking and background data are compatible, this minimum should be located close to $g^4_{10} = 0$.
For masses far away from the ones corresponding to the pressure setting, the expected number of photons N_{ik} will be very close to 0. Thus, the terms containing N_{ik} in Eq. (8.23) can be neglected, yielding a constant χ^2-function, which only depends on the background

$$\chi^2_k = \sum_{i=1}^{20} 2b_{ik} - \ln\left(b_{1k}\right)^2 - 2. \tag{8.24}$$

The value of this constant function is χ^2_{Null} and an example is indicated in the left part of Fig. 8.17 by the dotted line.
For masses between the effective photon mass and those far away from it, the χ^2-curves will have a wider apex angle and become more flat with increasing distance from the mass corresponding to the pressure setting. The same reasoning can be used in case of more than one event registered during a single density setting. The left part of figure 8.18 is illustrating this. The solid lines show (from bottom to top) the χ^2-curves at the effective photon mass for a pressure setting with zero events

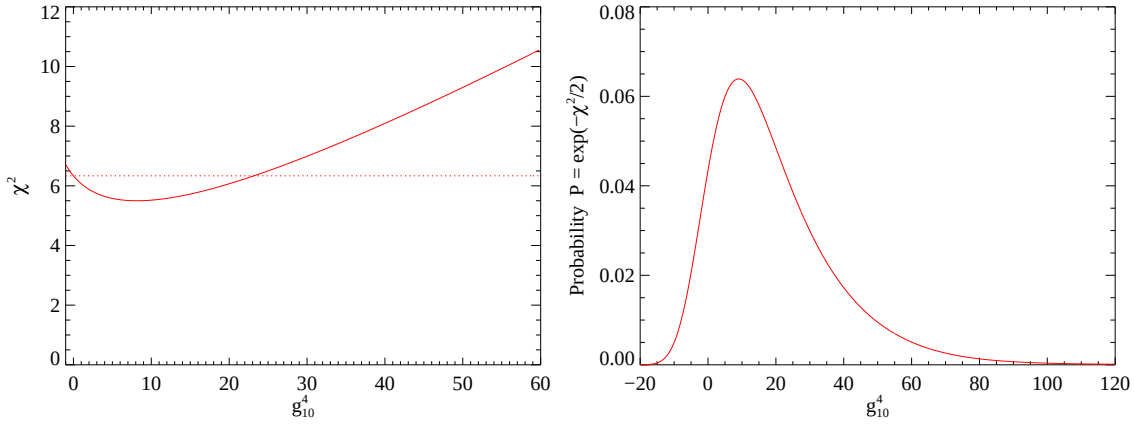

Figure 8.17: Left: χ^2-curve for the 26th pressure setting ($p_{26} = 2.33$ mbar), for which one event has been observed during tracking. The solid line corresponds to an axion mass $m_a = 0.160$ eV, which is close to the effective photon mass m_γ at this pressure, while the dotted line is for a mass far away from m_γ. Right: Corresponding probability function $P = \exp\left(-\chi^2/2\right)$ for $m_a = 0.16$ eV.

(yellow, $p_{16} = 1.42$ mbar at $m_a = 0.13$ eV), one event (red, $p_{26} = 2.33$ mbar at $m_a = 0.16$ eV), two events (blue, $p_{106} = 9.83$ mbar at $m_a = 0.33$ eV), three events (green, $p_{70} = 6.33$ mbar at $m_a = 0.27$ eV) and eight events (black, $p_{39} = 3.75$ mbar at $m_a = 0.20$ eV). The dotted lines of the same color correspond to the equivalent setting but are taken at a mass far away from the coherence. The shape of the χ^2-curve depends on the available statistics, e.g. two tracking runs have been spent at $p_{106} = 9.83$ mbar (blue, $t_{106} = 10681$ s) and 14 in total at $p_{39} = 3.75$ mbar (black, $t_{39} = 82555.5$ s) resulting in a narrower curve than the ones for only one tracking run (yellow: $t_{16} = 5401$ s, red: $t_{26} = 5821.5$ s, green: $t_{70} = 5460.5$ s).

Upper Limits for the Individual Density Settings

In both cases, $n_k = 0$ and $n_k > 0$, one can proceed with the limit calculation for each single pressure setting in exactly the same way: the probability function $P(g^4_{a\gamma}) = \mathrm{e}^{-\chi^2/2}$ from Eq. (8.17) can be integrated over the physical region of g^4_{10} up to 95% of the physical area as indicated in Eq. (8.16) for every mass.
Typical probability curves for zero events and one event are shown in the right part of Fig. 8.16 and Fig. 8.17, respectively. For a better overview, the probability curves corresponding to the χ^2-curves given in the left part of Fig. 8.18 are shown in the right part of the same figure. Note that the values larger than one for the probability function in case of zero events are an artefact and do not represent a real probability. The resulting exclusion plots for the same specific pressures are shown in Fig. 8.19.

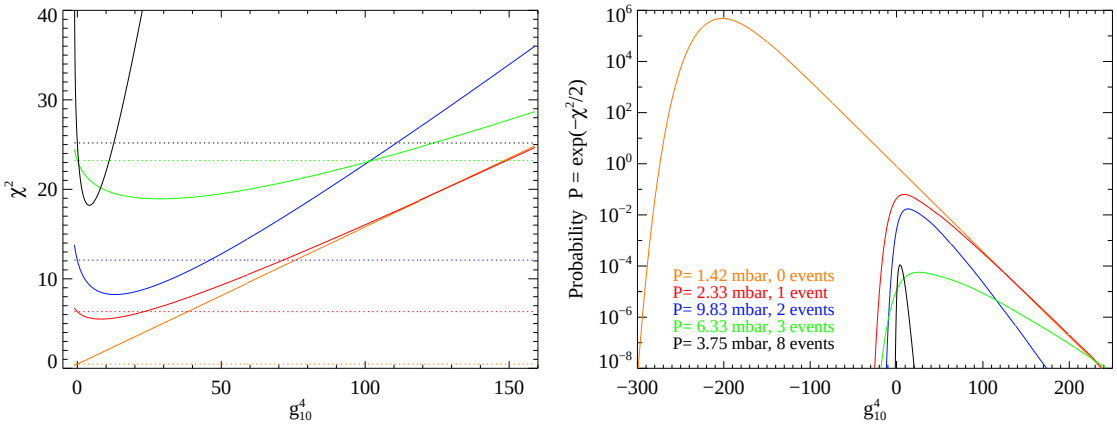

Figure 8.18: Left: χ^2-curves for different numbers of observed events. The solid lines are for an axion mass close to m_γ, the dotted lines are for a mass far away from the coherence region. The plotted curves correspond to zero events (yellow, $p_{16} = 1.42$ mbar at $m_a = 0.13$ eV, $t_{16} = 5401$ s), one event (red, $p_{26} = 2.33$ mbar at $m_a = 0.16$ eV, $t_{26} = 5821.5$ s), two events (blue, $p_{106} = 9.83$ mbar at $m_a = 0.33$ eV, $t_{106} = 10681$ s), three events (green, $p_{70} = 6.33$ mbar at $m_a = 0.27$ eV, $t_{70} = 5460.5$ s) and eight events (black, $p_{39} = 3.75$ mbar at $m_a = 0.20$ eV, $t_{39} = 82555.5$ s). Right: Corresponding probability functions for the same cases of different numbers of observed events. Note that the y-scale is logarithmic.

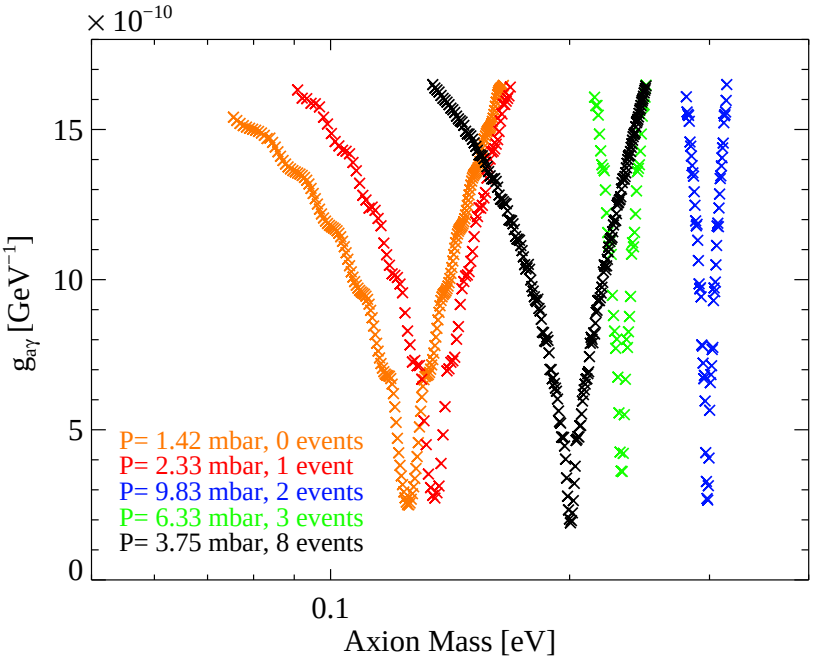

Figure 8.19: Exclusion plots for different numbers of observed events. The curves correspond to zero events (yellow, $p_{16} = 1.42$ mbar at $m_a = 0.13$ eV, $t_{16} = 5401$ s), one event (red, $p_{26} = 2.33$ mbar at $m_a = 0.16$ eV, $t_{26} = 5821.5$ s), two events (blue, $p_{106} = 9.83$ mbar at $m_a = 0.33$ eV, $t_{106} = 10681$ s), three events (green, $p_{70} = 6.33$ mbar at $m_a = 0.27$ eV, $t_{70} = 5460.5$ s) and eight events (black, $p_{39} = 3.75$ mbar at $m_a = 0.20$ eV, $t_{39} = 82555.5$ s).

8.4.2 Upper Limit for the Combination of all Pressure Settings

Having calculated the likelihood functions $\mathcal{L}_k$ and the χ^2-curves for each individual pressure setting χ^2_k, the global likelihood can be calculated by multiplying all $\mathcal{L}_k$ ($k = 0...148$) or, equivalently, adding up the χ^2_k for all density settings as explained before (see Eq. (8.12)).
After this, one can proceed in exactly the same way as it has been done for the single pressure settings: for each of the 1500 axion masses chosen for the analysis, one obtaines a χ^2-curve. The difference is that now the influence of all pressure settings on each single axion mass is taken into account.

The Construction of the Global χ^2-Functions

Following Eq. (8.13), the global χ^2-distributions can be calculated. Some typical example curves are shown in Fig. 8.20. Since neighboring pressure settings have an influence on the same masses, it is no longer possible to exactly distinguish different cases according to the number of observed events. This was only possible for the single settings. The upper plots of Fig. 8.20 show the most commonly observed types of χ^2-curves: either the χ^2-curve reveals a minimum (upper left) or only a straight line can be observed (upper right). A minimum is observable if the mass is close to the effective photon mass of a pressure setting in which one or more events have been registered. In the case of Fig. 8.20 (upper left), $m_a = 0.249$ eV corresponds to 61-st pressure setting ($p_{61} =$

5.58 mbar), during which one event has been registered, while at least three neighboring settings yielded zero events. The straight line as observable in the upper right part of Fig. 8.20 corresponds to an axion mass of $m_a = 0.105$ eV, which matches the effective photon mass of the 11-th pressure setting ($p_{11} = 0.10$ mbar). At this setting as well as during at least three neighboring settings to lower and higher pressures zero events have been observed. The lower plots of the same figure illustrate the behavior of the χ^2-function for masses around pressure settings with long exposure (lower left) and close to masses corresponding to missed pressure settings (lower right). All curves have been shifted to obtain $\chi^2_{\text{min}} = 0$, such that the shapes can be easily compared. It can be seen that a long exposure results in smaller opening angles of the observed curves, while missed density settings yield wider, flatter curves.
It should be noted that the exact shape of the χ^2-curve for a specific mass depends on various parameters, such as for example which measured pressure settings contribute dominantly to the

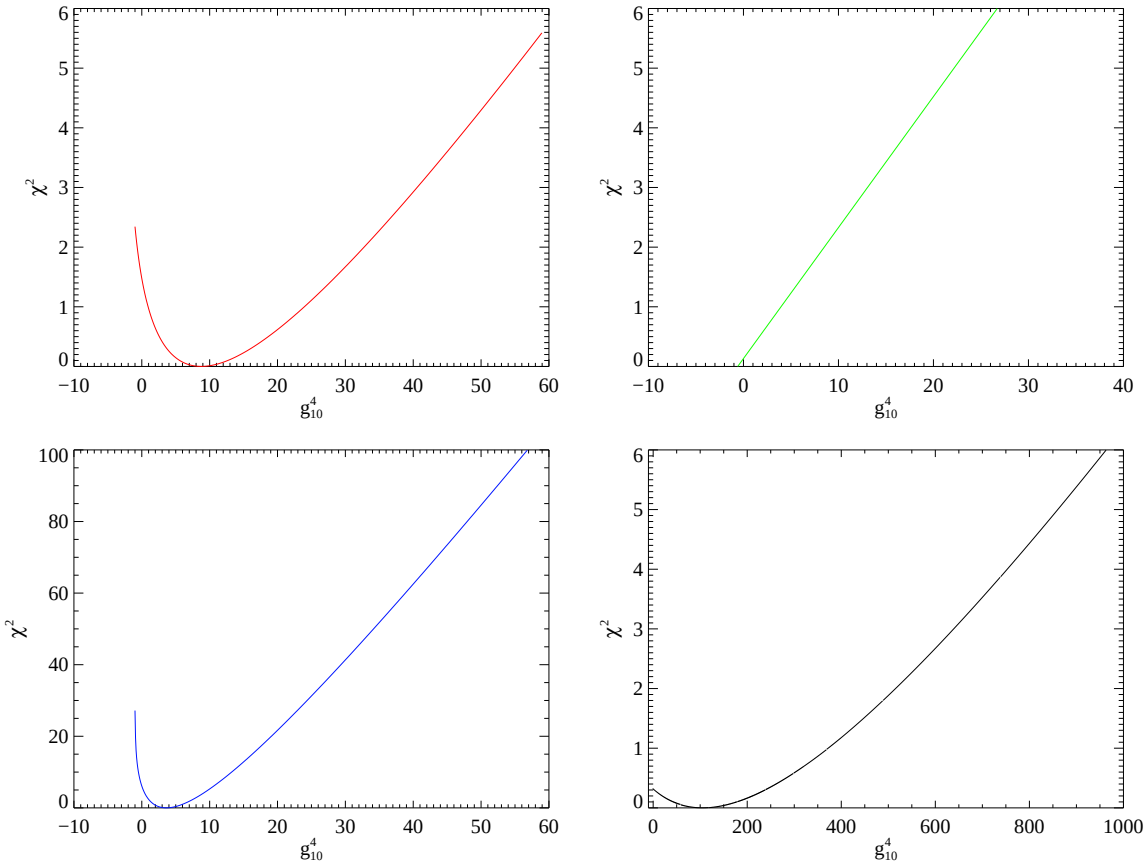

Figure 8.20: Typical global χ^2-curves. All curves have been shifted to obtain $\chi^2_{\text{min}} = 0$ such that the shapes can be easily compared. The upper left plot shows the first typical case of a χ^2-curve, here for a mass $m_a = 0.249$ eV. The second typical case is diplayed in the upper right plot for a mass $m_a = 0.105$ eV. Furthermore, the extreme case of an axion mass around a pressure setting with a long exposure time ($m_a = 0.204$ eV) can be seen in the lower left plot. A χ^2-curve for an axion mass around missed pressure settings ($m_a = 0.301$ eV) is shown in the lower right image.

considered mass, the number of events in neighboring settings as well as the energy of the registered photon.
A typical sequence of χ^2-curves for consecutive axion masses is shown in the left part of Fig. 8.21. This typical behavior yields the characteristic waveshape, which is observable in the extraction of the final exclusion plot displayed in the right image of Fig. 8.21. Due to a periodic decrease and increase of the value for $g^4_{10,\mathrm{min}}$, also the 95% upper limit value $g_{a\gamma}(95\%\ \mathrm{C.L.})$ shows this variation as typical pattern.

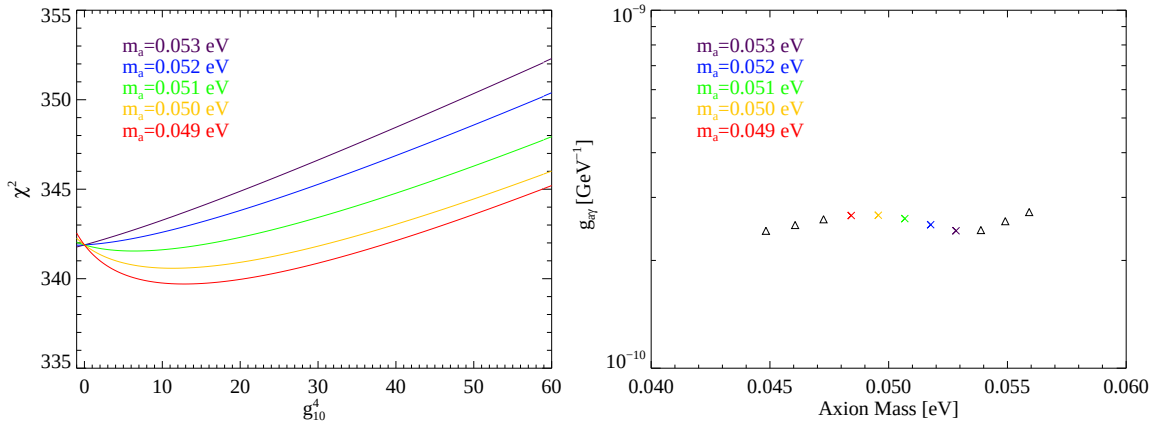

Figure 8.21: Left: Global χ^2-curves for neighboring masses. The displayed lines correspond (from bottom to top) to the axion masses $m_a = 0.049,\ 0.050,\ 0.051,\ 0.052,\ 0.053$ eV. Right: Corresponding exclusion plot for the axion-photon coupling constant at 95%CL. The black triangles represent masses preceding and succeeding the sequence of masses considered in the left plot.

Consideration of the Global $\Delta\chi^2$

At this point, a useful crosscheck to look for apparent systematic effects can be performed, due to the fact that background and tracking are compatible. Since there is only one free fit parameter for the global likelihood functions, the statistical fluctuations for the difference $\Delta\chi^2$ between χ^2_{Null} and χ^2_{min} should correspond to a Gaussian with mean 0 and $\sigma = 1$. Thus

$$\Delta\chi^2 = |\chi^2_{\mathrm{Null}} - \chi^2_{\mathrm{min}}| = \sigma^2 \leq 1 \tag{8.25}$$

should hold for 68.3% of all masses. Within 2σ, there should be found 95.4% of all points and within 3σ 99.7%. In Fig. 8.22, the square root of $\Delta\chi^2$ for the global likelihood at each considered axion mass is displayed. Here the standard definition of background (Background 1, spot during background time) has been used. It can be seen that for the chosen standard background, 86.14% of all minima are within 1σ of the null hypothesis, 13.06% are between 1σ and 2σ and only 0.80% are between 2σ and 3σ. No points are found outside the 3σ region. Note that in case that no minimum is observed, the value of χ^2_{min} equals the one of χ^2_{Null}, such that $\Delta\chi^2$ is obtained as zero.

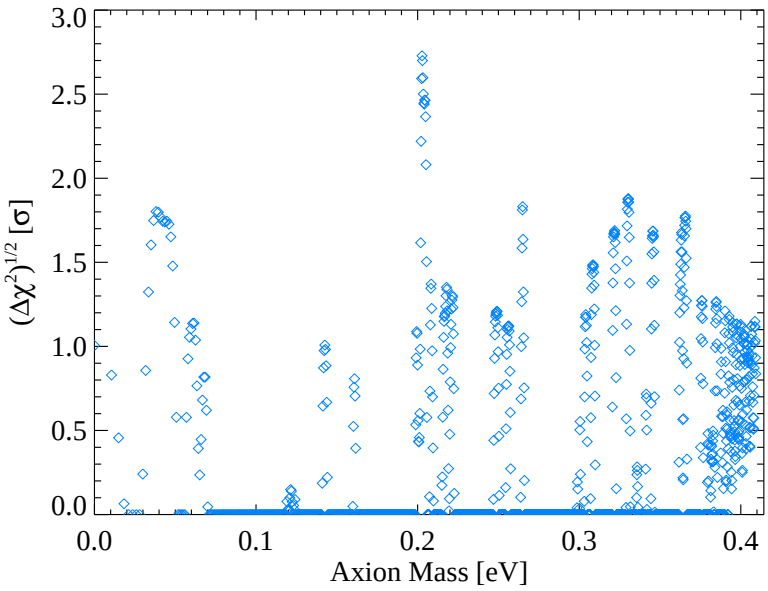

Figure 8.22: Square root of $\Delta\chi^2$ for all considered axion masses m_a. All obtained values for $\Delta\chi^2$, which is the absolute difference between χ^2_{Null} and χ^2_{min}, are within three sigmas.

The Upper Limit for the Combination of all Density Settings

In order to enable an easier handling of the data, a 10th order polynomial is fitted to each χ^2-curve. Using these functions for each mass with the standard background definition implemented, the probability function $P(g^4_{a\gamma})$ can be calculated for each mass.
In Fig. 8.23, the probability is shown for different axion masses. These masses correspond to those used in Fig 8.20 to illustrate the behavior of the global χ^2-functions. The first typical case, i.e. an axion mass for which a minimum is observable in the χ^2-curve, yields a probability distribution with its maximum value in the positive region of g^4_{10} around zero (red curve). If the χ^2-function is only a straight line without minimum for a specific axion mass (second typical case), then the maximum of the probability distribution is shifted towards negative values of g^4_{10}, favoring the physical value $g^4_{10} = 0$ (green curve). Note that the values larger than one for the probability function in this case are an artefact and do not represent a real probability. For a long exposure time, the probability function becomes very narrow (blue curve), while the distribution widens for masses corresponding to missed density settings.
From all these different probability curves, the global upper limit on the axion-photon coupling constant can then be obtained as described in Eq. (8.16) by integration of the physical region up to 95% of the area.

8.4.3 Determination of the Statistical Error

The standard deviation errors of the best fit value for g^4_{10}, i.e. $g^4_{10,\mathrm{min}}$, can be estimated using Eq. (8.15).

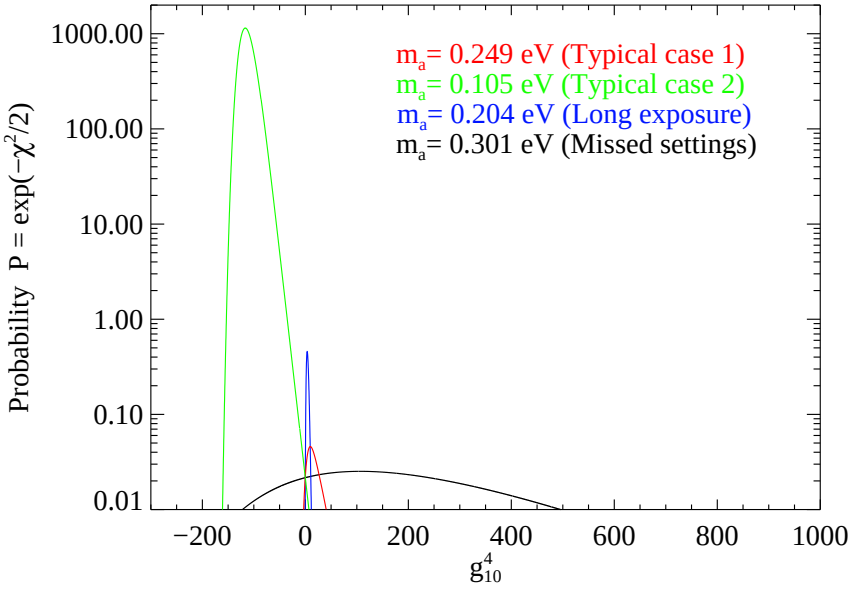

Figure 8.23: Typical global probability curves corresponding to the χ^2-functions at the same masses as in Fig. 8.20. The red and green curve represent the typical cases, while the blue line and the black line refer to long exposure and missed settings, respectively. Note that the y-axis is given in logarithmic scale and that the probability values larger than 1 are an artefact.

As indicated in the histogram in the left part of Fig 8.24, altogether 998 masses in the range $m_a \leq 0.387$ eV yield a straight line without minimum, providing $g_{10}^4 = 0$ as the best fit value. The remaining values can be described by a Gaussian distribution with a mean for $g_{10,\mathrm{min}}^4$ of 9.17 and $\sigma = 5.36$ as shown in the right part of Fig. 8.24. A few masses yield considerably higher values

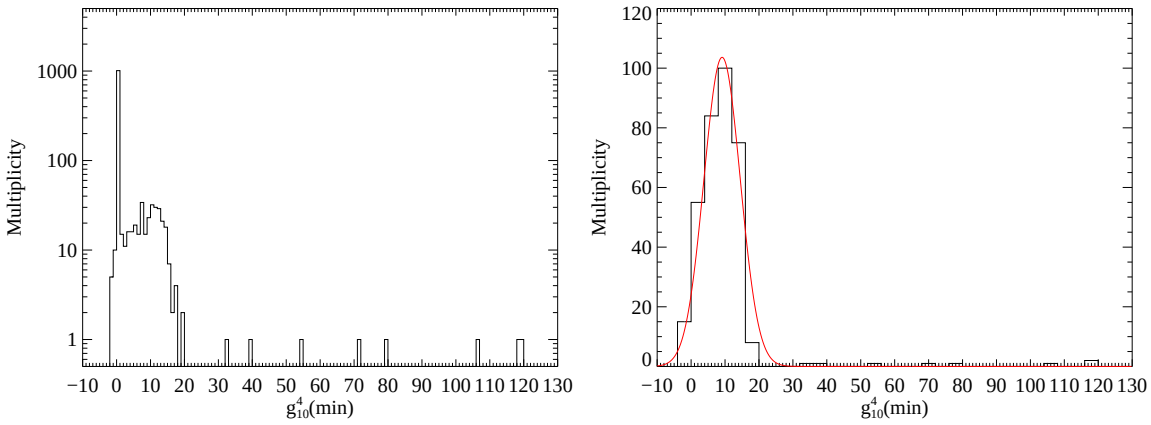

Figure 8.24: Left: Multiplicity representation for the $g_{10,\mathrm{min}}^4$ at the considered masses of the analysis. Right: Gaussian fit to the multiplicity of $g_{10,\mathrm{min}}^4$ values obtained for those masses up to 0.387 eV which did yield a real minimum and no straight line.

for the best fit value, but their statistical errors are also accordingly larger. These high values of $g^4_{10,\min}$ result from the fact that some pressure settings were missed. Therefore, masses close to these regions are not as well covered as the rest.
Taking into account just the mass range of largest sensitivity ($m_a \leq 0.387$ eV), one obtains as a median for $g^4_{10,\min}$ with asymmetric statistical errors

$$g^4_{10}(\min, \text{median}) = 9.39^{+16.19}_{-9.39}. \tag{8.26}$$

This values take only masses into account, which do not yield straight lines for the χ^2-curves.
If one consideres just the masses corresponding to the measured pressure settings, i.e. the best case scenario, this results in a median of

$$g^4_{10}(\min, \text{median}) = 7.52^{+14.10}_{-7.52}. \tag{8.27}$$

For this case, the values of $g^4_{10,\min}$ with their corresponding asymmetric errors are shown in Fig. 8.25. Only χ^2-curves, which do not yield a straight line, but reveal a real minimum, have been taken into account to determine the statistical error.

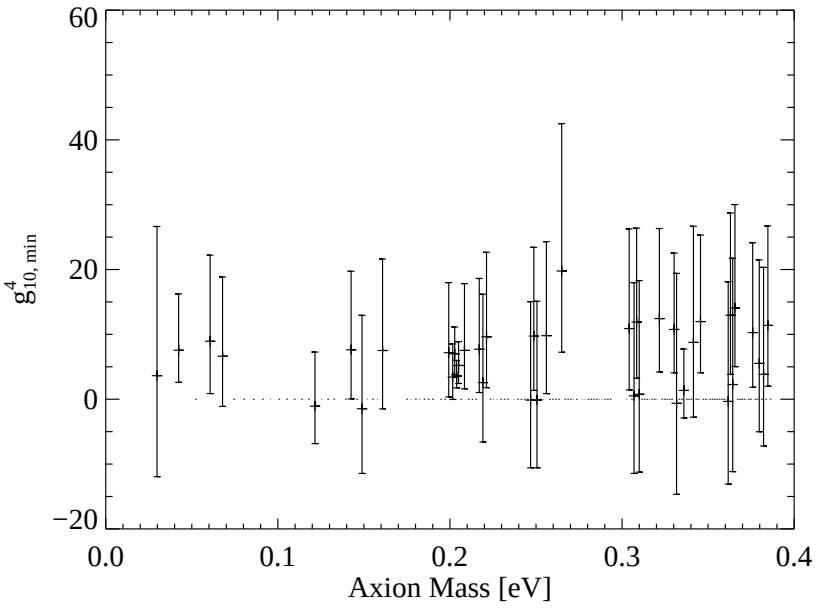

Figure 8.25: Best fit value for g^4_{10} for masses corresponding to the measured pressure settings. The asymmetric statistical errors are shown.

A detailed list containing the value of $g^4_{10,\min}$ for each mass considered in the analysis for which $g^4_{10,\min} \neq 0$ together with the asymmetric errors can be found in Tab. F.1 of Appendix F. The respective values for the masses corresponding to the measured density settings only are given in Tab. F.2 of Appendix F.

8.5 Studies of Systematic Uncertainties

So far, only the statistical errors have been considered in more detail. Before deriving the final result, a study of the systematics will be done. Hereby, the influence of experimental conditions such as magnetic field strength and its length on the upper limit should be considered. Furthermore, uncertainties in the absorption of photons in ^{4}He gas and the measured window transmission have to be taken into account. Moreover, a variation of the expected spot position can also modify the result and must be considered before turning to the definition of background as source of systematic errors. Additionally, the influence of the CAST overall pointing accuracy in following the Sun on the result are to be studied. This aspect is especially critical for the X-ray telescope and its efficiency, since one has to deal here with an imaging device. A possible further consideration is the potential consequences of a slight misalignment of the CAST magnet in following the Sun as indicated by the filming. The size of this effect will be estimated.
For each of the just mentioned sources of systematic uncertainty, the absolute error on the best fit value of g_{10}^4 is determined by taking into account the $g_{10,\mathrm{min}}^4$ of all for the analysis considered axion masses up to 0.387 eV. The possibly asymmetric errors to the left and right side of the minimal g_{10}^4 are then calculated as the mean values of the errors from all mass.

8.5.1 Influence of Magnetic Field and Length

The magnetic field and its uncertainties have been calculated to be (8.805 ± 0.037) T, while the length of the magnetic field is (9.26 ± 0.05) m (see Section 8.1.1).
In order to determine the systematic error resulting from this, the mean displacement for the minima of the χ^2-curves in comparison to the standard values has been studied. Only the most sensitive axion mass range ($m_a \leq 0.387$ eV) has been used to obtain a mean systematic error on $g_{10,\mathrm{min}}^4$, yielding for the magnet field strength variations

$$B = (8.805 \pm 0.037)\ \mathrm{T}: \quad g_{10,\mathrm{min}}^4{}^{+0.022}_{-0.022}, \tag{8.28}$$

and for the uncertainties in the length of the magnetic field

$$L = (9.26 \pm 0.05)\ \mathrm{m}: \quad g_{10,\mathrm{min}}^4{}^{+0.025}_{-0.019}. \tag{8.29}$$

8.5.2 Influence of Error in Absorption and Window Transmission

For the absorption fit function obtained using data of the NIST database, a conservative 5% uncertainty has been assumed. The mean displacement of the minimum for the χ^2-curves in comparison to standard conditions is rather small with

$$\mathrm{Absorption}\ \Gamma \pm 5\%: \quad g_{10,\mathrm{min}}^4{}^{+0.006}_{-0.007}, \tag{8.30}$$

and can thus be considered negligible.
A further possible source of systematic errors is the measured transmission of the cold windows. It has been determined at the PANTER test facility [151] and the results of the measurements are provided in Tab. 8.4 together with statistical errors. The mean displacement of the best fit value for g_{10}^4 is

$$\mathrm{Transmission}\ \pm\ \mathrm{statistical\ errors}: \quad g_{10,\mathrm{min}}^4{}^{+0.022}_{-0.022}. \tag{8.31}$$

Table 8.4: Transmission Measurements of the cold windows at the PANTER test facility with statistical errors at different energies.

Energy [keV]	**Transmission [%]**	**Statistical Error +/-**
0.27	6.94	0.06184
0.93	5.83	0.07020
1.49	38.51	0.50004
1.74	53.83	0.49778
2.29	68.24	0.57435
2.98	79.68	0.66660
4.51	84.41	0.71854
5.41	85.44	0.72700
6.40	87.52	0.74278
6.93	90.35	0.76838
8.04	88.46	0.76215

8.5.3 Influence of the Axion Signal Spot Position

In order to take into account possible uncertainties from the determination of the expected axion signal spot position, the influence of a shift of the spot center by ± 1 pixel in x and y direction has been investigated. The data in the new spot during background times can then be used as standard background. The mean systematic error on the most likely value for g_{10}^4 can be given for the variation of the spot center as

$$\text{Spot Center } \pm 1 \text{ pixel}: \quad g^4_{10,\min\,-0.599}{}^{+0.162}, \tag{8.32}$$

which is the most conservative mean systematic error for all considered positions of the spot center. Since the background definition is the most important source of systematic errors as will be seen later on, the change of the spot center position, which goes along with a slightly different background, already exhibits more significant errors than all other aspects considered before.

8.5.4 Influence of the Overall CAST Pointing Accuracy

The requirements for the precision of the tracking system are fairly strict in order to guarantee a high efficiency of the X-ray telescope. The overall pointing accuracy in following the Sun must always be better than 0.01°. Typically it is around 0.002°. Assuming the two extreme scenarios of a deviation of $\pm 0.01^\circ$, one can calculate that this results in a loss of 9.03% and gain of 4.30% in the overall efficiency, respectively. This loss or gain has to be considered in addition to effects like the tilt of the telescope, the correction for a known GRID offset and the cold windows as they have

been discussed in Chapter 8.1.2. An increase in efficiency caused by a slight off-pointing from the solar core is possible, since the telescope is not in its optimal position due to its tilt relative to the magnet axis (see Fig. 6.7 in Section 6.1.2). The tracking accuracy plays an important role:

$$\text{Perfect pointing } \pm 0.01^\circ : \quad g^4_{10,\min}{}^{+1.149}_{-0.475}, \tag{8.33}$$

and it becomes obvious, how crucial the precise pointing of the magnet to the Sun is for CAST and especially the X-ray telescope.

8.5.5 Influence of Background Definition

A further large source of systematic errors is the definition of background due to low statistics. The different definitions have been introduced in Section 7.4.2 and are referred to as Background 1 (standard background definition, events in spot during background time), Background 2 (full chip during background times), Background 3 (full chip without spot region during background time), and Background 4 (full chip without spot region during tracking time).
Since no signal is present in the data, the difference $\Delta\chi^2$ between $\chi^2_{\min}$ and χ^2_{Null} can be used as an indication for possible systematic errors of the different definitions of background. As introduced in Eq. (8.25), $\Delta\chi^2$ can be expressed in Gaussian sigmas. The absolute values of $\sqrt{(}\Delta\chi^2)$ are displayed for the three alternative definitions to the standard background in Fig. 8.26. It can be seen that for Background 2, 91.21% of all minima are within 1σ of the null hypothesis, 8.66% are between 1σ and 2σ and only 0.13% are between 2σ and 3σ. No points are found outside the 3σ region. For Background 3 the corresponding values are 91.07% (0σ-1σ), 8.79% (1σ-2σ) and 0.14% (2σ-3σ). Background 4 yields 89.87%, 9.53% and 0.60% for the three regions and thus in principle all alternative definitions of background could have been used for the analysis as standard background.
The mean systematic errors of the best fit value obtained from the comparison of the best fit value for the standard conditions with the minima of the other background definitions are then

$$\begin{aligned} \text{Background } 2 : &\quad g^4_{10,\min}{}^{+1.018}_{-2.799}, \\ \text{Background } 3 : &\quad g^4_{10,\min}{}^{+1.037}_{-2.856}, \\ \text{Background } 4 : &\quad g^4_{10,\min}{}^{+0.785}_{-1.478}. \end{aligned} \tag{8.34}$$

To give a conservative estimate, the largest uncertainties have been used as the error estimate for the background definition

$$\text{Background} : \quad g^4_{10,\min}{}^{+1.037}_{-2.856}, \tag{8.35}$$

thus providing along with the error due to the pointing accuracy the dominant systematic uncertainty.

8.5.6 Consideration of the Solar Filming Results

So far the solar filming has always confirmed that the CAST magnet is pointing to the solar core with the required precision. However, the filming also indicated that the magnet is slightly ahead in tracking. This has also been confirmed by a second independent filming system which has been

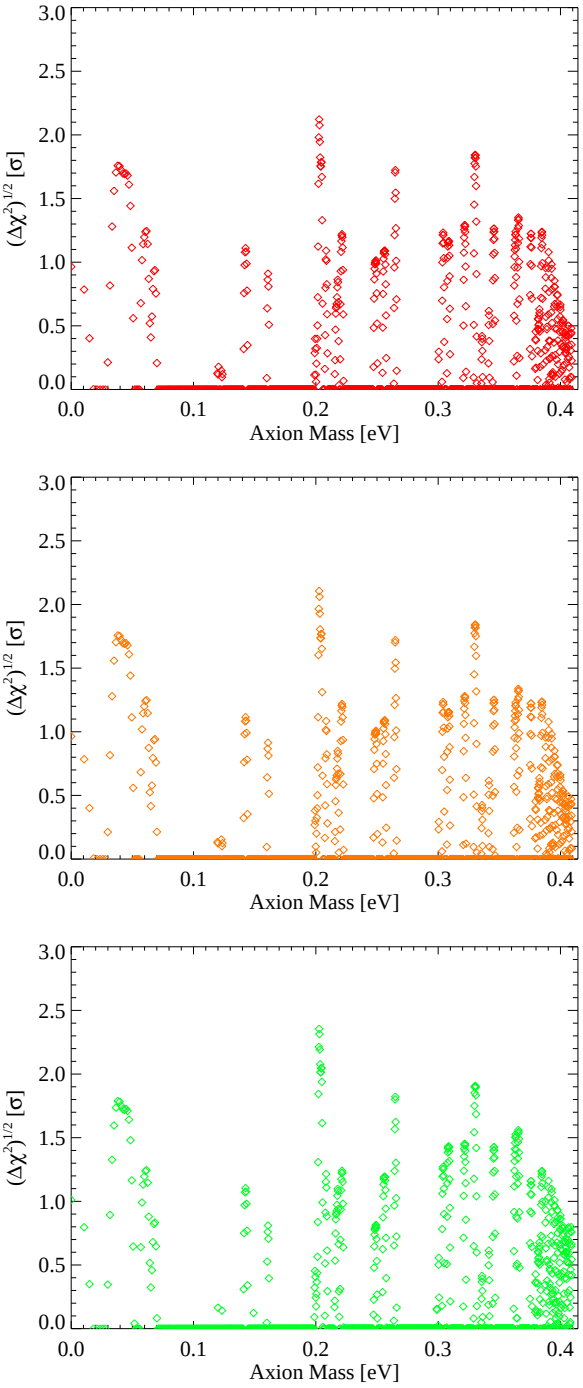

Figure 8.26: Square root of $\Delta\chi^2$ for all considered axion masses m_a using different definitions of background. All obtained values for $\Delta\chi^2$, which is the absolute difference between χ^2_{Null} and χ^2_{min}, are within three sigmas. The upper plot is for Background 2 (full chip during background times), the middle plot for Background 3 (full chip without spot during background times) and the lower plot was obtained using Background 4 (full chip without spot during tracking times).

set up for the first time in parallel to the existing one in March 2008. In the worst case scenario, the filming results would indicate an additional loss of efficiency for the X-ray telescope of roughly 20% yielding a systematic error for the best fit value of g_{10}^4 of

$$\text{Filming Deviation}: \quad g_{10,\min}^4{}^{+3.144}_{-0.289}. \tag{8.36}$$

In contrast to the other considered sources of systematic errors, the influence of the filming results should be considered as a rough indication, since the assumed deviation from the pointing to the solar center is not only an extreme case, but also within the uncertainties of the filming setup. Furthermore, one should keep in mind that the software used for axion tracking and solar filming differ, since an additional program corrects the magnet movement for refraction of light in the atmosphere. For these reasons, this uncertainty will not be included in the overall systematic error.

8.5.7 Overall Systematic Error and Influence on the Upper Limit on $g_{a\gamma}$

All considered contributions to the systematic error are summarized in Tab. 8.5 and the total mean systematic error taking into consideration axion masses up to 0.387 eV can be calculated as[8]

$$\text{Total mean systematic error}: \quad g_{10,\min}^4{}^{+1.56}_{-2.96}. \tag{8.37}$$

Therefore, the systematic effects are smaller than the uncertainties due to statistical fluctuations.
The influence on the upper limit for the coupling constant for each source of systematic uncertainty is given in Tab. 8.6. For each condition, the average deviation from the upper limit determined under standard conditions is given for axion masses up to 0.387 eV. One should keep in mind that for a few single masses, higher percental deviations might occur, but they never exceed $+9\%$ and -10% in these exceptional cases. Generally, they can be observed around masses corresponding to lost pressure settings.
Summarizing, the variations in the final upper limit on the coupling constant $g_{a\gamma}$ due to systematic uncertainties are expected to be less than 10%.

[8] If the filming results are taken into account this would change the overall systematic errors to $g_{10,\min}^4{}^{+3.51}_{-2.97}$, which, however, still yields a systematic uncertainty smaller than the statistical error.

Table 8.5: Summary of considered systematic uncertainties of the best fit value of g^4_{10}.

Origin of Uncertainty	**Mean Systematic Error on** $g^4_{10,\min}$
Magnetic field strength B	$g^4_{10,\min}{}^{+0.022}_{-0.022}$
Magnetic field length L	$g^4_{10,\min}{}^{+0.025}_{-0.019}$
Absorption Γ	$g^4_{10,\min}{}^{+0.006}_{-0.007}$
Transmission of cold windows	$g^4_{10,\min}{}^{+0.022}_{-0.022}$
Spot Center	$g^4_{10,\min}{}^{+0.162}_{-0.599}$
Overall pointing accuracy	$g^4_{10,\min}{}^{+1.149}_{-0.475}$
Definition of Background	$g^4_{10,\min}{}^{+1.037}_{-2.856}$
Total systematic uncertainty	$g^4_{10,\min}{}^{+1.56}_{-2.96}$

Table 8.6: Summary of considered systematic uncertainties of the upper limit on $g_{a\gamma}$.

Origin of Uncertainty	**Mean Systematic Error on** $g_{a\gamma}(95\%C.L.)$ [%]
Magnetic field strength B	$g_{a\gamma}(95\%\ \mathrm{C.L.})^{+0.21}_{-0.21}$
Magnetic field length L	$g_{a\gamma}(95\%\ \mathrm{C.L.})^{+0.12}_{-0.12}$
Absorption Γ	$g_{a\gamma}(95\%\ \mathrm{C.L.})^{+0.11}_{-0.11}$
Transmission of cold windows	$g_{a\gamma}(95\%\ \mathrm{C.L.})^{+0.21}_{-0.21}$
Spot Center	$g_{a\gamma}(95\%\ \mathrm{C.L.})^{+0.17}_{-0.62}$
Overall pointing accuracy	$g_{a\gamma}(95\%\ \mathrm{C.L.})^{+2.61}_{-1.15}$
Definition of Background	$g_{a\gamma}(95\%\ \mathrm{C.L.})^{+0.19}_{-1.08}$
Total systematic uncertainty	$g_{a\gamma}(95\%\ \mathrm{C.L.})^{+3.62}_{-3.50}$

8.6 Results

8.6.1 Final Exclusion Plot of the CCD Detector for Phase II with ^{4}He Gas

Since no significant signal over background was observed in the CCD data acquired with ^{4}He in the cold bore of CAST, an exclusion plot for the axion-to-photon coupling constant $g_{a\gamma}$ has been obtained as a result of the analysis[9]. The upper limit at 95% confidence level has been calculated by integrating the Bayesian probability over the physical region up to 95% of the total physical area and is shown in Fig. 8.27. A typical value for the upper limit on the axion-to-photon coupling constant can be set as

$$g_{a\gamma} \lesssim 2.5 \times 10^{-10}\ \mathrm{GeV}^{-1}\ (95\%\ \mathrm{C.L.}) \tag{8.38}$$

for 0.02 eV$< m_a <$ 0.4 eV. However, the exact upper limit at each axion mass slightly differs from this value depending on the pressure setting.

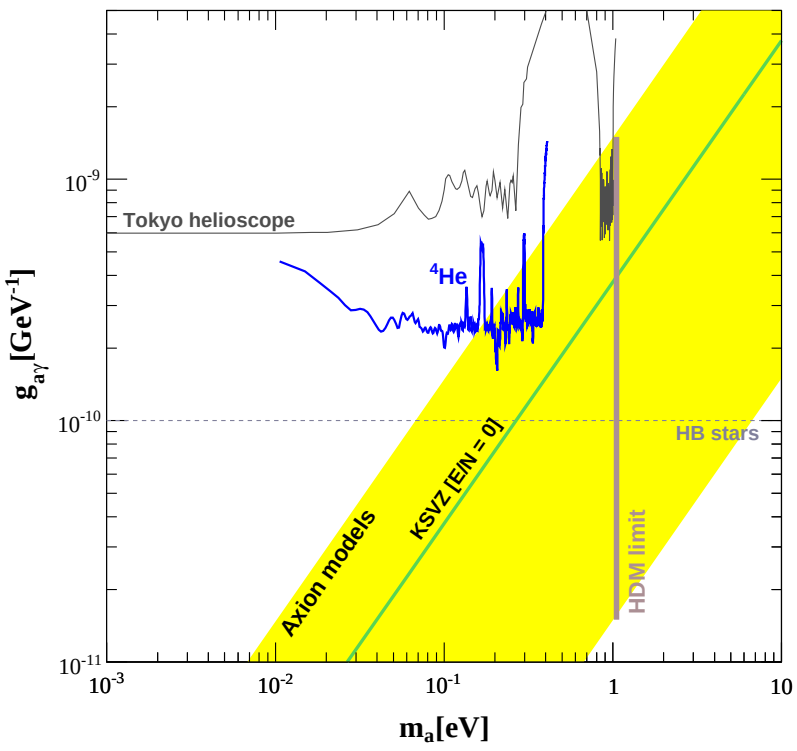

Figure 8.27: Final CCD exclusion plot of the axion-to-photon coupling constant at 95% CL for all data obtained in the ^{4}He part of CAST's Phase II. The achieved limit of the CCD detector is compared with the latest results of the Tokyo helioscope [102]. Furthermore, the Horizontal Branch (HB) star limit [32] and the Hot dark matter (HDM) limit [70] are included. The yellow band represents the typical theoretical axion models and the green solid line corresponds to the case of the KSVZ model with $E/N = 0$.

[9]The upper limit for each considered axion mass can be found in Appendix F (Tab. F.1 and Tab. F.2)

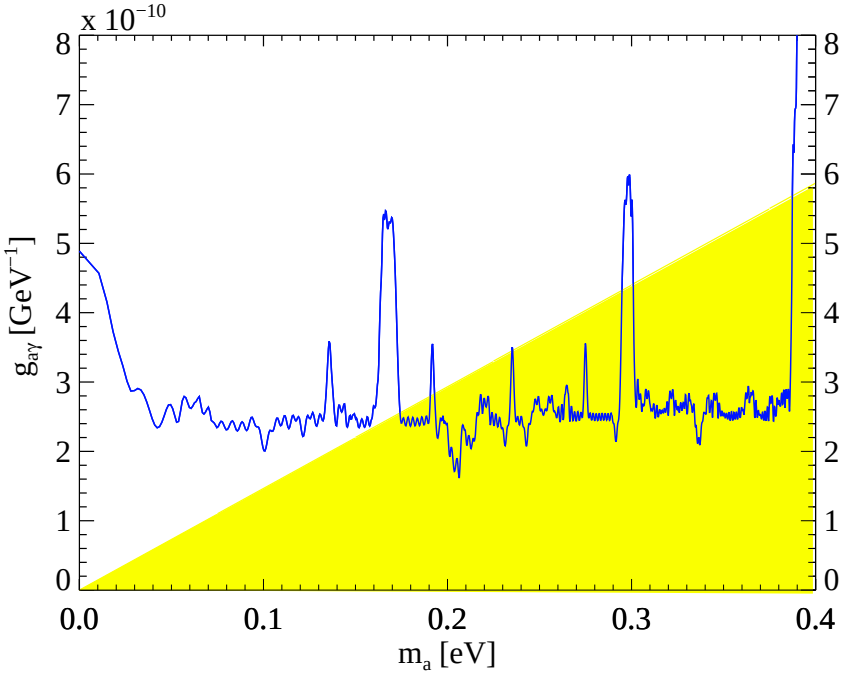

Figure 8.28: Close-up of the final CCD exclusion plot of the axion-to-photon coupling constant at 95% CL for all data obtained in the ^{4}He part of CAST's Phase II plotted in linear scale. The yellow region represents the typical theoretical axion models.

As can be seen in Fig. 8.27, with the measurements of the CCD detector it is possible to enter the region of the parameter space which is favored by theoretical axion models (yellow region).
In Fig. 8.28, an expanded view of the ^{4}He exclusion plot for the CCD detector is shown with linear axion mass scale in order to reveal detailed features.
The structure of the CCD exclusion plot can be explained taking into account the conditions of data taking with the CCD detector of CAST. There are four small maxima and two larger ones observable in the plot. They result from the influence of missed pressure settings with the CCD detector. While the smaller peaks at $m_a = 0.135$ eV, $m_a = 0.192$ eV, $m_a = 0.235$ eV and $m_a = 0.275$ eV show the effect of not taking data for one intermediate setting, the two larger maxima ($m_a \approx 0.16$-0.17 eV and $m_a \approx 0.29$-0.30 eV) are due to four and five missed consecutive settings, respectively. Furthermore, several dips are observable corresponding to extended exposure time in the respective regions. There are cases in which a longer exposure time, i.e. two or more trackings spend at the same pressure setting, did not yield a significant dip in the final exclusion plot. This can be explained by the observation of several events in close-by pressure settings in these cases. Especially apparent is the minimum at $m_a \approx 0.205$ eV. Here, the exposure time was much longer for several settings in order to rule out a potential candidate. Not only were settings repeated for this purpose, but also data at additional intermediate pressure steps were taken.
Both, Fig. 8.27 and Fig. 8.28, show that the most sensitive limits are obtained for axion masses up to 0.387 eV, which corresponds to the last measured pressure setting with ^{4}He of $p_{148} = 13.42$ mbar. After this, coherence is lost and the limits increase rapidly. In order to restore coherence for higher

masses, the pressure has to be further increased, which is done using ^{3}He in the cold bore, since ^{4}He reaches its vapor pressure at 16.4 mbar.

8.6.2 Combined Result of the CCD Detector for Phase I and II

It is also possible to combine the results of the CCD detector for Phase I with those obtained for Phase II with ^{4}He in the work at hand. This can be accomplished in exactly the same way as the combination of the different pressure settings, i.e. by multiplying the maximum likelihood function for vacuum (Phase I) with those for the pressure settings taken with ^{4}He in the cold bore (Phase II). Then the exclusion plot can be obtained by integrating the probability in the physical region up to 95% of the area. The combined result of the CCD detector for Phase I and the ^{4}He part of Phase II is presented in Fig. 8.29. Here, the influence of the difference in exposure time for Phase I and II can be observed. During Phase I the CCD detector took data at one single "pressure setting", namely at $p = 0.0$ mbar (vacuum), for 318.3 h, while the average time spent at a pressure setting in

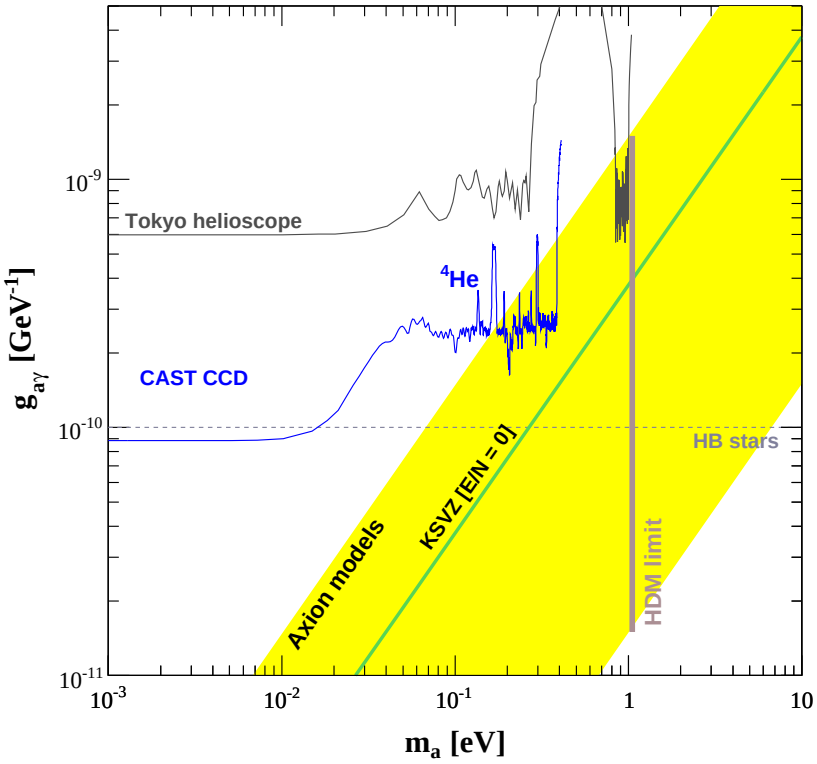

Figure 8.29: Final CCD exclusion plot of the axion-to-photon coupling constant at 95% CL for all data obtained in Phase I and Phase II with ^{4}He gas at CAST with the CCD detector. The achieved limit of the CCD detector is compared with the same experimental results and theoretical constraints as in Fig. 8.27. The yellow band represents the typical theoretical axion models and the green solid line corresponds to the case of the KSVZ model with $E/N = 0$.

Phase II is 1.6 h (5675.3 s). This results in a difference between the general level for the two phases of about a factor 2, which is due to the dependence of the limit on the 8-th root of the exposure time.

CAST investigated a large part of the interesting axion mass range below the hot dark matter limit [70] in the theoretical axion model region (yellow band). No other axion experiment has ever searched the axion mass region up to 0.39 eV with a sensitivity as high as the one provided by the CAST detectors.

The CCD provided herefore the highest discovery potential and this analysis contributed to the final CAST upper limit [121]. These CAST limits surpass former searches in a wide potential axion mass range.

Chapter 9

Summary

The CERN Axion Solar Telescope (CAST) is looking for solar axions in the eV-mass range making use of the Primakoff effect. The magnetic field to convert axions from the Sun into photons is provided by a superconducting magnet. On the ends of the dipole, different X-ray detectors are mounted to look for the photons from axion conversion. Up to the year 2006, these detectors were a Time Projection Chamber (TPC), a MICROMEGAS (MM) detector and an X-ray telescope consisting of mirror optics and a Charge Coupled Device (CCD) as focal plane detector.
In order to study axion masses in a range as wide as possible, the experiment consists of two phases. During Phase I (2003-2004), the magnetic field region was evacuated, while in Phase II (2005-2010) the cold bore is filled with helium gas. In vacuum, axion masses up to $m_a \lesssim 0.02$ eV were investigated and no significant signal above background was found [53]. As a result, an upper limit on the axion-to-photon coupling constant of $g_{a\gamma} < 8.8 \times 10^{-11}$ GeV^{-1} (95% C.L.) could be set for such masses. CAST's second phase can be subdivided into two stages. During the first part of Phase II in 2005 and 2006, ^{4}He has been used at various pressures in order to restore coherence for the axion-to-photon conversion and access masses up to 0.39 eV, thus entering so far unexplored regions favored by theoretical axion models. For the second part of Phase II, which started in 2007, the CAST magnet is filled with ^{3}He, since ^{4}He is no longer gaseous for pressures above 16.4 mbar at a temperature of 1.8 K.
This thesis is devoted to the analysis of the ^{4}He data acquired with the CCD detector at the CAST experiment and therefore based on the data taken during the years of 2005 and 2006.

CAST covered 162 different pressure settings reaching from 0.08 mbar to 13.4 mbar in the data taking period from November 2005 to December 2006. Due to coherence restrictions for the axion-to-photon conversion this allows for a study of axion masses from 0.02 to 0.39 eV with high sensitivity. The CCD detector acquired data for 149 different pressure settings yielding 294.8 h of high quality data under axion-sensitive conditions (solar tracking). During periods in which the magnet was not aligned with the Sun, background data were taken. These data amounted to a total of 2758.1 h. Before, during and after the ^{4}He part of Phase II, the alignment of the X-ray telescope has been continuously monitored with a parallel laser beam and an X-ray source. The center of the expected axion signal region was determined to be at $(x, y) = (40, 108)$ on the CCD chip, which consists of 64×200 pixels. The radius of the signal region has been optimized to be 11.5 pixels.

Applying this definition of the potential axion signal spot, tracking data were defined as events in the signal region, when following the Sun. The standard background for the analysis of the ^{4}He data was defined as all data acquired in the same circular region, when not following the Sun under otherwise identical conditions as solar tracking. Studies of the background stability showed no significant dependence of the background data on various experimental conditions.

In the ^{4}He data taken by the CCD detector, no significant axion signal above background was observed. In order to extract an upper limit, a maximum likelihood method had to be applied due to low counting statistics in the CCD detector. For every pressure setting measured at CAST, a likelihood function was determined. In order to obtain a global upper limit for all density settings together, a global likelihood function was calculated for each considered axion mass as the product of all likelihoods for single pressure settings. The 95% confidence level was then determined by integrating the Bayesian probability over the physically allowed region. The resulting final exclusion plot for the CCD detector with ^{4}He data was presented in this thesis (see Fig. 8.27). A typical upper limit on the axion-to-photon coupling constant was set as

$$g_{a\gamma} \lesssim 2.5 \times 10^{-10}\ \mathrm{GeV}^{-1}\ (95\%\ \mathrm{C.L.}) \tag{9.1}$$

for 0.02 eV$< m_a < 0.39$ eV.
Furthermore, the data acquired with the CCD detector at CAST during Phase I and Phase II with ^{4}He have been used to obtain a composite result. The exclusion plot of this combined result for the CCD detector was shown in Fig. 8.29.

The above results have been considered by the collaboration to derive the final CAST exclusion plot for the axion-to-photon coupling constant [121]. This combined upper limit includes the results of all three CAST detectors during both, Phase I and Phase II with ^{4}He and is displayed in the upper part of Fig. 9.1. The lower figure shows an expanded view of the limit for ^{4}He, obtained by combining the results of all CAST detectors. Through the combination of the results it is possible to smooth out peaks which are apparent in the single detector exclusion plots due to missed pressure settings. This can be accomplished, since it has been assured that every pressure setting has been measured by at least one of the CAST detectors.

The results obtained from the ^{4}He data allow CAST to enter as the first experiment into so far unexplored regions of the axion parameter space favored by theoretical models. CAST is thus to date the most sensitive experiment looking for axions in a wide and interesting mass range. With ^{3}He in the magnet bores, CAST will extend its axion search even further into the *terra incognita* of the favored axion models continuing the hunt for the elusive particle.
The goals of present and future axion searches remain challenging: Find the hypothetical particle or rule out its existence by closing the allowed mass window once and for all. CAST will certainly be able to help shedding light on this particular dark matter candidate. And, following the Sun at sunrise, it might as well be the first experiment able to say: The early bird catches the axion.

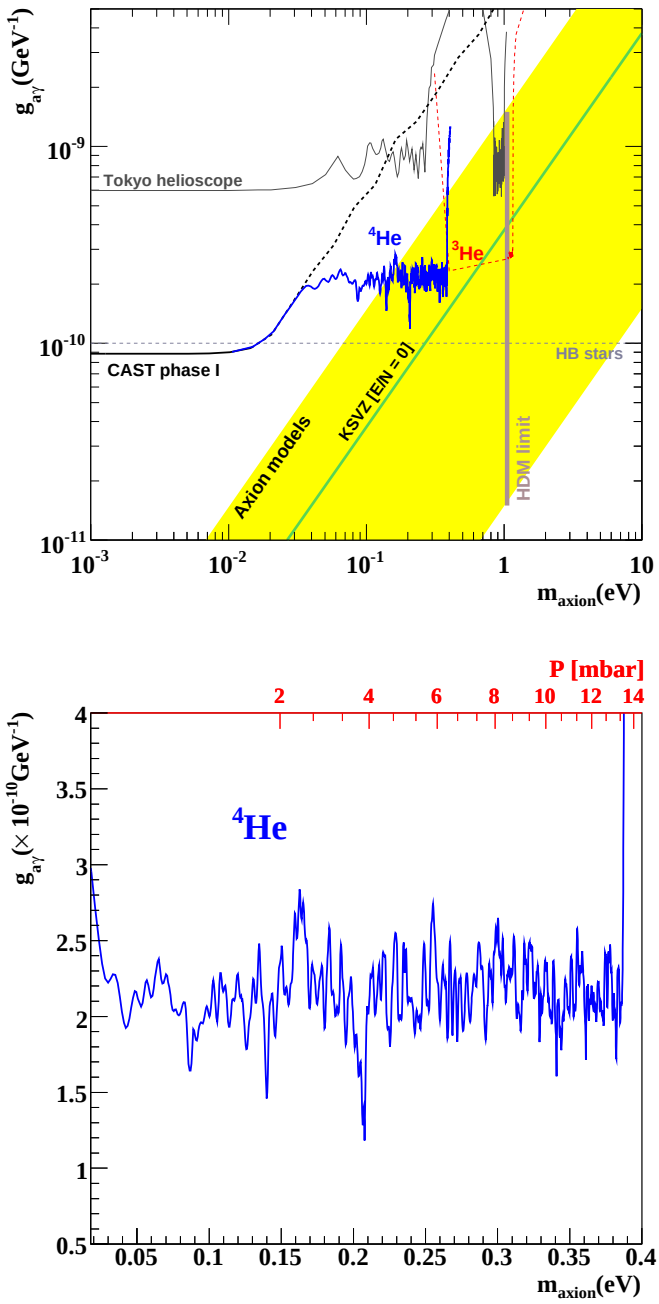

Figure 9.1: Top: Final CAST exclusion plot of the axion-to-photon coupling constant at 95% CL for all data obtained in Phase I and Phase II with ^{4}He gas at CAST with the three X-ray detectors of CAST (CCD, MM and TPC). The achieved limit of CAST is compared with the latest results of the Tokyo helioscope [102]. Furthermore, the Horizontal Branch (HB) star limit [32] and the hot dark matter (HDM) limit [70] are included. The yellow band represents the typical theoretical axion models and the green solid line corresponds to the case of the KSVZ model with $E/N = 0$. The prospects for data taking with ^{3}He have been included in red [121]. Bottom: Expanded view of the ^{4}He limit for all detectors combined. The upper bound is shown between axion masses of 0.02 eV and 0.39 eV, which corresponds to pressures from 0.08-13.4 mbar.

Appendix A

Plasma Frequency

A.1 Dispersion Relation

Generally speaking, a dispersion relation describes the relation between the energy of a system and its momentum. In case of an optical system, i.e for electromagnetic waves, the energy E and momentum p are proportional to frequency ω and wave number k, respectively [111]

$$E = \hbar\omega, \tag{A.1}$$

and

$$p = \frac{h}{\lambda} = \hbar k, \tag{A.2}$$

where λ represents the wavelength. In vacuum the dispersion relation in such a case is then:

$$\omega = ck. \tag{A.3}$$

A neutral plasma is a gas of neutral molecules with some of them being ionized, such that electrons are set free. When an electromagnetic wave traverses such a neutral plasma, then the dispersion relation is given by

$$\omega^2(k) = \omega_p^2 + c^2k^2, \tag{A.4}$$

where ω_p represents the frequency of the plasma oscillations and is given by

$$\omega_p^2 = 4\pi n_e \frac{e^2}{m}, \tag{A.5}$$

with n_e being the electron density, e and m representing the charge and mass of the electron, respectively. One can see in Eq. (A.4) that the lowest possible frequency in this case can be obtained for $k = 0$, i.e. λ tends to infinity (see Eq. (A.2)). This is comparable to the case of coupled pendulums, when all the pendulums oscillate with the same phase and amplitude. The dispersion relation in this case would be

$$\omega^2(k) = \frac{g}{l} + \frac{4D}{M}\sin^2\left(\frac{ka}{2}\right), \tag{A.6}$$

where g is the acceleration due to gravity, l the length of each individual pendulum, D is the spring constant, M the mass of each pendulum and a the separation of the pendulum beads. In this way, the case of $k = 0$ for plasma oscillations equals the coupled pendulums with $k = 0$, i.e. the familiar relation

$$\omega^2(k) = \frac{g}{l}. \tag{A.7}$$

In order to derive Eq. (A.5), which will be done in the following, it is easiest to consider the case of $k = 0$.

A.2 Plasma Oscillation Frequency w_p

On average the plasma is neutral, such that it does not provide an electrostatic field. But even in a neutral plasma, some ionized molecules and free electrons are present besides the neutral molecules. Thus, in case one just considers a specific region, it is possible to observe an excess of charge of one sign, while there is a lack of it in some neighboring area, i.e. a local electric field in the generally neutral plasma can be seen.
The effect of such an electric field is that the ions can be accelerated in one direction, while the electrons will experience a force driving them towards the opposite way. In this manner, excesses and deficits of charge cancel out and the electric field vanishes. Since the electrons and ions are accelerated, they have a certain speed, when the field disappears, such that they pass the point of equillibrium. Thus a new electric field is created having opposite sign in comparison to the originally accelerating field. Repetition of this process results in oscillations of the plasma.
We will now just consider the movement of the electrons, since we can neglect the motion of the ions, which have a significantly higher mass, while having the same absolute charge as an electron. Let us consider now a confined region of the plasma as shown in Fig. A.1. On one wall confining the plasma, an excess of charge Q will be observable, while there is a deficit of it ($-Q$) on the other through the motion of the free electrons. If A is the area of the wall, one obtains an electric field E_x in the plasma in one direction (here: x) as [163]

$$E_x = -4\pi\frac{Q}{A}. \tag{A.8}$$

Applying Newton's law leads to

$$\frac{d^2x}{dt^2} = \frac{F}{m} = \frac{eE_x}{m} = -4\pi e\frac{Q}{mA}, \tag{A.9}$$

where e is the charge of the electron. If the density of electrons per cm^3 is N_e and each electron is off its equillibrium position by a distance x, then the excess charge Q on one wall is given by

$$Q = n_e eAx. \tag{A.10}$$

If now Eq. (A.10) is differentiated twice with respect to time, this yields

$$\frac{d^2Q}{dt^2} = \frac{d^2}{dt^2}(n_e eAx) = n_e eA\frac{d^2x}{dt^2}, \tag{A.11}$$

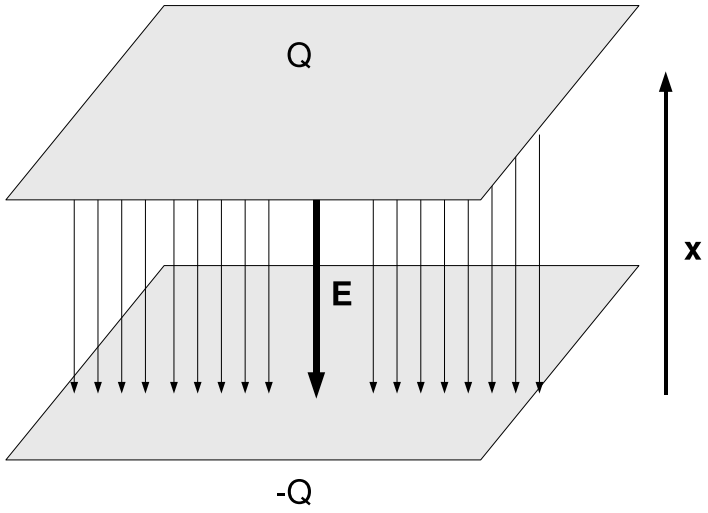

Figure A.1: Confined plasma between two walls. Caused by the motion of the electrons on one wall, there is an excess of charge (Q) while on the other a deficit ($-Q$) is found.

and by inserting Eq. (A.9), it follows

$$\frac{d^2Q}{dt^2} = -\frac{4\pi n_e e^2}{m}Q. \tag{A.12}$$

The solution of this differential equation is given by

$$Q = Q_0 cos(\omega t + \varphi), \tag{A.13}$$

with

$$\omega^2 = \frac{4\pi n_e e^2}{m} \equiv \omega_p^2, \tag{A.14}$$

where ω_p is then the so-called plasma oscillation frequency.

Appendix B

Heaviside-Lorentz Units

In the formula for the conversion probability of axions into photons in the presence of a transverse magnetic field as given in Chap. 4, Eq. (4.25), the so-called natural Heaviside-Lorentz units have been used. In this system, the dimensions GeV and $(\mathrm{T}\cdot\mathrm{m})$ are equivalent, due to the fact that charge is dimensionless and natural units are used ($c = 1$).
The speed of light c is given by

$$c = 299\,792\,458\ \frac{\mathrm{m}}{\mathrm{s}} = \{c\}[c], \tag{B.1}$$

where $c = 299\,792\,458$ is the numerical value of c and $[c]$ represents the unit, i.e. m/s. Equivalently one obtains for the electric charge

$$e = 1.602176487 \times 10^{-19}\ \mathrm{C} = \{\mathrm{e}\}[\mathrm{e}]. \tag{B.2}$$

Due to the fact that

$$\begin{aligned}
1\frac{\mathrm{GeV}}{\mathrm{c}} &= \frac{10^{\,9}\ \mathrm{eV}}{c} \\
&= \frac{10^{\,9} \times \{e\}\ \mathrm{J}}{\{c\}\frac{\mathrm{m}}{\mathrm{s}}} \\
&= \frac{10^{\,9} \times \{e\}\ \mathrm{C}\ \frac{\mathrm{J}}{\mathrm{C}}}{\{c\}\frac{\mathrm{m}}{\mathrm{s}}} \\
&= \frac{10^{\,9} \times \{e\}\ \mathrm{C}\ \frac{\mathrm{J}}{\mathrm{C}}}{\{c\}\frac{\mathrm{m}}{\mathrm{s}}} \\
&= \frac{10^{\,9}}{\{c\}} e \frac{\mathrm{J\,s}}{\mathrm{C\,m^2}}\mathrm{m} \\
&= \frac{10^{\,9}}{\{c\}} e\ \mathrm{T\,m},
\end{aligned} \tag{B.3}$$

and thus

$$1\frac{\mathrm{GeV}}{\mathrm{c}} = 3.335640952\ e\ \mathrm{T\ m}. \tag{B.4}$$

Using natural units, i.e. $c = 1$, Eq. (B.4) turns into

$$1\ \mathrm{GeV} = 3.335640952\ \mathrm{e\ T\ m}, \tag{B.5}$$

such that the relation between GeV and $\mathrm{T \cdot m}$ depends on the definition of the electric units. In Gaussian units, the electric charge is chosen to be

$$e = \sqrt{\alpha} \approx 0.085424542, \tag{B.6}$$

while Heaviside units differ from the Gaussian units by a factor of $\sqrt{4\pi}$ and yield

$$e = \sqrt{4\pi\alpha} \approx 0.30282212. \tag{B.7}$$

In both systems, the charge is dimensionless. Using now Heaviside-Lorentz units in Eq. (B.5) yields

$$1\ \mathrm{GeV} = 1.010105865\ \mathrm{T\ m}, \tag{B.8}$$

and the probability of conversion (Chap. 4, Eq. (4.25)) becomes dimensionless.

Appendix C

Data Overview for ^{4}He

In this part of the appendix a detailed list summarizing dates on which the CCD took data, the corresponding pressures, tracking time and average background counts can be found. The dates on which the CCD took data are provided in the form yy/mm/dd. While the pressure index labeled *CAST* numerates all full steps from 1 to 160 and includes half-sized steps as intermediate numbers, e.g. index 44.5 for a pressure of 3.705 mbar, the index *CCD* represents a renumeration for the settings taken by the CCD detector. This index starts at 0 and ends at 148, thus labeling all 149 different settings covered by the CCD detector. Furthermore, the following tables also include the tracking time for each pressure setting and the total number of background counts expected in the energy range from 1 to 7 keV during this time.

Table C.1: Tracking dates, Pressure settings, Tracking times per pressure setting and Background counts

Date CCD Tracking	Pressure [mbar]	Pressure Index CCD	Pressure Index CAST	Tracking time t [sec]	Total number of bgrd counts in t
051124	0.0799	0	1	3281.0	0.142
051125	0.1616	1	2	12361.0	0.535
051127	0.2445	2	3	6181.5	0.268
051128	0.3314	3	4	6241.5	0.270
051129	0.4152	4	5	6241.5	0.270
051130	0.4970	5	6	6180.0	0.268
051201	0.5799	6	7	6121.0	0.265
051202	0.6627	7	8	6060.5	0.262
051203	0.7455	8	9	6060.0	0.262
051204	0.8284	9	10	4681.0	0.203
051205	0.9118	10	11	11700.0	0.507
051207	0.9963	11	12	5760.0	0.249
051208	1.0809	12	13	5401.0	0.234
051209	1.1656	13	14	5640.0	0.244
051210	1.2488	14	15	5640.0	0.244
051211	1.3321	15	16	10442.0	0.452
051213	1.4153	16	17	5401.0	0.234
051214	1.4986	17	18	5461.0	0.236
051215	1.5819	18	19	5401.5	0.234
060124	1.7484	19	21	6001.0	0.260
060125	1.8316	20	22	5941.5	0.257
060126	1.9152	21	23	5940.5	0.257
060127	1.9981	22	24	5880.5	0.255
060128	2.0814	23	25	5941.5	0.257
060129	2.1647	24	26	5880.5	0.255
060130	2.2479	25	27	5821.5	0.252
060131	2.3312	26	28	5821.5	0.252
060505	2.7556	27	33	5641.5	0.244
060506	2.8354	28	34	5701.5	0.247
060507	2.9177	29	35	5701.5	0.247
060508	3.0001	30	36	5761.5	0.250
060509	3.0824	31	37	5759.0	0.249
060510	3.1648	32	38	5761.5	0.250
060511	3.2477	33	39	5821.5	0.252
060614	3.4140	34	41	10321.0	0.447
060616	3.4970	35	42	5580.5	0.242
060528	3.5799	36	43	11761.5	0.509
060529	3.6631	37	44	28504.5	1.234
060606	3.7051	38	44.5	6000.5	0.260
060530	3.7463	39	45	82555.5	3.575

Date CCD Tracking	Pressure [mbar]	Pressure Index CCD	Pressure Index CAST	Tracking time t [sec]	Total number of bgrd counts in t
060607	3.7883	40	45.5	5880.5	0.255
060531	3.8292	41	46	35674.5	1.545
060609	3.9148	42	47	11952.0	0.518
060611	3.9979	43	48	11544.5	0.500
060612	4.0810	44	49	11821.0	0.512
060613	4.1641	45	50	11820.0	0.512
060716	4.2449	46	51	6120.5	0.265
060717	4.3280	47	52	6120.5	0.265
060720	4.4112	48	53	6060.5	0.262
060721	4.4943	49	54	6060.5	0.262
060722	4.5775	50	55	6060.5	0.262
060723	4.6607	51	56	6000.5	0.260
060724	4.7438	52	57	5941.5	0.257
060727	4.8270	53	58	10982.0	0.476
060729	4.9101	54	59	5640.5	0.244
060805	5.0764	55	61	5761.5	0.250
060806	5.1595	56	62	5760.5	0.249
060807	5.2426	57	63	5700.5	0.247
060808	5.3257	58	64	11402.0	0.494
060810	5.4088	59	65	5640.5	0.244
060811	5.4920	60	66	5641.0	0.244
060812	5.5753	61	67	5641.5	0.244
060813	5.6586	62	68	5641.5	0.244
060814	5.7419	63	69	5581.5	0.242
060815	5.8253	64	70	5580.5	0.242
060816	5.9086	65	71	5580.5	0.242
060817	5.9919	66	72	5520.5	0.239
060818	6.0752	67	73	5520.5	0.239
060819	6.1585	68	74	5521.5	0.239
060820	6.2418	69	75	5461.5	0.237
060821	6.3253	70	76	5460.5	0.236
060822	6.4087	71	77	5460.5	0.236
060825	6.4920	72	78	5401.0	0.234
060826	6.5753	73	79	5400.5	0.234
060827	6.6586	74	80	5340.5	0.231
060828	6.7418	75	81	5340.5	0.231
060830	6.9084	76	83	5341.0	0.231
060831	6.9917	77	84	5341.0	0.231
060901	7.0750	78	85	5341.5	0.231
060902	7.1583	79	86	5341.5	0.231

Date CCD Tracking	Pressure [mbar]	Pressure Index CCD	Pressure Index CAST	Tracking time t [sec]	Total number of bgrd counts in t
060903	7.2416	80	87	5281.5	0.229
060904	7.3249	81	88	5281.5	0.229
060905	7.4081	82	89	5281.0	0.229
060906	7.4914	83	90	5281.5	0.229
060907	7.5747	84	91	5221.5	0.226
060908	7.6579	85	92	10441.5	0.452
060913	7.7412	86	93	5221.5	0.226
060920	8.2409	87	99	5220.5	0.226
060921	8.3361	88	100	5161.5	0.224
060922	8.4092	89	101	5221.0	0.226
060923	8.4923	90	102	5221.5	0.226
060924	8.5758	91	103	5220.5	0.226
060925	8.6590	92	104	5220.5	0.226
060926	8.7421	93	105	5220.5	0.226
060930	8.8255	94	106	5221.5	0.226
061001	8.9088	95	107	5280.5	0.229
061002	8.9920	96	108	5220.5	0.226
061003	9.0753	97	109	5220.5	0.226
061005	9.1586	98	110	5280.5	0.229
061006	9.2418	99	111	5281.0	0.229
061007	9.3251	100	112	5220.5	0.226
061008	9.4084	101	113	5281.5	0.229
061009	9.4917	102	114	5280.5	0.229
061011	9.5760	103	115	5341.5	0.231
061012	9.6605	104	116	5281.0	0.228
061013	9.7450	105	117	5340.5	0.231
061014	9.8295	106	118	10681.0	0.463
061016	9.9141	107	119	5340.5	0.231
061017	9.9988	108	120	5340.5	0.231
061018	10.0835	109	121	5400.5	0.234
061019	10.1683	110	122	16262.5	0.704
061022	10.2531	111	123	11042.0	0.478
061029	10.3379	112	124	5520.5	0.239
061030	10.4228	113	125	5581.5	0.242
061031	10.5078	114	126	5580.5	0.242
061101	10.5928	115	127	5400.5	0.234
061102	10.6778	116	128	5641.0	0.244
061103	10.7631	117	129	5640.5	0.244
061104	10.8483	118	130	5700.5	0.247
061105	10.9335	119	131	5701.0	0.247

Date CCD Tracking	Pressure [mbar]	Pressure Index CCD	Pressure Index CAST	Tracking time t [sec]	Total number of bgrd counts in t
061106	11.0188	120	132	5701.5	0.247
061107	11.1041	121	133	5761.0	0.249
061108	11.1895	122	134	5761.5	0.250
061109	11.2749	123	135	5821.5	0.252
061110	11.3604	124	136	5820.5	0.252
061111	11.4459	125	137	5820.5	0.252
061112	11.5314	126	138	5821.0	0.252
061113	11.6170	127	139	5580.5	0.242
061114	11.7027	128	140	5940.5	0.257
061115	11.7884	129	141	5941.0	0.257
061116	11.8741	130	142	5941.5	0.257
061117	11.9599	131	143	5940.5	0.257
061119	12.0458	132	144	6000.5	0.260
061120	12.1317	133	145	6060.5	0.262
061121	12.2176	134	146	6000.5	0.260
061122	12.3036	135	147	6061.5	0.263
061124	12.3897	136	148	6121.0	0.265
061125	12.4757	137	149	6121.5	0.265
061126	12.5619	138	150	6181.5	0.268
061127	12.6480	139	151	6181.5	0.268
061128	12.7342	140	152	6241.5	0.270
061129	12.8205	141	153	6241.5	0.270
061130	12.9068	142	154	6240.0	0.270
061201	12.9931	143	155	6120.0	0.265
061202	13.0795	144	156	6061.0	0.262
061203	13.1659	145	157	6060.0	0.262
061205	13.2524	146	158	5881.0	0.255
061206	13.3390	147	159	5820.0	0.252
061208	13.4256	148	160	5700.0	0.247

Appendix D

Tracking Data Overview for ^{4}He

All events registered in the signal spot of the CCD detector during the ^{4}He run in tracking times are summarized in the following table. A total of 45 counts were observed in the energy range from 1 to 7 keV. In the table, the pressure index of the CCD is given followed by the actual pressure in mbar. The date is provided in the form yy/mm/dd. Both the tracking times at the specific day and the total tracking time at the considered pressure setting are listed. Furthermore, the number of registered events and their energies are given. At pressure settings other than the provided ones 0 events were registered.

Table D.1: Summary of events for the CCD detector. The number of the pressure setting, the pressure and date of observation and the tracking time on that day are given. In addition, the total tracking time at the pressure setting is shown together with the number of events and their energies.

CCD Setting 0-148	Pressure Setting [mbar]	Date [yy/mm/dd]	Tracking Time [sec]	Total Tracking Time [sec]	No. of Counts	Energy [keV]
1	0.162	051125	6180.5	12361.0	1	3.80
1	0.162	051126	6180.5	12361.0	1	5.44
3	0.331	051128	6241.5	6241.5	1	2.92
4	0.415	051129	6241.5	6241.5	1	2.01
15	1.332	051212	5581.0	10442	1	6.40
20	1.832	060125	5941.5	5941.5	1	2.99
22	1.998	060127	5880.5	5880.5	1	1.43
26	2.331	060131	5821.5	5821.5	1	2.03
36	3.580	060620	5581.0	11761.5	1	1.76
37	3.663	060529	6180.5	28504.5	1	1.25
37	3.663	060623	5580.5	28504.5	2	6.47, 3.28
39	3.746	060530	6180.5	82555.5	3	4.40, 5.66, 6.88
39	3.746	060601	6179.5	82555.5	1	5.16
39	3.746	060604	6001.0	82555.5	1	3.93
39	3.746	060605	6000.5	82555.5	1	4.07
39	3.746	060627	5580.5	82555.5	1	4.06
39	3.746	060702	5760.5	82555.5	1	1.01
42	3.915	060712	6181.5	11952.0	1	1.31
42	3.915	060609	5770.5	11952.0	1	3.47
46	4.245	060716	6120.5	6120.5	1	5.83
48	4.411	060720	6060.5	6060.5	1	3.61
61	5.575	060812	5641.5	5641.5	1	5.79
65	5.909	060816	5580.5	5580.5	1	5.41
70	6.325	060821	5460.5	5460.5	3	3.58, 1.32, 1.52
88	8.336	060921	5161.5	5161.5	1	3.16
91	8.576	060924	5220.5	5220.5	1	4.97
100	9.325	061007	5220.5	5220.5	1	4.10
103	9.576	061011	5341.5	5341.5	1	1.04
106	9.830	061014	5340.5	10681.0	2	3.47, 5.36
107	9.914	061016	5340.5	5340.5	1	1.31
110	10.168	061019	5401.0	16262.5	1	2.88
114	10.508	061031	5580.5	5580.5	1	2.48
117	10.763	061103	5640.5	5640.5	1	4.09
130	11.874	061116	5941.5	5941.5	1	5.09
132	12.046	061119	6000.5	6000.5	1	4.10
140	12.734	061128	6241.5	6241.5	1	3.795
143	12.993	061201	6120.0	6120.0	1	2.37
145	13.166	061203	6060.0	6060.0	1	6.99
147	13.339	061206	5820.0	5820.0	1	3.57

Appendix E

Background Data Overview for ^{4}He

Several possibilities of defining the background have been studied using the full background set for ^{4}He as basis. Hereby, the same conditions as during tracking were required (magnetic field on, VT4 open, etc.), without following the Sun. The different definitions have been labeled Background 1, 2, 3 and 4 and are chosen as follows:

- Background 1: Spot during background times
- Background 2: Full chip during background times
- Background 3: Full chip without spot during background times
- Background 4: Full chip without spot during tracking times

The following table summarizes the CCD background count rates for the 4 different definitions. The background is given for every energy bin of 0.3 keV in the 1 to 7 keV range.

Table E.1: Background per energy bin of 0.3 keV in the range of $1 - 7$ keV if background condition is Background 1 (spot region during background times), Background 2 (full chip during background times), Background 3 (Full chip without spot region during background times) or Background 4 (Full chip without spot region during tracking times).

Index of Energy bin i	**Background 1 Total counts in i [$10^{-6}\times$ cts/sec]**	**Background 2 Total counts in i [$10^{-6}\times$ cts/sec]**	**Background 3 Total counts in i [$10^{-6}\times$ cts/sec]**	**Background 4 Total counts in i [$10^{-6}\times$ cts/sec]**
0	2.92± 0.54	3.12± 0.10	3.13± 0.11	3.27± 0.33
1	2.52± 0.50	3.02± 0.10	3.04± 0.10	2.44± 0.28
2	1.61± 0.40	2.59± 0.09	2.63± 0.10	2.77± 0.30
3	3.42± 0.59	2.97± 0.10	2.95± 0.10	3.40± 0.34
4	2.72± 0.52	2.78± 0.10	2.78± 0.10	2.87± 0.31
5	1.71± 0.42	2.45± 0.09	2.48± 0.09	2.67± 0.23
6	2.72± 0.52	2.35± 0.09	2.34± 0.09	2.38± 0.28
7	2.52± 0.50	2.35± 0.09	2.34± 0.09	2.21± 0.27
8	2.22± 0.47	2.31± 0.09	2.31± 0.09	2.31± 0.28
9	2.11± 0.46	2.27± 0.09	2.28± 0.09	2.51± 0.29
10	1.01± 0.32	2.21± 0.09	2.25± 0.09	1.72± 0.24
11	2.42± 0.49	2.27± 0.09	2.27± 0.09	1.88± 0.25
12	2.11± 0.46	1.95± 0.08	1.95± 0.08	2.71± 0.30
13	1.31± 0.36	2.15± 0.09	2.18± 0.09	1.42± 0.22
14	2.01± 0.45	2.06± 0.08	2.06± 0.09	1.75± 0.24
15	1.51± 0.39	2.00± 0.08	2.02± 0.08	2.67± 0.32
16	1.11± 0.33	2.18± 0.09	2.22± 0.09	1.58± 0.23
17	2.32± 0.48	2.42± 0.09	2.42± 0.09	2.71± 0.30
18	2.52± 0.50	2.91± 0.10	2.92± 0.10	3.04± 0.32
19	2.52± 0.50	2.10± 0.08	2.08± 0.09	1.98± 0.26

Appendix F

$g_{10}^4(\mathrm{min})$ and its Statistical Error

A detailed list containing the value of $g^4_{10,\mathrm{min}}$ for each mass considered in the analysis for which $g^4_{10,\mathrm{min}} \neq 0$ together with the asymmetric errors is provided in the following table F.1. The respective values for the masses corresponding to the measured density settings only are given in Tab. F.2. Furthermore both tables contain the calculated upper limit on $g_{a,\gamma}$ at 95% C.L. obtained in the analysis for each of the listed axion masses.

Table F.1: Axion mass index, Axion mass , g_{10}^4(min) and its errors

Mass step	**Axion mass [eV]**	$g_{10}^4(\mathrm{min})$	**Stat. error (left)**	**Stat. error (right)**	$g_{a\gamma}(95\%\mathrm{C.L.})$ **[GeV^{-1}]**
0	0.0000	119.840	119.314	183.365	4.8880e-10
1	0.0106	79.660	93.114	142.163	4.5694e-10
2	0.0149	32.138	63.905	97.356	4.1543e-10
3	0.0183	3.352	44.399	65.158	3.7243e-10
8	0.0299	4.260	15.534	23.005	2.8763e-10
9	0.0317	12.961	14.754	22.574	2.9066e-10
10	0.0334	16.442	13.141	20.857	2.8863e-10
11	0.0350	16.116	11.168	18.395	2.8168e-10
12	0.0366	14.098	9.197	15.611	2.7116e-10
13	0.0381	11.726	7.495	12.922	2.5901e-10
14	0.0395	9.613	6.161	10.755	2.4713e-10
15	0.0409	8.174	5.305	9.308	2.3807e-10
16	0.0423	7.565	4.958	8.697	2.3404e-10
17	0.0436	7.788	5.110	8.929	2.3570e-10
18	0.0448	8.748	5.726	9.924	2.4204e-10
19	0.0461	10.223	6.736	11.528	2.5116e-10
20	0.0473	11.834	8.039	13.455	2.6063e-10
21	0.0484	12.709	9.356	15.184	2.6699e-10
22	0.0496	11.475	10.298	15.977	2.6747e-10
23	0.0507	6.598	10.603	15.762	2.6176e-10
29	0.0569	8.086	13.001	19.690	2.7922e-10
30	0.0579	10.553	11.245	17.863	2.7736e-10
31	0.0588	9.870	9.452	15.365	2.6999e-10
32	0.0598	8.996	8.300	13.602	2.6326e-10
33	0.0607	8.965	8.079	13.303	2.6199e-10
34	0.0616	9.544	8.587	14.177	2.6530e-10
35	0.0625	9.849	9.557	15.527	2.7002e-10
36	0.0634	8.424	10.565	16.522	2.7178e-10
37	0.0643	5.572	12.760	19.198	2.7607e-10
38	0.0651	4.141	15.532	22.017	2.7905e-10
39	0.0660	5.349	10.881	16.506	2.6726e-10
40	0.0668	5.985	8.318	12.890	2.5586e-10
41	0.0677	6.516	7.724	12.150	2.5385e-10
42	0.0685	6.860	8.129	12.810	2.5649e-10
43	0.0693	6.202	9.361	14.422	2.6078e-10
44	0.0701	0.622	11.504	16.791	2.6382e-10
127	0.1191	-0.867	9.351	13.537	2.5003e-10
128	0.1196	0.244	8.807	12.846	2.4777e-10
129	0.1200	0.305	7.915	11.570	2.4151e-10
130	0.1205	-0.194	6.948	10.127	2.3318e-10

Mass step	Axion mass [eV]	$g_{10}^4(\mathrm{min})$	Stat. error (left)	Stat. error (right)	$g_{a\gamma}(95\%\mathrm{C.L.})$ [GeV^{-1}]
131	0.1209	-0.745	6.184	8.974	2.2565e-10
132	0.1214	-1.047	5.801	8.396	2.2154e-10
133	0.1219	-0.990	5.867	8.496	2.2225e-10
134	0.1223	-0.580	6.376	9.266	2.2764e-10
135	0.1228	0.040	7.249	10.583	2.3599e-10
136	0.1232	0.521	8.280	12.115	2.4455e-10
137	0.1237	0.320	9.157	13.363	2.5022e-10
138	0.1241	-1.039	9.658	13.972	2.5182e-10
178	0.1410	2.415	11.298	16.679	2.6657e-10
179	0.1414	6.795	9.914	15.241	2.6655e-10
180	0.1418	7.725	8.668	13.666	2.6272e-10
181	0.1422	7.693	7.856	12.510	2.5833e-10
182	0.1426	7.622	7.572	12.109	2.5665e-10
183	0.1430	7.775	7.892	12.581	2.5871e-10
184	0.1433	7.901	8.755	13.814	2.6348e-10
185	0.1437	7.096	10.041	15.473	2.6799e-10
186	0.1441	2.901	11.481	16.987	2.6844e-10
229	0.1599	-0.689	11.874	17.212	2.6564e-10
230	0.1603	5.651	9.938	15.120	2.6487e-10
231	0.1606	7.142	9.047	14.087	2.6309e-10
232	0.1610	7.669	9.189	14.372	2.6487e-10
233	0.1613	7.826	10.564	16.320	2.7211e-10
234	0.1616	5.967	13.653	20.494	2.8372e-10
354	0.1988	4.641	7.996	11.994	2.4259e-10
355	0.1991	6.594	6.985	11.045	2.4059e-10
356	0.1994	7.345	6.865	10.812	2.3900e-10
357	0.1997	8.035	7.563	11.198	2.4027e-10
358	0.1999	7.747	8.567	11.636	2.4034e-10
359	0.2002	4.575	7.654	10.466	2.3094e-10
360	0.2005	2.669	5.588	8.000	2.1762e-10
361	0.2008	2.007	4.205	6.209	2.0597e-10
362	0.2011	1.681	3.328	4.997	1.9572e-10
363	0.2013	1.977	3.055	4.644	1.9204e-10
364	0.2016	3.398	3.443	5.112	1.9624e-10
365	0.2019	5.956	4.077	5.406	2.0327e-10
366	0.2022	7.683	4.077	5.177	2.0634e-10
367	0.2024	7.973	3.778	4.773	2.0474e-10
368	0.2027	7.225	3.327	4.221	1.9914e-10
369	0.2030	5.966	2.799	3.594	1.9077e-10
370	0.2033	4.756	2.309	3.007	1.8169e-10

Mass step	**Axion mass [eV]**	$g_{10}^4(\mathbf{min})$	**Stat. error (left)**	**Stat. error (right)**	$g_{a\gamma}(\mathbf{95\%C.L.})$ **[GeV^{-1}]**
371	0.2035	3.956	1.978	2.598	1.7455e-10
372	0.2038	3.606	1.834	2.418	1.7110e-10
373	0.2041	3.641	1.855	2.450	1.7166e-10
374	0.2044	3.999	2.025	2.672	1.7550e-10
375	0.2046	4.570	2.309	3.042	1.8137e-10
376	0.2049	5.095	2.641	3.479	1.8705e-10
377	0.2052	5.145	2.920	3.854	1.9019e-10
378	0.2055	4.238	3.047	4.058	1.8875e-10
379	0.2057	1.880	3.065	4.065	1.8175e-10
385	0.2073	0.554	4.452	6.563	2.0653e-10
386	0.2076	3.866	5.011	7.851	2.2061e-10
387	0.2079	6.157	5.599	9.292	2.3148e-10
388	0.2082	7.500	5.980	10.255	2.3706e-10
389	0.2084	7.541	5.928	10.304	2.3824e-10
390	0.2087	6.678	5.691	9.765	2.3677e-10
391	0.2090	5.366	5.483	9.032	2.3407e-10
392	0.2092	4.104	5.558	8.763	2.3113e-10
393	0.2095	2.701	6.124	9.316	2.3151e-10
394	0.2098	-0.673	6.905	10.057	2.3070e-10
414	0.2150	-1.157	5.470	7.907	2.1847e-10
415	0.2153	1.428	5.572	8.323	2.2449e-10
416	0.2155	3.764	6.043	9.333	2.3509e-10
417	0.2158	5.914	6.686	10.643	2.4589e-10
418	0.2160	7.488	7.172	11.652	2.5364e-10
419	0.2163	8.086	7.220	11.833	2.5641e-10
420	0.2166	7.920	6.934	11.347	2.5449e-10
421	0.2168	7.626	6.652	10.867	2.5225e-10
422	0.2171	7.791	6.727	10.998	2.5305e-10
423	0.2173	8.716	7.329	12.056	2.5927e-10
424	0.2176	10.394	8.407	14.043	2.6889e-10
425	0.2178	12.347	9.704	16.384	2.7800e-10
426	0.2181	13.351	10.580	17.858	2.8247e-10
427	0.2184	12.407	10.625	17.612	2.8017e-10
428	0.2186	9.627	9.960	15.977	2.7207e-10
429	0.2189	6.090	9.186	14.153	2.6101e-10
430	0.2191	2.819	9.115	13.577	2.5419e-10
431	0.2194	0.272	10.571	15.432	2.5862e-10
432	0.2196	1.442	13.213	18.742	2.6792e-10
433	0.2199	6.693	12.819	19.071	2.7499e-10
434	0.2201	9.276	11.332	17.748	2.7705e-10

Mass step	Axion mass [eV]	$g_{10}^4(\mathrm{min})$	Stat. error (left)	Stat. error (right)	$g_{a\gamma}(95\%\mathrm{C.L.})$ [GeV^{-1}]
435	0.2204	9.816	9.873	15.757	2.7313e-10
436	0.2207	9.635	8.707	14.099	2.6805e-10
437	0.2209	9.428	8.007	13.142	2.6474e-10
438	0.2212	9.510	7.809	12.932	2.6392e-10
439	0.2214	9.984	8.070	13.489	2.6626e-10
440	0.2217	10.884	8.850	14.780	2.7100e-10
441	0.2219	11.780	9.955	16.470	2.7649e-10
442	0.2222	11.765	11.090	17.930	2.7984e-10
443	0.2224	9.385	11.996	18.599	2.7837e-10
444	0.2227	1.869	12.777	18.632	2.7063e-10
546	0.2469	1.074	10.243	15.023	2.5905e-10
547	0.2471	4.789	9.871	14.915	2.6273e-10
548	0.2474	7.494	9.926	15.370	2.6843e-10
549	0.2476	9.461	10.064	15.896	2.7326e-10
550	0.2478	10.546	9.990	16.003	2.7584e-10
551	0.2480	10.719	9.588	15.492	2.7478e-10
552	0.2483	10.317	9.010	14.631	2.7133e-10
553	0.2485	9.859	8.538	13.908	2.6805e-10
554	0.2487	9.727	8.376	13.700	2.6709e-10
555	0.2489	10.104	8.658	14.162	2.6933e-10
556	0.2492	10.838	9.283	15.161	2.7371e-10
557	0.2494	11.474	9.987	16.255	2.7819e-10
558	0.2496	11.380	10.433	16.835	2.7961e-10
559	0.2498	10.168	10.445	16.573	2.7659e-10
560	0.2501	7.961	10.152	15.764	2.7028e-10
561	0.2503	5.079	9.952	15.062	2.6364e-10
562	0.2505	1.353	10.236	15.037	2.5900e-10
580	0.2545	1.980	10.714	15.796	2.6310e-10
581	0.2547	5.920	10.673	16.191	2.6910e-10
582	0.2549	8.728	10.852	16.866	2.7505e-10
583	0.2552	10.416	10.848	17.180	2.7895e-10
584	0.2554	10.920	10.454	16.748	2.7848e-10
585	0.2556	10.575	9.777	15.781	2.7487e-10
586	0.2558	10.035	9.180	14.869	2.7088e-10
587	0.2560	9.798	8.938	14.491	2.6932e-10
588	0.2562	10.050	9.139	14.827	2.7072e-10
589	0.2565	10.692	9.741	15.779	2.7496e-10
590	0.2567	11.275	10.493	16.914	2.7953e-10
591	0.2569	11.102	11.014	17.576	2.8117e-10

Mass step	**Axion mass [eV]**	$g_{10}^4(\mathrm{min})$	**Stat. error (left)**	**Stat. error (right)**	$g_{a\gamma}(95\%\mathrm{C.L.})$ **[GeV^{-1}]**
592	0.2571	9.680	11.080	17.375	2.7812e-10
593	0.2573	7.031	10.835	16.583	2.7184e-10
594	0.2575	3.294	10.688	15.884	2.6471e-10
623	0.2638	1.571	13.112	19.221	2.7511e-10
624	0.2640	8.885	12.248	18.907	2.8178e-10
625	0.2642	11.236	11.249	17.914	2.8235e-10
626	0.2644	13.533	11.191	18.575	2.8684e-10
627	0.2646	17.077	11.975	21.129	2.9286e-10
628	0.2648	19.390	12.444	22.495	2.9468e-10
629	0.2650	19.689	12.551	22.723	2.9523e-10
630	0.2652	17.917	12.293	21.896	2.9472e-10
631	0.2654	14.466	11.556	19.443	2.8986e-10
632	0.2657	11.947	11.461	18.390	2.8455e-10
633	0.2659	9.714	12.355	19.210	2.8354e-10
634	0.2661	3.039	13.082	19.339	2.7676e-10
799	0.2987	15.199	316.939	461.219	5.9631e-10
800	0.2989	71.660	322.590	465.893	5.9905e-10
801	0.2991	54.563	310.222	452.155	5.9490e-10
807	0.3002	11.077	259.852	371.223	5.6285e-10
808	0.3004	118.243	215.332	319.610	5.5316e-10
809	0.3006	106.683	178.261	265.162	5.2912e-10
810	0.3007	39.747	145.947	210.755	4.9333e-10
823	0.3032	1.801	19.531	28.424	3.0085e-10
824	0.3033	12.563	17.047	26.308	3.0449e-10
825	0.3035	14.369	14.560	23.131	2.9974e-10
826	0.3037	13.370	12.207	19.670	2.9060e-10
827	0.3039	11.982	10.506	17.007	2.8155e-10
828	0.3041	11.074	9.609	15.578	2.7577e-10
829	0.3043	10.830	9.496	15.393	2.7473e-10
830	0.3044	11.106	10.087	16.302	2.7737e-10
831	0.3046	11.376	11.162	17.900	2.8135e-10
832	0.3048	10.551	12.422	19.478	2.8325e-10
833	0.3050	6.593	13.800	20.596	2.8089e-10
844	0.3070	1.312	11.858	17.368	2.6832e-10
845	0.3072	6.970	11.256	17.169	2.7376e-10
846	0.3074	10.663	11.284	17.861	2.8119e-10
847	0.3075	13.147	11.415	18.624	2.8743e-10
848	0.3077	14.303	11.255	18.665	2.9003e-10
849	0.3079	14.096	10.580	17.678	2.8788e-10
850	0.3081	13.198	9.726	16.207	2.8284e-10
851	0.3083	12.282	8.976	14.977	2.7780e-10

Mass step	Axion mass [eV]	$g_{10}^4(\mathrm{min})$	Stat. error (left)	Stat. error (right)	$g_{a\gamma}(95\%\mathrm{C.L.})$ [GeV^{-1}]
852	0.3084	11.902	8.669	14.479	2.7561e-10
853	0.3086	12.178	8.870	14.808	2.7718e-10
854	0.3088	12.935	9.475	15.800	2.8130e-10
855	0.3090	13.703	10.221	17.018	2.8570e-10
856	0.3092	13.859	10.788	17.848	2.8768e-10
857	0.3094	12.971	11.008	17.919	2.8575e-10
858	0.3095	11.011	10.947	17.418	2.8076e-10
859	0.3097	8.149	10.995	16.969	2.7487e-10
860	0.3099	3.837	11.517	17.136	2.6977e-10
920	0.3205	7.852	11.542	17.717	2.7679e-10
921	0.3207	11.859	11.001	17.688	2.8286e-10
922	0.3209	13.694	10.574	17.478	2.8663e-10
923	0.3210	14.140	9.930	16.658	2.8664e-10
924	0.3212	13.683	9.182	15.490	2.8335e-10
925	0.3214	12.975	8.640	14.559	2.7909e-10
926	0.3216	12.476	8.286	13.979	2.7627e-10
927	0.3217	12.507	8.284	13.979	2.7633e-10
928	0.3219	13.083	8.631	14.579	2.7950e-10
929	0.3221	13.972	9.310	15.743	2.8442e-10
930	0.3223	14.646	9.989	16.901	2.8854e-10
931	0.3224	14.484	10.682	17.846	2.8942e-10
932	0.3226	12.932	11.049	17.996	2.8582e-10
933	0.3228	9.551	11.363	17.748	2.7914e-10
934	0.3229	2.159	12.155	17.890	2.7109e-10
969	0.3289	-0.595	11.844	17.198	2.6571e-10
970	0.3291	7.612	12.394	18.779	2.7573e-10
971	0.3293	13.710	12.392	19.407	2.8179e-10
972	0.3295	15.713	11.391	18.548	2.8134e-10
973	0.3296	15.034	9.937	16.756	2.7562e-10
974	0.3298	13.391	8.514	14.661	2.6723e-10
975	0.3300	11.875	7.434	12.953	2.5942e-10
976	0.3301	10.951	6.819	11.993	2.5450e-10
977	0.3303	10.784	6.702	11.817	2.5354e-10
978	0.3305	11.392	7.086	12.438	2.5688e-10
979	0.3306	12.715	7.962	13.857	2.6367e-10
980	0.3308	14.401	9.227	15.853	2.7216e-10
981	0.3310	15.678	10.661	17.740	2.7917e-10
982	0.3311	15.464	12.002	19.241	2.8297e-10
983	0.3313	12.891	13.152	20.404	2.8386e-10
984	0.3315	7.303	13.456	20.258	2.7961e-10

Mass step	**Axion mass [eV]**	$g_{10}^4(\mathrm{min})$	**Stat. error (left)**	**Stat. error (right)**	$g_{a\gamma}(95\%\mathrm{C.L.})$ **[GeV^{-1}]**
985	0.3316	0.749	13.786	19.849	2.7295e-10
1008	0.3355	0.659	5.608	8.281	2.2349e-10
1009	0.3357	1.280	4.739	7.093	2.1638e-10
1010	0.3358	1.384	4.313	6.489	2.1206e-10
1011	0.3360	1.273	4.268	6.410	2.1139e-10
1012	0.3362	0.881	4.576	6.808	2.1372e-10
1013	0.3363	-0.266	5.220	7.619	2.1720e-10
1042	0.3411	3.942	12.871	19.131	2.7672e-10
1043	0.3413	7.516	11.859	18.171	2.7658e-10
1044	0.3414	8.680	11.527	17.884	2.7662e-10
1045	0.3416	8.724	11.903	18.410	2.7778e-10
1046	0.3418	7.138	13.027	19.733	2.8028e-10
1047	0.3419	0.535	14.852	21.612	2.8071e-10
1062	0.3444	-1.372	12.067	17.438	2.6602e-10
1063	0.3445	7.789	11.117	17.090	2.7475e-10
1064	0.3447	11.566	10.664	17.141	2.8096e-10
1065	0.3449	13.218	10.216	16.861	2.8410e-10
1066	0.3450	13.527	9.531	15.979	2.8358e-10
1067	0.3452	13.087	8.819	14.876	2.8040e-10
1068	0.3453	12.476	8.351	14.075	2.7658e-10
1069	0.3455	12.044	7.956	13.437	2.7395e-10
1070	0.3457	12.026	7.940	13.409	2.7385e-10
1071	0.3458	12.422	8.297	13.997	2.7622e-10
1072	0.3460	13.041	8.753	14.775	2.8012e-10
1073	0.3461	13.490	9.446	15.850	2.8333e-10
1074	0.3463	13.160	10.073	16.668	2.8367e-10
1075	0.3465	11.573	10.498	16.900	2.8038e-10
1076	0.3466	8.045	10.909	16.834	2.7423e-10
1077	0.3468	-0.203	11.806	17.157	2.6574e-10
1172	0.3618	4.271	12.178	18.133	2.7192e-10
1173	0.3619	9.031	11.655	18.122	2.7751e-10
1174	0.3621	11.624	11.392	18.304	2.8259e-10
1175	0.3622	12.771	11.003	17.993	2.8476e-10
1176	0.3624	12.749	10.288	16.908	2.8289e-10
1177	0.3625	12.199	9.464	15.615	2.7876e-10
1178	0.3627	11.906	8.954	14.886	2.7632e-10
1179	0.3628	12.168	8.858	14.982	2.7668e-10
1180	0.3630	13.000	9.144	15.801	2.7908e-10
1181	0.3632	14.352	9.794	17.153	2.8309e-10
1182	0.3633	15.928	10.673	18.806	2.8830e-10

Mass step	Axion mass [eV]	$g_{10}^4(\mathrm{min})$	Stat. error (left)	Stat. error (right)	$g_{a\gamma}(95\%\mathrm{C.L.})$ [GeV^{-1}]
1183	0.3635	17.176	11.575	20.304	2.9286e-10
1184	0.3636	17.191	12.140	20.937	2.9434e-10
1185	0.3638	15.098	12.010	20.095	2.9055e-10
1186	0.3639	10.972	11.216	17.881	2.8076e-10
1187	0.3641	6.461	10.618	16.191	2.6974e-10
1188	0.3642	2.987	11.990	17.747	2.7034e-10
1189	0.3644	3.392	14.412	20.536	2.7566e-10
1190	0.3645	7.785	12.676	19.230	2.7817e-10
1191	0.3647	10.233	10.894	17.247	2.7851e-10
1192	0.3648	11.830	9.993	16.272	2.7928e-10
1193	0.3650	13.321	9.780	16.340	2.8332e-10
1194	0.3651	14.195	9.525	16.401	2.8555e-10
1195	0.3653	14.375	9.402	16.410	2.8423e-10
1196	0.3654	14.137	9.084	16.030	2.8199e-10
1197	0.3656	14.068	9.041	15.959	2.8102e-10
1198	0.3658	14.238	9.114	16.132	2.8219e-10
1199	0.3659	14.667	9.504	16.712	2.8492e-10
1200	0.3661	14.799	9.764	17.078	2.8736e-10
1201	0.3662	14.318	10.241	17.411	2.8707e-10
1202	0.3664	12.628	10.391	17.069	2.8275e-10
1203	0.3665	9.597	10.478	16.500	2.7527e-10
1204	0.3667	4.043	10.954	16.366	2.6713e-10
1260	0.3751	5.301	11.977	17.984	2.7448e-10
1261	0.3752	9.503	11.343	17.701	2.7886e-10
1262	0.3754	10.933	10.529	16.840	2.7879e-10
1263	0.3755	10.993	9.626	15.610	2.7559e-10
1264	0.3757	10.603	8.877	14.505	2.7183e-10
1265	0.3758	10.313	8.476	13.907	2.6941e-10
1266	0.3760	10.359	8.520	13.978	2.6972e-10
1267	0.3761	10.725	9.007	14.705	2.7254e-10
1268	0.3763	11.128	9.816	15.893	2.7666e-10
1269	0.3764	10.998	10.764	17.169	2.7990e-10
1270	0.3766	9.368	11.599	18.053	2.7987e-10
1271	0.3767	4.651	12.292	18.359	2.7513e-10
1289	0.3794	2.867	13.093	19.344	2.7594e-10
1290	0.3795	5.315	11.411	17.194	2.7145e-10
1291	0.3797	5.573	10.593	16.045	2.6808e-10
1292	0.3798	4.871	10.674	16.063	2.6714e-10
1293	0.3800	2.689	11.749	17.349	2.6972e-10
1302	0.3813	-1.622	13.083	18.886	2.7086e-10

Mass step	**Axion mass [eV]**	$g_{10}^4(\mathbf{min})$	**Stat. error (left)**	**Stat. error (right)**	$g_{a\gamma}(\mathbf{95\%C.L.})$ **[GeV^{-1}]**
1303	0.3814	2.242	13.612	20.024	2.7826e-10
1304	0.3816	5.173	14.037	20.981	2.8348e-10
1305	0.3817	6.301	13.765	20.738	2.8374e-10
1306	0.3819	5.754	12.825	19.297	2.7901e-10
1307	0.3820	4.646	11.758	17.608	2.7208e-10
1308	0.3822	3.917	11.127	16.595	2.6778e-10
1309	0.3823	3.949	11.193	16.691	2.6821e-10
1310	0.3825	4.836	11.997	17.972	2.7352e-10
1311	0.3826	6.421	13.299	20.064	2.8133e-10
1312	0.3828	7.886	14.542	21.992	2.8754e-10
1313	0.3829	7.861	15.229	22.843	2.8893e-10
1314	0.3831	5.379	15.165	22.424	2.8544e-10
1315	0.3832	0.282	14.551	21.106	2.7858e-10
1320	0.3839	4.844	15.239	22.571	2.8618e-10
1321	0.3841	10.496	13.636	21.195	2.8938e-10
1322	0.3842	12.110	12.186	19.425	2.8780e-10
1323	0.3844	12.099	10.872	17.553	2.8313e-10
1324	0.3845	11.654	9.900	16.103	2.7855e-10
1325	0.3847	11.376	9.419	15.385	2.7602e-10
1326	0.3848	11.502	9.488	15.504	2.7652e-10
1327	0.3849	12.004	10.086	16.436	2.8015e-10
1328	0.3851	12.583	11.112	17.994	2.8497e-10
1329	0.3852	12.527	12.362	19.747	2.8915e-10
1330	0.3854	10.510	13.640	21.159	2.8993e-10
1331	0.3855	3.755	14.887	22.043	2.8552e-10
1345	0.3875	99.050	240.321	367.018	5.7322e-10
1346	0.3877	236.519	274.189	442.199	6.0807e-10
1347	0.3878	304.598	307.566	503.711	6.2908e-10
1348	0.3880	316.616	342.392	545.277	6.3981e-10
1349	0.3881	243.691	386.958	581.648	6.4284e-10
1350	0.3883	0.478	423.248	612.492	6.3735e-10
1353	0.3887	178.689	512.647	751.597	6.7574e-10
1354	0.3888	304.173	481.616	756.299	6.8766e-10
1355	0.3890	312.120	466.467	755.311	6.9281e-10
1356	0.3891	253.931	475.100	758.056	6.9415e-10
1357	0.3893	94.429	521.049	796.530	6.9470e-10
1361	0.3898	2.357	939.838	1327.734	7.6497e-10
1362	0.3900	695.339	913.114	1385.499	7.9580e-10
1363	0.3901	1003.878	944.115	1490.744	8.1676e-10
1364	0.3903	1153.215	995.435	1580.936	8.3016e-10

Mass step	Axion mass [eV]	$g_{10}^4(\mathrm{min})$	Stat. error (left)	Stat. error (right)	$g_{a\gamma}(95\%\mathrm{C.L.})$ [GeV^{-1}]
1365	0.3904	1174.076	1050.919	1634.220	8.3677e-10
1366	0.3906	1029.180	1112.430	1670.464	8.3687e-10
1367	0.3907	648.447	1154.760	1703.301	8.3040e-10
1368	0.3908	264.886	1176.265	1723.712	8.2484e-10
1369	0.3910	307.510	1312.072	1857.000	8.3609e-10
1370	0.3911	636.342	1318.273	1904.664	8.4992e-10
1371	0.3913	787.020	1222.620	1887.263	8.5660e-10
1372	0.3914	766.377	1157.511	1851.095	8.5742e-10
1373	0.3916	650.785	1159.710	1835.674	8.5550e-10
1374	0.3917	410.341	1261.756	1917.041	8.5640e-10
1378	0.3923	812.075	1876.472	2610.852	9.1363e-10
1379	0.3924	1541.464	1808.661	2641.304	9.3308e-10
1380	0.3926	1916.831	1808.903	2718.989	9.4661e-10
1381	0.3927	2117.917	1861.824	2813.180	9.5679e-10
1382	0.3928	2194.558	1952.939	2907.856	9.6437e-10
1383	0.3930	2097.296	2062.987	2999.261	9.6804e-10
1384	0.3931	1765.471	2161.585	3081.405	9.6645e-10
1385	0.3933	1362.638	2254.971	3154.154	9.6330e-10
1386	0.3934	1202.350	2376.472	3247.428	9.6551e-10
1387	0.3936	1228.796	2349.929	3277.352	9.6945e-10
1388	0.3937	1186.557	2174.520	3211.042	9.6938e-10
1389	0.3938	1041.312	2030.749	3099.922	9.6501e-10
1390	0.3940	850.633	2017.566	3068.527	9.6173e-10
1391	0.3941	631.372	2185.533	3231.369	9.6700e-10
1392	0.3943	449.941	2546.454	3585.467	9.8060e-10
1393	0.3944	666.189	2920.960	3911.043	9.9731e-10
1394	0.3945	1468.175	3012.796	4024.614	1.0154e-09
1395	0.3947	2337.691	2972.098	4061.493	1.0325e-09
1396	0.3948	2902.972	2923.455	4093.922	1.0444e-09
1397	0.3950	3162.418	2896.339	4136.092	1.0514e-09
1398	0.3951	3231.290	2909.486	4199.521	1.0560e-09
1399	0.3952	3175.829	2973.737	4286.868	1.0596e-09
1400	0.3954	2993.246	3085.909	4392.762	1.0617e-09
1401	0.3955	2682.648	3234.153	4512.289	1.0621e-09
1402	0.3957	2344.010	3408.443	4641.573	1.0623e-09
1403	0.3958	2118.140	3548.488	4760.019	1.0640e-09
1404	0.3960	1983.395	3529.198	4803.515	1.0653e-09
1405	0.3961	1808.870	3366.377	4731.795	1.0628e-09
1406	0.3962	1573.715	3215.239	4616.109	1.0573e-09
1407	0.3964	1351.348	3205.109	4612.216	1.0555e-09

Mass step	**Axion mass [eV]**	$g_{10}^4(\mathrm{min})$	**Stat. error (left)**	**Stat. error (right)**	$g_{a\gamma}(95\%\mathrm{C.L.})$ **[GeV^{-1}]**
1408	0.3965	1243.351	3381.778	4804.674	1.0623e-09
1409	0.3967	1424.841	3707.783	5114.188	1.0754e-09
1410	0.3968	2041.044	3989.025	5359.014	1.0915e-09
1411	0.3969	2917.804	4093.959	5494.903	1.1082e-09
1412	0.3971	3738.072	4122.765	5591.849	1.1233e-09
1413	0.3972	4313.911	4138.863	5671.315	1.1343e-09
1414	0.3974	4592.475	4148.084	5732.179	1.1407e-09
1415	0.3975	4603.842	4156.271	5782.143	1.1433e-09
1416	0.3976	4409.841	4183.312	5831.741	1.1431e-09
1417	0.3978	4076.855	4257.061	5901.288	1.1418e-09
1418	0.3979	3668.566	4398.841	6014.194	1.1406e-09
1419	0.3981	3236.448	4587.429	6167.395	1.1403e-09
1420	0.3982	2827.997	4730.788	6308.707	1.1404e-09
1421	0.3983	2500.260	4741.168	6364.177	1.1396e-09
1422	0.3985	2303.962	4670.126	6332.780	1.1379e-09
1423	0.3986	2256.757	4637.326	6326.035	1.1382e-09
1424	0.3988	2357.769	4700.648	6433.984	1.1437e-09
1425	0.3989	2607.224	4841.015	6613.591	1.1525e-09
1426	0.3990	2996.747	4990.350	6764.642	1.1614e-09
1427	0.3992	3499.773	5090.284	6866.349	1.1703e-09
1428	0.3993	4083.423	5151.533	6964.362	1.1802e-09
1429	0.3995	4709.652	5221.187	7091.251	1.1914e-09
1430	0.3996	5323.139	5324.786	5324.757	1.2028e-09
1431	0.3997	5839.819	5449.790	7390.191	1.2128e-09
1432	0.3999	6163.555	5568.997	7511.520	1.2199e-09
1433	0.4000	6213.201	5660.359	7600.777	1.2232e-09
1434	0.4002	5957.883	5728.128	7671.024	1.2228e-09
1435	0.4003	5406.326	5792.273	7743.459	1.2193e-09
1436	0.4004	4565.519	5856.352	7825.893	1.2134e-09
1437	0.4006	3471.430	5892.263	7884.490	1.2049e-09
1438	0.4007	2346.753	5879.510	7876.547	1.1950e-09
1439	0.4009	1646.397	5875.868	7862.609	1.1890e-09
1440	0.4010	1750.289	5975.956	7976.988	1.1937e-09
1441	0.4011	2680.236	6187.181	8232.822	1.2092e-09
1442	0.4013	4049.371	6402.893	8478.017	1.2283e-09
1443	0.4014	5295.180	6510.332	8613.210	1.2439e-09
1444	0.4016	6138.666	6531.508	8675.048	1.2544e-09
1445	0.4017	6644.821	6548.021	8738.498	1.2615e-09
1446	0.4018	6953.435	6610.475	8845.543	1.2676e-09
1447	0.4020	7108.396	6704.949	8979.303	1.2726e-09

Mass step	Axion mass [eV]	$g_{10}^4(\min)$	Stat. error (left)	Stat. error (right)	$g_{a\gamma}(95\%\mathrm{C.L.})$ [GeV^{-1}]
1448	0.4021	7109.038	6799.018	9099.690	1.2757e-09
1449	0.4022	6989.507	6888.817	9194.251	1.2770e-09
1450	0.4024	6771.370	6982.287	9273.616	1.2771e-09
1451	0.4025	6411.958	7071.396	9359.032	1.2761e-09
1452	0.4027	5842.163	7140.447	9457.161	1.2736e-09
1453	0.4028	5029.860	7169.419	9538.457	1.2690e-09
1454	0.4029	4085.503	7173.547	9571.047	1.2627e-09
1455	0.4031	3316.119	7213.855	9591.507	1.2575e-09
1456	0.4032	3125.257	7327.979	9688.513	1.2586e-09
1457	0.4034	3769.879	7525.676	9898.456	1.2690e-09
1458	0.4035	5090.764	7758.932	10147.473	1.2855e-09
1459	0.4036	6520.973	7916.762	10323.236	1.3016e-09
1460	0.4038	7537.320	7963.959	10416.028	1.3127e-09
1461	0.4039	7998.695	7952.287	10471.590	1.3185e-09
1462	0.4041	8019.846	7934.089	10526.452	1.3206e-09
1463	0.4042	7789.421	7942.237	10599.765	1.3207e-09
1464	0.4043	7520.726	7996.615	10699.227	1.3210e-09
1465	0.4045	7437.149	8116.862	10824.653	1.3232e-09
1466	0.4046	7657.822	8301.618	10965.368	1.3279e-09
1467	0.4047	8044.073	8490.283	11101.679	1.3338e-09
1468	0.4049	8266.695	8615.084	11219.804	1.3382e-09
1469	0.4050	8046.567	8661.676	11317.096	1.3388e-09
1470	0.4052	7291.416	8651.577	11379.800	1.3348e-09
1471	0.4053	6125.043	8650.155	11417.612	1.3274e-09
1472	0.4054	4857.093	8746.676	11505.600	1.3203e-09
1473	0.4056	3957.176	8960.893	11698.649	1.3179e-09
1474	0.4057	3987.479	9199.412	11926.776	1.3227e-09
1475	0.4058	5138.776	9339.824	12072.509	1.3340e-09
1476	0.4060	6884.057	9356.268	12135.747	1.3486e-09
1477	0.4061	8539.709	9352.244	12200.690	1.3629e-09
1478	0.4063	9754.413	9395.468	12301.301	1.3746e-09
1479	0.4064	10413.060	9471.667	12414.671	1.3821e-09
1480	0.4065	10521.159	9550.339	12522.329	1.3851e-09
1481	0.4067	10217.498	9628.498	12624.717	1.3850e-09
1482	0.4068	9775.451	9742.481	9742.135	1.3841e-09
1483	0.4069	9441.312	9927.845	12913.917	1.3848e-09
1484	0.4071	9189.744	10132.788	13090.595	1.3862e-09
1485	0.4072	8768.072	10242.078	13215.118	1.3856e-09
1486	0.4074	8021.522	10206.942	13258.282	1.3818e-09
1487	0.4075	7067.855	10106.369	13243.654	1.3759e-09

Mass step	**Axion mass [eV]**	$g_{10}^4(\mathbf{min})$	**Stat. error (left)**	**Stat. error (right)**	$g_{a\gamma}(\mathbf{95\%C.L.})$ **[GeV^{-1}]**
1488	0.4076	6176.668	10085.831	13259.937	1.3710e-09
1489	0.4078	5624.244	10225.527	13394.360	1.3701e-09
1490	0.4079	5678.834	10462.935	13629.350	1.3746e-09
1491	0.4080	6516.397	10709.934	13846.544	1.3839e-09
1492	0.4082	7996.798	10862.217	13984.095	1.3964e-09
1493	0.4083	9696.292	10934.303	14080.032	1.4100e-09
1494	0.4084	11183.848	10996.006	14189.451	1.4227e-09
1495	0.4086	12172.850	11071.186	14308.973	1.4320e-09
1496	0.4087	12534.262	11142.468	14416.799	1.4366e-09
1497	0.4089	12285.942	11197.694	14508.547	1.4367e-09
1498	0.4090	11576.545	11247.752	14593.630	1.4335e-09
1499	0.4091	10665.536	11327.596	14696.457	1.4293e-09
1500	0.4093	9818.045	11469.158	14839.006	1.4262e-09

Table F.2: Axion mass index, Axion mass , g_{10}^4(min) and its errors for masses corresponding to measured pressure settings.

Mass step	**Axion mass [eV]**	$g_{10}^4(\mathrm{min})$	**Stat. error (left)**	**Stat. error (right)**	$g_{a\gamma}(95\%\mathrm{C.L.})$ **[GeV^{-1}]**
0	0.0298	3.631	15.573	23.008	2.8763e-10
1	0.0423	7.556	4.954	8.686	2.3393e-10
3	0.0606	8.940	8.067	13.279	2.6202e-10
4	0.0679	6.635	7.746	12.213	2.5408e-10
15	0.1216	-1.069	5.772	8.352	2.2118e-10
20	0.1426	7.623	7.572	12.109	2.5666e-10
22	0.1489	-1.465	9.979	14.407	2.5295e-10
26	0.1608	7.518	9.001	14.098	2.6374e-10
36	0.1993	7.172	6.817	10.812	2.3919e-10
37	0.2016	3.413	3.448	5.117	1.9625e-10
38	0.2028	7.016	3.235	4.109	1.9775e-10
39	0.2039	3.580	1.824	2.407	1.7089e-10
40	0.2050	5.206	2.781	3.664	1.8891e-10
42	0.2084	7.530	5.923	10.297	2.3820e-10
46	0.2170	7.710	6.676	10.912	2.5271e-10
47	0.2191	2.570	9.170	13.627	2.5417e-10
48	0.2212	9.627	7.847	13.037	2.6449e-10
60	0.2469	-0.141	10.436	15.181	2.5776e-10
61	0.2487	9.730	8.377	13.703	2.6708e-10
62	0.2506	-0.109	10.457	15.218	2.5825e-10
65	0.2561	9.804	8.940	14.495	2.6921e-10
70	0.2649	19.777	12.525	22.724	2.9503e-10
88	0.3041	10.902	9.472	15.365	2.7488e-10
90	0.3070	0.525	11.972	17.463	2.6755e-10
91	0.3085	11.905	8.668	14.479	2.7561e-10
92	0.3100	0.766	12.006	17.533	2.6835e-10
100	0.3217	12.434	8.235	13.895	2.7592e-10
106	0.3303	10.756	6.686	11.786	2.5346e-10
107	0.3317	-0.635	14.033	20.047	2.7258e-10
110	0.3359	1.358	4.248	6.392	2.1138e-10
114	0.3415	8.762	11.537	17.915	2.7662e-10
117	0.3456	11.974	7.895	13.341	2.7356e-10
129	0.3617	-0.340	12.742	18.456	2.6890e-10
130	0.3630	12.958	9.128	15.754	2.7885e-10
131	0.3643	2.267	13.433	19.472	2.7270e-10
132	0.3656	14.068	9.042	15.960	2.8102e-10
140	0.3759	10.283	8.433	13.850	2.6931e-10
143	0.3797	5.523	10.543	15.968	2.6773e-10
145	0.3822	3.840	11.054	16.488	2.6728e-10
147	0.3847	11.385	9.383	15.341	2.7590e-10

List of Figures

List of Tables

Bibliography

[1] E. Noether, *Invariante Variationsprobleme*, Nachr. d. König. Gesellsch. d. Wiss. zu Göttingen, Math-phys. Klasse (1918), 235-257.

[2] D. Perkins, *Particle Astrophysics*, Oxford Master Series in Particle Physics, Astrophysics, and Cosmology, Oxford University Press, Ney York (2003).

[3] G. Lüders, *Proof of the TCP Theorem* Ann. Phys. **2** (1957), Issue 1, 1.
W. Pauli, *Niels Bohr and the development of Physics*, ed. W Pauli, L Rosenfeld and V Weisskopf, New York:McGraw Hill (1955) 30.

[4] K. Lande *et al.*, *Observation of Long-Lived Neutral V Particles*, Phys. Rev. **103** (1956) 1901.

[5] J. H. Christenson, J. W. Cronin, V. L. Fitch, and R. Turlay, *Evidence for the 2 pi Decay of the K_2^0 Meson*, Phys. Rev. Lett. **13** (1964) 138-140.

[6] C. Amsler *et al.* (Particle Data Group) *The Review of Particle Physics*, PL B **667** (2008), 1.

[7] B. Aubert *et al.* (BABAR Collaboration), *Observation of CP Violation in the B^0 Meson System*, Phys. Rev. Lett. **87** (2001) 091801.

[8] K. Abe *et al.* (BELLE Collaboration), *Observation of Large CP Violation in the Neutral B Meson System*, Phys. Rev. Lett. **87** (2001) 091802.

[9] J. R. Fry, *CP violation and the Standard Model*, Rep. Prog. Phys. **63** (2000) 117.

[10] N. Cabibbo, *Unitary Symmetry and Leptonic Decays*, Phys. Rev. Lett. **10** (1963) 531.
M. Kobayashi and T. Maskawa, *CP-Violation in the Renormalizable Theory of Weak Interaction*, Prog. Theor. Phys. **49** (1973) 652.

[11] L. H. Ryder, *Quantum Field Theory*, Cambridge University Press, Cambridge 2006.

[12] C. Quigg, *Gauge Theories of the Strong, Weak, and Electromagnetic Interactions*, Frontiers in Physics, Vol. 56, Addison-Wesley Publishing Company, Reading, Massachusetts (1983).

[13] S. Weinberg, *The $U(1)_A - Problem$*, Phys. Rev. D. **11** (1975) 3583.

[14] B. Povh, K. Rith, C. Scholz and F. Zetsche, *Teilchen und Kerne*, Springer-Verlag, Berlin (1997).

[15] G. t' Hooft, *Symmetry Breaking through Bell-Jackiw Anomalies*, Phys. Rev. Lett. **37** (1976) 8.
G. t' Hooft, *Computation Of The Quantum Effects Due To A Four-Dimensional Pseudoparticle*, Phys. Rev. D **14** (1976) 3432 [Erratum-ibid. D **18** (1978) 2199].

[16] H. V. Klapdor-Kleingrothaus and K. Zuber, *Particle Astrophysics*, Institute of Physics Publishing, Bristol and Philadelphia (1997).

[17] J. E. Kim, *Light Pseudoscalars, Particle Physics and Cosmology*, Phys. Rep.**150** (1987) 1.

[18] R. D. Peccei, *CP-Violation Advanced Series in High Energy Physics*, Vol 3 ed, C. Jarlskog, World Scientific, Singapore (1989).

[19] S. Dar, *The Neutron EDM in the SM: A Review*, (2000) [arXiv:hep-ph/0008248v2].

[20] V. Baluni, *CP-nonconserving effects in quantum chromodynamics*, Phys. Rev. D **19** (1979), 2227.

[21] R. Crewther *et al.*, *Chiral Estimate Of The Electric Dipole Moment Of The Neutron In Quantum Chromodynamics*, Phys. Lett. B **88** (1979) 123.

[22] N. F. Ramsey, *Electric Dipole Moment Of The Neutron*, Ann. Rev. Nucl. Part. Phys. **40** (1990) 1.
J. M. Pendlebury, *Fundamental Physics With Ultracold Neutrons*, Ann. Rev. Nucl. Part. Phys. **43** (1993) 687.
C. A. Baker *et al.*, *Improved Experimental Limit on the Electric Dipol Moment of the Neutron*, Phys. Rev. Lett. **97** (2006) 131801.

[23] G. 't Hooft, *Recent Developments of Gauge Theories*, eds. G. 't Hofft *et al.*, Plenum Press, New York and London (1979) 135.

[24] R. D. Peccei and H. R. Quinn, *CP Conservation In The Presence Of Pseudoparticles*, Phys. Rev. Lett. **38** (1977) 1440.
R. D. Peccei and H. R. Quinn, *Constraints imposed by CP conservation in the presence of pseudoparticles*, Phys. Rev. D **16** (1977) 1791.

[25] D. R. Nelson, *Partially Quenched Chiral Pertubation Theory and a Massless Up Quark: A Lattice Calculation of the Light-Quark-Mass Ratio*, Dissertation, Graduate School of the Ohio State University, USA, (2002).

[26] M. Leurer, Y. Nir and N. Seiberg, *Mass Matrix Models: The Sequel*, Nucl. Phys. B **420** (1994),468,[arXiv:hep-ph/9310320].
T. Banks, Y. Nir and N. Seiberg, *Missing (up) Mass, Accidental Anomalous Symmetries, and the Strong CP Problem*, (1994), [arXiv:hep-ph/9403203v1].
D. E. Kaplan *et al.*, *Fermion Masses and Gauge Mediated Supersymmetry Breaking from a Single $U(1)$*, Phys. Rev. D **60** (1999), 055003, [arXiv:hep-ph/9806430].

[27] D. R. Nelson, G. T. Flemming and G. W Kilcup, *Up Quark Mass in Lattice QCD with Three Light Dynamical Quarks and Implications for Strong CP Invariance*, Phys. Rev. Lett. **90** (2003) 021601.

[28] M. A. Beg and H. Tsao, *Strong P and T Noninvariances in a Superweak Theory*, Phys. Rev. Lett. **41** (1978) 278.
R. N. Mohapatra and G. Senjanovic, *Natural Suppression of Strong P and T Non-Invariance*, Phys. Lett. B **79** (1978) 283.
S. M. Barr, *Solving the Strong CP Problem without the Peccei-Quinn Symmetry*, Phys. Rev. Lett. **53** (1984) 329.

[29] J. E. Kim and G. Carosi, *Axions and the Strong CP Problem*, submitted to Rev. Mod. Phys. (2008), [arXiv:hep-ph/0807.3125].

[30] S. Weinberg, *A New Light Boson?*, Phys. Rev. Lett. **40** (1978) 223.

[31] F. Wilczek, *Problem Of Strong P And T Invariance In The Presence Of Instantons*, Phys. Rev. Lett. **40** (1978) 279.

[32] G. G. Raffelt, *Stars as Laboratories for Fundamental Physics*, University of Chicago Press, Chicago/London (1996).

[33] D. B. Kaplan, *Opening the Axion Window*, Nucl. Phys. B **260** (1985) 215.

[34] M. S. Turner, *Windows on the Axion*, Phys. Rep. **197** (1990) 67.

[35] W. A. Bardeen and S.-H. H. Tye, *Current Algebra Applied To Properties Of The Light Higgs Boson*, Phys. Lett. B **74** (1978) 229.

[36] J. Gasser and H. Leutwyler, *Quark Masses*, Phys. Rep. **87** (1982) 77.
H. Leutwyler, *The Ratios of the Light Quark Masses*, Phys. Lett. B **378** (1996) 313.

[37] M. Srednicki, *Axion Couplings to Matter. I. CP-conserving parts*, Nucl. Phys. B **260** (1985) 689.

[38] A. P. Zhitnitskiĭ, *On possible Suppression Of the Axion Hadron Interactions*, Sov. J. Nucl. Phys. **31** (1980) 260.

[39] M. Dine, W Fischler, M. Srednicki, *A Simple Solution To The Strong CP Problem With A Harmless Axion*, Phys. Lett. B **104** (1981) 199.

[40] J. E. Kim, *Weak Interaction Singlet and CP Invariance*, Phys. Rev. Lett. **43** (1979) 103.

[41] M. A. Shifman, A. I. Vainshtein, V. I. Zakharov, *Can Confinement Ensure Natural CP Invariance of Strong Interactions?*, Nucl. Phys. B **166** (1980) 493.

[42] R. Mayle *et al.*, *Constraints on axions from SN 1987A*, Phys. Lett. B **203** (1988) 188.
R. Mayle *et al.*, *Updated constraints on axions from SN1987A*, Phys. Lett. B **219** (1989) 515.

[43] J. Ellis and M. Karliner, *Determination of α_s and the nucleon spin decomposition unsing recent polarized structure function data*, Phys. Lett. B, **341** (1995) 397.

[44] V. Y. Alexakhin *et al.* (COMPASS Collaboration), *The Deuteron Spin-Dependent Structure Function g_1^d and its First Moment*, Phys. Lett. B, **645** (2007) 8, [arXiv:hep-ex/0609038].
A. Airapetian *et al.* (HERMES Collaboration), *Precise Determination of the Spin Structure Function g_1 of the Proton, Deuteron and Neutron*, Phys. Rev. D, **75** (2007) 012007, [arXiv:hep-ex/0609039].

[45] H. Primakoff, *Photo-Production of Neutral Mesons in Nuclear Electric Fields and the Mean Life of Neutral Meson*, Phys. Rev. **81** (1951) 899.

[46] E. W. Kolb and M. S. Turner, *The Early Universe*, Addison-Wesley Publishing Company, 1994.

[47] T. W. Donnelly *et al.*, *Do axions exist?*, Phys. Lett. D **18** (1978) 1607.

[48] E. D. Bloom and C. W. Peck, *Physics with the Crystal Ball Detector*, Ann. Rev. Nucl. Part. Sci. **33** (1983) 143.

[49] F. C. Porter and K. C. Königsmann, *Unambiguous test for the axion*, Phys. Rev. D **25** (1982) 1993.
C. Edwards *et al.*, *Upper Limit for $J/\psi \rightarrow \gamma +$ Axion*, Phys. Rev. Lett. **48** (1982) 903.

[50] M. B. Wise, H. Georgi and S. L. Glashow, *$SU(5)$ and the Invisible Axion*, Phys. Rev. Lett. **47** (1981) 402.

[51] R. D. Peccei, *Particle Physics Footprints of the Invisible Axion*, Physica Scripta **T36** (1991) 218.

[52] S. L. Cheng, C. Q. Geng and W.-T. Ni, *Axion-photon Couplings in Invisible Axion Models*, Phys. Rev. D **52** (1995) 3132 [arXiv:hep-ph/9506295].

[53] K. Zioutas *et al.*, *An improved limit on the axion-photon coupling from the CAST experiment*, Journal of Cosm. and Astropart. Phys. **4** (2007) 010.

[54] K. Ehret *et al.*, *Production and Detection of Axion-Like Particles in a HERA Dipole Magnet - Letter-of-Intent for the ALPS experiment -*, (2007) [arXiv:hep-ex/0702023v1s].

[55] M. Ahlers *et al.*, *Light from the hidden sector: Experimental signatures of paraphotons*, Phys. Rev. D **76** (2007) 115005.

[56] A. Ringwald *et al.*, Proceedings of the 4th Patras Workshop on Axions, WIMPs and WISPs, DESY, Hamburg, Germany (2008) (To be published).

[57] CAST Internal Communication with Dr. G. Raffelt, July 2008.

[58] M. S. Turner, *Early-Universe Thermal Production of Not-So-Invisible Axions*, Phys. Rev. Lett. **59** (1987) 2489, [Errata-ibid. **60** (1988) 1101].

[59] J. Preskill, M. Wise, and F. Wilczek, *Cosmology of the Invisible Axion*, Phys. Lett. B **120** (1983) 127.
L. Abbott and P. Sikivie, *A Cosmological Bound On The Invisible Axion*, Phys. Lett. B **120** (1983) 133.
M. Dine and W. Fischler, *The Not-So-Harmless Axion*, Phys. Lett. B **120** (1983) 137.

[60] R. L. Davis, *Cosmic Axions from Cosmic Strings*, Phys. Lett. B **180** (1986) 225.

[61] B. W. Lee and S. Weinberg, *Cosmological Lower Bound on Heavy-Neutrino Masses*, Phys. Rev. Lett. **39** (1977) 165.

[62] G. Raffelt, *Axions - Motivation, Limits and Searches*, Presentation in PONT d'Avignon, Avignon, France (21-25 April 2008).

[63] G. G. Raffelt, *Astrophysical axion bounds*, Lect. Notes Phys. **741** (2008) 51-71, [arXiv:hep-ph/0611350].

[64] G. G. Raffelt, *Particle Physics from Stars*, Annu. Rev. Nucl. Part. Sci. **49** (1999) 163-216, [arXiv:hep-ph/9903472].

[65] A. Buzzoni *et al.*, *Helium abundance in globular clusters: the R-method*, Astron. Astrophys. **128** (1983) 94.

[66] G. G. Raffelt, *Astrophysical axion bounds diminished by screening effects*, Phys. Rev. D **33** (1986) 897.

[67] G. G. Raffelt and A. Weiss, *Red giant bound on the axion-electron coupling revisited*, Phys. Rev. D **51** (1995) 1495.

[68] A. Burrows, M. S. Turner and R. P. Brinkmann, *Axions and SN 1987A*, Phys. Rev. D **39** (1989) 1020.
A. Burrows, M. T. Ressell and M. S. Turner, *Axions and SN 1987A: Axion Trapping*, Phys. Rev. D **42** (1990) 3297.

[69] P. Sikivie, *Axion Cosmology*, Lect. Notes Phys. **741** (2008) 19.

[70] S. Hannestad, A. Mirizzi, G. G. Raffelt and Y. Y. Y. Wong, *Cosmological constraints on neutrino plus axion hot dark matter: Update after WMAP-5*, JCAP **0804** (2008) 019, [arXiv:astro-ph/0803.1585].

[71] E. Massó and R. Toldra, *New constraints on a light spinless particle coupled to photons*, Phys. Rev. D **55** (1997) 7967.

[72] P. Sikivie, *Axion Searches*, Nucl. Phys. Proc. Suppl. **87** (2000) 41, [arXiv:hep-ph/0002154].

[73] E. P. S. Shellard and R. A. Battye, *Cosmic Axions*, (1998) [arXiv:astro-ph/9802216].

[74] P. Sikivie, *Experimental Tests of the "invisible" Axion*, Phys. Rev. Lett. **51** (1983) 1415 [Erratum ibid. **52** (1984) 695].

[75] W. Wuensch *et al.*, *Results of a laboratory search for cosmic axions and other weakly coupled light particles*, Phys. Rev. D **40** (1989) 3153.

[76] C. Hagmann *et al.*, *Results from a search for cosmic axions*, Phys. Rev. D **42** (1990) 1297.

[77] C. Hagmann *et al.*, *Results from a High-Sensitivity Search for Cosmic Axions*, Phys. Rev. Lett. **80** (1998) 2043.
S. J. Asztalos *et al.*, *Improved rf cavity search for halo axions*, Phys. Rev. D **69** (2004) 011101.
L. D. Duffy *et al.*, *A High Resolution Search for Dark-Matter Axions*, Phys. Rev. D **74** (2006) 012006, [arXiv:astro-ph/0603108].

[78] K. Yamamoto *et al.*, *The Rydberg atom cavity axion search*, Invited talk presented at the Dark2000, Heidelberg, Germany,10-15 July, (2000), [arXiv:hep-ex/0101200].
Y. Kishimoto *et al.*, *Systematic observation of tunneling field-ionization in highly excited Rb Rydberg atoms*, Phys. Lett. A **303** (2002) 279.
M. Tada *et al.*, *Manipulating ionization path in a Stark map: Stringent schemes for the selective field ionization in highly excited Rb Rydberg*, Phys. Lett. A **303** (2002) 285.

[79] M. T. Ressell, *Limits to the radiative decay of the axion*, Phys. Rev. D **44** (1991) 3001.

[80] M. A. Bershady, M. T. Ressell, and M. S. Turner, *Telescope search for a 3-eV to 8-eV axion*, Phys. Rev. Lett. **66** (1991) 1398.

[81] D. Grin *et al.*, *Telescope search for decaying relic axions*, Phys. Rev. D **75** (2007) 105018.

[82] B. D. Blout *et al.*, *A radio telescope search for axions*, Astrophys. J. **546** (2001) 825.

[83] K. van Bibber *et al.*, *Proposed experiment to produce and detect light pseudoscalars*, Phys. Rev. Lett. **59** (1987) 759.

[84] R. Cameron *et al.*, *Search for nearly massless, weakly coupled particles by optical techniques*, Phys. Rev. D **47** (1993) 3707.

[85] F. Hoogeveen and T. Ziegenhagen, *Production and detection of light bosons using optical resonators*, Nucl. Phys. B **358** (1991) 3.

[86] G. Ruoso *et al.*, *Search for photon regeneration in a magnetic field*, Z. Phys. **56** (1992) 505.

[87] E. Zavattini *et al.* (PVLAS Collaboration), *Experimental Observation of Optical Rotation Generated in Vacuum by a Magnetic Field*, Phys. Rev. Lett. **96** (2006) 110406.

[88] A. Afanasev *et al.* (LIPSS Collaboration), *Experimental limit on optical photon coupling to light neutral scalar bosons*, accepted Phys. Rev. Lett. (to be published), [arXiv:hep-ex/0806.2631].

[89] C. Robilliard *et al.* (BMV Collaboration), *No "Light Shining through a Wall": Results from a Photoregeneration Experiment*, Phys. Rev. Lett. **99** (2007) 190403.

[90] A. S. Chou *et al.* (GammeV Collaboration), *Search for Axionlike Particles Using a Variable-Baseline Photon-Regeneration Technique*, Phys. Rev. Lett. **100** (2008) 080402.

[91] P. Pugnat *et al.* (OSQAR Collaboration), *First results from the OSQAR photon regeneration experiment: No light shining through a wall*, [arXiv:hep-ex/0712.3362].

[92] Y. Semertzidis *et al.*, *Limits on the production of light scalar and pseudoscalar particles*, Phys. Rev. Lett. **64** (1990) 2988.

[93] E. Zavattini *et al.* (PVLAS Collaboration), *New PVLAS results and limits on magnetically induced optical rotation and ellipticity in vacuum*, Phys. Rev. D. **77** (2008) 032006.

[94] E. A. Paschos and K. Zioutas, *A Proposal for Solar Axion Detection via Bragg Scattering*, Phys. Lett. B **323** (1994) 367.
R. J. Creswick *et al.*, *Theory of the Direct Detection of Solar Axions by Coherent Primakoff Conversion in germanium Detectors*, Phys. Lett. B **427** (1998) 235, [arXiv:hep-ph/9708210].

[95] F. T. Avignone III *et al.* (SOLAX Collaboration), *Experimental Search for Solar Axions via Coherent Primakoff Conversion in a Germanium Spectrometer*, Phys. Rev. Lett. **81** (1998) 5068, [arXiv:astro-ph/9708008].

[96] A. Morales *et al.* (COSME Collaboration), *Particle Dark Matter and Solar Axion Searches with a Small Germanium Detector at the Canfranc Underground Laboratory*, Astropart. Phys. **16** (2002) 325, [arXiv:hep-ex/0101037].

[97] R. Bernabei *et al.*, *Search for Solar Axions by Primakoff Effect in NaI Crystals*, Phys. Lett. B **515** (2001) 6.

[98] S. Cebrián *et al.*, *Prospects of Solar Axion Searches with Crystal Detectors*, Astropart. Phys. **10** (1999) 397, [arXiv:astro-ph/9811359].

[99] K. Van Bibber, P. M. McIntyre, D. E. Morris, and G. G. Raffelt, *Design for a Practical Laboratory Detector for Solar Axions*, Phys. Rev. D. **39** (1989) 2089.

[100] D. M. Lazarus *et al.*, *Search for Solar Axions*, Phys. Rev. Lett. **69** (1992) 2333.

[101] S. Moriyama *et al.*, *Direct Search for Solar Axions by Using Strong Magnetic Field and X-Ray Detectors*, Phys. Lett. B **434** (1998) 147, [arXiv:hep-ex/9805026].

[102] M. Minowa *et al.*, *Tokyo Axion Helioscope*, (2008) to be published, [arXiv:astro-ph/0809.0596].

[103] K. Zioutas *et al.*, *First Results from the CERN Axion Solar Telescope (CAST)*, Phys. Rev. Lett. **94** (2005) 121301, [arXiv:hep-ex/0411033].

[104] H. Davoudiasl and P. Huber, *Detecting Solar Axions Using Earth's Magnetic Field*, (2006) Phys. Rev. Lett. **97** (2006) 141302.

[105] G. G. Raffelt, *Plasmon decay into low-mass bosons in stars*, Phys. Rev. D **37** (1988) 1356.

[106] J. N. Bahcall, W. F. Huebner, S. H. Lubow, P. D. Parker, and R. K. Ulrich, *Standard Solar Models and the Uncertainties in Predicted Capture Rates of Solar Neutrinos*, Rev. Mod. Phys. **54** (1982) 767.

[107] J. N. Bahcall and M. H. Pinsonneault, *What do we (not) know theoretically about solar neutrino fluxes?*, Phys. Rev. Lett. **92** (2004) 121301, [arXiv:astro-ph/0402114]. See also http://www.sns.ias.edu/~jnb/SNdata/sndata.html

[108] P. D. Serpico and G. G. Raffelt, *New Calculations of Solar Axion Flux*, Internal CAST Report (12 January 2005).

[109] H. Schlattl, A. Weiss, and G. G. Raffelt, *Helioseismological constraint on solar axion emission*, Astropart. Phys. **10** (1999) 353, [arXiv:hep-ph/9807476].

[110] G. G. Raffelt and L. Stodolsky, *Mixing of the Photon with Low-Mass Particles*, Phys. Rev. D **37** (1988) 1237.

[111] F. S. Crawford, Jr. *Waves - Berkley Physics Course Volume 3*, Mcgraw-Hill College, Newton, Massachusetts, USA (1968).

[112] National Institute for Standards and Technology, *XCOM Photon Cross Sections Database*, http://physics.nist.gov/PhysRefData/Xcom/Text/XCOM.html.

[113] M. Bona *et al.*, *Performance of the first CERN - INFN* 10 *m long superconducting dipole prototype for the LHC*, CERN-AT-94-26-MA, 4th European Particle Accelerator Conference (EPAC 94), London, England, (27 Jun - 1 Jul 1994).
E. Acerbi *et al.*, *Development and Fabrication of the First* 10 *m Long Superconducting Dipole Prototype for the LHC*, CERN-AT-93-43-MA, 13th International Conference on Magnet Technology (MT13), Victoria, Canada, (20 - 24 Sept. 1993).

[114] http://cdsweb.cern.ch/collection/Photos.

[115] Private Communication with L. Walckiers, July 2004.

[116] K. Barth *et al.*, *Commissioning and first operation of the cryogenics for the CERN Axion Solar Telescope (CAST)*, AIP Conference Proceeding **710** (2004) 168.

[117] NOVAS (Naval Observatory Vector Astrometry Subroutines), http://www.usno.navy.mil/, http://aa.usno.navy.mil/software/

[118] J. I. Collar, 5th CAST Collaboration Meeting, CERN, Geneva, Switzerland, (March 2001).
J. I. Collar, 11th CAST Collaboration Meeting, CERN, Geneva, Switzerland, (July 2002).
J. I. Collar, 12th CAST Collaboration Meeting, Halkidiki, Greece, (September 2002).

[119] O. Montenbruck, *Practical Ephimeris Calculations*, Springer-Verlag, Heidelberg, Germany, (1989).

[120] J. Vogel, *The Precision of the Tracking System in Search of Solar Axions*, Diploma Thesis, Albert-Ludwigs-Universität Freiburg (2005).
J. Vogel *et al.*, *Report of the Filming in Fall 2007*, Internal CAST Report, EDMS Document ID 899049, (March 2007), https://edms.cern.ch/document/899049/1.
J. Vogel *et al.*, *Filming the Sun in Spring 2008 (Freiburg System)*, Internal CAST Report,

EDMS Document ID 930995, (June 2008), https://edms.cern.ch/document/930995/1.
M. Karuza *et al.*, *Filming the Sun in Spring 2008 (Triest System)*, Internal CAST Report, EDMS Document ID 953184, (August 2008), https://edms.cern.ch/document/953184/1.
M. Karuza and J. Vogel, *Summary Filming Sping 2008 (Triest/Freiburg)*, Internal CAST Report, EDMS Document ID 953185, (2008), https://edms.cern.ch/document/953185/1.

[121] K. Zioutas *et al.* (CAST Collaboration), *Probing eV-Scale Axions with CAST*, Journal of Cosmology and Astroparticle Physics **02** (2009), 008.

[122] T. O. Niinikoski *et al.*, *Thin Cryogenic X-Ray Windows*, submitted to Proc. ICEC 22, Seoul, (2008).

[123] N. A. Rio Duarte Elias *et al.*, *Technical Design Report of the CAST ^{3}He Gas System*, CERN-SPSC-2006-029, SPSC-TDR-001, CAST TDR 1, (2006), see http://doc.cern.ch//archive/electronic/cern/preprints/spsc/public/spsc-2006-029.pdf
N. A. Rio Duarte Elias, PhD Thesis, to be published.

[124] B. Lakić, Workshop on CAST Phase II, CERN, Geneva, Switzerland, (March 2004).
B. Lakić, 35th CAST Collaboration Meeting, CERN, Geneva, Switzerland, (February 2008).

[125] M. Krcmar and B. Lakić, *Density gradients and absorption effects in gas-filled magnetic helioscopes*, Internal CAST Report (June 2008).

[126] A. P. Dowling, *The Calculation of Thermoacoustic Oscillations*, Journal of Sound and Vibration **180(4)** (1995), 557.

[127] B. L. Henke *et al.*, *X-Ray Interactions: Photoabsorption, Scattering, Transmission, and Reflection at E=$50 - 30000$ eV, Z= $1 - 92$*, Atomic Data Nucl. Data Tables **54** (1993) 181, [http://www-cxro.lbl.gov].

[128] J. Ruz, *Search for solar axions with the Time Projection Chamber of the CERN Axion Solar Telscope with 4-Helium as buffer gas*, PhD Thesis, Universidad de Zaragoza, Spain, (2008).

[129] D. Autiero *et al.*, *The CAST Time Projection Chamber*, New Journal of Phys. **9** (2007) 171, [arXiv:physics/0702189].

[130] Y. Giomataris *et al.*, *Micromegas: a high-granularity position-sensitive gaseous detector for high particle-flux environments*, Nucl. Instrum. Methods Phys. Res. A **376** (1996) 29-35.
G. Charpak *et al.*, *Micromegas, a multipurpose gaseous detector*, Nucl. Instrum. Methods Phys. Res. A **478** (2002) 26-36.

[131] P. Abbon *et al.*, *The Micromegas detector of the CAST Experiment*, New Journal of Phys. **9** (2007) 170, [arXiv:physics/0702190].

[132] M. Kuster *et al.*, *The X-Ray Telescope of CAST*, New Journal of Phys. **9** (2007) 169, [arXiv:physics/0702188].

[133] D. Kang, *Search for Solar Axions with the CCD Detector at CAST (CERN Axion Solar Telescope)*, PhD Thesis, Albert-Ludwigs-Universität Freiburg (2007).

[134] T. Dafni, *A Search for Solar Axions with the MICROMEGAS Detector in CAST*, PhD Thesis, Technische Universität Darmstadt, Germany, (2005).
K. Kousouris, *Search for Solar Axions in the CAST Experiment with the Micromegas Detector*, PhD Thesis, University of Athens, Greece, (2006), in Greek only.
B. Beltran, *A TPC for Axion Searches in the CAST Experiment at CERN*, PhD Thesis, Universidad de Zaragoza, Spain, (2006).

[135] J. Altmann *et al.*, *Mirror System for the German X-ray Satellite ABRIXAS: I. Flight Mirror Fabrication, Integration, and Testing*, in X-Ray Optics, Instruments, and Missions II, Proc. SPIE **3444**, ed. R. B. Hoover and A. B. Walker (Bellingham,WA:SPIE) (1998) 350.
W. J. Egle *et al.*, *Mirror System for the German X-ray Satellite ABRIXAS: II. Design and Mirror Development*, in X-Ray Optics, Instruments, and Missions II, Proc. SPIE **3444**, ed. R. B. Hoover and A. B. Walker (Bellingham,WA:SPIE) (1998) 359.

[136] A. H. Compton and S. K. Allison, *X-Rays in Theory and Experiment*, 2nd ed., D. Van Nostrand, New York (1935).

[137] E. Abbe, *Abhandlungen über die Theorie des Mikroskops*, Fischer Verlag, Jena (1904).

[138] R. Giacconi, G. W. Clark, and B. B. Rossi, *A Brief Review of Experimental and Theoretical Progress in X-Ray Astronomy*, Technical Note of American Science and Engineering, ASE-TN-49 (1960).

[139] H. Wolter, *Spiegelsysteme streifenden Einfalls als abbildende Optiken für Röntgenstrahlen*, Ann. Phys. **10** (1952) 94.
H. Wolter, *Verallgemeinerte Schwarzschildsche Spiegelsysteme streifender Reflexion als Optiken für Röntgenstrahlen*, Ann. Phys. **10** (1952) 286.

[140] Private communication with Dr. Markus Kuster.

[141] M. Kuster *et al.*, *The X-Ray Mirror Telescope and the pn-CCD Detector of CAST*, Proc. SPIE **5500** (2004) 139.

[142] M. J. Freyberg *et al.*, *The MPE X-Ray Test Facility PANTER: Calibration of Hard X-Ray ($15 - 50$ keV) Optics*, Exp. Astron **20** (2005) 405.

[143] L. Strüder, *High-Resolution Imaging X-Ray Spectrometers*, Nucl. Instr. and Meth. A **454** (2000) 73.
L. Strüder *et al.*, *The MPI/AIT X-Ray Imager (MAXI) - High Speed pn CCDs for X-Ray Detection*, Nucl. Instr. and Meth. A **288** (1990) 227.

[144] E. Gatti and P. Rehak, *Semiconductor Drift Chamber - an Application of a Novel Charge Transport Scheme*, Nucl. Instr. and Meth. **225** (1984) 608.

[145] W. R. Leo, *Techniques for Nuclear and Particle Physics Experiments: A How-To Approach*, Springer-Verlag, Berlin/ Heidelberg, 2nd ed. (1994).

[146] G. Lutz, *Semiconductor Radiation Detectors*, Springer-Verlag, Berlin/ Heidelberg, Germany (1999).

[147] H. Bräuninger *et al., First Results with the pn-CCD Detector System for the XMM Satellite Mission*, Nucl. Instr. and Meth. A **326** (1993) 129.
M. Kuster, *Untersuchung spezieller Eigenschaften des pn-CCD Arrays für die Röntgensatelliten XMM und ABRIXAS*, Diploma Thesis, Eberhard-Karls-Universität Tübingen (1997).

[148] E. Pinotti *et al., The pn-CCD On-Chip Electronics*, Nucl. Instr. and Meth. A **326** (1993) 85.

[149] J. R. Janesick, *Scientific Charge-Coupled Devices*, SPIE Publications, Washington, USA (2001).

[150] R. Hartmann *et al., The Quantum Efficiency of the XMM pn-CCD Camera*, Proc. SPIE **3765** (1999) 703.

[151] H. Bräuninger *et al., Transmission Measurements of 5 Cold Windows F1, F2, F4, F6 and F8*, Internal CAST Report, CSTR-07-001, June-September (2005).

[152] G. Hoffmeister, *Bestimmung der Energiekalibration des pn-CCD-Detektors von CAST*, Bachelor Thesis, Technische Universität Darmstadt (2006).

[153] M. Popp *et al., Modelling the Energy Response of pn-CCDs in the* $0.2 - 10$ *keV band*, Nucl. Instr. and Meth. A **439** (2000) 567.
S. M. Kahn and R. J. Blisett, *The direct Deconvolution of X-ray Spectra*, Astrophys. J. **238** (1980) 417.

[154] M. Kuster, A. Nordt and J. Vogel, *X-ray-finger Measurement Report*, Internal CAST Report, CSTR-06-001, July (2006).
M. Kuster *et al., Telescope Alignment for Phase II of CAST*, Internal CAST Report, CSTR-05-002, November (2005).
M. Kuster *et al., X-Ray Alignment Measurement Report*, Internal CAST Report, CSTR-04-003, August (2005).
M. Kuster *et al., X-Ray Alignment Measurement Report*, Internal CAST Report, CSTR-04-002, September (2004).

[155] D. Weber, *Simulation der Refraktion im Konversionsvolumen des CERN Axion Solar Telescope (CAST)*, Bachelor Thesis, Technische Universität Darmstadt (2006).

[156] S. Cebrián *et al., pn-CCDs in a Low-Background Environment: Detector Background of the CAST X-ray Telescope*, Astropart. Phys. **28** (2007) 205, [arXiv:physics/0508064].

[157] NASA's HEASARC Software, *Online Documentation: FITS Data Format*, http://heasarc.gsfc.nasa.gov/docs/heasarc/fits.html.

[158] S. Borghi, *Tracking Variables*, Internal CAST Documentation (2008), http://cast.web.cern.ch/CAST/internal/SilviaDoc/TrackingVariable.pdf.

[159] S. Borghi, *List of Data Stored by the Slow Control System*, Internal CAST Documentation (2008), http://cast.web.cern.ch/CAST/internal/SilviaDoc/SCdoc.pdf.

[160] NASA's HEASARC Software, *Online Documentation: FTOOLS*, http://heasarc.gsfc.nasa.gov/docs/software/ftools/ftools_menu.html.

[161] M. Kuster, *X-Ray Telescope Quick-Look on Data*, Presentation, 37^{th} CAST Collaboration Meeting, 15.-17. October (2008).

[162] I. G. Irastorza, *Some Considerations towards a Protocol to deal with Candidate Events in CAST Phase II*, Internal CAST Report (24 July 2006).

[163] E. M. Purcell, *Electricity and Magnetism - Berkley Physics Course Volume 2*, McGraw Hill Higher Education, Newton, Massachusetts, USA (1965).

Acknowledgements

First and foremost I would like to thank Prof. Dr. Kay Königsmann for giving me the opportunity to work on my PhD in his group with the CAST experiment. Even being in great demand as dean of the Freiburg physics department amongst many other important obligations, he always took time to patiently discuss and answer my questions whenever I knocked on his office door. I am very grateful that he made it possible for me to become a part of CAST.
I am furthermore sincerely indebted to Prof. Dr. Horst Fischer and Dr. Jürgen Franz for the help and advise I received from them throughout the past years. Prof. Dr. Horst Fischer's inspiring support and catching enthusiasm have guided me through my time in Freiburg and he taught me that there is always a solution to every problem, I might have just not thought of it yet. Since the times of my diploma thesis, Dr. Jürgen Franz has been a special mentor for me. He introduced me to the CAST experiment and its collaboration. I would like to thank him for this effort as well as for the numerous enlightening and interesting discussions. Even being retired (if one ever really retires from being a physicist) he enthusiastically kept up his vivid interest for the work at CAST. He has been always available for any help, for which I am deeply grateful, and proofread this thesis from the first to the last page. I feel very fortunate to have worked with a committed physicist like him.

I have had the pleasure and the honor of working together with a team of excellent scientist on the CCD detector of CAST. Most influential for me has been my work with Dr. Markus Kuster, to whom I am very much obliged. He always puts his heart and soul into his work and inspires his mentees to do the same. I feel lucky that he introduced me to the fascinating world of space technology and semiconductor detectors. I am deeply grateful that he became a constant advisor for me, always answering my questions in the twinkling of an eye. I truly appreciate the tremendous effort he put in supporting me.

My PhD time would not have been as enjoyable as it was without the people of my Freiburg group. I thank you all for your support and discussions as well as for the fun we had. Thanks to our postdocs Dr. Andreas Mutter, Dr. Frank Nerling and Dr. Christian Schill for help with computers, physics and anything else. For sure I will not forget the hardware group with Florian Herrmann, Louis Lauser, Sebastian Schopferer, Stefan Bartknecht and Roland Hagemann. I already miss all the boxes and Gandalfs around me. I will also keep the COMPASS analysis team in mind with Heiner Wollny and his always welcome visits to the CAST office, Jochen Barwind, Donghee Kang, Wolfgang Käfer and Anselm Vossen.
Special thanks go to the CAST group members at Freiburg, which I will also truly miss: Elisabeth

Gruber and Tillmann Guthörl, who both joined the quest for the axion and revived the CAST spirit in Freiburg, and Donghwa Kang, who helped me getting started and became a dear friend.
One should always bear in mind the helping hands that make our daily lifes so much easier and friendlier: thanks to you Rainer Fastner, Khalil Rehmani and Susanne Rombach-Mikl.

Thinking of CAST, I would like to thank most sincerely Prof. Dr. Konstantin Zioutas for his support at CERN. Not only was he the one to bring CAST into being, but he is also keeping its spirit alive. Thanks for teaching us youngsters to “feel the magnet” amongst so many other valuable things. Moreover I am deeply indebted to Dr. Martyn Davenport. I am convinced it is for him that CAST is actually running. His energetic commitment, his concentrated efforts and unparalleled willingness to bring things to perfection have left me deeply impressed and influenced my way of working. Furthermore I would like to thank Dr. Heinrich Bräuninger for various instructive discussions. Thanks to Jean-Noël Joux and his team from the EST division at CERN for their patience and exactness to guarantee that CAST is looking to the Sun and to Laura and the Cryogenics team for making CAST one of the “coolest” places of the universe.
Furthermore I would like to express my gratitude to all my colleagues and friends at CAST for their help and support as well as for their loyalty and friendship: Jaime, Thomas, Silvia, Theopisti, Igor, Biljana, Kreso, Javier, Nuno, Hector, Asun, Mary, David, Annika, Theodoros and everybody else, who will hopefully forgive me for not being mentioned explicitly. I will not forget the times we shared, the discussions we had, the barbecues and all the fun. I think I might even miss the shifts. And I never thought I would seriously say that...

Unfortunately, there have also been most tragic events and I would like to use this opportunity to remember Berkol Dogan and Engin Arik who perished in the plane accident in Southern Turkey on 30 November 2007 together with several other cherished colleagues. Their memory will always remain in our hearts and we will never forget their smiles which brightened up our days.

Not without pride I am thinking of the friends who kept up their friendship with me despite large distances and long periods apart. Thanks for accepting me for who I am and putting a smile on my face:
Sebastian Trippel, Jana Ebner, Nine Miller with her lovely family, Stefan Meckler, Miriam Straub, and Angelika Walter.
Muchas gracias a la familia Ruz-Armendáriz con Rafael, Ana-María, Jorge y Elena para dar me una bienvenida muy cariñosa.

I would like to thank my father Manfred Vogel and his wife Roswitha as well as my adventurous brother Konstantin, my gorgeous sister Sophia and my charming brother Maximilian for always being there for me.
“Ich möchte meinem Vater Manfred Vogel und seiner Frau Roswitha zusammen mit meinem unerschrockenen Bruder Konstantin, meiner hinreißenden Schwester Sophia und meinem erstaunlichen Bruder Maximilian dafür danken, dass sie immer für mich da sind.”

Somebody once said that life is not measured by the number of breaths we take but by those moments that take our breath away. I thank you for these moments, Jaime, for your support and

the strength you give me to do what I always wanted to.

I feel very lucky and deeply proud of the fact that I have been accompanied in all situations of my life by my precious family and therefore my sincerest appreciation and my utmost respect belong to my dear mother Veronika Straub, her admirable husband Franz-Josef Straub and to my beloved brother Mario Straub. I thank you from the bottom of my heart!
It is for my family and my friends that I became who I am today. My gratitude and love will always be with them.
"Ich schätze mich sehr glücklich und bin wirklich stolz darauf, dass ich in allen Momenten und Situationen meines Lebens stets von meiner Familie begleitet wurde. Dafür gebührt meiner lieben Mutter Veronika Straub, ihrem bewunderswerten Mann Franz-Josef Straub und meinem Bruderherz Mario Straub meine äußerste Dankbarkeit und mein tiefster Respekt. Ich danke Euch aus tiefstem Herzen!
Meine Familie und meine Freunde sind der Grund dafür, dass ich zu dem wurde, was ich heute bin. Meine Dankbarkeit und Liebe gehört ihnen."